

Reconfigurable Antennas for Beam-Space MIMO Transmission with a Single Radio

THÈSE N° 6752 (2015)

PRÉSENTÉE LE 6 NOVEMBRE 2015

À LA FACULTÉ DES SCIENCES ET TECHNIQUES DE L'INGÉNIEUR
LABORATOIRE D'ÉLECTROMAGNÉTISME ET ACOUSTIQUE
PROGRAMME DOCTORAL EN GÉNIE ÉLECTRIQUE

ÉCOLE POLYTECHNIQUE FÉDÉRALE DE LAUSANNE

POUR L'OBTENTION DU GRADE DE DOCTEUR ÈS SCIENCES

PAR

Mohsen YOUSEFBEIKI

acceptée sur proposition du jury:

Prof. H. Shea, président du jury
Prof. J. R. Mosig, Prof. A. P. Burg, directeurs de thèse
Prof. C. Caloz, rapporteur
Prof. C. Mecklenbräuer, rapporteur
Prof. N. Kuster, rapporteur



ÉCOLE POLYTECHNIQUE
FÉDÉRALE DE LAUSANNE

Suisse
2015

*Nothing is so good for an ignorant man as silence;
and if he was sensible of this he would not be ignorant.*
— Saadi, Gulistan, Principles of Social Conduct, Maxim 23

in tribute to the memory of my late supervisor and friend
Julien Perruisseau-Carrier

*to my dear wife, HaleH,
for her wonderful love and support*

Acknowledgements

*Every breath when inhaled prolongs life, and when expired it exhilarates our nature;
wherefore every breathing confers two benefits, and for every benefit gratitude is due.*

— Saadi, Gulistan, Preface

Beyond a shadow of a doubt, I owe a debt of gratitude to a great many people who have either directly or indirectly contributed to my success and achievements, *if any*. What follows is my effort at seizing the opportunity right here to register my deep appreciation of their contributions.

I wish to express my deepest gratitude to my late thesis director, Prof. Julien Perruisseau-Carrier, who saved my academic career when I was at a particularly difficult juncture of my life journey. It was an unforgettable privilege to work under the supervision of such a brilliant and enthusiastic researcher, though this was cut short too soon by his untimely decease in June 2014. Julien was an honest and supportive friend, and his memory continues to serve as an inspiration to me:

*Life would be the unique stage of art;
everyone sings his own song and departs the stage.*

*The stage lasts forever;
greet the song that remains engraved in the people's memory.*

— Jaleh Esfahani, Migrating Birds

I am truly grateful to Prof. Juan Ramon Mosig and Prof. Andreas Peter Burg for taking over the supervision of my dissertation after the decease of Julien, and for their support and guidance in the last year. In particular, I thank Juan for having welcomed me back in the great family of LEMA and for his patience, kindness and helpful advice throughout the years of our acquaintance. I am very thankful to Andy for his insightful comments and constructive criticisms at different stages of my research, from the candidacy exam to the oral exam.

Besides my thesis directors, I would like to thank the rest of my thesis committee: Prof. Herbert Shea as the jury president from EPFL, Prof. Niels Kuster from ETH Zürich, Prof. Christophe Caloz from École Polytechnique de Montréal, and Prof. Christoph Mecklenbräuker from TU Wien, for investing time to review my dissertation and for their encouraging words.

Acknowledgements

I am very grateful to Osama Alrabadi for occasional but valuable discussions that helped me to form some ideas behind this work. My sincere thanks also go to Jean-François Zürcher and Tomislav Debogovic, for their assistance in the realization and measurements of the antennas presented in the thesis. I would like to acknowledge Pavle Belanovic and Raffael Hochreutener, who collaborated with me in developing the beam-space MIMO testbed. I would like to extend my gratitude to Andrew Austin for the time he dedicated to helping me with his technical expertise in over-the-air experiments. My appreciation also goes to Halima Najibi, my bachelor student, for her help with Chapter 6.

I am also indebted to the members of LEMA, GR-JPC, and TCL with whom I have been fortunate to work over the past five years: Prof. Anja Skrivervik and Dr. Michael Mattes for their encouragement; Eulalia, Sylvie, and Mercedes for their friendly help in dealing with administrative issues; David for the system administration and support; my office mates, Marco, Gabriele, Mohsen, and Lei, for the stimulating discussions and for all the fun we had together in the 'detached' DIA001; Laleh, Ruzica, Francesco, Athanasios, Maddalena, Benjamin, Roberto, Rafal, Eden, Ioannis, Nuno, Apostolos, Jovanche, Marc, Pietro, Michele, Hamed, Hussein, Maria, Eduardo, Sebastian, Baptiste, Anton, Joana, Mina, Santiago, Alexios, Nicholas, and Reza for being great colleagues and friends.

Many thanks should be given to my wonderful friends who made my stay in Switzerland extremely memorable. In particular, I would like to acknowledge the support of Pedram and Noushin, Banafsheh, Ali and Maryam, Amin and Marjan, and Nemat during the first months of my arrival in Lausanne. I deeply value the friendship of Hossein and Nahal, Vahid and Maryam, Alireza and Sara, Reza, Somayyeh, Mohammad, Nastaran, Omid, Behrouz and Fatemeh, Amir Hessam and Negar, Ali and Maryam, Armin and Paris, Naser and Sanaz, Ahmad and Behnaz, Arash and Mitra, Ebrahim and Fereshteh, Fazel and Fatemeh, Meysam and Hoda, Sina and Nasibeh, Hamed and Shirin, Farid, Saeid and Behnaz, Masih and Maryam, and so many others.

Finally and most importantly, none of this would have been possible without the unwavering love, support and encouragement of my family. Sincerest thanks go to my mother and father, Masoumeh and Fazlollah, who made numerous selfless sacrifices to provide me with every opportunity throughout my life. I give huge thanks to my sister and brother, Anousheh and Mohammad Hossein, for being a constant source of love, concern, encouragement and strength over the years. My thanks would not be complete without acknowledging the invaluable support of my parents-in-law and my brother-in-law. And the last in sequence but truly the first in importance, my wholehearted appreciation goes to my other half, HaleH, for her unconditional and unfailing love, tolerance, and support, and also for staying by my side through thick and thin.

Lausanne, 17 August 2015

*Mohsen
Cousefbeikey*

Abstract

Multiple-input multiple-output (MIMO) techniques allow remarkable improvements in the reliability and/or transmission rate of wireless communication systems. However, there are several major challenges towards the implementation of conventional MIMO concept in terminals with size, cost, and power constraints. First of all, insufficient space impedes the design of efficient and decorrelated MIMO antennas. Second, MIMO traditionally demands each antenna to be fed by its own RF chain, which in turn results in greater hardware complexity, larger power consumption, and higher implementation cost. Among all reduced-complexity and antenna-decoupling schemes proposed so far, the so-called *beam-space MIMO* has attracted great interest as a potential solution for addressing both problems concurrently. The key idea therein is to engineer the radiation pattern of a single-feed antenna structure for each symbol period, such that multiple independent symbols directly modulate a predefined set of orthogonal virtual patterns in the far-field, therefore allowing true MIMO transmission using a single RF chain and a compact antenna structure. More important in practice, the transmitted information can be retrieved using a *conventional* MIMO receiver. However, the transformation of this idea into reality entails dealing with various practical aspects that are commonly overlooked in theoretical and conceptual developments. This dissertation explores the beam-space MIMO concept from the perspective of the antenna engineering, and aims at addressing several key issues associated with the actual design and implementation of beam-space MIMO systems.

The early developments of beam-space MIMO concerned switched parasitic arrays. However, the requirement of utilizing several physically-separate radiators is inconvenient for practicable implementation in compact portable devices. To solve this problem, a single-radiator load-modulated antenna solution is proposed in this dissertation. Another primary challenge consists in emulating high-order modulation schemes such as phase shift keying (PSK) with realistic hardware. Here, an efficient beam-space MIMO strategy is developed, which allows transmitting PSK data streams of any modulation order using only purely reactive reconfigurable loads, and without the need for a symbol-rate dynamic matching network. The approach is illustrated by the design and fabrication of a realistic antenna for QPSK signaling. The performance of a beam-space MIMO system which utilizes the fabricated antenna is then investigated through over-the-air experiments, and compared with conventional MIMO in realistic environments.

Embedding information in the radiation patterns, beam-space MIMO systems are expected to

Abstract

be inherently prone to multiplexing performance degradation in the presence of external field perturbation. This makes the study of near-field interaction influence on beam-space MIMO distinct from those carried out for the case of conventional systems. This issue is considered for the first time in this dissertation. Moreover, like any reconfigurable system, a beam-space MIMO system may suffer from bandwidth expansion of the transmitted signals. The final part of the work is directed towards this important issue. To reduce out-of-band radiation effect, a solution based on shaping the time-domain response of the reconfigurable components is presented.

The studies presented in this thesis constitute a crucial step towards MIMO with simpler and cheaper hardware for real-life wireless terminals.

Key words: beam-space MIMO, bit error rate, channel capacity, data multiplexing, multi-port radiator, out-of-band radiation, over-the-air experiment, p-i-n diode, PSK modulation, reconfigurable antenna, reduced-complexity MIMO, single-radio MIMO, user effect, varactor diode, variable load.

Résumé

Les techniques « entrées multiples, sorties multiples » (Multiple-Input Multiple-Output ou MIMO) permettent des améliorations considérables dans la fiabilité et le débit de transmission des systèmes de communication sans fil. Cependant, il y a plusieurs défis majeurs pour implémenter les concepts conventionnels MIMO dans de terminaux avec des contraintes en taille, coût et puissance. D'une part, le manque d'espace empêche la conception d'antennes MIMO découpées et efficaces. D'autre part dans l'approche traditionnelle, chaque antenne doit être alimentée par sa propre chaîne RF, ce qui résulte dans une plus grande complexité matérielle, une consommation de puissance augmentée et des coûts de fabrication plus élevés. Parmi les techniques proposées pour réduire la complexité des antennes et leur couplage, l'approche appelée « MIMO à faisceau spatial » (beam-space MIMO) est de grand intérêt par sa promesse d'attaquer simultanément les deux problèmes. L'idée de base ici est d'ajuster le diagramme de rayonnement d'une antenne à un seul accès pour chaque symbole de transmission de façon que un ensemble multiple de symboles indépendants peut moduler directement un ensemble prédéfini de diagrammes virtuels de champ lointain orthogonaux. Ceci permet une vraie transmission MIMO avec une seule chaîne RF et une antenne compacte. Encore plus important en pratique, l'information transmise peut être récupérée en utilisant un récepteur MIMO conventionnel. La réalisation de cette idée demande la considération de plusieurs aspects pratiques qui sont souvent ignorés dans les constructions théoriques et conceptuelles. Cette thèse explore le concept « Beam-space MIMO system » du point de vue de l'ingénieur antennes et essaie de traiter les problèmes essentiels associés à la conception et réalisation pratique d'un tel système.

Les premiers développements de l'idée Beam-space MIMO concernaient des réseaux parasites commutables. Cependant, l'obligation d'utiliser plusieurs radiateurs physiquement distincts n'est pas pratique du point de vue de la portabilité. Pour résoudre ce problème, cette thèse propose une antenne avec un élément rayonnant unique à charge variable. Un autre défi est celui de simuler des systèmes modulations d'ordre élevé comme la modulation par changement de phase (Phase-Shift Keying, PSK) avec un matériel réaliste. Ici, on développe une stratégie efficace basée sur le concept Beam-space MIMO, et qui permet la transmission d'un flux de données PSK d'ordre quelconque, en utilisant seulement des charges purement réactives et sans demander un circuit d'adaptation dynamique. L'approche préconisée est illustrée par la conception et fabrication d'une antenne capable de signalisation PSK en quadrature (QPSK). Les performances d'un système Beam-space MIMO utilisant cette antenne sont alors évaluées

Résumé

grâce à des expériences en transmission hertzienne dans des environnements réalistes et comparées avec celles des systèmes MIMO conventionnels.

Avec l'information implantée dans les diagrammes de rayonnement, les systèmes Beam-space MIMO sont sensibles par nature à une dégradation de ses performances multiplex en présence de champs externes perturbateurs. Ceci rend l'étude de l'influence des interactions en champ proche sur les systèmes Beam-space MIMO différente des celles réalisées sur des systèmes conventionnels. Ce problème est analysé pour la première fois dans cette thèse. De plus, comme tout système reconfigurable, un système Beam-space MIMO peut souffrir de l'élargissement de la bande des signaux transmis. La partie finale de la thèse traite cette question si importante. Pour réduire l'effet du rayonnement hors-bande, on introduit une solution basée sur le modelage de la réponse temporelle des composants reconfigurables.

Les études présentées dans cette thèse constituent une étape cruciale vers des systèmes MIMO avec composants plus simples et moins chers, donc bien adaptés aux terminaux réels.

Mots clés : antenne reconfigurable, beam-space MIMO, capacité du canal, charge variable, diode PIN, diode varicap, effet de l'utilisateur, MIMO à complexité réduite, MIMO avec une seule chaîne RF, modulation par changement de phase, multiplexage des données, radiateur multi-port, rayonnement hors-bande, taux d'erreur.

Contents

Acknowledgements	i
Abstract (English/Français)	iii
List of Figures	xi
List of Tables	xvii
Acronyms and Abbreviations	xix
1 Introduction	1
1.1 Background	1
1.2 Motivation and Thesis Objectives	3
1.2.1 Research Framework	4
1.3 Layout and Original Contributions	5
1.4 Notation	7
2 Beam-Space MIMO: Basics and State-of-the-Art	9
2.1 Overview	9
2.2 Recall on Conventional MIMO	9
2.2.1 Channel Modeling	10
2.2.2 Spatial Correlation	11
2.3 Beam-Space MIMO: Concept	13
2.4 Beam-Space MIMO: State-of-the-Art	15
2.5 Conclusion	17
3 Beam-Space MIMO: Realistic Antennas	19
3.1 Overview	19
3.2 Compact Antenna Solutions	20
3.3 Efficient Antenna Modeling	21
3.4 Hardware Technologies for Variable Loads	23
3.5 Decomposition Techniques/Basis Definition	24
3.5.1 Gram-Schmidt Approach	25
3.5.2 Mirror Image Pattern Pair Approach	26
3.6 Antenna Design Approaches	28

Contents

3.7	Modeling and Measurement of Variable Loads	30
3.7.1	Methodology	31
3.7.2	Experimental Verification	33
3.8	Realistic Antenna Prototype for BPSK Signaling	35
3.8.1	Design and Structure	36
3.8.2	Results and Discussion	40
3.8.3	Frequency Reconfigurability	44
3.9	Conclusion	48
4	Beam-Space MIMO: High-Order Modulation Support	49
4.1	Overview	49
4.2	Multiplexing Strategy: Theory and Implementation	50
4.2.1	Incident Power Wave Vector	50
4.2.2	Basis Vectors	52
4.2.3	Multiplexing Technique	55
4.2.4	Discussion and Implementation	57
4.2.5	Passive Reactive Loading Constraint	58
4.2.6	Case of Lossless Radiators	61
4.3	Design Procedure and Antenna Prototype	62
4.3.1	Design	63
4.3.2	Results and Discussion	67
4.4	Conclusion	72
5	Beam-Space MIMO: Over-the-Air Experiments	75
5.1	Overview	75
5.2	Receiver Architecture for Beam-Space MIMO	76
5.3	Proof-of-Concept Experiments	78
5.3.1	Testbed Setup	78
5.3.2	System Design and Functionality	79
5.3.3	Results	81
5.4	Performance Analysis	83
5.4.1	Experimental Methodology and Procedure	83
5.4.2	Measurement Setup	84
5.4.3	Measurement Results	86
5.5	Conclusion	97
6	Beam-Space MIMO: Near-Field Perturbation Effects	99
6.1	Overview	99
6.2	Near-Field Perturbation Effects in Beam-Space MIMO	100
6.3	User Effects: a Case Study of BPSK Beam-Space MIMO Antenna	102
6.3.1	Adaptive Variable Loads	106
6.4	User Effects: a Case Study of QPSK Beam-Space MIMO Antenna	106
6.5	Conclusion	110

7 Beam-Space MIMO: Out-of-Band Radiation Suppression	113
7.1 Overview	113
7.2 Time-Domain Study of Beam-Space MIMO Antennas	114
7.3 Time-Domain Response Shaping of Variable Loads	117
7.3.1 Theoretical Analysis	117
7.3.2 Numerical Results	120
7.3.3 Practical Implementation and Preliminary Experiments	124
7.4 Conclusion	125
8 Conclusions and Perspectives	127
A PSK Constrained MIMO Capacity	131
Bibliography	133
Curriculum Vitae	143

List of Figures

1.1	A conventional MIMO transceiver with P transmit antennas and Q receive antennas requires $P + Q$ RF chains.	2
1.2	Symbolic representation of the beam-space MIMO concept. (a) Single-feed parasitic antenna array. (b) Equivalent virtual co-located antennas radiating modulated basis patterns.	3
1.3	Connection between the different chapters of the thesis.	5
2.1	Discrete physical model for MIMO channel.	11
2.2	Symbolic representation of beam-space MIMO transmission. Each complex symbol x_n modulates a virtual antenna of complex basis pattern \mathcal{B}_n	14
2.3	Schematic diagram of 3-element ESPAR proposed in prior art for single-radio MIMO transmission of PSK modulation schemes.	16
2.4	(a) Symbolic diagram of the technique proposed where the first symbol is modulated, up-converted and fed into the central active element whereas the second symbol is XORed with the first one. The output control signal is used for swapping the reactive loads jX_1 and jX_2 . (b) Photograph of the parasitic antenna array designed.	17
3.1	Proposed antenna system solution for beam-space MIMO, generally composed of connected multi-port radiator rather than physically-separate multi-element arrays.	21
3.2	Techniques for implementing variable loads based on solid state technology. (a) Diodes directly as variable loads. (b) Switch implementation technique. . .	24
3.3	Proposed compact antenna solution for beam-space MIMO based on the mirror image pattern pair approach.	28
3.4	Compact antenna solution with control elements (here p-i-n diodes) directly as variable loads to obviate complex variable load circuits.	30
3.5	(a) Measurement of the lumped element (or the load circuit) under test using a TRL calibration, and then extracting the initial model. (b) Simulation of the exact setup of the measurement, including the initial extracted model of the element, and then extracting the full-wave model.	32

List of Figures

3.6	An intuitive idealistic illustration of the error introduced by the measurement setup itself prior to correction. The extracted capacitance includes the coupling through the substrate. A similar phenomenon occurs with the series inductive element.	32
3.7	The fabricated circuits for measuring the calibrated S-parameters.	34
3.8	A comparison among the series branches of the measured, initial full-wave and corrected models. (a) When the p-i-n diode is reverse biased. (b) When the p-i-n diode is forward biased.	34
3.9	A comparison among the series reactance values obtained from the measured raw data, the initial model extracted from the measurement, the initial full-wave model, and the final full-wave model (extracted from the simulation of the corrected model). (a) When the p-i-n diode is reverse biased. (b) When the p-i-n diode is forward biased.	35
3.10	Unfolded schematic of antenna system prototype for beam-space multiplexing of two BPSK signals.	36
3.11	Baseband paths of the antenna system in Fig. 3.10.	37
3.12	Current distribution on the prototype's conductors at the center frequencies of the uplink and downlink bands, when the upper and lower p-i-n diode are forward and reverse biased ('on' and 'off'), respectively.	38
3.13	Two additional configurations for investigating the effects of the arms and the stubs.	39
3.14	Effects of the stubs and the arms on the frequency-domain impedance response of the antenna.	39
3.15	Fabricated beam-space MIMO antenna prototype, integrated to a hypothetical hand-held device; (b) top view, (c) bottom view. (c) Beryllium-copper (BeCu) strips for realizing the arms before folding.	40
3.16	Reflection coefficient of the beam-space MIMO antenna obtained from simulations (with corrected and uncorrected circuit models) and measurements (for both antenna's operational states).	41
3.17	Setup for far-field measurements of the fully-operational beam-space MIMO antenna in an anechoic chamber (in the plane of the platform).	41
3.18	Simulated and measured radiation patterns of the beam-space MIMO antenna prototype at 1.95 GHz in the plane of the device platform (a) in State 1, and (b) in State 2.	42
3.19	Simulated magnitude of the angular basis patterns of the antenna prototype at 1.95 GHz. Note that the orthogonality between the basis patterns applies to the complex patterns over the full sphere and not to their magnitudes.	43
3.20	Power radiated by the radiation patterns and the basis patterns in the far-field for a unit power excitation.	44

3.21	Channel capacity under BPSK signaling for two E_s/N_0 values as a function of frequency; solid curves: beam-space MIMO using the designed antenna prototype, and dashed curves: ideal 2×2 conventional MIMO. The capacity was calculated based on the Monte-Carlo averaging where $1e+6$ channel and noise realizations were used. Pulse shaping is not included.	45
3.22	Maximum achievable capacity under BPSK signaling, when the antenna's loadings are properly tuned at each frequency.	46
3.23	Corresponding total efficiency and power imbalance ratio as functions of frequency, when the antenna's loadings are properly tuned at each frequency. . .	46
3.24	Required reactance values for achieving maximum channel capacity.	47
3.25	A contour map of the capacity under BPSK signaling with respect to X_I and X_{II} at 1.95 GHz. The figure shows that a wide range of reactance values can provide an acceptable level of channel capacity.	47
4.1	(a) A load-modulated antenna composed of a symmetric three-port radiator. Note that the single-port structure (i.e., when two passive ports are loaded) is not generally symmetrical. (b) Equivalent signal flow of the antenna. The incident and reflected power waves are denoted by a_p and b_p , $p \in \{0, 1, 2\}$, respectively. For the sake of simplicity, the source impedance Z_0 is chosen to be equal to the reference impedance of the S-parameters.	51
4.2	Symbolic representation of the proposed system capable of multiplexing two input symbol streams.	59
4.3	(a) Corrected voltage-reactance curves of the varactor diodes. (b) Corrected voltage-resistance curves of the varactor diodes. The reverse breakdown voltage of the diodes is reported to be around 22 V.	64
4.4	Method to include the resistive loss of the variable loads in the design procedure.	65
4.5	Proposed three-port radiator with an axis of symmetry in yz -plane. The quarter-wavelength balun acts as an open-end termination at the edge of the antenna. (a) Top view. (b) Bottom view.	66
4.6	Required reactance values at the passive ports of the optimized three-port radiator as a function of the free parameter X_I . The possible tuning range of the varactor diodes has been specified by a solid rectangle.	67
4.7	Flowchart of the beam-space MIMO antenna design.	68
4.8	Fabricated QPSK beam-space MIMO antenna. (a) Top view. (b) Bottom view. .	68
4.9	Reflection coefficient of the QPSK beam-space MIMO antenna.	69
4.10	3D view of the antenna's radiation patterns in dB at 2.45 GHz; (a) the total magnitude, (b) the magnitude of the θ -component, and (c) the magnitude of the φ -component.	70
4.11	3D view of the antenna's basis patterns in dB at 2.45 GHz; (a) the total magnitude, (b) the magnitude of the θ -component, and (c) the magnitude of the φ -component.	71
4.12	Setup for far-field measurements of the fully-operational QPSK beam-space MIMO antenna in an anechoic chamber.	72

List of Figures

4.13	Measured EVM of the QPSK beam-space MIMO antenna.	72
4.14	Channel capacity under QPSK signaling as a function of E_s/N_0 . The capacity was calculated based on the Monte-Carlo averaging on 1e+6 random channel and noise realizations while assuming a Kronecker flat-fading channel modeling. Pulse shaping is not included.	73
5.1	The hardware connectivity in the beam-space MIMO testbed.	78
5.2	Amplifier circuit used for amplifying the baseband control signals.	79
5.3	(a) Frame structure used for beam-space MIMO experiments. (b) Corresponding antenna state, \mathcal{S} , and the symbol combination ratio, x_r , during the frame transmission.	80
5.4	Receiver block diagram.	81
5.5	Baseband control signals (during the data segment) at the outputs of the amplifier.	82
5.6	Scatter plot of received signal constellation after ZF equalization.	82
5.7	Diagram outlining the experimental procedure for the measurement of the channel matrices and the computation of mutual information and BER.	84
5.8	(a) Experimental Platform used for the performance analysis of beam-space MIMO. (b) Experimental Platform used for the performance analysis of conventional 2×2 MIMO.	85
5.9	(a) XY positioner used in our measurement campaign. (b) Antenna support fixture mounted on the positioner.	85
5.10	Frame structure used for conventional MIMO experiments.	86
5.11	Measurement points for transmit antenna(s).	87
5.12	Laboratory where the experiments were performed.	87
5.13	Floor plan of the measurement environment and the positions of the transmitter and the receiver. Blue areas represent the work desks and storage cabinets. The receiver location is marked by a red/green rectangle in the first/second scenario.	88
5.14	Polarization of the receive antennas; (a) vertically polarized, (b) perpendicular angled at 45°	88
5.15	Magnitude of the channel coefficients in the conventional MIMO experiment regarding the position of the transmit antennas. Dark blue pixels show the locations with no valid measurement.	90
5.16	Magnitude of the channel coefficients in the beam-space MIMO experiment with the receive antennas vertically polarized regarding the position of the transmit antennas. Dark blue pixels show the locations with no valid measurement.	91
5.17	Magnitude of the channel coefficients in the beam-space MIMO experiment with the receive antennas angled at 45° regarding the position of the transmit antennas. Dark blue pixels show the locations with no valid measurement.	92
5.18	CDF of the channel ellipticity.	92
5.19	Mutual information (MI) and ergodic capacity (EC) curves obtained from Monte-Carlo simulations using the measured and normalized channel matrices.	93
5.20	CDF of the mutual information for different SNR values.	93

5.21 SER obtained from Monte-Carlo simulations using the measured and normalized channel matrices.	94
5.22 CDF of the channel ellipticity.	96
5.23 Mutual information curves obtained from Monte-Carlo simulations using the measured and normalized channel matrices.	96
5.24 CDF of the mutual information for different SNR values.	97
5.25 SER obtained from Monte-Carlo simulations using the measured and normalized channel matrices.	97
6.1 The placement of the beam-space MIMO antenna under study in different scenarios: (a) nearby SAM head phantom, (b) in SAM hand phantom, and (c) in SAM hand phantom nearby SAM head phantom.	102
6.2 Reflection coefficient of the beam-space MIMO antenna under study. The parameter d determines the minimum spacing between the antenna and the head.	103
6.3 Channel capacity under BPSK signaling as a function of E_s/N_0 . The capacity was calculated based on the Monte-Carlo averaging on 1e+6 random channel and noise realizations. Pulse shaping is not included.	104
6.4 Achievable capacity improvement as a function of E_s/N_0 for different scenarios.	104
6.5 Multiplexing efficiency variations versus antenna performance parameters.	105
6.6 Contour map of the channel capacity with respect to X_I and X_{II} for a E_s/N_0 of 0 dB.	106
6.7 The placement of the QPSK beam-space MIMO antenna under study near the SAM hand ($\epsilon_r = 31.0$ and $\sigma = 1.64 \text{ S.m}^{-1}$).	107
6.8 Constellation distortion of the transmitted signals at $\{\theta, \varphi\} = \{45^\circ, 294^\circ\}$ when placing the antenna near the hand (Fig. 6.7a).	108
6.9 EVM of the transmitted signals when placing the antenna near the hand; (a) in the case of Fig. 6.7a, and (b) in the case of Fig. 6.7b.	109
6.10 Constellation distortion of the received signals for the receiving antennas at $\{\theta_1, \varphi_1, \theta_2, \varphi_2\} = \{45^\circ, 294^\circ, 45^\circ, 298^\circ\}$ when placing the transmitting antenna near the hand (Fig. 6.7a).	110
6.11 CDF plot of the RCE of the received signal for 1.4e+6 random single-path LOS transmit-receive scenarios while considering two receive antennas with an angular distance of 3° - 5°	110
7.1 Bandwidth expansion caused by abrupt switching of the variable loads (the p-i-n diodes) for the BPSK beam-space MIMO antenna fabricated in Chapter 3. The symbol rate of transmission was 390625 symbols/s. A root-raised cosine pulse shaping filter with a roll-off factor of 0.5 was used on the RF path.	114
7.2 Beam-space MIMO antenna presented in Chapter 4 as a combination of time-variant and time-invariant subsystems.	114

List of Figures

7.3	In-phase (top) and quadrature (bottom) components of the symbol combination ratio signal for different pulse shaping schemes. The symbol rate, f_s , is 380 ksymbols/s. For the raised-cosine scheme, $\beta = 0.5$	121
7.4	Power spectral density of the symbol combination ratio signal using Welch method for different pulse shaping schemes.	122
7.5	Time-domain response of the loads' reactive parts for different pulse shaping schemes.	122
7.6	Time-domain response of the loads' resistive parts for the raised-cosine pulse shaping scheme.	122
7.7	Power spectral density of the radiated signal for different pulse shaping schemes, calculated at 1000 random solid angles for both polarizations.	123
7.8	(a) Power spectral density of the radiated signal when using only the reactive part solutions of the raised-cosine pulse shaping scheme. (b) Power spectral density of the radiated signal when changing the reactances linearly over time. The blue and red densities are taken from Fig. 7.7 for comparison.	124
7.9	Time-varying $\tilde{b}_0(t)$ when directly shaping the reactance values over time.	124
7.10	Effect of analogue pre-distortion filter on the out-of-band radiation from the QPSK beam-space MIMO antenna. The symbol rate of transmission was 390625 symbols/s.	125
7.11	Effect of pre-distortion filter on out-of-band radiation from the BPSK beam-space MIMO antenna. The symbol rate of transmission was 390625 symbols/s.	126
7.12	Shaping the actuation waveform using a digital pre-distortion filter for the BPSK beam-space MIMO antenna.	126

List of Tables

1.1	Connection between publications and thesis chapters.	7
3.1	Combinations of two BPSK signals.	27
3.2	Initial and corrected models of the embedded lumped elements.	37
3.3	Radiation efficiency of the antenna prototype.	42
4.1	Combination of two QPSK symbols.	63
4.2	Corrected equivalent circuit models of the lumped elements.	66
4.3	Selected reactance set and corresponding bias voltages of the varactor diodes.	67
5.1	Actual biasing voltages versus voltages at the amplifier outputs.	79
5.2	System parameters used in the validation experiment.	82
5.3	Valid measurements.	89
5.4	Global average of average received power.	89
5.5	Average RCE of the received data.	89
5.6	Magnitude of the spatial correlation matrix and the channel ellipticity.	91
5.7	Valid measurements.	94
5.8	Global average of average received power.	95
5.9	Magnitude of the spatial correlation matrix and the channel ellipticity.	95
6.1	User body effects on the performance of the beam-space MIMO antenna.	103
6.2	Case studies for assessing the contribution of each parameter impairment to beam-space MIMO performance degradation.	105
6.3	Load optimization effect on the channel capacity for a E_s/N_0 of 0 dB. MI_0 and MI_{opt} are the channel capacity values when the antenna embeds the p-i-n diodes and the optimal loads, respectively.	107
6.4	User body effects on the characteristics of the beam-space MIMO antenna.	108

Acronyms and Abbreviations

AoA	Angle of Arrival
AoD	Angle of Departure
AWGN	Additive White Gaussian Noise
BER	Bit Error Rate
BPSK	Binary Phase-Shift Keying
CDF	Cumulative Distribution Function
DPSK	Differential Phase Shift Keying
DSP	Digital Signal Processing
ESPAR	Electronically Steerable Passive Array Radiators
EVM	Error Vector Magnitude
FPGA	Field-Programmable Gate Array
GMSK	Gaussian minimum-shift keying
i.i.d.	Independent and Identically Distributed
LOS	Line-of-Sight
LS	Least Squares
LTE	Long Term Evolution
LTI	Linear Time-Invariant
LTV	Linear Time-Variant
MEMS	MicroElectroMechanical Systems
MIMO	Multiple-Input Multiple-Output
ML	Maximum Likelihood
MMSE	Minimum Mean Square Error
MSK	Minimum-Shift Keying
NLOS	Non-Line-of-Sight
OFDM	Orthogonal Frequency-Division Multiplexing
OOK	On-Off-Keying
PAS	Power Angular Spectrum
PCB	Printed Circuit Board
PIFA	Planar Inverted-F Antenna
PSK	Phase-Shift Keying
QAM	Quadrature Amplitude Modulation
QPSK	Quadrature Phase-Shift Keying
RCE	Received Constellation Error

Acronyms and Abbreviations

RF	radio frequency
RMS	Root Mean Square
Rx	Receiver
SAM	Specific Anthropomorphic Mannequin
SAR	Specific Absorption Rate
SER	Symbol Error Rate
SISO	Single-Input Single-Output
SNR	Signal-to-Noise Ratio
SPA	Switched Parasitic Array
TRL	Thru-Reflect-Line
Tx	Transmitter
USRP	Universal Software Radio Peripheral
WBAN	Wireless Body Area Network
ZF	Zero-Forcing

1 Introduction

*But for the cravings of the belly, not a bird would have fallen into the snare;
nay, the fowler would not have spread his net.*

— Saadi, Gulistan, Principles of Social Conduct, Maxim 51

1.1 Background

Wireless devices have become ubiquitous and an indispensable part of our everyday life. Meanwhile, despite the scarce spectrum and energy resources available for wireless communications, there is an ever-increasing demand for higher data rates and more robust performance. To meet these growing needs, multiple-input multiple-output (MIMO) systems have emerged as a most promising technology for current and future wireless communication systems. Unlike traditional single-input single-output (SISO) systems, MIMO systems utilize multiple active antennas at both the transmitting and receiving ends, and thus make benefit of the extra spatial dimension in order to enhance the spectral efficiency [1, 2].

However, the implementation of the MIMO concept in small and low-cost communication devices is subject to several design challenges. First of all, the performance of MIMO systems critically depends on the availability of independent multiple sub-channels [3]. This is typically achieved by placing the multiple antennas far enough from each other [4, 5], a requirement that is not practical in real-life terminals with strict size constraints. Insufficient antenna spacing might cause high correlation of MIMO channels, and in turn degrade the capacity performance. Moreover, as the platform size is reduced, the isolation between antennas decreases, and a higher fraction of power is coupled into adjacent ports instead of being radiated. The isolation between a pair of coupled antennas is traditionally achieved by creating an artificial reverse path to the coupling path, using for example a decoupling network [6, 7]. However, such networks have negative impact on the bandwidth of the multiple antenna system besides being complex and lossy.

Secondly, the integration of conventional MIMO architectures in small platforms adds com-

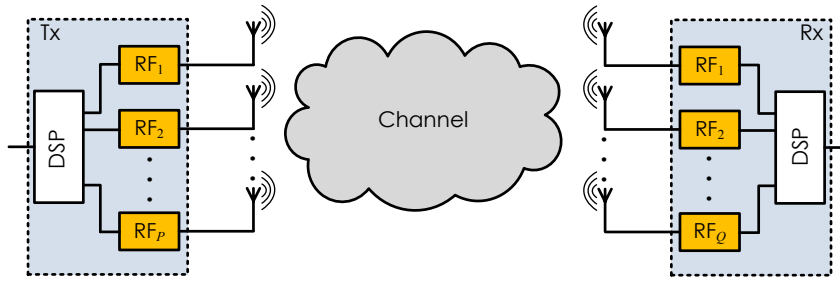


Figure 1.1: A conventional MIMO transceiver with P transmit antennas and Q receive antennas requires $P + Q$ RF chains.

plexity, cost and power constraints since, as shown in Fig. 1.1, each antenna requires a complete radio frequency (RF) chain (including power or low-noise amplifier, up- or down-converter, digital-to-analogue or analogue-to-digital converter, filters). Moreover, due to likely spurious emission and imperfect filtering, extreme care should be taken in order to mitigate the self-interference among the parallel RF chains. To overcome this limitation, several MIMO architectures with reduced RF hardware complexity have been proposed in the literature such as antenna selection [8, 9], analogue antenna combining [10, 11], time-division multiplexing [12], code-modulated path-sharing [13] and spatial modulation [14–16]. However, most of the aforementioned techniques are applicable only at the receiver side and do not support spatial multiplexing of independent signals with a single RF chain. In fact, spatial multiplexing, unlike the other MIMO modes such as diversity and power focusing (beam-forming), is often referred to as the true MIMO. Spatial modulation, though being an open-loop transmit technique, achieves only a logarithmic increase of the spectral efficiency with the number of transmit antennas compared to the linear growth provided by spatial multiplexing. Moreover, such reduced-complexity MIMO techniques still requires multiple antennas, and thus are more suited to base stations than small portable devices. This emphasizes the need for a different MIMO architecture addressing both problems concurrently, otherwise it is questionable whether a real advantage results from the use of multiple antenna systems at the expense of placing them very close together.

To this end, Kalis *et al.* in [17] introduced a novel technique, referred to as *beam-space* MIMO, which allows data multiplexing using wireless transmitters equipped with a single RF chain and a parasitic antenna array. Instead of driving each symbol stream to a distinct active antenna element as in conventional MIMO transmission, information symbols are embedded in the radiation patterns of a single-feed parasitic antenna array by modulating an orthonormal set of virtual basis functions in the beam-space domain. In other words, multiple symbol streams are assigned to multiple virtual antennas having orthogonal radiation patterns, as symbolically depicted in Fig. 1.2. Therefore, diverse streams are simultaneously transmitted towards different angles of departure. In rich-scattering environments, decorrelation between the channel coefficients is guaranteed by the basis definition and thereby the transmitted mixture of information can be reliably decoded using a conventional MIMO receiver. Since

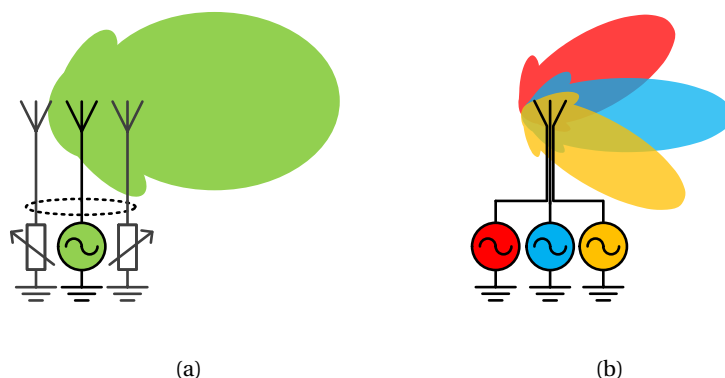


Figure 1.2: Symbolic representation of the beam-space MIMO concept. (a) Single-feed parasitic antenna array. (b) Equivalent virtual co-located antennas radiating modulated basis patterns.

the operational principle of parasitic antenna arrays is based on the strong near-field coupling between a single active element and several parasitics, the reduction of the inter-element spacing does not entail any power loss. Therefore, beam-space MIMO shows the potential of simultaneously addressing both the size and multiple RF chain challenges of conventional MIMO techniques.

1.2 Motivation and Thesis Objectives

The beam-space MIMO concept allows emulating conventional true MIMO transmission but with a single RF chain and a compact antenna structure, and thus can bring the MIMO benefits to small and low-cost wireless platforms. However, while quite straight-forward on paper, the actual design of operational beam-space MIMO systems is faced with various implementation issues and major practical constraints, that are commonly overlooked in early theoretical and conceptual developments. Some important issues deserving particular attention are described below.

Realistic antennas: Parasitic arrays composed of monopole or dipole antennas, though interesting for setting the theoretical basis of the beam-space MIMO concept, are unsuitable to small portable devices, mainly due to their dimensions. Indeed, despite having much smaller inter-element spacing than conventional MIMO arrays, the elements themselves remain large to be used in platforms with size constraints. Alternative antenna designs to be readily incorporated in a portable device are highly desired.

Support of high-order modulation schemes: In beam-space MIMO, pattern reconfiguration is utilized as a mean of analogue signal modulation. Therefore, successful data multiplexing is highly dependent on creating proper radiation patterns. The basic limita-

tions in the hardware technology platform enabling the required reconfiguration, such as switching speed, tuning range, cost and complexity, make the efficient emulation of high-order modulation schemes extremely difficult.

Performance in real channels: Another challenge of beam-space MIMO lies in maintaining independent and identically distributed (i.i.d.) sub-channels in real propagation scenarios. In rich-scattering environments, such sub-channels can be achieved by mapping the data symbols onto an orthogonal set of basis patterns. However, when the angular spread of the multi-path components is not wide enough, an orthogonal basis is not sufficient to have decorrelated sub-channels. The channel decorrelation impairment degrades the capacity performance of any MIMO system.

Near-field interaction with environment: The operating environment of a portable device, such as the user's hand in the case of a handheld platform, affects the antenna's radiation properties through near-field coupling. Since beam-space MIMO relies on embedding information symbols in the antenna's radiation patterns, it would be more prone to performance degradation than its conventional counterpart in the presence of external field perturbation.

Out-of-band radiation: The transmission concept in beam-space MIMO requires time-varying components for the symbol-rate reconfiguration of the antenna's radiation pattern. Such components can produce out-of-input-band frequencies in their outputs. Consequently, the wave radiated by the antenna might possess a wider frequency spectrum than the input excitation. This can seriously undermine the interest in beam-space MIMO.

In this context, *this dissertation contributes to the further development and evolution of beam-space MIMO by addressing several critical issues.* More specifically, the main objectives of this research are as follows:

- to explore realistic antenna designs for portable applications, which differ from simple parasitic arrays of monopole and dipole elements;
- to develop beam-space MIMO techniques supporting higher order modulations using realistic and low-complexity hardware;
- to investigate and analyze the performance of beam-space MIMO systems in real propagation environments;
- to study and determine the effects of external perturbation in beam-space MIMO;
- to explore possible solutions to suppress unwanted out-of-band radiation.

1.2.1 Research Framework

The PhD thesis was carried out in the framework of a research project entitled 'Reconfigurable Microwave Technology for Novel Telecom and Sensing Applications' funded by Swiss

National Science Foundation (SNSF) under grant n°133583. Some parts of the research was supported within two collaborative research agreements between EPFL and ‘Electronics and Telecommunications Research Institute’ (ETRI), South Korea.

1.3 Layout and Original Contributions

The thesis is organized in eight chapters. Fig. 1.3 shows the structure of the thesis and the connection between the different chapters. Chapter 2 presents the basic knowledge and the state-of-the-art of beam-space MIMO. Chapters 3 and 4 develop new antenna designs for beam-space MIMO. Chapter 5 investigates the over-the-air performance of beam-space MIMO systems. Chapters 6 and 7 focus on practical issues of beam-space MIMO transmission. The following paragraphs give an overview of each chapter and its original contributions.

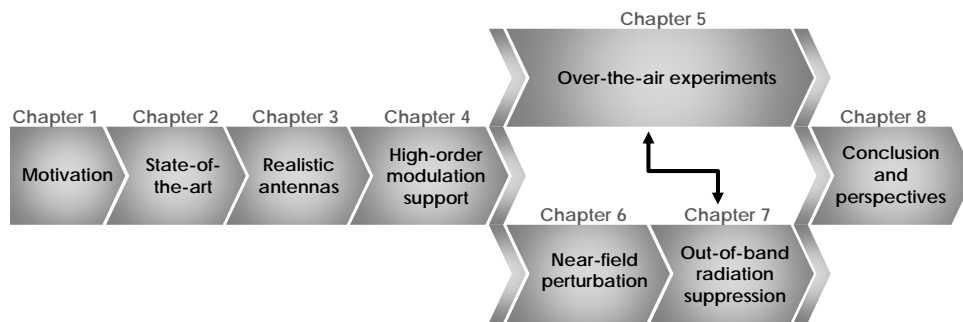


Figure 1.3: Connection between the different chapters of the thesis.

Chapter 2 – Beam-Space MIMO: Basics and State-of-the-Art

Outline: The basic concept of beam-space MIMO is described, and the related mathematical developments are presented from the perspective of the antenna engineering. Thereafter, a literature review of the state-of-the-art on this topic is provided, and the strengths and drawbacks of existing related works are discussed. This overview serves to act as a point of reference for later chapters, and to motivate the research directions.

Chapter 3 – Beam-Space MIMO: Realistic Antennas

Outline: Single-radiator load-modulated antennas are introduced as alternative designs to parasitic antenna arrays for practical beam-space MIMO applications. A brief recall on the theory of multi-port antennas is presented, which describes how to deduce the characteristics of load-modulated antennas from a single electromagnetic full-wave simulation and post-processing. Afterwards, considerations related to selection and modeling of variable loads are discussed. A concrete operational prototype for single-radio multiplexing of binary phase shift-keying (BPSK) signals is designed and measured.

Original contributions: (i) An efficient methodology to accurately model the variable loads in full-wave solvers is presented. (ii) First integrated beam-space MIMO antenna for BPSK signaling is designed and measured.

Chapter 1. Introduction

Chapter 4 – Beam-Space MIMO: High-Order Modulation Support

Outline: This chapter introduces an efficient beam-space MIMO strategy which enables multiplexing two PSK streams of any modulation order with a realistic single-feed antenna system. The approach makes the use of only variable passive loads for pattern reconfiguration, and ensures a constant input impedance independently of the two data streams. The procedure is demonstrated by an antenna design prototype supporting the single-radio transmission of two quadrature phase shift-keying (QPSK) symbol streams.

Original contributions: (i) An efficient beam-space MIMO approach for multiplexing higher order PSK streams with no need for active loads or reconfigurable matching networks is proposed. (ii) First-ever fully-operational QPSK beam-space MIMO antenna is designed and measured.

Chapter 5 – Beam-Space MIMO: Over-the-Air Experiments

Outline: This chapter describes a detailed experimental evaluation of beam-space MIMO in real propagation environments. A test-bed consisting of transmit and receive subsystems is constructed to conduct over-the-air experiments. A beam-space MIMO system, using the antenna developed and manufactured in the previous chapter, is compared with a conventional 2×2 MIMO system in different indoor environments.

Original contributions: (i) To our best knowledge, first successful demonstration of single-radio MIMO transmission under QPSK signaling is presented. (ii) This is the first time that performance analysis of beam-space MIMO systems in real channels is carried out.

Chapter 6 – Beam-Space MIMO: Near-Field Perturbation Effects

Outline: A rigorous study on the effects of external perturbation in beam-space MIMO is given. First, the variations of different performance parameters are evaluated when placing a BPSK beam-space MIMO antenna in close proximity to the user body. Thereafter, the study is extended to the case of higher order modulation schemes, where the external perturbation may affect the modulation quality in beam-space MIMO.

Original contributions: (i) The near-field perturbation effects in beam-space MIMO are studied for the first time. (ii) It is shown that under BPSK signaling, beam-space MIMO is not more vulnerable to near-field perturbation than conventional MIMO, and has the potential to perform very well in typical human body interaction scenarios. (iii) When using linear zero-forcing receivers, near-field interaction of the higher-order beam-space MIMO antenna with its immediate environment causes the actual constellation points to deviate from their ideal locations.

Chapter 7 – Beam-Space MIMO: Out-of-Band Radiation Suppression

Outline: The issue of the spectrum expansion associated with pattern reconfiguration is investigated. A solution based on control waveform shaping of reconfigurable components is presented. The simulation and measurement results are given.

Original contributions: (i) Bandwidth expansion of transmitted signals in beam-space MIMO is discussed and partially addressed for the first time.

Chapter 8 – Conclusions and Perspectives

Outline: The chapter summarizes the contributions of the thesis, and suggests some possible areas for further work.

The original contributions presented in this dissertation have been disseminated through one book chapter, several publications in peer-reviewed journals and through presentations at scientific conferences. The connection between the publications and thesis chapters is summarized in Table 1.1.

Table 1.1: Connection between publications and thesis chapters.

Publications	Topic	Chapter
[18]	Design and implementation of load-modulated antennas for beam-space MIMO	3
[19, 20]	Compact integrated antenna solution for beam-space MIMO	3
[21]	Accurate modeling of lumped components in full-wave simulations	3
[22]	beam-space MIMO technique for higher order modulation schemes	4
[23]	QPSK beam-space MIMO antenna	4
[24]	Performance analysis of beam-space MIMO systems in real channels	5
[25–27]	Effects of near-field interaction in beam-space MIMO	6
[28]	Out-of-band radiation reduction in beam-space MIMO	7

1.4 Notation

In the following, boldface lower-case and upper-case characters denote vectors and matrices, respectively. The operators $(\cdot)^*$, $(\cdot)^T$, and $(\cdot)^H$ designate complex conjugate, transpose, and complex conjugate transpose (Hermitian) operators, respectively. The notation \mathbf{I}_N indicates an identity matrix of size $N \times N$. $(\cdot)_{ij}$ returns the $\{i, j\}$ entry of the enclosed matrix and $(\cdot)_i$ returns the i th element of the enclosed vector whereas $|\cdot|$ and $\|\cdot\|_F$ return the absolute value and the Frobenius norm, respectively. The operator \in indicates that the (random) variable belongs to a certain set of numbers. The $\text{vec}(\cdot)$ operation stacks all columns of a matrix into a single column vector. $\mathbb{E}[\cdot]$ denotes the expectation while \otimes indicates a Kronecker product. The operator $\text{diag}(\mathbf{v})$ returns a square matrix with the elements of the vector \mathbf{v} laid across the main diagonal of the matrix.

2 Beam-Space MIMO: Basics and State-of-the-Art

[...] *Having been asked how he had attained to such a pitch of knowledge, replied: 'Whatever I was ignorant of myself, I was not ashamed to inquire about.'*

— Saadi, Gulistan, Principles of Social Conduct, Maxim 79

2.1 Overview

In this chapter, we present the basic knowledge and the state-of-the-art of beam-space MIMO, as an effective alternative for conventional true MIMO but with reduced hardware complexity and cost. The chapter starts with a recall on conventional MIMO, where a general physical model for multi-antenna channels is presented and the spatial correlation properties are derived. Based on this introductory section, the idea of beam-space MIMO architectures is elaborated on in Section 2.3. Afterwards, Section 2.4 presents a general state-of-the-art on this single-radio MIMO technique, covering various aspects from theory to early developments. The literature survey allows us to gain an insight into practical aspects and implementation challenges and, therefore, to define the research paths required to come to the realistic beam-space MIMO systems.

2.2 Recall on Conventional MIMO

Let us assume a frequency-flat, slow-fading MIMO channel with P transmit and Q receive antennas. In complex baseband, the signal vector \mathbf{y} corresponding to one symbol interval at the Q receive antennas reads

$$\mathbf{y} = \mathbf{H}\mathbf{x} + \mathbf{n}, \quad (2.1)$$

where $\mathbf{x} \in \mathbb{C}^{P \times 1}$ is the transmit signal vector, $\mathbf{H} \in \mathbb{C}^{Q \times P}$ denotes the channel matrix, and $\mathbf{n} \in \mathbb{C}^{Q \times 1}$ is the noise vector at the receiver. Entries of \mathbf{H} , indexed as $h_{qp} : q = 1, 2, \dots, Q, p = 1, 2, \dots, P$, describe the channel coefficient between the p th input and the q th output. Addi-

tionally, we consider far-field scattering condition where the scatterers are far enough from both the transmitter and the receiver.

2.2.1 Channel Modeling

Existing models of the MIMO channel can be categorized into two groups. On the one hand are the so-called analytical channel representations, such as Kronecker model [29, 30], virtual channel representation [31, 32], and eigen-beam model [33]. This group provides a mathematical representation of the MIMO channel matrix, but is typically unable to establish the link between system performance and antenna configuration. On the other hand, physical modeling of scattering environment gives a more explicit insight into how the channel coefficients are related to propagation parameters and antenna characteristics [34–36].

Here we formulate the channel based on a full-vector representation of the propagation environment and the antenna patterns. Let $\mathcal{F}_{\text{Tx},p}(\Omega_{\text{Tx}}) \in \mathbb{C}^{2 \times 1}$ and $\mathcal{F}_{\text{Rx},q}(\Omega_{\text{Rx}}) \in \mathbb{C}^{2 \times 1}$ denote the far-field (embedded) radiation patterns associated with the p th transmit antenna and the q th receive antenna, respectively^{1,2}. The radiation patterns are represented by complex vectors, and contain both amplitude and phase information on the θ and φ components. Ω_{Tx} and Ω_{Rx} are the solid angles at the transmitter and the receiver, respectively. The entries of \mathbf{H} , h_{qp} , can be modeled as

$$h_{qp} = \iint_{\Omega_{\text{Rx}}, \Omega_{\text{Tx}}} \mathcal{F}_{\text{Rx},q}^{\text{T}}(\Omega_{\text{Rx}}) \mathcal{O}(\Omega_{\text{Rx}}, \Omega_{\text{Tx}}) \mathcal{F}_{\text{Tx},p}(\Omega_{\text{Tx}}) d\Omega_{\text{Tx}} d\Omega_{\text{Rx}}, \quad (2.2)$$

where

$$\mathcal{O}(\Omega_{\text{Rx}}, \Omega_{\text{Tx}}) = \begin{bmatrix} \mathcal{O}_{\theta\theta}(\Omega_{\text{Rx}}, \Omega_{\text{Tx}}) & \mathcal{O}_{\theta\varphi}(\Omega_{\text{Rx}}, \Omega_{\text{Tx}}) \\ \mathcal{O}_{\varphi\theta}(\Omega_{\text{Rx}}, \Omega_{\text{Tx}}) & \mathcal{O}_{\varphi\varphi}(\Omega_{\text{Rx}}, \Omega_{\text{Tx}}) \end{bmatrix} \quad (2.3)$$

represents the physical scattering (spatial spreading) taking into account path loss, polarization transformation, scattering, diffraction, and other channel effects. To further simplify the notation, we denote $\mathbf{\Omega} = (\Omega_{\text{Rx}}, \Omega_{\text{Tx}})$. Accordingly, (2.2) can be written as

$$h_{qp} = \int_{\mathbf{\Omega}} \mathcal{F}_{qp}^{\text{T}}(\mathbf{\Omega}) \text{vec}(\mathcal{O}(\mathbf{\Omega})) d\mathbf{\Omega}, \quad (2.4)$$

where

$$\mathcal{F}_{qp}(\mathbf{\Omega}) = \mathcal{F}_{\text{Tx},p}(\Omega_{\text{Tx}}) \otimes \mathcal{F}_{\text{Rx},q}(\Omega_{\text{Rx}}). \quad (2.5)$$

¹The radiation patterns of all transmit (receive) antennas are expressed in the transmit (receive) array coordinate system: $\mathcal{E}(r, \Omega) = \mathcal{F}(\Omega) \frac{e^{-jkr}}{r}$, where \mathcal{E} is the far-field electric-field intensity vector, k is the angular wavenumber, and r is the distance from the origin of the coordinate system to the observation point.

²The embedded radiation pattern (also called active radiation patterns) of a transmit (receive) antenna is computed when driving the antenna with a unit power level and terminating all other transmit (receive) antennas with the reference impedance Z_0 [37].

Many realistic environments can be modeled via a set of scattering clusters with limited angular spread, as illustrated in Fig. 2.1, and thus $\Theta(\Omega_{\text{Rx}}, \Omega_{\text{Tx}})$ is vanishing except for small regions of $\Omega_{\text{Tx}}\Omega_{\text{Rx}}$ -plane. In extreme case, a discrete physical model is used in which the transmitter and the receiver are coupled via propagation along L paths, each path characterized by an angle of departure (AoD) $\Omega_{\text{Tx},l}$ and an angle of arrival (AoA) $\Omega_{\text{Rx},l}$:

$$\Theta(\Omega_{\text{Rx}}, \Omega_{\text{Tx}}) = \sum_{l=1}^L \Theta_l \delta(\Omega_{\text{Rx}} - \Omega_{\text{Rx},l}) \delta(\Omega_{\text{Tx}} - \Omega_{\text{Tx},l}), \quad (2.6)$$

where $\Theta_l = \Theta(\Omega_{\text{Rx},l}, \Omega_{\text{Tx},l})$. Accordingly, the entries of the MIMO channel matrix can be expressed as

$$h_{qp} = \sum_{l=1}^L \mathcal{F}_{\text{Rx},q}^{\text{T}}(\Omega_{\text{Rx},l}) \Theta_l \mathcal{F}_{\text{Tx},p}(\Omega_{\text{Tx},l}). \quad (2.7)$$

2.2.2 Spatial Correlation

The advantage of MIMO techniques originates from the exploitation of the spatial structure of the propagation environment. Therefore, the spatial characteristics of the channel dictates the ultimate performance of a multi-antenna system. Given a particular propagation environment described by \mathbf{H} , the full spatial correlation matrix can be constructed using

$$\mathbf{R}_{\mathbf{H}} := \mathbb{E}_{\mathbf{H}} [\text{vec}(\mathbf{H}) \text{vec}(\mathbf{H})^{\text{H}}]. \quad (2.8)$$

This $QP \times QP$ matrix describes the correlation between all pairs of transmit-receive channels. Assuming that the field radiated into (or received from) one angle is uncorrelated with that

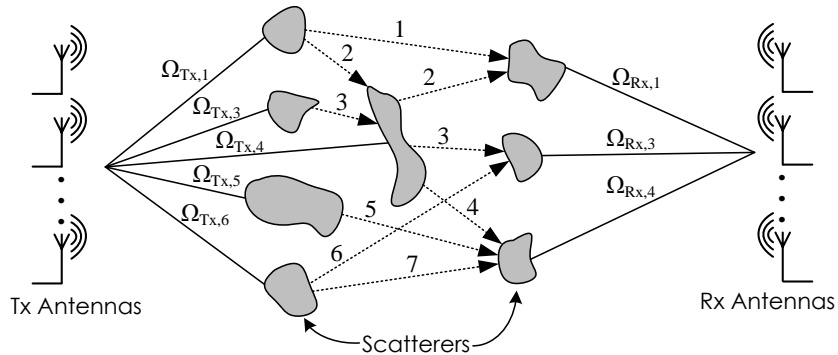


Figure 2.1: Discrete physical model for MIMO channel.

radiated into (or received from) another [36], according to (2.4) the elements of \mathbf{R}_H becomes

$$R_{mn,st} = \mathbb{E}[h_{mn}h_{st}^*] = \int \mathcal{F}_{mn}^T(\boldsymbol{\Omega})\mathcal{A}(\boldsymbol{\Omega})\mathcal{F}_{st}^*(\boldsymbol{\Omega})d\boldsymbol{\Omega}, \quad (2.9)$$

where $\mathcal{A}(\boldsymbol{\Omega}) = \mathbb{E}[\text{vec}(\mathcal{O}(\boldsymbol{\Omega}))\text{vec}(\mathcal{O}(\boldsymbol{\Omega}))^H]$ represents the joint power angular spectrum (PAS) of the propagating electromagnetic field. This makes it clear that the correlation coefficient between two individual channels directly depends on the transmit and receive radiation patterns and the joint PAS.

The analysis can be further simplified by assuming that the angular dispersion can be modeled independently at the transmit and receive ends using the marginal angular spectra $\mathcal{A}_{R_x}(\Omega_{R_x})$ and $\mathcal{A}_{T_x}(\Omega_{T_x})$. Accordingly, transmit and receive correlation matrices \mathbf{R}_{T_x} and \mathbf{R}_{R_x} are defined as

$$\mathbf{R}_{T_x} \triangleq \mathbb{E}[\mathbf{H}^T\mathbf{H}^*] \quad (2.10)$$

$$\mathbf{R}_{R_x} \triangleq \mathbb{E}[\mathbf{H}\mathbf{H}^H]. \quad (2.11)$$

Similarly, the transmit (or receive) correlation is related to the transmit (or receive) PAS and the transmit (or receive) radiation patterns:

$$R_{T_x,np} = \int \mathcal{F}_{T_x,n}^T(\Omega_{T_x})\mathcal{A}_{T_x}(\Omega_{T_x})\mathcal{F}_{T_x,p}^*(\Omega_{T_x})d\Omega_{T_x}, \quad (2.12)$$

$$R_{R_x,mq} = \int \mathcal{F}_{R_x,m}^T(\Omega_{R_x})\mathcal{A}_{R_x}(\Omega_{R_x})\mathcal{F}_{R_x,q}^*(\Omega_{R_x})d\Omega_{R_x}. \quad (2.13)$$

Transmit (or receive) correlation generally reduces the effective dimensionality of the transmitter (or receiver) [38, 39]. Therefore, the basic principle in MIMO antenna design is to decorrelate the signals transmitted from (or received at) multiple antennas, namely to find mechanisms for making the off-diagonal entries of \mathbf{R}_{T_x} (or \mathbf{R}_{R_x}) as small as possible. In open-loop MIMO systems, where there is no channel state information at the transmitter, the optimum strategy is to split the power equally over all transmit antennas, and thus an \mathbf{R}_{T_x} equal to the identity matrix is ideally desired. It is important to emphasize that the correlation coefficients depend on the antenna properties and the angular spread of multi-path components. Therefore, it is not always possible to satisfy the decorrelation condition, particularly for poor scattering environments with small angular spread [40]. For a very rich scattering environment with a uniform energy distribution around the transmitter (or receiver), the PAS is nearly constant and independent of the solid angle, and the transmit (or receive) correlation only depends on the transmit (or receive) radiation patterns. Consequently, by employing antennas with orthogonal radiation patterns, namely

$$\int \mathcal{F}_{T_x,n}^T(\Omega_{T_x})\mathcal{F}_{T_x,p}^*(\Omega_{T_x})d\Omega_{T_x} = 0, \quad n \neq p, \quad (2.14)$$

the signals undergo reflections and diffraction among the scatterers in such a way that uncorrelated channels can be achieved. Typically, the same strategy is adopted when the characteristics of the propagation channel is unknown to antenna designers.

From an antenna perspective, different physical mechanisms can be used to guarantee the pattern orthogonality among multiple antennas. A common approach, widely used in conventional MIMO, is to maintain a minimum distance (of at least half a wavelength) between the adjacent antennas such that the resultant radiation patterns (defined relative to a common coordinate system) become nearly orthogonal [4]. However, as discussed in Chapter 1, this approach is impractical in real-life wireless devices with strict size constraints. Another way to produce orthogonal radiation patterns is to pair co-located antennas with orthogonal polarizations (i.e., dual-polarized antennas) [5, 41] or with angularly disjoint radiation patterns [42, 43]. Ideally, this approach ensures uncorrelated transmission or reception by multiple co-located antennas, and thus allows for the antenna size reduction compared to the former approach. In the next section, we will show how this mechanism is developed and utilized in a beam-space MIMO architecture to enable MIMO transmission with a single-radio.

2.3 Beam-Space MIMO: Concept

The modeling approach followed in the previous section shows that in non-line-of-sight (NLOS) scattered environments optimum MIMO performance is achieved provided that the antenna system at the transmitter (or receiver) is able to produce multiple orthogonal radiation patterns concurrently. In conventional MIMO, where the transmit signal vector \mathbf{x} is upconverted to \mathbf{s} using P RF chains and fed into the P transmit antennas, the total far-field electric field corresponding to one symbol interval can be expressed as

$$\mathcal{E}(r, \Omega_{\text{Tx}}) = \mathcal{E}_\circ(\Omega_{\text{Tx}}) \frac{e^{-jkr}}{r}, \quad (2.15)$$

where

$$\mathcal{E}_\circ(\Omega_{\text{Tx}}) = \sum_{p=1}^P x_p \mathcal{F}_{\text{Tx},p}(\Omega_{\text{Tx}}). \quad (2.16)$$

Therefore, it can be concluded that the primary task of the transmit antennas in conventional MIMO is to map diverse transmit symbols onto orthogonal radiation patterns in the far-field.

As explained in Chapter 1, the implementation of the conventional MIMO concept in small and low-cost devices is subject to several design challenges, mainly due to the necessity of employing multiple active antennas. The question now is how to emulate the conventional MIMO transmission with only a single active antenna. The answer lies in the *beam-space* domain representation of radiation patterns. In beam-space domain, any radiation pattern

can be uniquely represented by one N -tuple vector $\mathbf{w} = [w_1, w_2, \dots, w_N]^T$ such that

$$\mathcal{E}_o(\Omega) = \sum_{n=1}^N w_n \mathcal{B}_n(\Omega), \quad (2.17)$$

where $\{\mathcal{B}_n(\Omega)\}_{n=1}^N$ denote the basis patterns which are mutually orthogonal and span an N -dimensional space. To ease the notation in the formulation, we dropped the subscript ‘Tx’. Note that $\mathcal{E}_o(\Omega) \longleftrightarrow \mathbf{w}$ is a one-to-one mapping from the angular domain to the beam-space domain. This representation suggests that the radiation pattern of a single active antenna can be employed as extra dimension to encode information. Provided that the radiation pattern at each symbol period can be expressed as a linear combination of the basis patterns with weights that correspond to the baseband symbols to be transmitted in the far-field (i.e., $\mathbf{w} = \mathbf{x}$), the conventional MIMO transmission is exactly emulated: the symbols are driven to N virtual co-located antennas whose embedded radiation patterns are equal to the basis patterns [17]. This technique, referred to as beam-space MIMO, allows transmitting multiple data streams while using a single RF chain and a much more compact antenna system to that of conventional MIMO systems. Moreover, since the pattern orthogonality obtained by the basis definition ensures the decorrelation between the channel coefficients in rich scattering environments, the transmitted mixture of information can be reliably decoded using a traditional MIMO receiver.

In contrast to conventional MIMO transmitters, a beam-space MIMO transmitter allocates each symbol to a distinct basis pattern (see Fig. 2.2). Thus, the number of symbols that can be concurrently transmitted is restricted by the dimension of the beam-space domain of the antenna (i.e., the number of available basis patterns). Apparently, the radiation pattern at each symbol period is determined by the symbol vector \mathbf{x} :

$$\mathcal{E}_o(\Omega) = \sum_{n=1}^N x_n \mathcal{B}_n(\Omega). \quad (2.18)$$

The implementation of the beam-space MIMO principle in practice is strongly dependent on

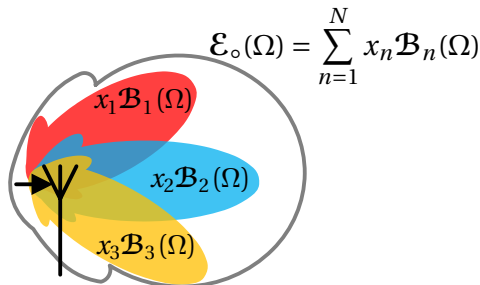


Figure 2.2: Symbolic representation of beam-space MIMO transmission. Each complex symbol x_n modulates a virtual antenna of complex basis pattern \mathcal{B}_n .

designing a single-feed reconfigurable antenna whose radiation pattern satisfies (2.18) for all possible symbol vectors from the considered signal constellation diagram.

To conclude, we would like to stress that, the beam-space MIMO concept must not be confused with the antenna pattern modulation technique, introduced in [44, 45] as a variant of spatial modulation. Although both techniques can increase the spectral efficiency by utilizing only one active transmit antenna capable of creating multiple radiation patterns, they inherently differ in the transmission-reception principle. Instead of emulating the conventional MIMO transmission by mapping the symbols onto the basis patterns as in beam-space MIMO, antenna pattern modulation uses the index of the current radiation pattern as an added source of information. Therefore, while a conventional MIMO receiver can reliably decode the symbols transmitted by a beam-space MIMO system, antenna pattern modulation requires a special detector that jointly estimates the pattern index and the symbols applied to the active antenna. Moreover, the spectral efficiency is increased by base-two logarithm of the number of uncorrelated radiation patterns in antenna pattern modulation, but linearly by the number of orthogonal basis patterns in beam-space MIMO.

2.4 Beam-Space MIMO: State-of-the-Art

Beam-space MIMO has been addressed in several previous publications such as [17, 46–61]. The general concept of beam-space MIMO was first introduced on a theoretical level in [17, 46]. Parasitic antenna arrays, in both switched parasitic array (SPA) and electronically steerable passive array radiator (ESPAR) configurations, were considered for supporting on-off-keying (OOK), BPSK and QPSK modulation formats. The reason behind the choice of parasitic antenna arrays for beam-space MIMO is clear: as shown in Fig. 1.2a, the existence of a single active antenna and multiple closely-spaced parasitics loaded by switches or variable reactive impedances offers high pattern-reconfiguration capabilities³ in a compact structure. The beam-space MIMO transmission in [17, 46] was achieved by creating radiation patterns as linear combinations of weakly correlated beams (cardioids). However, these works were based on simple analytical description of ideal omni-directional elementary radiators in two-dimensional planes, and limited to lower order PSK modulation schemes.

An iterative stochastic algorithm was proposed in [47] for enabling an ESPAR to form desired radiation patterns of beam-space MIMO. The algorithm attempts to minimize a cost function of the cross-correlation coefficient between the desired and current radiation patterns, and find the proper set of parasitic loadings. A similar optimization problem solved by a genetic algorithm with binary encoded chromosomes in [48]. In [49–51], it was claimed that by decomposing the far-field radiation patterns of a compact three-element ESPAR into a natural basis that inherently exists in the array factor itself, beam-space MIMO for PSK modulation of any order could be supported. As shown in Fig. 2.3, the authors proposed feeding the

³Namely, a functionality similar to that of a conventional antenna array fed by a feed network embedding RF phase shifters.

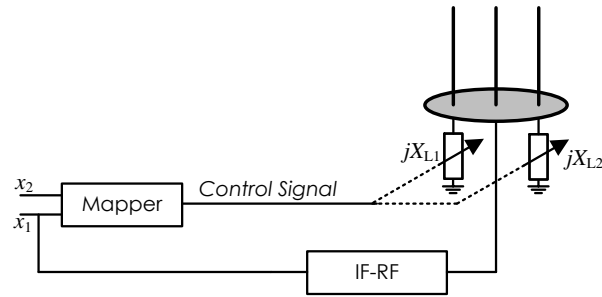


Figure 2.3: Schematic diagram of 3-element ESPAR proposed in [51] for single-radio MIMO transmission of PSK modulation schemes.

active element with the first PSK symbol, while simultaneously changing the loading of the two parasitic elements at the symbol rate according to the ratio of two baseband PSK symbols to be spatially multiplexed. The methodology was later generalized in [52, 53] using Gram-Schmidt decomposition for constructing a set of orthogonal functions. Unfortunately, all these works relied on restrictive or unrealistic theoretical assumptions, such as the requirement of considering ideal dipole antennas, while approximating their far-field by two-dimensional horizontal cuts for the modulating-loads calculations. More importantly, from the perspective of antenna engineering, the dependency of the active antenna's input impedance to the terminating loads were overlooked in the above-mentioned methods. Therefore, switching the reactive loading would result in large dynamic variation of the input impedance. This seriously undermines the interest in beam-space MIMO since the need for a symbol-rate dynamic matching network would offset the main benefit of the single-radio MIMO system, namely, reduced RF hardware complexity.

The next key steps towards the implementation of the beam-space MIMO concept were reported in [54–56]. The authors in [54] demonstrated that a parasitic antenna array with the capability of creating mirror image radiation patterns can be used for transmitting two BPSK signals simultaneously. Consequently, the first fully-operational antenna for beam-space MIMO was designed in [55], where the mirrored radiation patterns were created by permuting the reactive loads of a symmetric parasitic array of three printed dipoles (see Fig. 2.4). The first successful experimental demonstration of the beam-space MIMO concept was then reported in [56], where the designed antenna was employed for multiplexing two BPSK data streams over-the-air. However, while applying such an approach to BPSK signaling is straightforward, scaling to higher order PSK modulation is not possible.

Adaptive reconfiguration of basis patterns for providing channel-aware beam-space MIMO transmission was discussed in [57]. It was theoretically shown that pattern adaptation based on channel knowledge could provide improvement in the achieved ergodic capacity. However, the feasibility of creating all of required radiation patterns in practice is questionable. Moreover, huge computational complexity for finding the appropriate set of loads at the parasitic

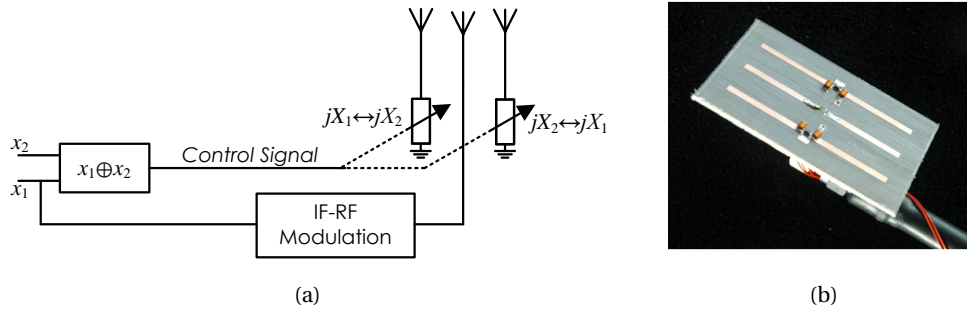


Figure 2.4: (a) Symbolic diagram of the technique proposed in [54] where the first symbol is modulated, up-converted and fed into the central active element whereas the second symbol is XORed with the first one. The output control signal is used for swapping the reactive loads jX_1 and jX_2 . (b) Photograph of the parasitic antenna array designed in [55].

elements prohibits the use of channel-aware beam-space MIMO algorithms practically.

In [58], the Vertical Bell Laboratories Layered Space-Time (V-BLAST) reception scheme for beam-space MIMO was adapted in order to precisely simulate the performance of realistic receiver operation. The estimation algorithms, such as linear least squares (LS) and minimum mean square error (MMSE), were then formulated in [58], where the authors concluded that the estimation procedures are quite similar with conventional MIMO algorithms.

Finally, multiplexing quadrature amplitude modulation (QAM) signals over the air was reported in [60], where a two-element ESPAR and a loading circuit composed of resistors and active components were used in simulations. Apart from various unrealistic assumptions in the design procedure and obvious errors in presenting the results, we would like to stress that the use of lossy and active loading circuits in the RF frequency band would degrade the power efficiency and the stability of the system, while seriously increasing the RF hardware complexity. Another questionable work was published in [61], where an ESPAR with *decoupled elements* were used for the beam-space MIMO transmission of QAM signals. We draw the attention of the reader to the fact that according to the operation principle of parasitic antenna arrays strong electromagnetic coupling among the antenna elements are required for providing pattern reconfiguration capabilities.

2.5 Conclusion

It has been shown that in the beam-space MIMO architecture a single-feed reconfigurable antenna is able to emulate the MIMO transmission from multiple antennas, thus allowing the use of MIMO benefits in cost and size sensitive wireless devices. To do so, the radiation pattern at each symbol period must be decomposable into a linear combination of the symbols with the orthogonal basis patterns. Previously-known parasitic arrays of dipoles and monopoles has been used in the literature to implement the beam-space MIMO concept.

Chapter 2. Beam-Space MIMO: Basics and State-of-the-Art

Nevertheless, the literature review reveals that the practical implementation of beam-space MIMO is in its early developments, requiring dealing with numerous challenges that are generally overlooked in the prior art. The following chapters in this thesis are devoted to the exploration and discussion of important research directions for further development of realistic beam-space MIMO systems.

3 Beam-Space MIMO: Realistic Antennas

*Whosoever acquired knowledge, and did not practise it,
resembleth him who ploughed, but did not sow.*
— Saadi, Gulistan, Principles of Social Conduct, Maxim 41

3.1 Overview

In the previous chapter, we explained how parasitic antenna arrays can be used to multiplex multiple symbols with a single RF chain when seen from a novel perspective. Indeed, these antenna structures have been widely utilized over the past to achieve analogue beam steering [62, 63] and angular pattern diversity [64, 65]. Obviously, the novel application of beam-space MIMO sets its own requirements and constraints. This naturally makes the design and implementation procedure for the beam-space MIMO operation different from those reported in the literature for classical applications (for instance in [66–69]). In this context, this chapter contributes to the effective design and modeling of realistic antennas for beam-space MIMO transmission, and provides an extensive discussion on related practical challenges.

Section 3.2 discusses the possibility to consider realistic load-modulated antenna solutions for small portable applications. A simple yet powerful modeling approach is described in Section 3.3 to deduce the general parameters of load-modulated antennas from a single electromagnetic full-wave simulation and post-processing. Section 3.4 deals with hardware technology platforms for enabling dynamic reconfiguration in beam-space MIMO antennas, and discusses the basic limitations of the controllable elements.

Section 3.5 is devoted to the basis definition in beam-space MIMO, where existing approaches for pattern decomposition are presented, and their strengths and weaknesses are compared from a practical point of view. Section 3.6 discusses different design practices and strategies for achieving optimum performance in beam-space MIMO systems. In Section 3.7, special emphasis is put on critical aspects related to the the measurement and modeling of variable

Parts of this chapter have been published earlier in [19–21].

loads, targeting minimum discrepancy between simulated and measured results.

Finally, the proposed design and modeling strategies are illustrated in Section 3.8 by designing a concrete operational prototype for the single-radio multiplexing of two BPSK signals. The possibility of using the designed antenna to achieve the multiplexing gain at a dynamically-controllable frequency is also studied.

3.2 Compact Antenna Solutions

As discussed in Section 2.4, parasitic antenna arrays composed of monopole and dipole elements allowed setting the theoretical basis and the experimental demonstration of the beam-space MIMO concept in early developments. However, despite having much smaller inter-element spacing than conventional MIMO arrays, the dipole and monopole elements in such arrays remain large to be utilized in modern compact portable devices. In theory, the elements can be shortened by operating them below resonance but at the expense of lowering the efficiency and requiring a complex matching network. Anyway, the requirement of employing several disconnected radiators (active and parasitic ones) is inconvenient not only in terms of size but also from the perspective of fabrication and sensitivity to the influence of the immediate environment on the antenna performance.

For the reasons outlined above, monopoles and other wire antennas in analogue first generation systems were superseded by more complicated *built-in* antennas in modern communication platforms. Nowadays, planar antennas, typically variations of planar inverted-F antenna (PIFA) [70–74], are extensively utilized in portable communication systems due to their salient characteristics such as low profile, compactness, low manufacturing cost, sensitivity to both vertical and horizontal polarizations, and multi-band operation capabilities. The design of an appropriate built-in antenna for implementing the beam-space MIMO concept in actual portable devices also requires careful attention to similar design considerations. Particularly, strong electromagnetic coupling between a built-in antenna and other components of the platform in the close proximity necessitates the antenna to be treated as a component of the whole platform rather than an isolated element within the design process.

In this work, we present an antenna system solution for beam-space MIMO that can be effectively incorporated in a compact, low-cost portable terminal. As depicted in Fig. 3.1, rather than a multi-element structure in which each element (passive or parasitic) is regarded as a distinct and physically-separate radiator, we propose the use of a single multi-port radiating structure integrated into a device platform. One port is the active input and connected to a single RF chain, while the other are passive and terminated with variable loads. By reconfiguring the variable loads, currents flowing on the multi-port radiator are changed and in turn the radiation pattern of the antenna system is reconfigured. Therefore, like in conventional parasitic antenna arrays, the existence of strong coupling among the radiator ports improves the beam-shaping capabilities of such an antenna system. Obviously, parasitic arrays of dipole and monopole antennas are a subset of the proposed load-modulated antenna systems, where

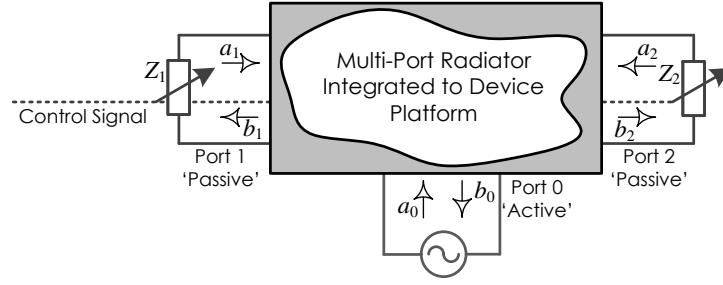


Figure 3.1: Proposed antenna system solution for beam-space MIMO, generally composed of connected multi-port radiator rather than physically-separate multi-element arrays.

each port corresponds to a separate antenna element.

Like in most electromagnetic structures, an optimal design approach for beam-space MIMO antennas needs to seek for the right balance between initial good physical insight and a tool for accurate modeling and optimization, while considering several factors such as the employed enabling technology and the design objective in terms of functionality. In the following sections, general modeling and design strategies for beam-space MIMO antennas are discussed, while more specific aspects are illustrated by the design of the first integrated beam-space MIMO antenna for BPSK signaling.

3.3 Efficient Antenna Modeling

As aforementioned, the performance of a load-modulated antenna is dependent on its terminating loads at the passive ports. On initial consideration, this might imply that a full-wave simulation should in principle be performed for any set of the load values. However, when the load-modulated antenna embeds localized load circuits¹, it is possible to compute all performance parameters for any set of the load values based on a single electromagnetic full-wave simulation with subsequent post-processing [75]. This is done by performing a simulation of the multi-port radiator with ports placed at the location of the variable loads.

According to the theory of multi-port antennas, a P -port radiator can be fully described by a scattering matrix $\mathbf{S} \in \mathbb{C}^{P \times P}$ and P embedded radiation patterns $\{\mathcal{F}_p(\Omega)\}_{p=0}^{P-1}$. Assuming a linear medium, the scattering parameters are defined as

$$\mathbf{b} = \mathbf{S}\mathbf{a}, \quad (3.1)$$

where $\mathbf{a}_p = (\mathbf{a})_p$ and $\mathbf{b}_p = (\mathbf{b})_p$, $p \in \{0, 1, \dots, P-1\}$, are the incident and reflected power waves at port p , respectively. Here, we define the power waves in such a way that a unit magnitude

¹A localized circuit can be accurately represented by a lumped element model.

corresponds to a unit power level of the incident and reflected waves, i.e.,

$$\mathcal{P}_{\text{inc},p} = |a_p|^2, \quad (3.2)$$

$$\mathcal{P}_{\text{ref},p} = |b_p|^2. \quad (3.3)$$

As mentioned in Chapter 2, the embedded radiation pattern $\mathcal{F}_q(\Omega)$ is defined as the radiation pattern obtained when driving port q with a unit power level and terminating all other ports with the reference impedance Z_0 , namely, when $a_q = 1$ [W^{1/2}] and $a_{p \neq q} = 0$. We would like to stress that the energy absorbed inside the system or carried away from the system in reflected waves and absorbed in terminating matched loads has been already considered in the definition of the embedded pattern. Therefore, the total radiated field of the system can be expressed as the superposition of the embedded patterns [76], i.e.,

$$\mathcal{E}_\circ(\Omega) = \sum_{p=0}^{P-1} a_p \mathcal{F}_p(\Omega), \quad (3.4)$$

where the units of $\mathcal{E}_\circ(\Omega)$ and $\mathcal{F}_p(\Omega)$ are [V] and [V/W^{1/2}], respectively. The total power radiated from the P -port radiator into free space is given by

$$\begin{aligned} \mathcal{P}_{\text{rad}} &= \frac{1}{2} \eta_0 \int \mathcal{E}_\circ(\Omega) \cdot \mathcal{E}_\circ^*(\Omega) d\Omega \\ &= \sum_{q=0}^{P-1} \sum_{p=0}^{P-1} a_p^* \left[\frac{1}{2} \eta_0 \int \mathcal{F}_q(\Omega) \cdot \mathcal{F}_p^*(\Omega) d\Omega \right] a_q \\ &= \sum_{q=0}^{P-1} \sum_{p=0}^{P-1} a_p^* \mathcal{R}_{pq} a_q = \mathbf{a}^H \mathbf{R} \mathbf{a}, \end{aligned} \quad (3.5)$$

where

$$\mathcal{R}_{pq} = \frac{1}{2} \eta_0 \int \mathcal{F}_q(\Omega) \cdot \mathcal{F}_p^*(\Omega) d\Omega \quad (3.6)$$

is defined as the beam-coupling coefficient between p th and q th embedded patterns [76], η_0 denotes the free-space characteristic admittance, and $d\Omega = \sin\theta d\theta d\varphi$. Obviously, according to the definition in (3.6), we have $\mathcal{R}_{pq} = \mathcal{R}_{qp}^*$.

By terminating $P - 1$ ports of the radiator with linear loads, a single-feed load-modulated antenna, such as the one shown in Fig. 3.1, is formed. Assuming port 0 denotes the only active input, the reflection coefficient from terminating load Z_p at passive port p is given by

$$\Gamma_p = \frac{a_p}{b_p} = \frac{Z_p - Z_0}{Z_p + Z_0} \quad p \in \{1, 2, \dots, P-1\}. \quad (3.7)$$

For the sake of simplicity, the source impedance Z_0 is chosen to be equal to the reference impedance of the scattering parameters. Accordingly, using (3.1) and (3.7), all the reflected

and incident power waves can be expressed in terms of the input power wave a_0 , i.e.,

$$\mathbf{b} = a_0 (\mathbf{S}^{-1} - \mathbf{\Gamma})^{-1} [1, 0, \dots, 0]^T, \quad (3.8)$$

$$\mathbf{a} = a_0 \mathbf{S}^{-1} (\mathbf{S}^{-1} - \mathbf{\Gamma})^{-1} [1, 0, \dots, 0]^T = a_0 (\mathbf{I}_P - \mathbf{\Gamma} \mathbf{S})^{-1} [1, 0, \dots, 0]^T, \quad (3.9)$$

where

$$\mathbf{\Gamma} = \text{diag}([0, \Gamma_1, \dots, \Gamma_{P-1}]^T). \quad (3.10)$$

Therefore, it is possible to deduce the actual performance of the antenna system for any sets of loads by post-processing in negligible computation time. Particularly, the reflection coefficient, the radiation pattern (for a unit power excitation), and the total efficiency² of the load-modulated antenna are respectively obtained by

$$\Gamma_{\text{in}} = \frac{b_0}{a_0} = \frac{1}{a_0} \sum_{p=0}^{P-1} a_p S_{0p} = S_{00} + \frac{1}{a_0} \sum_{p=1}^{P-1} a_p S_{0p}, \quad (3.11)$$

$$\mathcal{E}_{\text{u}}(\Omega) = \mathcal{E}_{\circ}(\Omega)|_{a_0=1} = \frac{1}{a_0} \sum_{p=0}^{P-1} a_p \mathcal{F}_p(\Omega) = \mathcal{F}_0(\Omega) + \frac{1}{a_0} \sum_{p=1}^{P-1} a_p \mathcal{F}_p(\Omega), \quad (3.12)$$

$$e_{\text{tot}} = \frac{\mathcal{P}_{\text{rad}}}{\mathcal{P}_{\text{inc}}} = \frac{\mathbf{a}^H \mathcal{R} \mathbf{a}}{|a_0|^2}. \quad (3.13)$$

Finally, we would like to emphasize that this modeling procedure is applicable to all load-modulated antennas with localized load circuits.

3.4 Hardware Technologies for Variable Loads

Successful data multiplexing in beam-space MIMO, as discussed in Section 3.2, critically relies on the availability of suitable dynamically controllable loads. Obviously, the use of a load with non-negligible positive real part degrades the radiation efficiency of the load-modulated antenna. Employing active loads (composed of active devices such as transistors) also drastically increases the implementation complexity and cost, and potentially leads to cumbersome stability issues. For these reasons, purely reactive load solutions are generally more attractive for realistic applications.

The variable reactive loads, in principle, can be implemented using any established or emerging hardware technology of microwave dynamic reconfiguration. However, since localized loads allow efficient design procedures as discussed previously in Section 3.3, they are strongly preferred to their distributed counterparts such as liquid crystals. Two established and widely available technologies enabling the implementation of localized variable reactive loads in RF applications are semiconductor p-i-n/varactor diodes and microelectromechanical systems

²Total efficiency is defined here as the product of radiation and matching efficiencies.

(MEMS), see for instance [54, 77–83] which are just a few examples of the numerous works on reconfigurable structures. While MEMS devices outperform semiconductor diodes in terms of insertion loss, linearity and power consumption, their poor switching times (in the order of 2-50 μs) are prohibitive in the particular application of beam-space MIMO which requires symbol-rate reconfiguration. Bearing in mind that the switching times of the control elements must be significantly smaller than the symbol period, today the main technology for implementing variable reactive loads in beam-space MIMO antennas remains semiconductor diodes.

The semiconductor devices can be employed either directly as variable loads by adjusting their activation voltage, or as RF switches to select among different fixed load circuits, each providing the required reactance for a given state (see Fig. 3.2). In the former case, lumped elements, such as capacitors and/or inductors, can be used in series or parallel with the diodes to provide desired reactance tunability range. In the latter case, the proper load circuit is selected through control bits of the switch. When compared to the switch implementation technique, diode-based variable loads provide a more controllable and finer tuning range, and require fewer lumped elements, thereby resulting in more compact realization. In both configurations, non-linear effects of RF power level must be taken into account.

3.5 Decomposition Techniques/Basis Definition

The beam-space MIMO principle requires the antenna radiation pattern at each symbol interval to be decomposed into a linear combination of orthogonal basis patterns, as given in (2.18). Therefore, the radiation patterns required for all possible symbol combinations not only depend on the symbols to be multiplexed, but are also dependent on how the basis patterns are defined. This implies that the basis definition strongly affects the design procedure and functionality of beam-space MIMO antennas. In the following, we briefly describe two existing approaches for the definition of orthogonal basis patterns, and point out their strengths and limitations in the implementation of realistic beam-space MIMO systems.

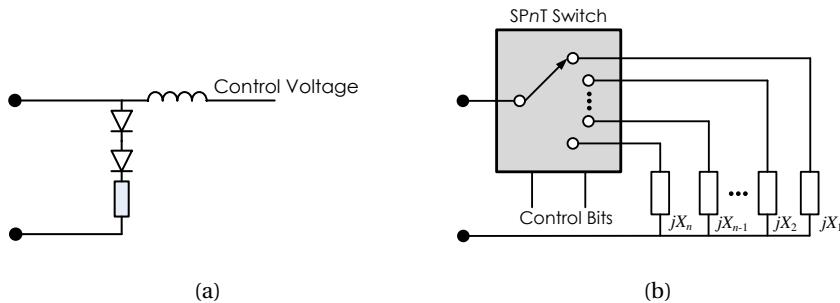


Figure 3.2: Techniques for implementing variable loads based on solid state technology. (a) Diodes directly as variable loads. (b) Switch implementation technique.

3.5.1 Gram-Schmidt Approach

In mathematics, the Gram-Schmidt process is a procedure for constructing an orthonormal basis from a non-orthogonal set of linearly independent functions in an inner product space [84]. In [53], the Gram-Schmidt procedure was used to decompose the radiation pattern of an ESPAR in a similar manner. Here, we generalize the approach for any load-modulated antenna such as the one shown in Fig. 3.1.

As mentioned in Section 3.3, the radiation pattern of a load-modulated antenna can be expressed using (3.12) as a linear combination of the radiator's embedded radiation patterns. The Gram-Schmidt process can be applied on the set of P embedded radiation patterns, $\{\mathcal{F}_p(\Omega)\}_{p=0}^{P-1}$, to construct $N \leq P$ orthonormal functions, $\{\mathcal{B}_n(\Omega)\}_{n=0}^{N-1}$, that span an N -dimensional space, namely,

$$\mathcal{F}_p(\Omega) = \sum_{n=0}^{N-1} v_{pn} \mathcal{B}_n(\Omega), \quad (3.14)$$

where

$$v_{pn} = (V)_{pn} = \int \mathcal{F}_p(\Omega) \cdot \mathcal{B}_n^*(\Omega) d\Omega \quad (3.15)$$

denotes the projection of the embedded radiation pattern $\mathcal{F}_p(\Omega)$ onto the basis pattern $\mathcal{B}_n(\Omega)$. By definition, the Gram-Schmidt procedure can provide different sets of basis patterns by selecting a different initial term [53], which can be any embedded radiation pattern. For instance, starting from $\mathcal{F}_0(\Omega)$, the orthonormalization process works as follows:

$$\mathcal{B}_0(\Omega) = \frac{1}{Y_0} \mathcal{F}_0(\Omega), \quad (3.16a)$$

$$\mathcal{B}_n(\Omega) = \frac{1}{Y_n} \left[\mathcal{F}_n(\Omega) - \sum_{q=0}^{n-1} v_{nq} \mathcal{B}_q(\Omega) \right] \quad n \in \{1, \dots, N-1\}, \quad (3.16b)$$

where

$$Y_0 = \left(\int |\mathcal{F}_0(\Omega)|^2 d\Omega \right)^{1/2}, \quad (3.17a)$$

$$Y_n = \left(\int \left| \mathcal{F}_n(\Omega) - \sum_{q=0}^{n-1} v_{nq} \mathcal{B}_q(\Omega) \right|^2 d\Omega \right)^{1/2} \quad n \in \{1, \dots, N-1\}. \quad (3.17b)$$

The decomposition based on the Gram-Schmidt procedure implies that the number of the basis patterns, N , is theoretically equal to the number of the radiator's ports, P . However, it has been shown in [53] that the number of basis patterns which effectively participate to the total radiated field is limited, and strongly dependent on the radiator geometry.

Combining (3.12) and (3.14), the radiation pattern of the load-modulated antenna can be

expressed as a linear combination of the modulated basis patterns, i.e.,

$$\begin{aligned}
 \mathcal{E}_u(\Omega) &= \frac{1}{a_0} \sum_{p=0}^{P-1} a_p \sum_{n=0}^{N-1} v_{pn} \mathcal{B}_n(\Omega) \\
 &= \frac{1}{a_0} \sum_{n=0}^{N-1} \mathcal{B}_n(\Omega) \sum_{p=0}^{P-1} v_{pn} a_p \\
 &= \frac{1}{a_0} \sum_{n=0}^{N-1} w_n \mathcal{B}_n(\Omega),
 \end{aligned} \tag{3.18}$$

where

$$w_n = (\mathbf{w})_n = (\mathbf{V}^T \mathbf{a})_n = \sum_{p=0}^{P-1} v_{pn} a_p. \tag{3.19}$$

Therefore, to implement the beam-space MIMO concept, the antenna is designed in such a way that the weight vector \mathbf{w} becomes identical to the symbol vector \mathbf{x} at each symbol period. For a given P -port radiator, whose scattering matrix and P embedded radiation patterns are known, the projection matrix \mathbf{V} is straightforwardly obtained from (3.16) and (3.15). Then, the incident and reflected power wave vectors \mathbf{a} and \mathbf{b} are computed using (3.19) and (3.1), respectively. Finally, the load set required for transmitting \mathbf{x} is simply calculated using (3.7). Obviously, selecting a different initial term in (3.16) leads to a different load set.

Although the Gram-Schmidt method is a convenient tool to define basis patterns for any load-modulated antenna, it does not provide an estimation of the effective dimensionality of the beam-space domain. Even more important in practice, the Gram-Schmidt process lacks a mechanism to fulfill two vital requirements of reactive passive loading and state-independent input impedance as the need for active loads and symbol-rate dynamic matching networks would offset the main benefit of the beam-space MIMO system, namely, reduced hardware complexity. This is why we have chosen in this thesis to focus on alternative approaches for the basis definition.

3.5.2 Mirror Image Pattern Pair Approach

Consider a reconfigurable antenna system which has a single active input port and allows the formation of two radiation patterns, $\mathcal{E}_{u,1}(\Omega)$ (in State 1) and $\mathcal{E}_{u,2}(\Omega)$ (in State 2), that are mirror images of each other, for instance $\mathcal{E}_{u,2}(\theta, \varphi) = \mathcal{E}_{u,1}(\theta, \pi - \varphi)$ for a mirror plane at $\varphi = 90^\circ - 270^\circ$. It has been proved in [54] that for the angular functions defined as

$$\mathcal{B}_1(\Omega) = \frac{\mathcal{E}_{u,1}(\Omega) + \mathcal{E}_{u,2}(\Omega)}{2} \tag{3.20a}$$

$$\mathcal{B}_2(\Omega) = \frac{\mathcal{E}_{u,2}(\Omega) - \mathcal{E}_{u,1}(\Omega)}{2}, \tag{3.20b}$$

3.5. Decomposition Techniques/Basis Definition

$\int \mathcal{B}_1(\Omega) \cdot \mathcal{B}_2^*(\Omega) d\Omega = 0$. Therefore, $\mathcal{B}_1(\Omega)$ and $\mathcal{B}_2(\Omega)$ create an orthogonal set of basis patterns for decomposing the antenna's radiation patterns.

Letting the active port of such an antenna system be fed by the up-converted version of the BPSK signal x_1 , according to (3.20) the antenna's radiation pattern becomes either $\mathcal{E}_o(\Omega) = x_1 \mathcal{E}_{u,1}(\Omega) = x_1 [\mathcal{B}_1(\Omega) - \mathcal{B}_2(\Omega)]$ in State 1 or $\mathcal{E}_o(\Omega) = x_1 \mathcal{E}_{u,2}(\Omega) = x_1 [\mathcal{B}_1(\Omega) + \mathcal{B}_2(\Omega)]$ in State 2, or in general

$$\mathcal{E}_o(\Omega) = x_1 \left[\mathcal{B}_1(\Omega) + (-1)^{\mathcal{S}} \mathcal{B}_2(\Omega) \right] \quad (3.21a)$$

$$= x_1 \mathcal{B}_1(\Omega) + x_2 \mathcal{B}_2(\Omega), \quad (3.21b)$$

where \mathcal{S} denotes the state of the antenna system ($\mathcal{S} := 1$ for State 1 and $\mathcal{S} := 2$ for State 2). From (3.21b), it is obvious how the two BPSK symbols, namely the real x_1 and the virtual $x_2 = (-1)^{\mathcal{S}} x_1$, are independently mapped onto the basis patterns $\mathcal{B}_1(\Omega)$ and $\mathcal{B}_2(\Omega)$, respectively. Therefore, any arbitrary single-feed antenna system capable of creating a mirror image pattern pair is capable of transmitting two BPSK signals simultaneously. Table 3.1 shows the State \mathcal{S} required for transmitting x_2 according to the value of x_1 , where $[b_1 \ b_2]^T$ is the input vector of bits modulated to $[x_1 \ x_2]^T$.

Table 3.1: Combinations of two BPSK signals.

$[b_1 \ b_2]^T$	$[x_1 \ x_2]^T$	\mathcal{S}
$[0 \ 1]^T$	$[-1 \ +1]^T$	1
$[1 \ 0]^T$	$[+1 \ -1]^T$	1
$[1 \ 1]^T$	$[+1 \ +1]^T$	2
$[0 \ 0]^T$	$[-1 \ -1]^T$	2

This beam-space MIMO technique was implemented in [54] using a symmetrical three-element SPA of printed dipoles. However, as mentioned in Section 3.2, such physically-separate antenna structures are unsuitable to small portable devices. Therefore, we propose an antenna solution, as symbolically shown in Fig. 3.3, composed of a symmetric three-port radiator integrated into a device platform. The central port (port 0) is the active input fed with the first BPSK data stream, while the other two are passive and terminated with variable loads, Z_1 and Z_2 . Obviously, by permuting the impedance values of the loads, Z_1 and Z_2 , at the passive ports according to \mathcal{S} , the antenna system has capability of creating two mirror image patterns with regard to the plane of symmetry depicted in Fig. 3.3, and can thus simultaneously transmit two BPSK streams out of a single radio.

The proposed beam-space MIMO antenna solution guarantees the orthogonality of the basis patterns according to the mirror image pattern pair approach and irrespective of the loads' impedance values, Z_1 and Z_2 . Obviously, it allows the designer to use purely reactive loads as the real part of a complex load degrades the total efficiency of the antenna system. Further-

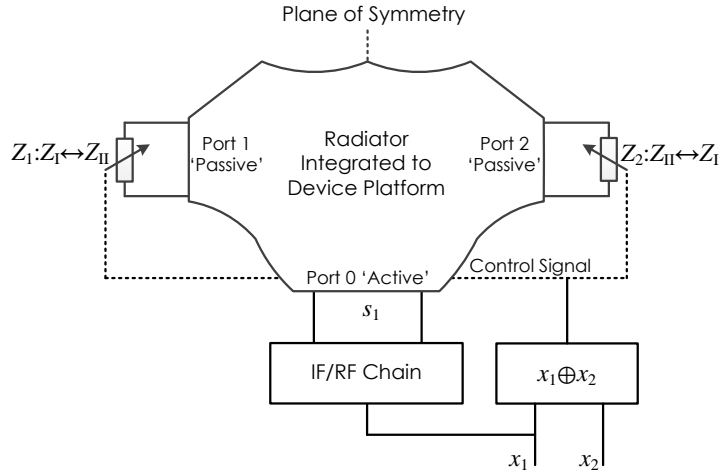


Figure 3.3: Proposed compact antenna solution for beam-space MIMO based on the mirror image pattern pair approach.

more, the symmetry of the three-port radiator and the swap of the loads at the passive ports ensure that the input impedance at the active port remains constant over the two antenna states. Unlike in the Gram-Schmidt approach, here the power distribution across the basis patterns depends on the load values. Therefore, the power balance between the basis patterns as well as the impedance matching is obtained by optimizing the variable loads and/or the radiator structure as detailed later. However, while applying such an approach to BPSK signaling is straightforward, scaling it to higher order PSK modulation is not possible. In Chapter 4, we propose an efficient strategy which enables multiplexing higher order PSK streams based on the mirror image pattern pair approach for the basis definition. In the following of this chapter, we employ this approach to design the first compact antenna system for single-radio multiplexing of BPSK signals.

3.6 Antenna Design Approaches

Obviously, the main functionality of a beam-space MIMO antenna is to form all the required radiation patterns according to (2.18). Furthermore, like in conventional MIMO systems, the ultimate goal in the design of beam-space MIMO systems is to maximize the data transmission rate. In [54], the beam-space MIMO antenna was optimized according to an upper-bound on the average rate, which is the rate achieved when assuming the input signal with a Gaussian distribution. However, the used upper-bound criterion is a rough approximation of real data rate in beam-space MIMO systems with finite-alphabet signaling. Assuming open-loop MIMO scenarios with rich scattering, the optimum system performance can be translated into additional requirements to the beam-space MIMO antenna design process, namely, maximizing the total efficiency of the antenna (for all operational states) while equally distributing the

transmitted power among the orthogonal basis patterns.

The prior-art approach to design a beam-space MIMO antenna starts with making some initial choices on the structure of the radiator such as the elementary elements of the SPA and their relative positions in the array. Then, the load values at the passive ports (or at the parasitic elements) are optimized for the required radiation patterns and desired performance criteria. According to the modeling technique described in Section 3.3, such a design approach is computationally fast since only one full-wave electromagnetic simulation of the radiator is sufficient to compute the complete set of the antenna parameters as functions of the load values in the following post-processing. However, with this approach the load values obtained from optimum operation calculations generally differ from those of available control components, such as for instance p-i-n diodes [54]. Consequently, another step in the antenna system design procedure must be devoted to the realization of required variable loads by a circuit embedding the control devices as well as other lumped components. The proper design and operation of these load control circuits are always challenging in terms of design effort, system performance, and cost.

In this thesis, we propose to introduce several geometrical parameters of the radiator in the optimization procedure such that the control components can be directly utilized as the variable loads in the design of beam-space MIMO antennas, thereby avoiding the design of the aforementioned complex variable load circuits. Obviously, this approach comes at the cost of significantly increased computational time in order to carry out various full-wave simulations and puts more burdens on the design of the radiator structure. However, the simplicity of the load circuits effectively reduces the overall design complexity and enhances the certainty and consistency in the proper operation of the beam-space MIMO terminals. For instance, such an approach can be easily applied to the design of the antenna system already shown in Fig. 3.3. As shown in Fig. 3.4, each two-state variable load is realized using a single p-i-n diode with two *forward*- and *reverse*-biased states. Accordingly, the symmetric radiator must be optimized such that the desired performance criteria of the beam-space MIMO antenna are met for the impedance values corresponding the each of the two states of the p-i-n diodes.

According to (3.13), the total efficiency in state \mathcal{S} corresponds to the spatial integration of the radiation pattern $\mathcal{E}_{\mathbf{u},\mathcal{S}}(\Omega)$ over the full sphere, i.e.,

$$e_{\text{tot},\mathcal{S}} = \mathcal{P}_{\mathcal{E}_{\mathbf{u},\mathcal{S}}} = \frac{1}{2}\eta_0 \int \mathcal{E}_{\mathbf{u},\mathcal{S}}(\Omega) \cdot \mathcal{E}_{\mathbf{u},\mathcal{S}}^*(\Omega) d\Omega. \quad (3.22)$$

Since the antenna shown in Fig. 3.3 creates mirror image radiation patterns in its two states, the total efficiency obviously remains constant irrespective of the state, i.e., $e_{\text{tot},1} = e_{\text{tot},2}$. The power imbalance ratio between the basis patterns is defined as

$$r = \frac{\mathcal{P}_{\mathcal{B}_1}}{\mathcal{P}_{\mathcal{B}_2}}, \quad (3.23)$$

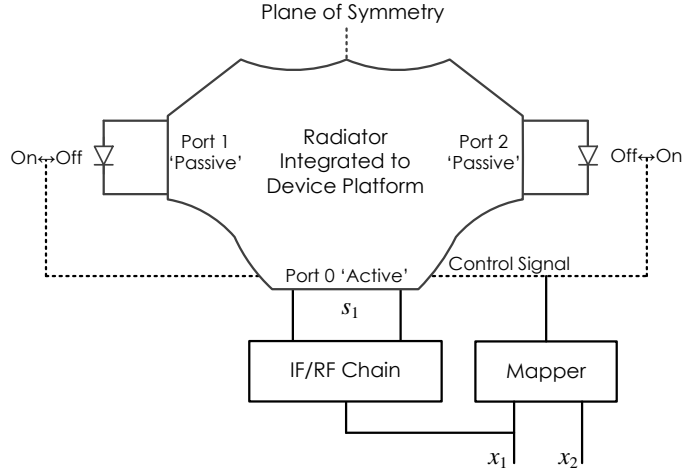


Figure 3.4: Compact antenna solution proposed in Fig. 3.3 with control elements (here p-i-n diodes) directly as variable loads to obviate complex variable load circuits.

where

$$\begin{aligned}
 \mathcal{P}_{\mathcal{B}_1} &= \frac{1}{2} \eta_0 \int \mathcal{B}_1(\Omega) \cdot \mathcal{B}_1^*(\Omega) d\Omega \\
 &= \frac{1}{8} \eta_0 \int [\mathcal{E}_{u,1}(\Omega) + \mathcal{E}_{u,2}(\Omega)] \cdot [\mathcal{E}_{u,1}(\Omega) + \mathcal{E}_{u,2}(\Omega)]^* d\Omega \\
 &= \frac{1}{4} [\mathcal{P}_{\mathcal{E}_{u,1}} + \mathcal{P}_{\mathcal{E}_{u,2}} + \mathcal{R}_{\mathcal{E}_{u,1}\mathcal{E}_{u,2}} + \mathcal{R}_{\mathcal{E}_{u,2}\mathcal{E}_{u,1}}], \tag{3.24}
 \end{aligned}$$

$$\begin{aligned}
 \mathcal{P}_{\mathcal{B}_2} &= \frac{1}{2} \eta_0 \int \mathcal{B}_2(\Omega) \cdot \mathcal{B}_2^*(\Omega) d\Omega \\
 &= \frac{1}{8} \eta_0 \int [\mathcal{E}_{u,2}(\Omega) - \mathcal{E}_{u,1}(\Omega)] \cdot [\mathcal{E}_{u,2}(\Omega) - \mathcal{E}_{u,1}(\Omega)]^* d\Omega \\
 &= \frac{1}{4} [\mathcal{P}_{\mathcal{E}_{u,1}} + \mathcal{P}_{\mathcal{E}_{u,2}} - \mathcal{R}_{\mathcal{E}_{u,1}\mathcal{E}_{u,2}} - \mathcal{R}_{\mathcal{E}_{u,2}\mathcal{E}_{u,1}}] \tag{3.25}
 \end{aligned}$$

are the power radiated in the far-field by the basis patterns $\mathcal{B}_1(\Omega)$ and $\mathcal{B}_2(\Omega)$, respectively.

3.7 Modeling and Measurement of Variable Loads

In the previous sections of this chapter, we discussed efficient modeling and design approach of the load-modulated antenna solutions for beam-space MIMO. We also stated that semiconductor diodes are the most appropriate enabling hardware technology to implement required variable loads. The accurate modeling of such localized elements within the antenna's full-wave simulations is often challenging. In particular - and as will be explained in detail below - inserting the circuit model of a lumped element in a commercial solver without particular care and methodology can lead to significant discrepancies between simulations and measure-

ments, thereby increasing the cost and time of development. In fact, despite common belief, such effects are typically much more important than the lumped components' tolerances. In this section, we describe a practical technique for the precise modeling of lumped elements in commercial full-wave simulators.

3.7.1 Methodology

The first step of the proposed modeling approach is to obtain an initial circuit model from accurate measured S-parameters of the isolated element (or the load circuit). A thru-reflect-line (TRL) calibration for the measurement of the S-parameters is recommended³ since it allows removing the effect of any transition and placing the measurement reference planes exactly at the boundaries of the element under test (see Fig. 3.5a). Although doing otherwise will have a very limited effect on the accuracy of the method, thanks to the correction procedure described below, it is obviously wise to measure the isolated element on a substrate and pad width similar to those of the antenna where the element will be eventually incorporated. The measured data are then fitted to a Π -model circuit, as depicted in Fig. 3.5a. The series branch Z_s represents the actual electromagnetic response of the element. The shunt branches, Z_{p1} and Z_{p2} , are simple capacitances associated with the shunt fringing fields in the microstrip or coplanar waveguide used, and thereby are not used afterwards. Depending on the element under consideration, a proper RLC network configuration is selected and precisely fitted to the measured raw impedance Z_s .

The next step in the proposed procedure is to introduce the series branch of the initial model, Z_s , in a full-wave solver to simulate the exact setup of the isolated element measurement, as depicted in Fig. 3.5b. Note that there are different possibilities to introduce the circuit model of lumped elements in commercial finite-elements-based solvers, which were discussed and compared in [86]⁴. Obviously, the full-wave simulation of the exact measurement setup, including the extracted model of the element, should match the measured data very well if the procedure for the measurement-extraction-insertion works correctly. However, this is in general not the case. The reason can be explained as follows. The series branch of the initial model, Z_s , already includes some effects that are accounted once again by the full-wave simulation of the setup. In other words, some effects are considered twice, once when measuring and extracting the initial model, and again by the full-wave simulation. For an intuitive understanding of these effect, let us consider the simple example of the modeling of an element behaving as an ideal lumped capacitance, C_{DUT} . First, the S-parameters of the lumped capacitance are measured, as shown in Fig. 3.6, and the initial model is then extracted. Fig. 3.6 illustrates that there is a capacitance, which models the coupling capacitance between

³Note that the reference impedance of the TRL-calibrated S-parameters is equal to the characteristic impedance of the standards [85].

⁴In this work, we use the so-called internal port method, where the lumped elements are represented by internal ports in the simulation. These internal ports are then loaded by given circuit models in the post-processing of the obtained multi-port S-parameters. As stated in Section 3.3, the internal port technique is particularly efficient since only a single full-wave simulation is run for all variations of the reconfigurable elements.

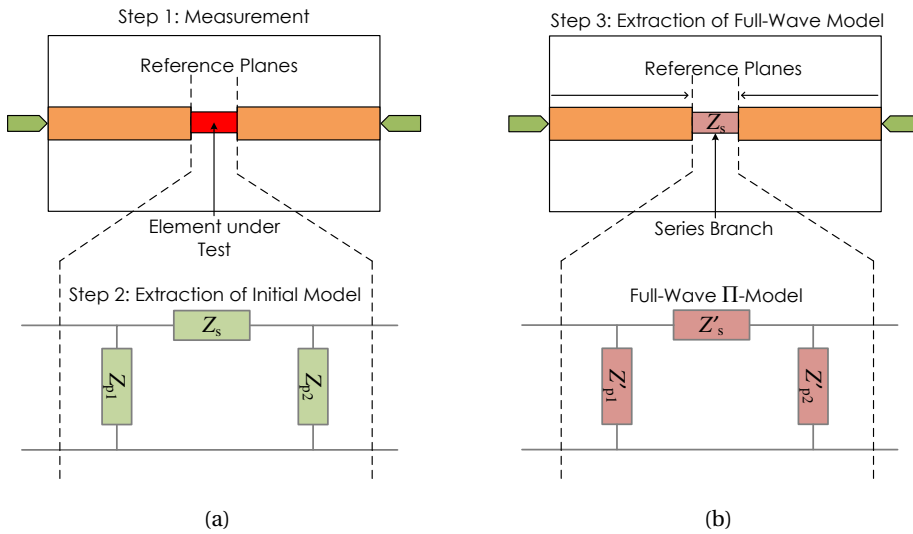


Figure 3.5: (a) Measurement of the lumped element (or the load circuit) under test using a TRL calibration, and then extracting the initial model. (b) Simulation of the exact setup of the measurement, including the initial extracted model of the element, and then extracting the full-wave model.

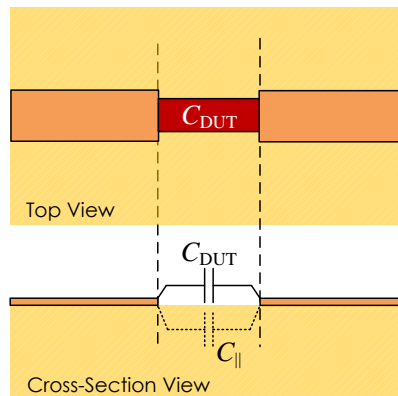


Figure 3.6: An intuitive idealistic illustration of the error introduced by the measurement setup itself prior to correction. The extracted capacitance includes the coupling through the substrate. A similar phenomenon occurs with the series inductive element.

two edges of the transmission lines, denoted by $C_{||}$, parallel to the element's capacitance C_{DUT} . Therefore, the series branch of the extracted initial model consists of a total capacitance $C_{tot} = C_{DUT} + C_{||}$. Now, introducing the extracted capacitance, C_{tot} , in the full-wave simulator in the exact setup of the measurement will clearly lead to an error, since the effect of the coupling through the substrate, $C_{||}$, has already been accounted for. Although the case of the parallel capacitance was chosen here for easy understanding, the same reasoning applies and was verified for the series inductive effect related to the finite length of the modeled lumped

elements.

In order to avoid accounting for some effects twice, and thereby to achieve excellent agreement between the simulation and measurement, a correction must be made on the extracted model of measurement prior to its introduction in the full-wave simulator. The correction can in principle be made through a detailed rigorous procedure, where all effects are carefully assessed and corrected based on separate full-wave simulations. However, the following semi-empirical approach is faster while yielding similar precision:

- The series branch of the initial model, Z_s , extracted from the measurement, is inserted in the full-wave simulation. The Π -model extraction procedure is repeated on the simulation results, yielding the series branch denoted by Z'_s .
- The series branches of the initial and full-wave models, namely Z_s and Z'_s , are compared in order to obtain an estimation of the effects accounted twice. A corresponding correction is made on Z_s to cancel out the extra effects. The corrected version of Z_s is called $Z_{s,cor}$.
- Instead of Z_s , the corrected model, $Z_{s,cor}$, is inserted in the simulation of the setup. Then, Z'_s is updated using the current simulation results, yielding $Z'_{s,cor}$. This is in general sufficient for Z_s and $Z'_{s,cor}$ values to be in very good agreement, which means that the corrected model, $Z_{s,cor}$, is validated for its insertion in the simulation of the antenna. However, if the agreement is still not considered sufficient, some little extra tuning of the corrected model must be carried out.

3.7.2 Experimental Verification

To illustrate and validate the correction approach, we describe the precise modeling of a fast-switching silicon p-i-n diode (Aeroflex/Metelics MPN7310A-0805-2) in its forward-biased and reverse-biased states. This diode will be used as the variable load in the design of a BPSK beam-space MIMO, as will be discussed in detail in the following section. The diode was measured on a 1.6 mm-thick FR4 substrate over a frequency range of 1-3 GHz. Fig. 3.7 shows the fabricated circuits for the S-parameter measurements of the diode, using a TRL calibration.

Let us first consider the reversed-biased case with a reverse voltage of -0.6 V. The initial series branch of the circuit model, extracted from the measured data set, is displayed in Fig. 3.8a. As expected, the p-i-n diode in this state is modeled by a dominantly capacitive series RLC network in the series branch of the model. There is very good agreement between the series branch results of the original measured raw data and the initial model, Z_s , as depicted in Fig. 3.9a, which confirms that the RLC model accurately fits the raw measured impedance. We employed the internal port method for the insertion of the initial model into the full-wave analysis of the exact measurement setup of the isolated diode using ANSYS HFSS. The corresponding circuit model, Z'_s , depicted in Fig. 3.8a, is extracted. Comparison of the series RLC

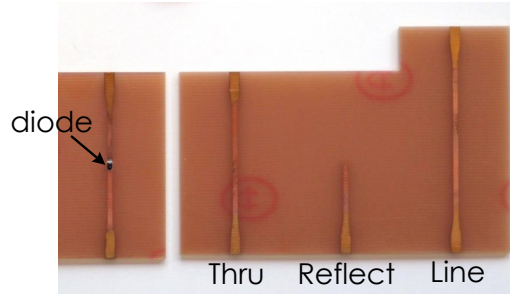


Figure 3.7: The fabricated circuits for measuring the calibrated S-parameters.

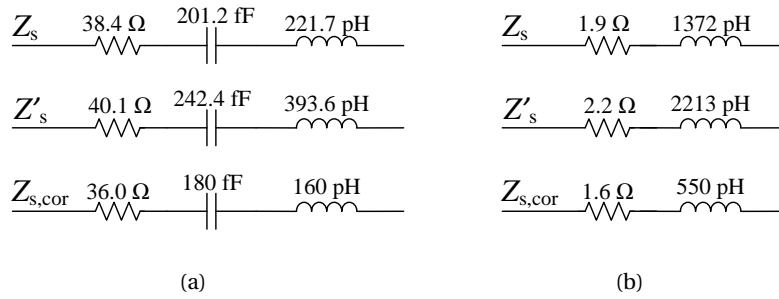
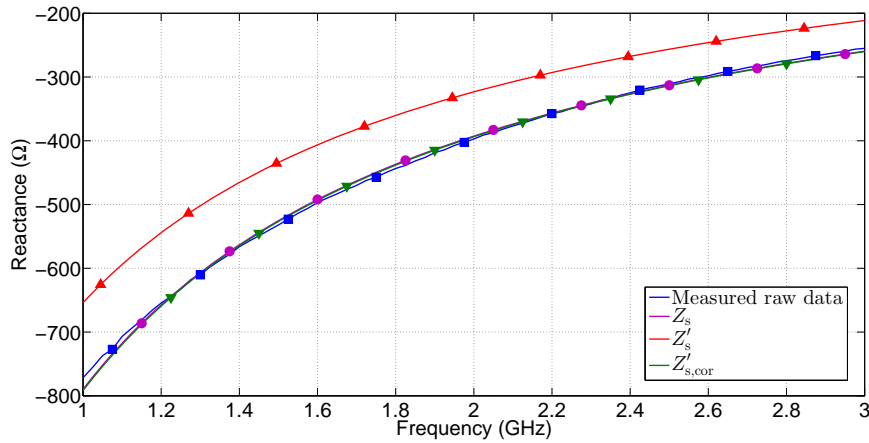


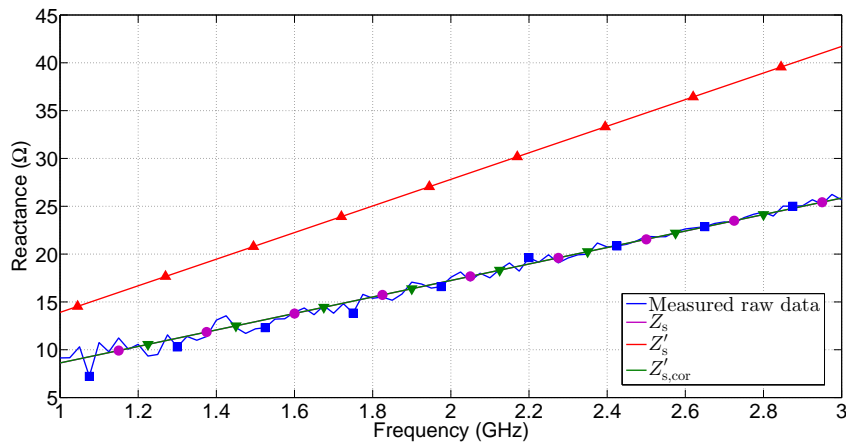
Figure 3.8: A comparison among the series branches of the measured, initial full-wave and corrected models. (a) When the p-i-n diode is reverse biased. (b) When the p-i-n diode is forward biased.

networks, Z_s and Z'_s , in Fig. 3.8a reveals a difference of 41.2 fF (about 20%) in the capacitance, which clearly illustrates the imprecision of the method if no correction is carried out. The significant difference is also depicted in terms of the total element's reactance in Fig. 3.9a. It is noticeable that this error is much larger than typical element-manufacturing tolerances, to which authors usually attribute discrepancies between simulation and measurement results. Applying the proposed correction strategy, we adjusted the initial series branch for full-wave simulations. The final corrected model, $Z_{s,\text{cor}}$, is given in Fig. 3.8a. The comparison between the results of the initial circuit model, Z_s , and the final full-wave circuit model, $Z'_{s,\text{cor}}$, obtained from inserting the corrected model, $Z_{s,\text{cor}}$, is also shown in Fig. 3.9a. There is an excellent agreement between the curves over the desired frequency band, which validates the approach for accurate modeling of the p-i-n diode within the full-wave simulation.

A similar approach was followed for modeling the diode when forward biased with a current of 19 mA. Fig. 3.8b compares the series branch of the circuit models in different phases of the correction approach. As shown in Fig. 3.9b, the series reactance values obtained from the initial model, Z_s , and the final full-wave model, $Z'_{s,\text{cor}}$, are in very good agreement over the frequency range.



(a)



(b)

Figure 3.9: A comparison among the series reactance values obtained from the measured raw data, the initial model extracted from the measurement, the initial full-wave model, and the final full-wave model (extracted from the simulation of the corrected model). (a) When the p-i-n diode is reverse biased. (b) When the p-i-n diode is forward biased.

3.8 Realistic Antenna Prototype for BPSK Signaling

In this section, the compact antenna solution and design strategies presented so far are illustrated by designing a concrete operational prototype, which enables the beam-space multiplexing of two BPSK signals in a hypothetical portable platform. The corresponding results obtained from simulations and measurements are presented and discussed. Finally, we show that it is possible to use the designed antenna to achieve the multiplexing gain at a dynamically-controllable frequency. This result is very promising for the future convergence of MIMO and cognitive frequency allocation concepts via low-cost and reduced-complexity transceivers.

3.8.1 Design and Structure

The prototype was designed for an uplink frequency range of 1920-1980 MHz and a downlink frequency range of 2110-2170 MHz, and realized in close proximity to a grounded FR4 substrate of $75\text{ mm} \times 50\text{ mm} \times 1.6\text{ mm}$. The optimization criterion was to minimize the power imbalance ratio between the basis patterns in the uplink frequency band while simultaneously achieving a return loss better than 10 dB over both working frequency ranges.

Fig. 3.10 shows the unfolded view of the proposed antenna prototype, where a compact planar radiating architecture is employed. According to the solution explained in detail in Section 3.5.2, the antenna system consists of a single symmetric three-port radiator and two variable loads. The central port of the radiator is the active input, and matched to a 50- Ω coaxial excitation while the other two are passive and terminated with the variable loads.

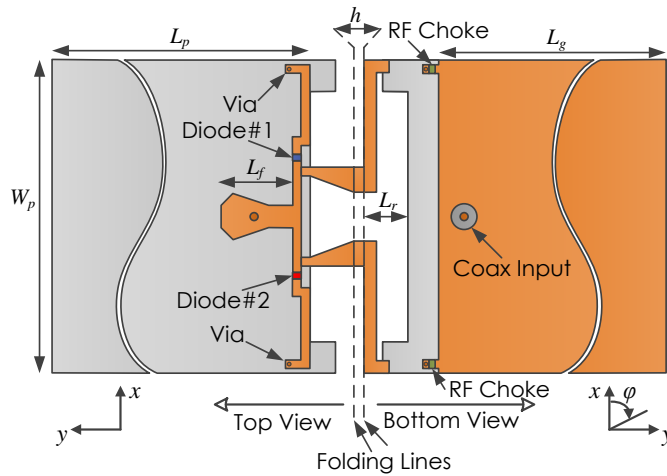


Figure 3.10: Unfolded schematic of the BPSK beam-space MIMO antenna prototype. Some important parameters: $W_p = 50\text{ mm}$, $L_p = 80\text{ mm}$, $h = 1.6\text{ mm}$, $L_r = 7\text{ mm}$, $L_f = 11.45\text{ mm}$, $L_g = 75\text{ mm}$.

According to the design approach described in Section 3.6, we decided to use two p-i-n diodes (similar to the one used in Section 3.7.2) as the sole mounted components at the two passive ports. The p-i-n diodes are embedded in the antenna system in such a way that depending on the antenna state, when one of the diodes is forward biased, the other is reverse biased with the negative of the diode voltage drop. Accordingly, by swapping the states of both p-i-n diodes at the same time, the radiation pattern of the antenna becomes mirrored thanks to the symmetry of the three-port radiator. As depicted in Fig. 3.10 and portrayed in Fig. 3.11, there is a DC path from each p-i-n diode to the ground plane of the substrate and thereby to the outer conductor of the coaxial connector through a metalized via and a RF choke (Murata LQW15AN82N) mounted on the backside of the substrate. Therefore, the bias voltages for controlling the states of the p-i-n diodes can be applied through the connector's inner

3.8. Realistic Antenna Prototype for BPSK Signaling

conductor using a simple bias tee. In other words, the state of the antenna system is simply selected by the polarity of the DC bias source. This allows significant complexity reduction since no DC decoupling biasing circuit must be introduced in the antenna structure.

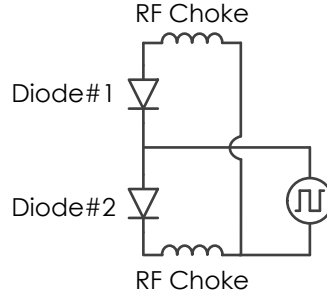


Figure 3.11: Baseband paths of the antenna system in Fig. 3.10.

Full-wave analyses of the radiator were carried out using ANSYS HFSS. As explained in Section 3.7, the equivalent series RLC models of the RF chokes and the p-i-n diodes (in both states) were extracted using a TRL calibration technique and then corrected for their insertion in the simulation and optimization processes. The impedances of the p-i-n diodes for a forward current of 19 mA and a reverse voltage of -0.6 V at the design frequency of 1.95 GHz were measured $1.9 + j17 \Omega$ and $35.4 - j407 \Omega$, respectively. Table 3.2 gives the initial measured and the corrected models of the lumped elements. We would like to stress that, since the p-i-n diodes were directly utilized as the two-state variable loads, the optimization approach was applied on the three-port radiator itself rather than the variable loads in order to meet the aforementioned requirements. Accordingly, extensive full-wave simulations on different radiator parameters were performed. Then, the obtained S-parameters and radiation patterns were used to find the optimal radiator parameters.

Table 3.2: Initial and corrected models of the embedded lumped elements.

Lumped Element	Initial Series RLC Model			Corrected Series RLC Model		
	R (Ω)	L (H)	C (F)	R (Ω)	L (H)	C (F)
p-i-n diode (forward-biased)	1.9	1372 p	-	1.6	550 p	-
p-i-n diode (reversed-biased)	38.4	222 p	201 f	36.0	160 p	180 f
RF choke	19.5 k	82.5 n	60.2 f	49.1 k	79.0 n	25.4 f

Fig. 3.12 shows the surface current density on the antenna's conducting traces at 1.95 GHz and 2.14 GHz for the case where the upper and lower p-i-n diodes are forward and reverse biased, respectively. This case is representative of the antenna operation in all the four possible combinations of two BPSK symbols (see Table 3.1) since the three-port radiator is symmetrical and according to Fig. 3.4 in each state of the beam-space MIMO antenna one of the p-i-n

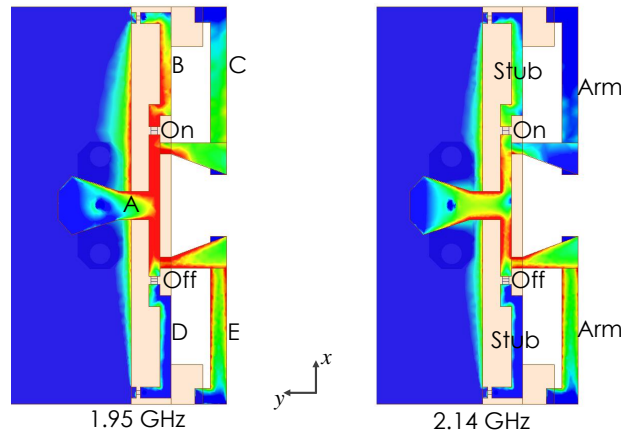


Figure 3.12: Current distribution on the prototype's conductors at the center frequencies of the uplink and downlink bands, when the upper and lower p-i-n diode are forward and reverse biased ('on' and 'off'), respectively.

diodes is 'on' and the other is 'off'. As expected, it is observed that the p-i-n diode in its reverse-biased state roughly acts as an open circuit, thus the lower stub (part D in Fig. 3.12) has a negligible effect on the antenna functionality. To illustrate the effect of the arms and the stubs on the antenna's impedance behavior, we examined the reflection coefficient in three different configurations: the antenna structure without the upper arm and stub (shown in Fig. 3.13a), the antenna structure without the lower arm (shown in Fig. 3.13b), and the whole antenna. As depicted in Fig. 3.14, in the absence of the upper arm and the upper stub, the antenna shows a deep resonance in the downlink frequency band. This is well in accordance with the surface current density at 2.14 GHz shown in Fig. 3.12: the current is distributed mostly on the lower arm and less on the upper part of the antenna. The results imply that the dimensions of the lower arm affect the antenna's second resonant frequency, however, the presence of the upper arm and stub causes a slight decrease of the resonance level, as shown in Fig. 3.14. This figure also shows that the antenna structure without the lower arm yields a moderate resonance at the uplink frequency. Then, when the lower arm is included in the structure, this resonance is well tuned to the upload center frequency and its level is improved. Therefore, it can be inferred that the first resonance of the antenna structure is nearly determined by the dimensions of the upper stub and arm as well as the impedance of the p-i-n diode in its forward-biased state, and adjusted by the lower arm. This is also in agreement with the current distribution shown in Fig. 3.12. Finally, we would like to recall that the above explanation is related to the impedance matching in each of the two operational states for the beam-space MIMO operation.

The optimized radiator was realized using the printed circuit board (PCB) processing technique. The fully-operational fabricated built-in antenna is shown in Fig. 3.15a and Fig. 3.15b. A part of the radiator was directly printed on both sides of the ungrounded portion of the substrate, while the other part (the arms) was realized by the use of beryllium-copper (BeCu)

3.8. Realistic Antenna Prototype for BPSK Signaling

strips as shown in Fig. 3.15c.

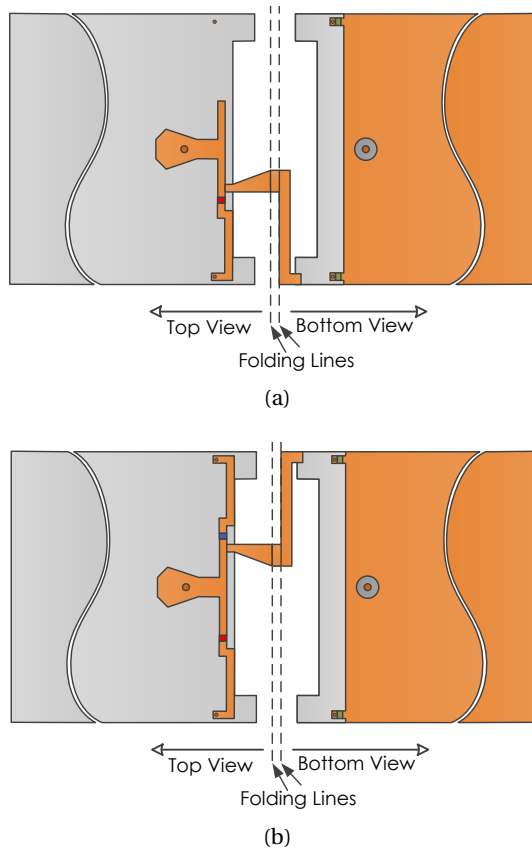


Figure 3.13: Two additional configurations for investigating the effects of the arms and the stubs.

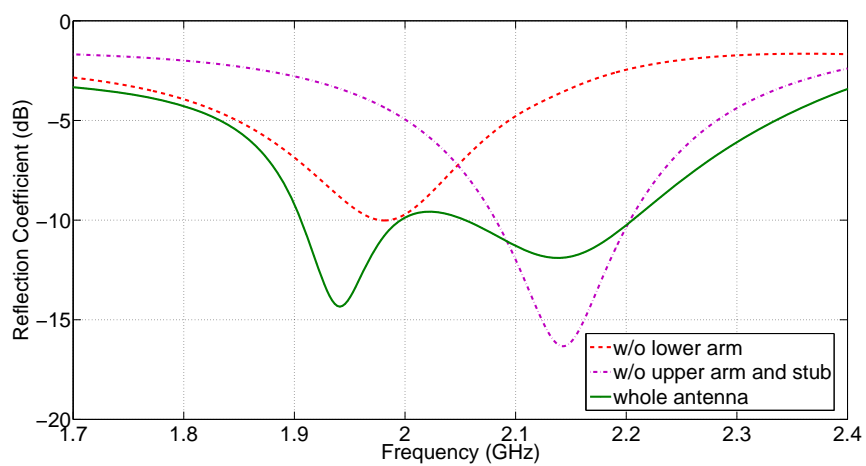


Figure 3.14: Effects of the stubs and the arms on the frequency-domain impedance response of the antenna.

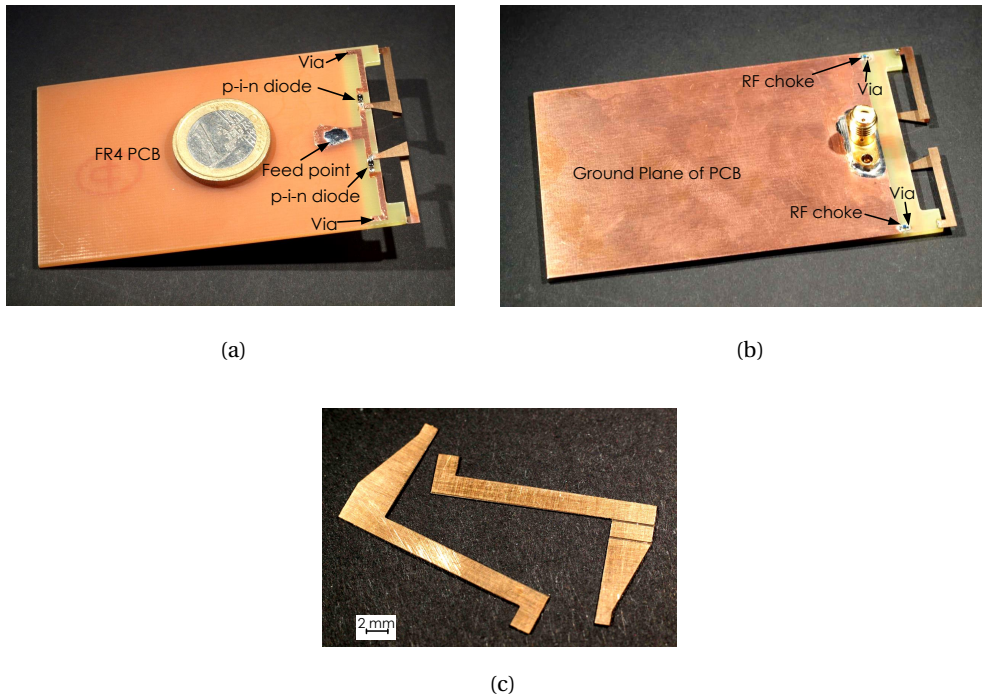


Figure 3.15: Fabricated beam-space MIMO antenna prototype, integrated to a hypothetical hand-held device; (b) top view, (c) bottom view. (c) Beryllium-copper (BeCu) strips for realizing the arms before folding.

3.8.2 Results and Discussion

Fig. 3.16 shows the comparison among the measured and simulated reflection coefficients of the beam-space MIMO antenna around the design frequency bands. In order to assess the importance of considering the correction technique described in Section 3.7, the figure includes the results obtained from the simulations with both the initial uncorrected and the final corrected models. It is clearly observed that the correction allows excellent prediction of the antenna response, while the use of the initial uncorrected model only provides a poor estimation of the actual return loss. Furthermore, the similarity between the measured results for both states confirms the symmetry of the fabricated antenna. The measured return loss is better than 10 dB for both system states over the upload/download bands.

The setup employed for far-field measurements of the antenna prototype is shown in Fig. 3.17. As explained earlier, the bias voltage was applied through the connector's inner conductor using a commercial bias tee. The co- and cross-polarized components of the antenna's radiation patterns in the plane of the device platform (i.e., $\theta = 90^\circ$) are depicted in Fig. 3.18. Here again, very good agreement is obtained between measurements and simulations. Moreover, as expected, radiation pattern becomes mirrored with regard to the plane of the radiator's symmetry at $\varphi = 90^\circ - 270^\circ$ when the system state is changed. This implies that the antenna

3.8. Realistic Antenna Prototype for BPSK Signaling

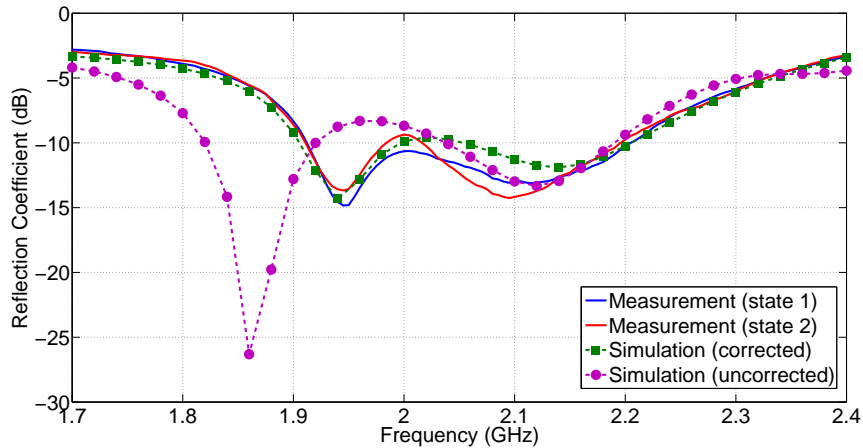


Figure 3.16: Reflection coefficient of the beam-space MIMO antenna obtained from simulations (with corrected and uncorrected circuit models) and measurements (for both antenna's operational states).

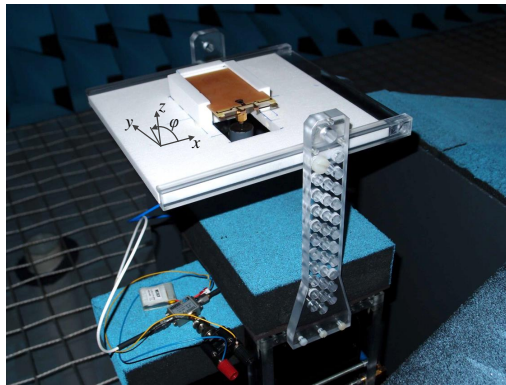


Figure 3.17: Setup for far-field measurements of the fully-operational beam-space MIMO antenna in an anechoic chamber (in the plane of the platform).

is capable to create an orthogonal basis onto which the BPSK signals are mapped, as discussed earlier in Section 3.5.2. The small discrepancy between the measured and simulated cross-polarized components can be safely attributed to spurious radiation effects of the measurement setup (including the supporting structure, the coaxial cable and the bias tee) and antenna fabrication tolerances.

Simulations show a radiation efficiency of 76-83% and 87-89% for the upload and download frequency bands, respectively, which are in good agreement with the values obtained from gain measurements. The corresponding losses can be divided into two parts: the loss introduced by the resistance of the lumped elements (i.e., the real part of the impedance values for the two p-i-n diodes and two RF chokes), and the thermal loss in the dielectric substrate and metallized parts. As shown in Table 3.3, the lumped elements have little contribution to the

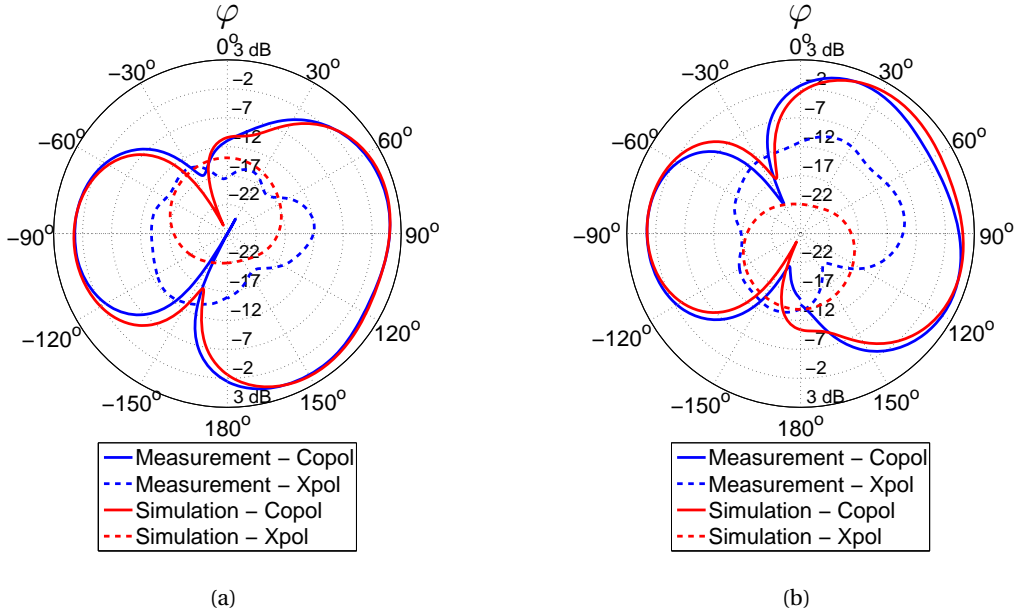


Figure 3.18: Simulated and measured radiation patterns of the beam-space MIMO antenna prototype at 1.95 GHz in the plane of the device platform (a) in State 1, and (b) in State 2.

Table 3.3: Radiation efficiency of the antenna prototype.

Frequency (MHz)	Radiation Efficiency	Metallic/Dielectric Losses (dB)	Lumped Elements' Losses (dB)
1920	76%	0.76	0.55
1950	78%	0.68	0.48
1980	83%	0.52	0.33
2110	89%	0.38	0.12
2140	88%	0.41	0.12
2170	87%	0.45	0.11

total loss, namely less than 0.55 dB at all design frequencies.

Based on the the mirrored radiation patterns obtained from the full-wave simulations, the basis patterns were computed by using (3.20). The corresponding angular basis patterns of the antenna prototype at 1.95 GHz are shown in Fig. 3.19. The first basis pattern looks like a doughnut in the hemisphere $y > 0$, while the second basis pattern is bi-directional and end-fire in the y direction. By spatial integration over the full sphere as given in (3.24) and (3.25), we found the power associated with each basis pattern. Fig. 3.20 shows the distribution of the radiated power ($\mathcal{P}_{\mathcal{E}_{u,1}} = \mathcal{P}_{\mathcal{E}_{u,2}}$) across the basis patterns as a function of frequency. The basis has a small power imbalance ratio of -0.15 dB, -1.28 dB, and 0.13 dB at 1.92 GHz, 1.95 GHz, and 1.98 GHz, respectively, namely very close the ideal power balance for open-loop MIMO operation. Note that according to (3.22), $\mathcal{P}_{\mathcal{E}_{u,1}}$ corresponds to the total efficiency (ϵ_{tot}) of the

3.8. Realistic Antenna Prototype for BPSK Signaling

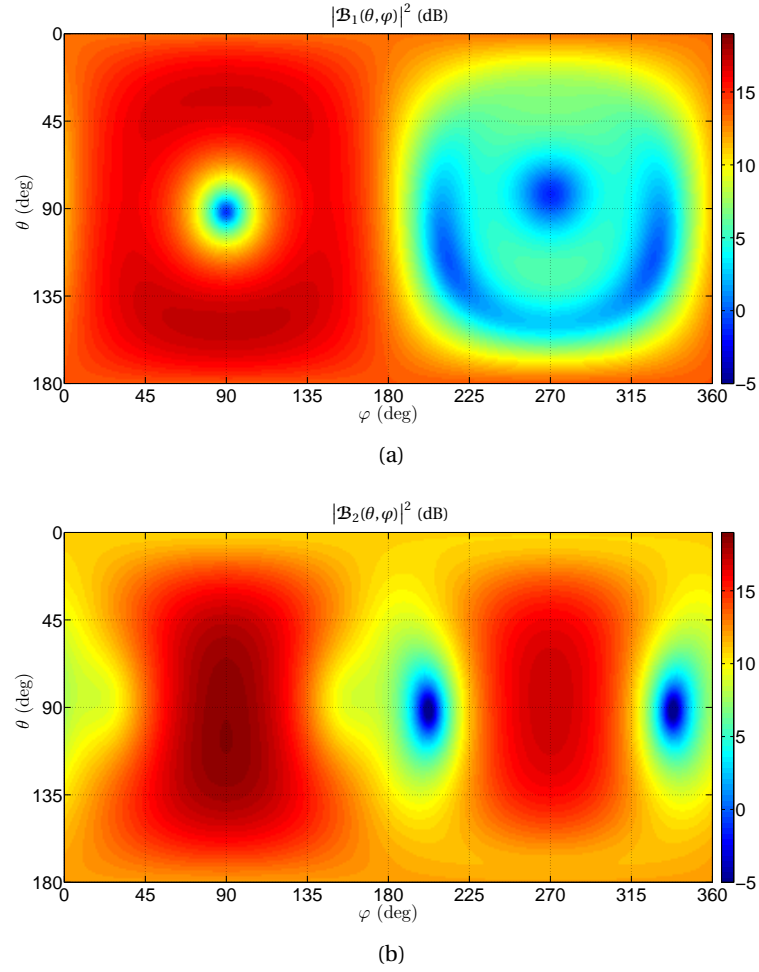


Figure 3.19: Simulated magnitude of the angular basis patterns of the antenna prototype at 1.95 GHz. Note that the orthogonality between the basis patterns applies to the complex patterns over the full sphere and not to their magnitudes.

antenna system, namely, the product of the radiation and matching efficiencies.

To provide some insight into the multiplexing performance of the designed beam-space MIMO antenna prototype, we computed the system capacity under BPSK signaling based on the obtained full-wave simulation results. To do that, we assumed a Kronecker narrowband flat-fading channel [87], where two BPSK signals are simultaneously transmitted over the two basis patterns. The transmitted signals are then received using two uncorrelated and uncoupled antenna elements in an open-loop MIMO operation. Therefore, the channel transfer function can be written as

$$\mathbf{H}_{\text{ch}} = \mathbf{H}_w \mathbf{R}_{\text{Tx}}^{1/2} \quad (3.26)$$

where the elements of the matrix $\mathbf{H}_w \in \mathbb{C}^{2 \times 2}$ are i.i.d. complex Gaussian random variables with zero mean and unit variance. Since the basis patterns are defined when exciting the active

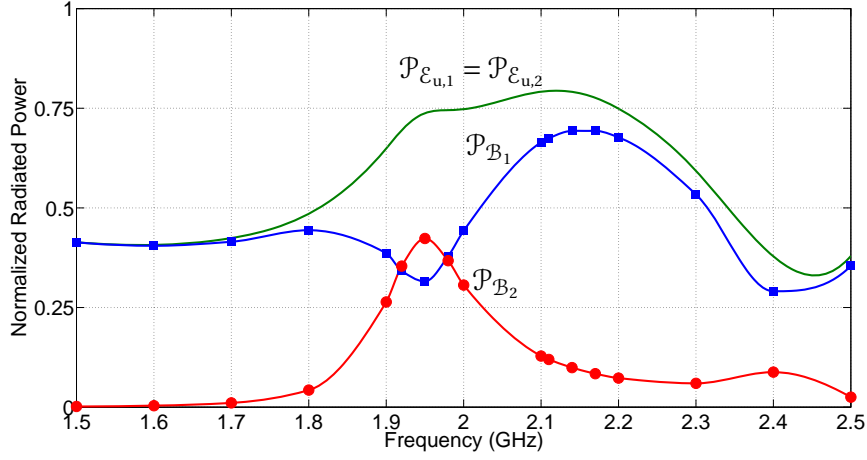


Figure 3.20: Power radiated by the radiation patterns and the basis patterns in the far-field for a unit power excitation. Note that $\mathcal{P}_{\mathcal{B}_1} + \mathcal{P}_{\mathcal{B}_2} = \mathcal{P}_{\epsilon_{u,1}}$ according to (3.24) and (3.25).

port with a unit power, the transmit covariance matrix \mathbf{R}_{Tx} is given by

$$\mathbf{R}_{\text{Tx}} = 2 \begin{bmatrix} \mathcal{P}_{\mathcal{B}_1} & \mathcal{R}_{\mathcal{B}_2, \mathcal{B}_1} \\ \mathcal{R}_{\mathcal{B}_1, \mathcal{B}_2} & \mathcal{P}_{\mathcal{B}_2} \end{bmatrix} \quad (3.27a)$$

$$= \text{diag}[2\mathcal{P}_{\mathcal{B}_1}, 2\mathcal{P}_{\mathcal{B}_2}]. \quad (3.27b)$$

The channel capacity under BPSK signaling was then evaluated according to the approach presented in Appendix A. Fig. 3.21 shows the channel capacity for two signal-to-noise ratio (SNR) values of 0 dB and 10 dB versus the operating frequency. The graph also depicts the channel capacity of an ideal⁵ 2×2 conventional MIMO system under identical assumptions. The excellent behavior of the designed antenna is confirmed, since the corresponding capacity converges to that of the ideal 2×2 MIMO system over the desired frequency band. The discrepancy between the beam-space MIMO and conventional MIMO curves, particularly for the low-SNR case, is due to the losses in the designed antenna.

3.8.3 Frequency Reconfigurability

An important trend in wireless communications is towards a more efficient use of limited spectrum resources. Therefore, and in addition to MIMO techniques, the concept of cognitive radio was brought forward for, among other, achieving dynamic frequency allocation in varying environments [88, 89]. Therefore, in this section we briefly investigate the capability of including frequency reconfiguration in the design of beam-space MIMO antenna, and thereby extending the low-complexity MIMO benefits for technologies providing dynamic spectrum

⁵By ‘ideal’, we mean a covariance matrix equal to the identity matrix, i.e., lossless, decorrelated and balanced MIMO transmission.

3.8. Realistic Antenna Prototype for BPSK Signaling

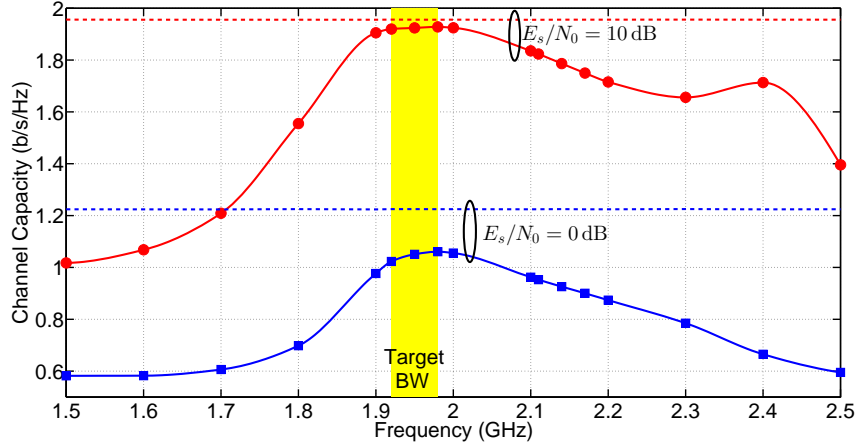


Figure 3.21: Channel capacity under BPSK signaling for two E_s/N_0 values as a function of frequency; solid curves: beam-space MIMO using the designed antenna prototype, and dashed curves: ideal 2×2 conventional MIMO. The capacity was calculated based on the Monte-Carlo averaging where $1e+6$ channel and noise realizations were used. Pulse shaping is not included.

access such as cognitive radio.

Since the S-parameters and the embedded radiation patterns of the three-port radiator are frequency-dependent, the employed technique for the optimization of the antenna yields optimal beam-space MIMO performance around the design frequency only, which is obvious from Fig. 3.21. In order to provide frequency reconfigurability in the optimization procedure, we employ the antenna solution proposed in Fig. 3.3, and terminate the passive ports of the three-port radiator with variable loads whose reactance values are selected according to the instant frequency (f) of operation, namely $Z_I = jX_I(f)$ and $Z_{II} = jX_{II}(f)$. It is clear that the reactance values cannot be simply the impedance values of p-i-n diodes in the ‘on’ and ‘off’ states as in the case of fixed frequency operation.

To evaluate the capability of the designed antenna prototype in frequency reconfiguration, we used the S-parameters and the embedded radiation patterns of the three-port radiator extracted from full-wave simulations to compute the channel capacity under BPSK signaling for a 2D range of $\{X_I, X_{II}\}$ (with a resolution of 10Ω) under assumptions identical to those in Section 3.8.2. Then, we selected the reactance values which achieve the maximum channel capacity under BPSK signaling at each frequency for $E_s/N_0 = 10$ dB. Fig. 3.22 shows that satisfactory capacity is maintained within a frequency band of 1.35-2.4 GHz with a reference of 1.8 b/s/Hz (which corresponds to 92% of the capacity of an ideal 2×2 conventional MIMO system for the same SNR), when the designed radiator is properly loaded at each single frequency. As shown in Fig. 3.23, the use of the optimal reactance values guarantees a total efficiency better than 45% and a power imbalance ratio less than 3.7 dB on the same frequency range. Fig. 3.24 plots the optimal reactance values as functions of frequency. Interestingly, plotting a contour map of the channel capacity with respect to X_I and X_{II} , such as done in

Fig. 3.25, shows that the performance is in general quite insensitive to moderate variations in the reactance values.

Obviously, the possibility of dynamic frequency operation comes at the cost of more complicated variable load circuits and relies on the availability of appropriate dynamically-controllable reactive loads based on semiconductor diodes. A possible method for reducing the load complexity in frequency-flexible operation is to divide the bandwidth into multiple sub-bands, and then to select an optimal reactance pair for each sub-band so that satisfactory beam-space MIMO performance is ensured over the whole bandwidth. In this way, the desired frequency flexibility can be achieved using just a few reactance pairs. To illustrate the applicability of this

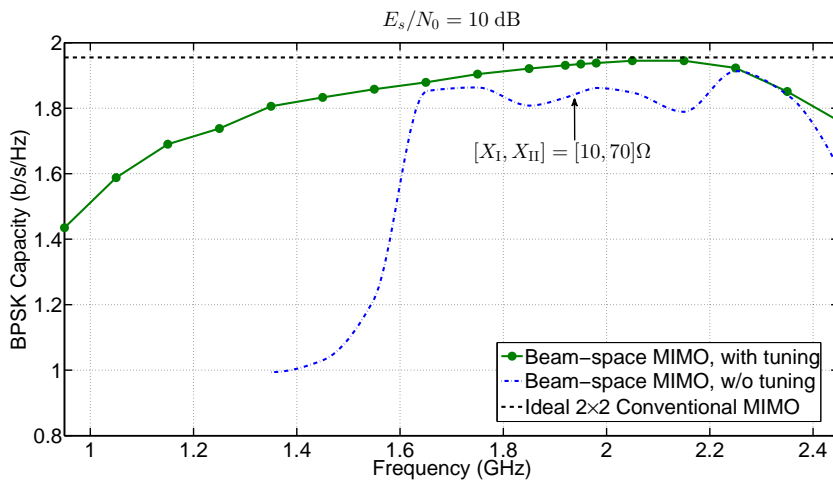


Figure 3.22: Maximum achievable capacity under BPSK signaling, when the antenna's loadings are properly tuned at each frequency.

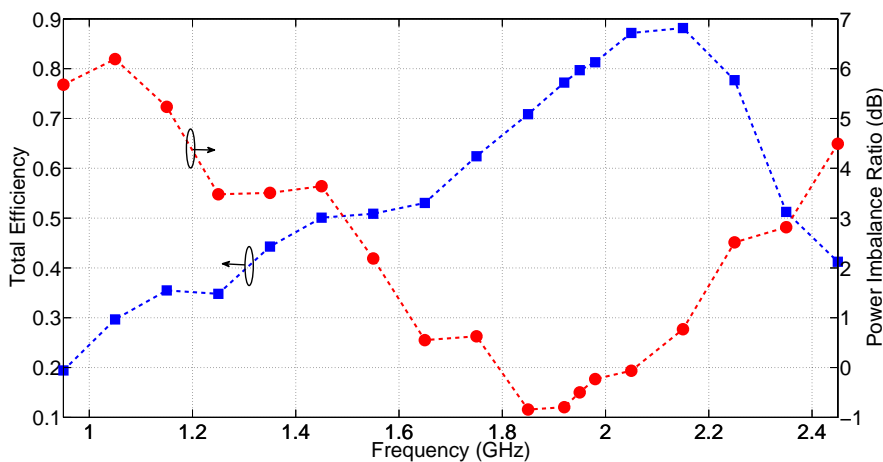


Figure 3.23: Corresponding total efficiency and power imbalance ratio as functions of frequency, when the antenna's loadings are properly tuned at each frequency.

3.8. Realistic Antenna Prototype for BPSK Signaling

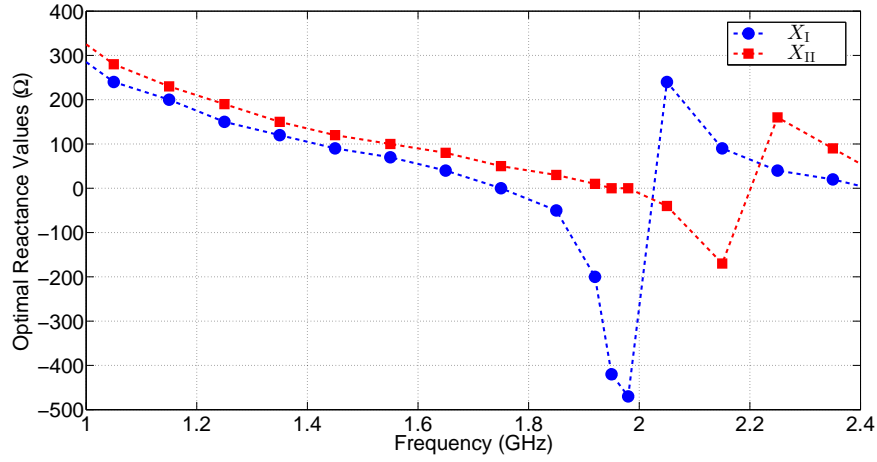


Figure 3.24: Required reactance values for achieving maximum channel capacity.

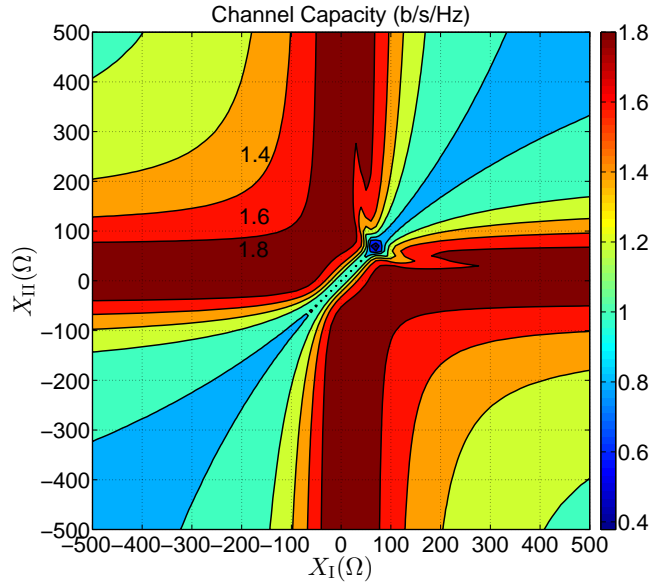


Figure 3.25: A contour map of the capacity under BPSK signaling with respect to X_I and X_{II} at 1.95 GHz. The figure shows that a wide range of reactance values can provide an acceptable level of channel capacity.

approach, Fig. 3.22 shows the channel capacity achievable using an optimal load pair, which is higher than 1.8 b/s/Hz within a frequency range of 1.63-2.38 GHz.

Finally, we would like to stress that, the developed antenna hardware used here for beam-space MIMO can readily be used to achieve other functionalities. Indeed, it has been shown in [54] that the antenna's radiation patterns, $\mathcal{E}_{u,1}$ and $\mathcal{E}_{u,2}$, are themselves orthonormal when the basis patterns are orthonormal. Therefore, for the power imbalance ratios close to 0 dB the radiation patterns are quasi-orthogonal, and therefore the existing hardware can be employed

for receive pattern diversity to dynamically compensate channel variations, or for receive spatial multiplexing by oversampling received signals [90]. Thus, the beam-space MIMO technique can support dynamic selection of the operation mode (transmission/reception) and the operating frequency, paving the way for MIMO-based cognitive radio communications with just a limited increase in hardware complexity.

3.9 Conclusion

Throughout this chapter, we have discussed numerous practical issues encountered during the actual design and implementation of reconfigurable antennas for the particular application of beam-space MIMO. A compact antenna solution for implementing the beam-space MIMO concept in real small portable devices has been proposed. The solution employs a single-radiator load-modulated antenna, and can be integrated to the device platform.

An efficient approach for the modeling and simulation of load-modulated antennas with localized loads has been reviewed, which allows computing the antenna parameters for any set of loads using a single full-wave simulation. Different technologies for enabling the variable loads has been compared according to the main requirements of beam-space MIMO. It has been shown that semiconductor devices are currently the most appropriate technology for realizing the control elements for beam-space MIMO applications. A comprehensive discussion has been made on the pros and cons of the existing approaches for the pattern decomposition in beam-space MIMO, where we showed the mirror image pattern pair technique is the most favorable one in practice.

A practical methodology for the accurate modeling of reconfigurable lumped elements in commercial full-wave solvers has been presented and validated. The proposed technique employs a correction strategy to avoid accounting some extra effects in full-wave simulations, and ensures excellent agreement between simulated and measured results.

A general design approach has been discussed for load-modulate antennas, which simplifies the implementation of variable load circuits and DC biasing networks. A practical compact antenna system prototype for single-radio multiplexing of BPSK modulated signals has been designed and measured, showing very good agreement with simulations in terms of return loss and radiation patterns. Finally, an early demonstration of the possibility of dynamic frequency allocation in beam-space MIMO transmission has been provided. These results constitute significant progress towards the future implementation of the beam-space MIMO concept in real applications.

4 Beam-Space MIMO: High-Order Modulation Support

*Whatever was not designed, the hand can not reach;
and whatever was ordained, it can attain in any situation.*
— Saadi, Gulistan, Principles of Social Conduct, Maxim 68

4.1 Overview

Although the novel beam-space MIMO concept revolutionizes the antenna and the RF chain in MIMO transmission by reducing the hardware size and complexity, its advantages come with a number of limitations that do not exist in conventional MIMO systems. As explained in Chapter 2 and formulated in (2.18), a beam-space MIMO antenna functions as an analogue modulator, and maps the symbols to be multiplexed at each symbol period onto a predefined set of orthogonal basis patterns in the far-field. This demands that the antenna be precisely capable of forming all required radiation patterns according to the signal constellation diagram. Therefore, successful data multiplexing, when utilizing a load-modulated antenna, strongly depends on finding the correct impedance values at every symbol period and then realizing the required variable loads. In practice, the use of only passive reactive loads is generally favorable since the complexity and stability concerns of active loads counteract the benefits of beam-space MIMO. On the other hand, considerable care must be exercised to ensure that the load reconfiguration does not lead to large dynamic variation of the input impedance at the active port in order to obviate the need for symbol-rate dynamic matching networks. This is why emulating high-order modulation schemes, such as PSK and QAM, with realistic and low-complexity single-radio MIMO hardware becomes a primary challenge.

In the previous chapter, we derived the orthogonal basis functions required for pattern decomposition from mirror image radiation patterns of a load-modulated antenna composed of a symmetric radiator, based on that the first integrated antenna solution for implementing the single-radio MIMO concept in real small portable devices was presented. Although such a decomposition approach addresses the complexity issues associated with loads and matching

Parts of this chapter have been published earlier in [22, 23].

network, it is limited to BPSK signaling, and can not be scaled to other modulation schemes.

In this chapter, we propose an efficient beam-space MIMO strategy which enables multiplexing *higher order* PSK signals with a realistic single-feed reconfigurable antenna. This is achieved by reconsidering the signal-space multiplexing approach and viewing it as a multi-layer analogue precoding. In the proposed strategy, multiplexing of basis patterns is replaced with multiplexing of basis vectors as the basis vectors can be precisely obtained without extracting complex far-field radiation patterns, so avoiding tedious far-field calculations when deriving the multiplexing expression. The strategy makes use of only variable passive loads for pattern reconfiguration, and ensures a constant reflection coefficient at the antenna's active port independently of the symbols to be multiplexed. The procedure is illustrated by an antenna design example supporting the single-feed transmission of two QPSK data streams.

The rest of this chapter is organized as follows. Section 4.2 introduces a general framework for expressing the spatial multiplexing relation of the transmit signals only from the radiator's S-parameters and the impedance values of the variable loads. Then, the mathematical developments related to the novel proposed methodology are described in detail. The proposed strategy is then employed in Section 4.3 to design and implement the first fully-operational beam-space MIMO antenna for transmitting two QPSK signals.

4.2 Multiplexing Strategy: Theory and Implementation

In this section, our goal is to make the implementation of (2.18) possible for higher-order PSK modulation schemes using a compact single-feed antenna with only passive loads embedded. In the following, we start with defining the incident power wave vector for a single-feed load-modulated antenna, based on that we recall the analytical expressions of the reflection coefficient and the radiation pattern. This allows us later to define our set of orthogonal basis vectors, and present our approach for single-radio multiplexing.

4.2.1 Incident Power Wave Vector

Let us consider a single-feed load-modulated antenna, in accord with the solution proposed in Section 3.2, comprising a symmetric three-port radiator and two variable loads, Z_1 and Z_2 , connected to the radiator's passive ports. Fig. 4.1a shows a symbolic representation of such an antenna. As explained in Section 3.3, the radiator can be completely described by a 3×3 scattering matrix, \mathbf{S} , and three embedded radiation patterns, $\{\mathcal{F}_p(\Omega)\}_{p=0}^2$. Accordingly, the load-modulated antenna can be modeled by the signal flow graph of Fig. 4.1b, where Γ_1 and Γ_2 are the reflection coefficients, given by (3.7), at the passive ports. Note that, by reciprocity, $S_{10} = S_{01}$, $S_{20} = S_{02}$, and $S_{21} = S_{12}$, while by the radiator's symmetry, $S_{11} = S_{22}$ and $S_{01} = S_{02}$. Moreover, $\mathcal{F}_1(\Omega)$ and $\mathcal{F}_2(\Omega)$ form a mirror image pattern pair with respect to the plane of the radiator's symmetry, whereas $\mathcal{F}_0(\Omega)$ is symmetrical with regard to the same plane.

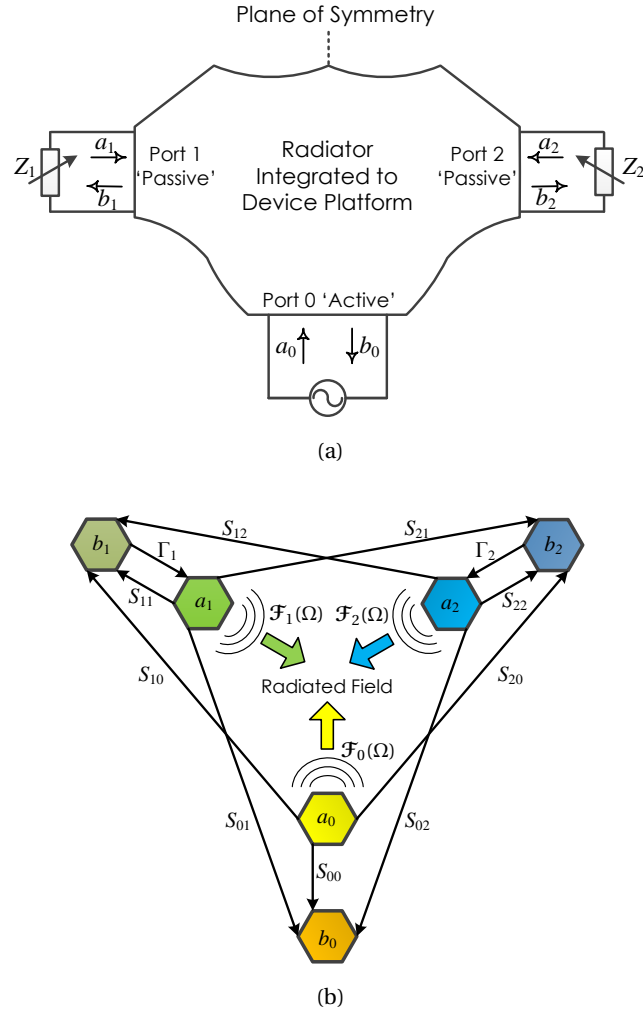


Figure 4.1: (a) A load-modulated antenna composed of a symmetric three-port radiator. Note that the single-port structure (i.e., when two passive ports are loaded) is not generally symmetrical. (b) Equivalent signal flow of the antenna. The incident and reflected power waves are denoted by a_p and b_p , $p \in \{0, 1, 2\}$, respectively. For the sake of simplicity, the source impedance Z_0 is chosen to be equal to the reference impedance of the S-parameters.

Using Mason's rule [91] or equivalently using (3.9), the incident power waves at the passive ports when exciting the active port with a unit power (i.e., $a_0 = 1$) become

$$a_{1,u} = \frac{a_1}{a_0} = \Gamma_1 S_{01} \frac{1 - \Gamma_2 (S_{11} - S_{21})}{1 - S_{11} (\Gamma_1 + \Gamma_2) + \Gamma_1 \Gamma_2 (S_{11}^2 - S_{21}^2)} \quad (4.1a)$$

$$a_{2,u} = \frac{a_2}{a_0} = \Gamma_2 S_{01} \frac{1 - \Gamma_1 (S_{11} - S_{21})}{1 - S_{11} (\Gamma_1 + \Gamma_2) + \Gamma_1 \Gamma_2 (S_{11}^2 - S_{21}^2)}. \quad (4.1b)$$

Therefore, the antenna's radiation pattern can be expressed, according to (3.12), as a linear

combination of the three embedded radiation patterns, namely,

$$\mathcal{E}_u(\Omega) = \mathcal{F}_{\text{emb}}(\Omega)\mathcal{A}_u, \quad (4.2)$$

where

$$\mathcal{F}_{\text{emb}}(\Omega) = \begin{bmatrix} \mathcal{F}_0(\Omega) & \mathcal{F}_1(\Omega) & \mathcal{F}_2(\Omega) \end{bmatrix} \in \mathbb{C}^{2 \times 3} \quad (4.3)$$

is the matrix of the radiator's embedded radiation patterns, and

$$\mathcal{A}_u = \begin{bmatrix} 1 & a_{1,u} & a_{2,u} \end{bmatrix}^T \in \mathbb{C}^{3 \times 1} \quad (4.4)$$

is defined here as the antenna's incident power wave vector. Let us emphasize that the radiator's embedded radiation patterns and the antenna's radiation pattern are complex vectorial angular functions.

According to (3.11), the reflection coefficient at the antenna's active port can be also expressed in terms of the incident power wave vector, i.e.,

$$\Gamma_{\text{in}} = \begin{bmatrix} S_{00} & S_{01} & S_{01} \end{bmatrix} \mathcal{A}_u. \quad (4.5)$$

It is easily seen from (4.4) and (4.5) that if reconfiguring the variable loads at the passive ports does not change the value of $a_{1,u} + a_{2,u}$, the reflection coefficient at the active port remains constant.

Due to the symmetry of the radiator and according to (4.1), the permutation of the loads at the passive ports as $Z_1 \leftrightarrow Z_2$ will swap the values of the incident power waves, i.e., $a_{1,u} \leftrightarrow a_{2,u}$, thereby mirroring the antenna's radiation pattern with respect to the plane of the radiator's symmetry. This feature is employed in Section 4.2.2, where the desired basis for single-radio MIMO transmission is defined.

4.2.2 Basis Vectors

Here, we look at the mirror image pattern pair approach for the basis definition from a different perspective than what has been done before in Section 3.5.2. For the load-modulated antenna symbolically represented in Fig. 4.1a, the definition of angular functions \mathcal{B}_1 and \mathcal{B}_2 as

$$\mathcal{B}_1(\Omega) = \frac{\mathcal{E}_u^{\{Z_{\text{II}}, Z_1\}}(\Omega) + \mathcal{E}_u^{\{Z_1, Z_{\text{II}}\}}(\Omega)}{2} \quad (4.6a)$$

$$\mathcal{B}_2(\Omega) = \frac{\mathcal{E}_u^{\{Z_{\text{II}}, Z_1\}}(\Omega) - \mathcal{E}_u^{\{Z_1, Z_{\text{II}}\}}(\Omega)}{2} \quad (4.6b)$$

creates the desired orthogonal basis for the pattern decomposition. In (4.6), the superscript notation determines two distinct system states, namely, (i) State $\{Z_1, Z_{\text{II}}\}$ where the loads Z_1

4.2. Multiplexing Strategy: Theory and Implementation

and Z_{II} are connected to the ports 1 and 2, respectively, i.e., $\Gamma_1^{\{Z_I, Z_{II}\}} = \Gamma_I$ and $\Gamma_2^{\{Z_I, Z_{II}\}} = \Gamma_{II}$; and (ii) State $\{Z_{II}, Z_I\}$ where the loads Z_I and Z_{II} are connected to the ports 2 and 1, respectively, i.e., $\Gamma_1^{\{Z_{II}, Z_I\}} = \Gamma_{II}$ and $\Gamma_2^{\{Z_{II}, Z_I\}} = \Gamma_I$. According to (4.2), the antenna's radiation patterns for the given system states are derived as

$$\mathcal{E}_u^{\{Z_I, Z_{II}\}}(\Omega) = \mathcal{F}_{\text{emb}}(\Omega) \mathcal{A}_u^{\{Z_I, Z_{II}\}} \quad (4.7a)$$

$$\mathcal{E}_u^{\{Z_{II}, Z_I\}}(\Omega) = \mathcal{F}_{\text{emb}}(\Omega) \mathcal{A}_u^{\{Z_{II}, Z_I\}}, \quad (4.7b)$$

where

$$\mathcal{A}_u^{\{Z_I, Z_{II}\}} = \begin{bmatrix} 1 & a_{1,u}^{\{Z_I, Z_{II}\}} & a_{2,u}^{\{Z_I, Z_{II}\}} \end{bmatrix}^T \quad (4.8a)$$

$$\mathcal{A}_u^{\{Z_{II}, Z_I\}} = \begin{bmatrix} 1 & a_{2,u}^{\{Z_{II}, Z_I\}} & a_{1,u}^{\{Z_{II}, Z_I\}} \end{bmatrix}^T \quad (4.8b)$$

are the corresponding incident power wave vectors since

$$\begin{aligned} a_{1,u}^{\{Z_I, Z_{II}\}} &= a_{2,u}^{\{Z_{II}, Z_I\}} \\ &= \Gamma_I S_{01} \frac{1 - \Gamma_{II} (S_{11} - S_{21})}{1 - S_{11} (\Gamma_I + \Gamma_{II}) + \Gamma_I \Gamma_{II} (S_{11}^2 - S_{21}^2)} \end{aligned} \quad (4.9a)$$

$$\begin{aligned} a_{2,u}^{\{Z_I, Z_{II}\}} &= a_{1,u}^{\{Z_{II}, Z_I\}} \\ &= \Gamma_{II} S_{01} \frac{1 - \Gamma_I (S_{11} - S_{21})}{1 - S_{11} (\Gamma_I + \Gamma_{II}) + \Gamma_I \Gamma_{II} (S_{11}^2 - S_{21}^2)}. \end{aligned} \quad (4.9b)$$

It can be easily inferred from (4.7) and (4.8) that $\mathcal{E}_u^{\{Z_I, Z_{II}\}}(\Omega)$ is a mirrored version of $\mathcal{E}_u^{\{Z_{II}, Z_I\}}(\Omega)$ regarding the plane of the radiator's symmetry.

Now, let us write the analytical expressions of the basis patterns directly in terms of the radiator's embedded radiation patterns. Inserting (4.7) into (4.6), the basis patterns become

$$\mathcal{B}_1(\Omega) = \mathcal{F}_{\text{emb}}(\Omega) \mathcal{A}_{\mathcal{B}_1}^{\{Z_I, Z_{II}\}} \quad (4.10a)$$

$$\mathcal{B}_2(\Omega) = \mathcal{F}_{\text{emb}}(\Omega) \mathcal{A}_{\mathcal{B}_2}^{\{Z_I, Z_{II}\}}, \quad (4.10b)$$

where

$$\mathcal{A}_{\mathcal{B}_1}^{\{Z_I, Z_{II}\}} = \begin{bmatrix} 1 & a_{\mathcal{B}_1}^{\{Z_I, Z_{II}\}} & a_{\mathcal{B}_1}^{\{Z_I, Z_{II}\}} \end{bmatrix}^T \quad (4.11a)$$

$$\mathcal{A}_{\mathcal{B}_2}^{\{Z_I, Z_{II}\}} = \begin{bmatrix} 0 & a_{\mathcal{B}_2}^{\{Z_I, Z_{II}\}} & -a_{\mathcal{B}_2}^{\{Z_I, Z_{II}\}} \end{bmatrix}^T \quad (4.11b)$$

denote the basis vectors, and

$$\begin{aligned} \mathbf{a}_{\mathcal{B}_1}^{\{Z_I, Z_{II}\}} &= \frac{\mathbf{a}_{1,u}^{\{Z_I, Z_{II}\}} + \mathbf{a}_{2,u}^{\{Z_I, Z_{II}\}}}{2} \\ &= \frac{1}{2} \cdot \frac{S_{01} [\Gamma_I + \Gamma_{II} - 2\Gamma_I \Gamma_{II} (S_{11} - S_{21})]}{1 - S_{11} (\Gamma_I + \Gamma_{II}) + \Gamma_I \Gamma_{II} (S_{11}^2 - S_{21}^2)} \end{aligned} \quad (4.12a)$$

$$\begin{aligned} \mathbf{a}_{\mathcal{B}_2}^{\{Z_I, Z_{II}\}} &= \frac{\mathbf{a}_{2,u}^{\{Z_I, Z_{II}\}} - \mathbf{a}_{1,u}^{\{Z_I, Z_{II}\}}}{2} \\ &= \frac{1}{2} \cdot \frac{S_{01} [\Gamma_{II} - \Gamma_I]}{1 - S_{11} (\Gamma_I + \Gamma_{II}) + \Gamma_I \Gamma_{II} (S_{11}^2 - S_{21}^2)}. \end{aligned} \quad (4.12b)$$

Indeed, each basis vector can be regarded as the incident power wave vector of a virtual load-modulated antenna composed of the same three-port radiator. In the first virtual antenna (corresponding to $\mathcal{A}_{\mathcal{B}_1}^{\{Z_I, Z_{II}\}}$), port 0 is the active input, while the other two are terminated with identical loads. By contrast, in the second virtual antenna (corresponding to $\mathcal{A}_{\mathcal{B}_2}^{\{Z_I, Z_{II}\}}$), ports 1 and 2 are active and excited in anti-phase, whereas port 0 is matched to Z_0 .

The beam-coupling coefficient between $\mathcal{B}_1(\Omega)$ and $\mathcal{B}_2(\Omega)$ can be calculated using (3.6) as

$$\begin{aligned} \mathcal{R}_{\mathcal{B}_1 \mathcal{B}_2} &= \frac{1}{2} \eta_0 \int \mathcal{B}_2(\Omega) \cdot \mathcal{B}_1^*(\Omega) d\Omega \\ &= \frac{1}{2} \eta_0 \int \left[\mathcal{F}_{\text{emb}}(\Omega) \mathcal{A}_{\mathcal{B}_2}^{\{Z_I, Z_{II}\}} \right] \cdot \left[\mathcal{F}_{\text{emb}}(\Omega) \mathcal{A}_{\mathcal{B}_1}^{\{Z_I, Z_{II}\}} \right]^* d\Omega \\ &= \frac{1}{2} \eta_0 \int \mathbf{a}_{\mathcal{B}_2}^{\{Z_I, Z_{II}\}} [\mathcal{F}_1(\Omega) - \mathcal{F}_2(\Omega)] \cdot \left[\mathcal{F}_0(\Omega) + \mathbf{a}_{\mathcal{B}_1}^{\{Z_I, Z_{II}\}} [\mathcal{F}_1(\Omega) + \mathcal{F}_2(\Omega)] \right]^* d\Omega \\ &= \frac{1}{2} \eta_0 \mathbf{a}_{\mathcal{B}_2}^{\{Z_I, Z_{II}\}} \left[(\mathcal{R}_{01} - \mathcal{R}_{02}) + \mathbf{a}_{\mathcal{B}_1}^{\{Z_I, Z_{II}\}*} (\mathcal{R}_{11} - \mathcal{R}_{22} + \mathcal{R}_{21} - \mathcal{R}_{12}) \right]. \end{aligned} \quad (4.13)$$

Since by symmetry of the radiator, $\mathcal{R}_{01} = \mathcal{R}_{02}$, $\mathcal{R}_{11} = \mathcal{R}_{22}$ and $\mathcal{R}_{21} = \mathcal{R}_{12}$,

$$\mathcal{R}_{\mathcal{B}_1 \mathcal{B}_2} = 0, \quad (4.14)$$

demonstrating that $\mathcal{B}_1(\Omega)$ and $\mathcal{B}_2(\Omega)$ as defined in (4.6) form an orthogonal basis.

The power radiated in the far-field by the basis patterns $\mathcal{B}_1(\Omega)$ and $\mathcal{B}_2(\Omega)$ can be obtained using (3.6) as

$$\begin{aligned} \mathcal{P}_{\mathcal{B}_1} &= \mathcal{R}_{\mathcal{B}_1 \mathcal{B}_1} = \frac{1}{2} \eta_0 \int |\mathcal{B}_1(\Omega)|^2 d\Omega \\ &= \frac{1}{2} \eta_0 \int \left| \mathcal{F}_{\text{emb}}(\Omega) \mathcal{A}_{\mathcal{B}_1}^{\{Z_I, Z_{II}\}} \right|^2 d\Omega \\ &= \frac{1}{2} \eta_0 \int \left| \mathcal{F}_0(\Omega) + \mathbf{a}_{\mathcal{B}_1}^{\{Z_I, Z_{II}\}} [\mathcal{F}_1(\Omega) + \mathcal{F}_2(\Omega)] \right|^2 d\Omega \\ &= \mathcal{R}_{00} + \left| \mathbf{a}_{\mathcal{B}_1}^{\{Z_I, Z_{II}\}} \right|^2 (\mathcal{R}_{11} + \mathcal{R}_{22} + \mathcal{R}_{12} + \mathcal{R}_{21}) + \mathbf{a}_{\mathcal{B}_1}^{\{Z_I, Z_{II}\}} (\mathcal{R}_{01} + \mathcal{R}_{02}) \\ &\quad + \mathbf{a}_{\mathcal{B}_1}^{\{Z_I, Z_{II}\}*} (\mathcal{R}_{10} + \mathcal{R}_{20}) \end{aligned}$$

$$= \mathcal{R}_{00} + 2 \left| a_{\mathcal{B}_1}^{\{Z_I, Z_{II}\}} \right|^2 (\mathcal{R}_{11} + \mathcal{R}_{21}) + 4 \operatorname{Re} \left(a_{\mathcal{B}_1}^{\{Z_I, Z_{II}\}} \mathcal{R}_{01} \right) \quad (4.15a)$$

$$\begin{aligned} \mathcal{P}_{\mathcal{B}_2} &= \mathcal{R}_{\mathcal{B}_2 \mathcal{B}_2} = \frac{1}{2} \eta_0 \int |\mathcal{B}_2(\Omega)|^2 d\Omega \\ &= \frac{1}{2} \eta_0 \int \left| \mathcal{F}_{\text{emb}}(\Omega) \mathcal{A}_{\mathcal{B}_2}^{\{Z_I, Z_{II}\}} \right|^2 d\Omega \\ &= \frac{1}{2} \eta_0 \int \left| a_{\mathcal{B}_2}^{\{Z_I, Z_{II}\}} [\mathcal{F}_1(\Omega) - \mathcal{F}_2(\Omega)] \right|^2 d\Omega \\ &= \left| a_{\mathcal{B}_2}^{\{Z_I, Z_{II}\}} \right|^2 (\mathcal{R}_{11} + \mathcal{R}_{22} - \mathcal{R}_{12} - \mathcal{R}_{21}) \\ &= 2 \left| a_{\mathcal{B}_2}^{\{Z_I, Z_{II}\}} \right|^2 (\mathcal{R}_{11} - \mathcal{R}_{21}). \end{aligned} \quad (4.15b)$$

As explained in Chapter 3, a balanced power distribution between the multiple streams is ideally desired for open-loop MIMO operation.

It is worth noting that the orthogonality of $\mathcal{B}_1(\Omega)$ and $\mathcal{B}_2(\Omega)$ is valid independent of the impedance values Z_I and Z_{II} (hereafter also called the *basis impedances*). However, their values affect the total reflection coefficient at the single active port as well as the powers $\mathcal{P}_{\mathcal{B}_1}$ and $\mathcal{P}_{\mathcal{B}_2}$ radiated by the basis patterns.

4.2.3 Multiplexing Technique

Up to this point in this section, we have proved the existence of a natural orthogonal basis for the single-feed load-modulated antenna shown in Fig. 4.1a. We follow here by demonstrating an efficient approach that makes such an antenna capable of multiplexing two data streams of any modulation order.

For mapping each arbitrary symbol combination of $\{x_1, x_2\}$ from the considered signal constellation diagram on the basis patterns already defined in (4.6) and enabling single-radio spatial multiplexing, we need to find the impedance values of the variable loads, denoted by $Z_1^{\{x_1, x_2\}}$ and $Z_2^{\{x_1, x_2\}}$, such that the antenna's actual radiation pattern becomes

$$\begin{aligned} \mathcal{E}_o(\Omega) &= x_1 \mathcal{B}_1(\Omega) + x_2 \mathcal{B}_2(\Omega) \\ &= \mathcal{F}_{\text{emb}}(\Omega) \left[x_1 \mathcal{A}_{\mathcal{B}_1}^{\{Z_I, Z_{II}\}} + x_2 \mathcal{A}_{\mathcal{B}_2}^{\{Z_I, Z_{II}\}} \right]. \end{aligned} \quad (4.16)$$

On the other hand, $\mathcal{E}_o(\Omega)$ can generally be written as the multiplication of the antenna's radiation pattern for a unit power excitation, $\mathcal{E}_u^{\{Z_1^{\{x_1, x_2\}}, Z_2^{\{x_1, x_2\}}\}}(\Omega)$, and the signal applied to the antenna system at its single active input, which we define as $x_{\text{in}}(x_1, x_2)$, thus

$$\begin{aligned} \mathcal{E}_o(\Omega) &= x_{\text{in}}(x_1, x_2) \mathcal{E}_u^{\{Z_1^{\{x_1, x_2\}}, Z_2^{\{x_1, x_2\}}\}}(\Omega) \\ &= \mathcal{F}_{\text{emb}}(\Omega) \left[x_{\text{in}}(x_1, x_2) \mathcal{A}_u^{\{Z_1^{\{x_1, x_2\}}, Z_2^{\{x_1, x_2\}}\}} \right], \end{aligned} \quad (4.17)$$

where according to (4.4),

$$\mathcal{A}_u^{\{Z_1^{\{x_1, x_2\}}, Z_2^{\{x_1, x_2\}}\}} = \begin{bmatrix} 1 & \mathbf{a}_{1,u}^{\{Z_1^{\{x_1, x_2\}}, Z_2^{\{x_1, x_2\}}\}} & \mathbf{a}_{2,u}^{\{Z_1^{\{x_1, x_2\}}, Z_2^{\{x_1, x_2\}}\}} \end{bmatrix}^T. \quad (4.18)$$

Combining (4.16) and (4.17), the far-field terms disappear from the equation that allows finding the unknowns $Z_1^{\{x_1, x_2\}}$ and $Z_2^{\{x_1, x_2\}}$, thereby dispensing with cumbersome calculation of the far-field radiation patterns and replacing the multiplexing of basis patterns with the multiplexing of basis vectors:

$$x_{in}(x_1, x_2) \mathcal{A}_u^{\{Z_1^{\{x_1, x_2\}}, Z_2^{\{x_1, x_2\}}\}} = x_1 \mathcal{A}_{B_1}^{\{Z_1, Z_{II}\}} + x_2 \mathcal{A}_{B_2}^{\{Z_1, Z_{II}\}}, \quad (4.19)$$

or using (4.11) and (4.18),

$$x_{in}(x_1, x_2) \begin{bmatrix} 1 \\ \mathbf{a}_{1,u}^{\{Z_1^{\{x_1, x_2\}}, Z_2^{\{x_1, x_2\}}\}} \\ \mathbf{a}_{2,u}^{\{Z_1^{\{x_1, x_2\}}, Z_2^{\{x_1, x_2\}}\}} \end{bmatrix} = x_1 \begin{bmatrix} 1 \\ \mathbf{a}_{B_1}^{\{Z_1, Z_{II}\}} \\ \mathbf{a}_{B_1}^{\{Z_1, Z_{II}\}} \end{bmatrix} + x_2 \begin{bmatrix} 0 \\ \mathbf{a}_{B_2}^{\{Z_1, Z_{II}\}} \\ -\mathbf{a}_{B_2}^{\{Z_1, Z_{II}\}} \end{bmatrix}. \quad (4.20)$$

It is easily seen that a necessary condition for satisfying (4.20) is $x_{in}(x_1, x_2) = x_1$. This reveals an important practical aspect of the proposed approach: the single active port of the antenna system must be excited with one of the two data streams. In this case, (4.20) reduces to a system of two equations, allowing finding unique solutions for the unknowns $Z_1^{\{x_1, x_2\}}$ and $Z_2^{\{x_1, x_2\}}$ as functions of the radiator's scattering parameters, the basis impedances, and the symbols pair $\{x_1, x_2\}$, i.e.,

$$\begin{bmatrix} \mathbf{a}_{1,u}^{\{Z_1^{\{x_1, x_2\}}, Z_2^{\{x_1, x_2\}}\}} \\ \mathbf{a}_{2,u}^{\{Z_1^{\{x_1, x_2\}}, Z_2^{\{x_1, x_2\}}\}} \end{bmatrix} = \mathbf{a}_{B_1}^{\{Z_1, Z_{II}\}} \begin{bmatrix} 1 \\ 1 \end{bmatrix} + \frac{x_2}{x_1} \mathbf{a}_{B_2}^{\{Z_1, Z_{II}\}} \begin{bmatrix} 1 \\ -1 \end{bmatrix}. \quad (4.21)$$

However, as seen in (4.21), the multiplexing relation only depends on the ratio of x_2 and x_1 and not on their individual values. In other words, the same load pair is required for transmitting any symbol pair $\{x_1, x_2\}$ having the same ratio,

$$x_r = \frac{x_2}{x_1}. \quad (4.22)$$

As a result, we simplify the notation in (4.21), replacing the superscript $\{x_1, x_2\}$ with $\{x_r\}$, i.e.,

$$\begin{bmatrix} \mathbf{a}_{1,u}^{\{Z_1^{\{x_r\}}, Z_2^{\{x_r\}}\}} \\ \mathbf{a}_{2,u}^{\{Z_1^{\{x_r\}}, Z_2^{\{x_r\}}\}} \end{bmatrix} = \mathbf{a}_{B_1}^{\{Z_1, Z_{II}\}} \begin{bmatrix} 1 \\ 1 \end{bmatrix} + x_r \mathbf{a}_{B_2}^{\{Z_1, Z_{II}\}} \begin{bmatrix} 1 \\ -1 \end{bmatrix}, \quad (4.23)$$

4.2. Multiplexing Strategy: Theory and Implementation

where $Z_1^{\{x_r\}}$ and $Z_2^{\{x_r\}}$ (or equivalently their corresponding reflection coefficients, $\Gamma_1^{\{x_r\}}$ and $\Gamma_2^{\{x_r\}}$) are the unknowns and using (4.1),

$$a_{1,u}^{\{Z_1^{\{x_r\}}, Z_2^{\{x_r\}}\}} = \Gamma_1^{\{x_r\}} S_{01} \frac{1 - \Gamma_2^{\{x_r\}} (S_{11} - S_{21})}{1 - S_{11} (\Gamma_1^{\{x_r\}} + \Gamma_2^{\{x_r\}}) + \Gamma_1^{\{x_r\}} \Gamma_2^{\{x_r\}} (S_{11}^2 - S_{21}^2)} \quad (4.24a)$$

$$a_{2,u}^{\{Z_1^{\{x_r\}}, Z_2^{\{x_r\}}\}} = \Gamma_2^{\{x_r\}} S_{01} \frac{1 - \Gamma_1^{\{x_r\}} (S_{11} - S_{21})}{1 - S_{11} (\Gamma_1^{\{x_r\}} + \Gamma_2^{\{x_r\}}) + \Gamma_1^{\{x_r\}} \Gamma_2^{\{x_r\}} (S_{11}^2 - S_{21}^2)}. \quad (4.24b)$$

After some mathematical manipulations on (4.23), (4.24) and (4.12), the unknowns $\Gamma_1^{\{x_r\}}$ and $\Gamma_2^{\{x_r\}}$ can directly be found by solving the following equations,

$$\Gamma_1^{\{x_r\}} = \frac{\Gamma_{II}(1 + x_r) + \Gamma_I(1 - x_r) - 2\Gamma_I\Gamma_{II}(S_{11} - S_{21})}{2 - [\Gamma_I(1 + x_r) + \Gamma_{II}(1 - x_r)](S_{11} - S_{21})} \quad (4.25a)$$

$$\Gamma_2^{\{x_r\}} = \frac{\Gamma_{II}(1 - x_r) + \Gamma_I(1 + x_r) - 2\Gamma_I\Gamma_{II}(S_{11} - S_{21})}{2 - [\Gamma_I(1 - x_r) + \Gamma_{II}(1 + x_r)](S_{11} - S_{21})}. \quad (4.25b)$$

4.2.4 Discussion and Implementation

Equation (4.25) shows that the impedance values of the load pair required for single-radio multiplexing of the symbol pair $\{x_1, x_2\}$ depend on their symbol combination ratio x_r . This implies that for each possible symbol combination ratio of the considered modulation the load pair at the passive ports must be reconfigured to distinct impedance values. For instance, in the case of an M -ary PSK modulation scheme, since there are M different values of x_r , a variable load with M distinct impedance values is required at each passive port for enabling the proposed single-radio multiplexing. On the other hand, it is seen from (4.25) that altering the polarity of the combination ratio (i.e., $x_r \rightarrow -x_r$) swaps the impedance values of the loads at the passive ports (i.e., $\Gamma_1^{\{-x_r\}} = \Gamma_2^{\{x_r\}}$ and $\Gamma_2^{\{-x_r\}} = \Gamma_1^{\{x_r\}}$). Therefore, in the case of rotationally symmetric constellations exactly the same set of impedance values is required at both passive ports.

In the special case of BPSK signaling, the symbol combination ratio is either $+1$ or -1 , i.e., $x_r = \pm 1$. According to (4.25), the impedance values $Z_1^{\{\pm 1\}}$ and $Z_2^{\{\pm 1\}}$ are identical to the basis impedances (i.e., the ones used when defining the basis patterns),

$$\Gamma_1^{\{+1\}} = \Gamma_2^{\{-1\}} = \Gamma_{II} \quad (4.26a)$$

$$\Gamma_2^{\{+1\}} = \Gamma_1^{\{-1\}} = \Gamma_I. \quad (4.26b)$$

This is in full agreement with the basis definition in (4.6) as well as the results presented in Section 3.5.2, and demonstrates the validity of our proposed approach at least while dealing with BPSK modulation scheme.

As mentioned in Section 4.1, a particular concern in practical implementation of beam-space MIMO is related to the large dynamic variation of the antenna's input impedance associated with the reconfiguration of the variable loads. Interestingly, the technique proposed here provides a constant input impedance for all possible symbol combinations of x_1 and x_2 . Using (4.5), (4.23) and (4.12), the reflection coefficient at the active port for a given x_r becomes

$$\begin{aligned}
 \Gamma_{\text{in}}^{\{Z_1^{x_r}, Z_2^{x_r}\}} &= \begin{bmatrix} S_{00} & S_{01} & S_{01} \end{bmatrix} \mathcal{A}_{\text{u}}^{\{Z_1^{x_r}, Z_2^{x_r}\}} \\
 &= S_{00} + S_{01} \left[\mathbf{a}_{1,\text{u}}^{\{Z_1^{x_r}, Z_2^{x_r}\}} + \mathbf{a}_{2,\text{u}}^{\{Z_1^{x_r}, Z_2^{x_r}\}} \right] \\
 &= S_{00} + 2S_{01} \mathbf{a}_{\text{B}_1}^{\{Z_1, Z_{\text{II}}\}} \\
 &= S_{00} + S_{01} \left[\mathbf{a}_{1,\text{u}}^{\{Z_1, Z_{\text{II}}\}} + \mathbf{a}_{2,\text{u}}^{\{Z_1, Z_{\text{II}}\}} \right] \\
 &= S_{00} + S_{01}^2 \frac{\Gamma_{\text{I}} + \Gamma_{\text{II}} - 2\Gamma_{\text{I}}\Gamma_{\text{II}}(S_{11} - S_{21})}{1 - S_{11}(\Gamma_{\text{I}} + \Gamma_{\text{II}}) + \Gamma_{\text{I}}\Gamma_{\text{II}}(S_{11}^2 - S_{21}^2)}, \tag{4.27}
 \end{aligned}$$

which remains constant regardless of the symbol combination ratio, x_r . This is of great practical importance as no external reconfigurable matching network at the active port is required. It is obvious from (4.27) that the selection of the basis impedances, Z_{I} and Z_{II} , affects the reflection coefficient at the active port.

We have so far shown that a load-modulated antenna composed of a symmetric three-port radiator and two variable loads is capable of transmitting two symbol streams of any modulation scheme. Fig. 4.2 depicts an antenna system solution based on the proposed approach. The inputs to the system consist of two streams of symbols in the baseband domain, $x_1[n]$ and $x_2[n]$. The first stream, $x_1[n]$ is up-converted to $s_1(t)$ and fed into the radiator's central active port. Unlike the classical MIMO, the second stream, $x_2[n]$, does not leave the digital signal processing (DSP) unit. A *load control system* provides the control signals for reconfiguring the variable loads at the passive ports according to the ratio of two symbols in the baseband domain, $x_r[n]$. By doing this, each symbol stream is independently mapped onto the corresponding virtual basis pattern in the far-field.

4.2.5 Passive Reactive Loading Constraint

For the sake of completeness, all the derivations so far considered the use of loads with complex-valued impedance values at the passive ports. However, as discussed in Section 3.4, highly-resistive and active loads are not attractive for realistic applications. In this context, it is desirable to analyze the proposed approach when constrained to only purely reactive load solutions.

The condition of purely reactive loads at the passive ports is that for all possible symbol combination ratios from the considered modulation, $Z_1^{x_r} = jX_1^{x_r}$ and $Z_2^{x_r} = jX_2^{x_r}$, or

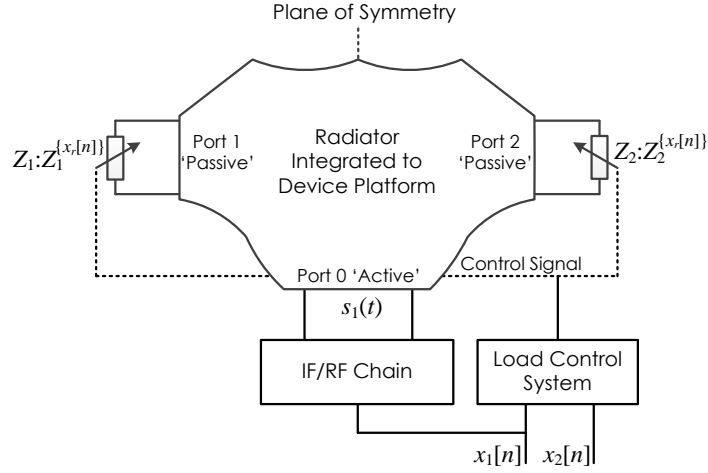


Figure 4.2: Symbolic representation of the proposed system capable of multiplexing two input symbol streams.

equivalently,

$$\left| \Gamma_1^{\{x_r\}} \right| = \left| \Gamma_2^{\{x_r\}} \right| = 1. \quad (4.28)$$

According to (4.26), (4.28) implies that the basis impedances are also purely imaginary, i.e., $Z_I = jX_I$ and $Z_{II} = jX_{II}$. Inserting (4.28) into (4.25) and after some mathematical simplification, Γ_I and Γ_{II} must simultaneously satisfy the following two equations,

$$\frac{1 - |S_{11} - S_{21}|^2}{1 + |S_{11} - S_{21}|^2} \frac{1 - |x_r|^2}{2|x_r|} \sin(\vartheta_1) = \sin(\vartheta_2) \left[\cos(\vartheta_1) - \frac{2|S_{11} - S_{21}|}{1 + |S_{11} - S_{21}|^2} \cos(\vartheta_3) \right] \quad (4.29a)$$

$$\frac{1 + |S_{11} - S_{21}|^2}{1 - |S_{11} - S_{21}|^2} \frac{1 - |x_r|^2}{2|x_r|} \sin(\vartheta_1) = \sin(\vartheta_2) \left[\cos(\vartheta_1) - \frac{2|S_{11} - S_{21}|}{1 + |S_{11} - S_{21}|^2} \cos(\vartheta_3) \right], \quad (4.29b)$$

where for the sake of compactness, we denoted

$$\begin{aligned} \vartheta_1 &= \frac{\arg \Gamma_I - \arg \Gamma_{II}}{2} \\ \vartheta_2 &= \arg x_r \\ \vartheta_3 &= \arg(S_{11} - S_{21}) + \frac{\arg \Gamma_I + \arg \Gamma_{II}}{2}. \end{aligned}$$

In general, such a solution for Γ_I and Γ_{II} does not exist. However, for the particular case of $|x_r| = 1$, namely for PSK modulation, both equations in (4.29) become equivalent, i.e.,

$$\cos(\vartheta_1) - \frac{2|S_{11} - S_{21}|}{1 + |S_{11} - S_{21}|^2} \cos(\vartheta_3) = 0. \quad (4.30)$$

After some mathematical manipulations on (4.30), Γ_{II} is expressed as a rational function of Γ_{I} ,

$$\Gamma_{\text{II}} = \frac{\Gamma_{\text{I}} - \frac{2(S_{11} - S_{21})^*}{1 + |S_{11} - S_{21}|^2}}{\frac{2(S_{11} - S_{21})}{1 + |S_{11} - S_{21}|^2} \Gamma_{\text{I}} - 1}. \quad (4.31)$$

This equation provides a bijective mapping between the basis reactance values, X_{I} and X_{II} . In other words, each imaginary impedance jX_{I} is paired with a unique imaginary impedance jX_{II} . Inserting (4.31) into (4.25), other reactance values for the considered PSK modulation scheme can be calculated as

$$X_{\text{I}}^{\{x_r\}} = X_{\text{II}}^{\{-x_r\}} = -Z_0 \frac{\kappa_1 X_{\text{I}} + \kappa_2}{\kappa_3 X_{\text{I}} + \kappa_4} = -Z_0 \frac{\kappa_1 X_{\text{I}}^{\{-1\}} + \kappa_2}{\kappa_3 X_{\text{I}}^{\{-1\}} + \kappa_4}, \quad (4.32)$$

where

$$\kappa_1 = 2 \operatorname{Im}(S_{11} - S_{21}) \cos\left(\frac{\arg x_r}{2}\right) + [1 - |S_{11} - S_{21}|^2] \sin\left(\frac{\arg x_r}{2}\right)$$

$$\kappa_2 = Z_0 |1 + S_{11} - S_{21}|^2 \cos\left(\frac{\arg x_r}{2}\right)$$

$$\kappa_3 = |1 - S_{11} + S_{21}|^2 \cos\left(\frac{\arg x_r}{2}\right)$$

$$\kappa_4 = Z_0 \left[2 \operatorname{Im}(S_{11} - S_{21}) \cos\left(\frac{\arg x_r}{2}\right) - [1 - |S_{11} - S_{21}|^2] \sin\left(\frac{\arg x_r}{2}\right) \right].$$

These results are of significant practical importance: the proposed technique still allows the single-radio multiplexing of higher order PSK data streams with a single load-modulated antenna when (i) only the use of purely reactive loads is permitted, and (ii) no reconfigurable impedance matching circuit is utilized.

Inserting the reactive load condition in (4.31) into (4.27), the reflection coefficient at the active port can be expressed in terms of the radiator's S-parameters only,

$$\Gamma_{\text{in}} = S_{00} + S_{01}^2 \frac{2(S_{11} - S_{21})^*}{1 - (S_{11} - S_{21})^* (S_{11} + S_{21})}. \quad (4.33)$$

This implies that the input impedance of the load-modulated antenna is independent of the basis reactance values. Similarly, it can be demonstrated that satisfying the reactive loading constraint also removes the dependency of the power radiated by the basis patterns on the basis reactance values. Inserting (4.31) into (4.12), it can be shown that

$$a_{\mathcal{B}_1}^{\{Z_{\text{I}}, Z_{\text{II}}\}} = \frac{S_{01} (S_{11} - S_{21})^*}{1 - (S_{11} - S_{21})^* (S_{11} + S_{21})} \quad (4.34a)$$

$$\left| a_{\mathcal{B}_2}^{\{Z_{\text{I}}, Z_{\text{II}}\}} \right| = \left| \frac{S_{01}}{1 - (S_{11} - S_{21})^* (S_{11} + S_{21})} \right|. \quad (4.34b)$$

4.2. Multiplexing Strategy: Theory and Implementation

Therefore, according to (4.15) and (4.34), the dependency of $\mathcal{P}_{\mathcal{B}_1}$ and $\mathcal{P}_{\mathcal{B}_2}$ on X_I and X_{II} is removed, i.e.,

$$\begin{aligned} \mathcal{P}_{\mathcal{B}_1} = & \mathcal{R}_{00} + 2 \left| \frac{S_{01} (S_{11} - S_{21})^*}{1 - (S_{11} - S_{21})^* (S_{11} + S_{21})} \right|^2 (\mathcal{R}_{11} + \mathcal{R}_{21}) \\ & + 4 \operatorname{Re} \left(\frac{S_{01} (S_{11} - S_{21})^*}{1 - (S_{11} - S_{21})^* (S_{11} + S_{21})} \mathcal{R}_{01} \right) \end{aligned} \quad (4.35a)$$

$$\mathcal{P}_{\mathcal{B}_2} = 2 \left| \frac{S_{01}}{1 - (S_{11} - S_{21})^* (S_{11} + S_{21})} \right|^2 (\mathcal{R}_{11} - \mathcal{R}_{21}). \quad (4.35b)$$

Moreover, using (4.16), (3.13) and (4.14), the total efficiency of the antenna can be calculated as

$$\begin{aligned} e_{\text{tot}}^{\{Z_1^{x_r}, Z_2^{x_r}\}} &= \frac{\mathcal{P}_{\text{rad}}}{\mathcal{P}_{\text{inc}}} = \frac{\frac{1}{2} \eta_0 \int \mathcal{E}_o(\Omega) \cdot \mathcal{E}_o^*(\Omega) d\Omega}{|x_1|^2} \\ &= \frac{1}{2} \eta_0 \int [\mathcal{B}_1(\Omega) + x_r \mathcal{B}_2(\Omega)] \cdot [\mathcal{B}_1(\Omega) + x_r \mathcal{B}_2(\Omega)]^* d\Omega \\ &= \mathcal{P}_{\mathcal{B}_1} + |x_r|^2 \mathcal{P}_{\mathcal{B}_2} + x_r \mathcal{R}_{\mathcal{B}_1 \mathcal{B}_2} + x_r^* \mathcal{R}_{\mathcal{B}_2 \mathcal{B}_1} \\ &= \mathcal{P}_{\mathcal{B}_1} + \mathcal{P}_{\mathcal{B}_2}. \end{aligned} \quad (4.36)$$

Therefore, despite having one of the basis reactance values (for example, $X_I = X_1^{[-1]}$) as a degree of freedom in our proposed approach, the performance of the beam-space MIMO antenna in terms of the basis power imbalance ratio and the total efficiency is only dependent on the radiator's parameters. This implies that optimizing the beam-space MIMO antenna requires the three-port radiator itself to be engineered.

4.2.6 Case of Lossless Radiators

According to (3.6), the set of beam-coupling coefficients required for the calculation of $\mathcal{P}_{\mathcal{B}_1}$ and $\mathcal{P}_{\mathcal{B}_2}$ in (4.35) are typically obtained through tedious far-field calculations. This may increase the computational complexity associated with the optimization procedure of beam-space MIMO antennas. However, when the thermal losses in the radiator's materials are negligible, energy conservation implies that the knowledge of the scattering parameters suffices for calculating the beam-coupling coefficients (see proof in [22]), i.e.,

$$\mathcal{R}_{nm} = - \sum_{p=0}^2 S_{pn}^* S_{pm}, \quad n \neq m \quad (4.37a)$$

$$\mathcal{R}_{nn} = 1 - \sum_{p=0}^2 |S_{pn}|^2. \quad (4.37b)$$

Inserting (4.37) into (4.35), the powers $\mathcal{P}_{\mathcal{B}_1}$ and $\mathcal{P}_{\mathcal{B}_2}$ radiated by the basis patterns in the far-field can be expressed in terms of only the radiator's S-parameters,

$$\begin{aligned} \mathcal{P}_{\mathcal{B}_1} = & 1 - \sum_{n=0}^2 |S_{n0}|^2 + 2 \left| \frac{S_{01} (S_{11} - S_{21})^*}{1 - (S_{11} - S_{21})^* (S_{11} + S_{21})} \right|^2 \left(1 - \sum_{n=0}^2 |S_{n1}|^2 - \sum_{n=0}^2 S_{n2}^* S_{n1} \right) \\ & - 4 \operatorname{Re} \left(\frac{S_{01} (S_{11} - S_{21})^*}{1 - (S_{11} - S_{21})^* (S_{11} + S_{21})} \sum_{n=0}^2 S_{n0}^* S_{n1} \right) \end{aligned} \quad (4.38a)$$

$$\mathcal{P}_{\mathcal{B}_2} = 2 \left| \frac{S_{01}}{1 - (S_{11} - S_{21})^* (S_{11} + S_{21})} \right|^2 \left(1 - \sum_{n=0}^2 |S_{n1}|^2 + \sum_{n=0}^2 S_{n2}^* S_{n1} \right), \quad (4.38b)$$

thus eliminating the need for cumbersome far-field calculations.

4.3 Design Procedure and Antenna Prototype

In this section, we illustrate the beam-space multiplexing approach described in the previous section by designing a compact antenna which is capable of transmitting two QPSK data streams simultaneously using a single RF chain. As discussed in Section 4.2.4, the antenna consists of a three-port radiator and two variable loads. The radiator is designed on a FR4 substrate of 32 mm × 33 mm × 30 mil with a dielectric constant of 4.4. The substrate area is very small, about $0.07\lambda^2$ at the design frequency of 2.45 GHz. A good impedance matching at the single active port (i.e., $|\Gamma_{\text{in}}|^2 \leq -10$ dB) and nearly balanced basis patterns (i.e., $|r| \leq 3$ dB) are the design requirements to ensure optimum open-loop MIMO performance in rich-scattering environments.

Table 4.1 shows the possible symbol combination ratios of two QPSK signals, where $[b_1 b_2 b_3 b_4]^T$ is the input vector of bits modulated into $[x_1 x_2]^T$. There are four distinct symbol combination ratios, namely, $\{x_{r,s}\}_{s=1}^4 \in \{-1, +1, +j, -j\}$, thus four antenna states are sufficient for transmitting the two QPSK data streams. In each state \mathcal{S} , the passive ports are loaded with two distinct reactance values, $X_1^{\{x_{r,s}\}}$ and $X_2^{\{x_{r,s}\}}$. However, since QPSK is a rotationally symmetric modulation scheme, as explained in Section 4.2.4, the same set of four reactance values are required at both passive ports: the first two reactance values associated with State 1 and State 2 are identical to the basis reactance values, i.e., $X_1^{\{-1\}} = X_2^{\{+1\}} = X_{\text{I}}$ and $X_2^{\{-1\}} = X_1^{\{+1\}} = X_{\text{II}}$, and the other two related to State 3 and State 4 (when $x_r = \pm j$), i.e., $X_1^{\{+j\}} = X_2^{\{-j\}} = X_{\text{III}}$ and $X_2^{\{+j\}} = X_1^{\{-j\}} = X_{\text{IV}}$.

In the following, the step-by-step design procedure is fully described and the results demonstrating the efficiency of the approach are presented.

Table 4.1: Combination of two QPSK symbols.

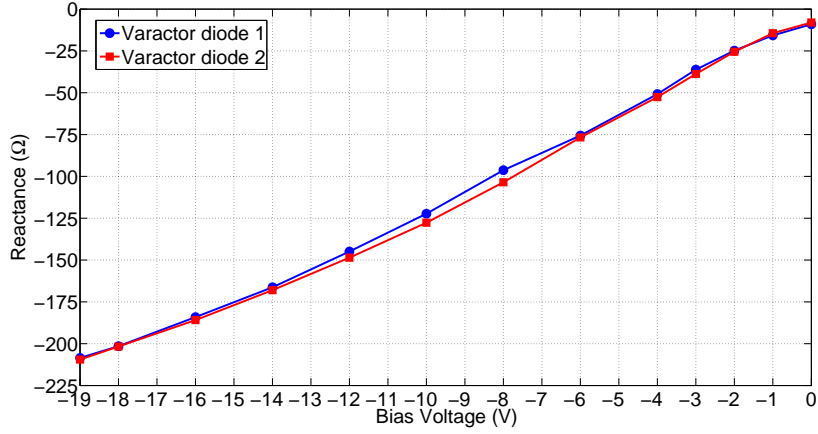
$[b_1 b_2 b_3 b_4]^T$	$[x_1 x_2]^T$	x_r	Antenna State	$X_1^{\{x_r\}}$	$X_2^{\{x_r\}}$
$[00 00]^T$	$[e^{-j3\pi/4} e^{-j3\pi/4}]^T$	+1	2	X_{II}	X_I
$[00 01]^T$	$[e^{-j3\pi/4} e^{+j3\pi/4}]^T$	-j	4	X_{IV}	X_{III}
$[00 11]^T$	$[e^{-j3\pi/4} e^{+j\pi/4}]^T$	-1	1	X_I	X_{II}
$[00 10]^T$	$[e^{-j3\pi/4} e^{-j\pi/4}]^T$	+j	3	X_{III}	X_{IV}
$[01 00]^T$	$[e^{+j3\pi/4} e^{-j3\pi/4}]^T$	+j	3	X_{III}	X_{IV}
$[01 01]^T$	$[e^{+j3\pi/4} e^{+j3\pi/4}]^T$	+1	2	X_{II}	X_I
$[01 11]^T$	$[e^{+j3\pi/4} e^{+j\pi/4}]^T$	-j	4	X_{IV}	X_{III}
$[01 10]^T$	$[e^{+j3\pi/4} e^{-j\pi/4}]^T$	-1	1	X_I	X_{II}
$[11 00]^T$	$[e^{+j\pi/4} e^{-j3\pi/4}]^T$	-1	1	X_I	X_{II}
$[11 01]^T$	$[e^{+j\pi/4} e^{+j3\pi/4}]^T$	+j	3	X_{III}	X_{IV}
$[11 11]^T$	$[e^{+j\pi/4} e^{+j\pi/4}]^T$	+1	2	X_{II}	X_I
$[11 10]^T$	$[e^{+j\pi/4} e^{-j\pi/4}]^T$	-j	4	X_{IV}	X_{III}
$[10 00]^T$	$[e^{-j\pi/4} e^{-j3\pi/4}]^T$	-j	4	X_{IV}	X_{III}
$[10 01]^T$	$[e^{-j\pi/4} e^{+j3\pi/4}]^T$	-1	1	X_I	X_{II}
$[10 11]^T$	$[e^{-j\pi/4} e^{+j\pi/4}]^T$	+j	3	X_{III}	X_{IV}
$[10 10]^T$	$[e^{-j\pi/4} e^{-j\pi/4}]^T$	+1	2	X_{II}	X_I

4.3.1 Design

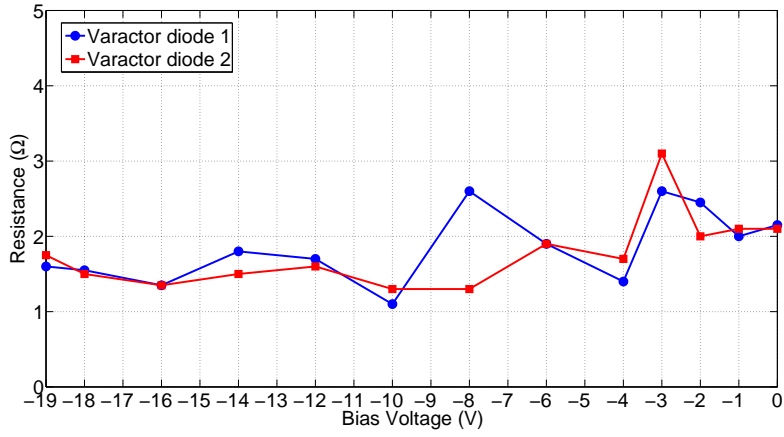
Let us start with enabling hardware for variable loads. As discussed in Section 3.4, semiconductor devices such as p-i-n diodes and varactor diodes are currently considered as the most appropriate control elements for the use in beam-space MIMO antennas. Varactor diodes are superior to p-i-n diodes in two respects: linear voltage-reactance characteristic and higher switching speed¹. As proposed in Section 3.6, the control devices can be utilized directly as the variable loads to drastically simplify the design and implementation of the load circuits. Accordingly, we selected two GaAs hyperabrupt varactor diodes (Aeroflex/Metelics MGV125-22) as the two variable loads to be mounted at the passive ports of the radiator. The precise voltage-impedance curves of the varactor diodes were extracted from separate measurements using a TRL calibration method. Then, the measured impedance curves were corrected for use in simulations according to the technique described in detail in Section 3.7. As shown in Fig. 4.3a, the two varactor diodes offer a reactance tuning range of $[-209, -9] \Omega$ and $[-210, -8] \Omega$, respectively, at the design frequency while varying the bias voltage between -19 V and 0 V . Fig. 4.3b shows that the real part of the impedance for both diodes is negligible (about 2Ω) and remains relatively constant over the bias voltage range.

Since the derivations given in Section 4.2.5 considered the use of purely reactive variable loads, the resistive loss of the varactor diodes may be included in the scattering matrix of the

¹Varactor diodes when operated in the reverse-bias region have no minority carrier charge storage. Therefore, the rate at which the depletion region changes its width is fast.



(a)



(b)

Figure 4.3: (a) Corrected voltage-reactance curves of the varactor diodes. (b) Corrected voltage-resistance curves of the varactor diodes. The reverse breakdown voltage of the diodes is reported to be around 22 V.

three-port radiator, as depicted in Fig. 4.4, in order to maintain the accuracy of the calculations. In this case, the amended S-matrix, \mathbf{S}' , can be expressed as

$$\begin{aligned}
 \mathbf{S}' &= (\mathbf{Z}' - Z_0 \mathbf{I}_3) (\mathbf{Z}' + Z_0 \mathbf{I}_3)^{-1} \\
 &= (\mathbf{Z} + \text{diag}([0, R_1, R_2]) - Z_0 \mathbf{I}_3) (\mathbf{Z} + \text{diag}([0, R_1, R_2]) + Z_0 \mathbf{I}_3)^{-1} \\
 &= (Z_0 (\mathbf{I}_3 + \mathbf{S}) (\mathbf{I}_3 - \mathbf{S})^{-1} + \text{diag}([0, R_1, R_2]) - Z_0 \mathbf{I}_3) \\
 &\quad (Z_0 (\mathbf{I}_3 + \mathbf{S}) (\mathbf{I}_3 - \mathbf{S})^{-1} + \text{diag}([0, R_1, R_2]) + Z_0 \mathbf{I}_3)^{-1}, \tag{4.39}
 \end{aligned}$$

where \mathbf{Z} and \mathbf{Z}' are the impedance matrices before and after including the losses, and R_1 and R_2 are the average resistance values of the variable loads, respectively.

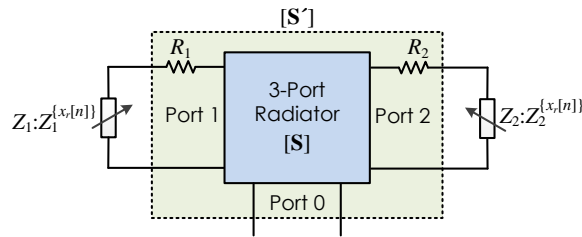


Figure 4.4: Method to include the resistive loss of the variable loads in the design procedure.

In the next step, after determining the reactance tuning range of the variable loads, a three-port radiator must be designed according to the aforementioned physical constraints and performance requirements. Fig. 4.5 shows the proposed radiator inspired from a folded slot antenna, where two passive ports are introduced to bridge the slot while keeping the mirror symmetry of the structure. The central port is matched for a 50- Ω coaxial connection to the single RF module. The other two ports will be terminated with the varactor diodes characterized above. Two DC-decoupling 56-pF capacitors (Murata GRM1885C2A560J) and two RF-blocking 56-nH (Murata LQW15AN56NG) inductors were embedded in the design of the radiator to filter unwanted RF and control signals, respectively. Accordingly, the bias voltages of the varactor diodes can be applied between the control wires and the inner conductor of the coaxial cable.

When designing a radiating structure with a small ground plane, accurate modeling of the excitation might be challenging. In real-world practice, a feeding cable is typically used to connect the antenna to other parts of the system or the measurement setup. However, when the antenna's ground plane is small, current can flow back to the outer surface of the feeding cable, causing the cable itself to contribute to radiation and to change the input impedance of the antenna. This introduces significant uncertainties in the results of full-wave simulations where the antenna is fed using a lumped excitation or a finite-length feeding cable. Therefore, a standard sleeve balun choke was designed and placed in the path of the coaxial cable very close to the radiator in order to suppress unwanted cable currents. Similarly, the wires used to convey the control waveforms are also in the near field of the radiator, and may re-radiate the induced currents. To prevent such undesired radiation, four chip ferrite beads (Murata BLM15GA750), with very high RF impedance values, were placed in the path of the wires as shown in Fig. 4.5. Furthermore, to precisely model the embedded lumped components, their equivalent circuit models were measured and corrected using the method presented in Section 3.7. Table 4.2 gives the equivalent circuit models inserted into the simulations.

As concluded in Section 4.2.5, the three-port radiator itself needs to be optimized in order to meet the performance requirements of the beam-space MIMO antenna. Full-wave analyses of the radiator were performed using ANSYS HFSS. At each iteration step of the radiator design process, the S-parameters and the embedded radiation patterns were exported to MATLAB to evaluate (i) the required reactance values for the variable loads using (4.32) as a function

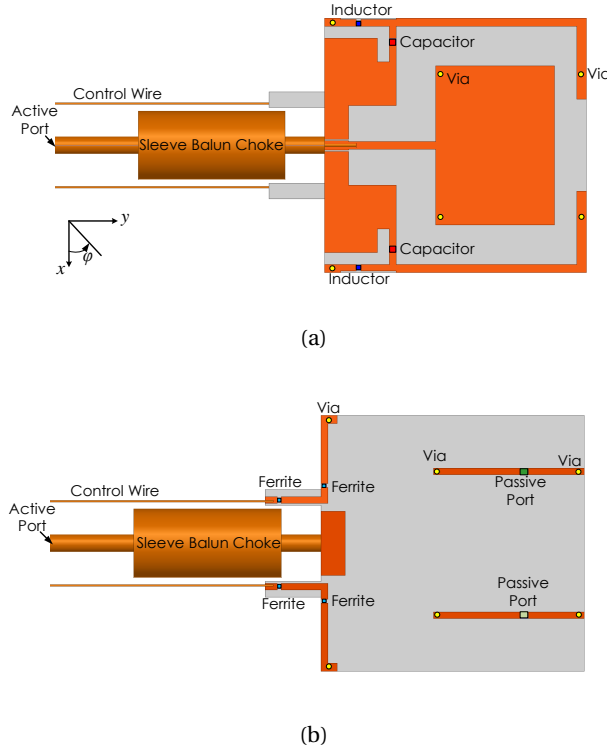


Figure 4.5: Proposed three-port radiator with an axis of symmetry in yz -plane. The quarter-wavelength balun acts as an open-end termination at the edge of the antenna. (a) Top view. (b) Bottom view.

Table 4.2: Corrected equivalent circuit models of the lumped elements.

Component	Circuit Model	R (Ω)	L (H)	C (F)
Capacitor 56 pF	Series RLC	1.0	-	100.0 p
Inductor 56 nH	Parallel RLC	35.5 k	49.5 n	40.8 f
Ferrite chip	Parallel RLC	1.9 k	128.2 n	32.0 f

of the free parameter (for instance, $X_1 = X_1^{(-1)}$), (ii) the power imbalance ratio, r , between the basis patterns using (3.23) and (4.35), (iii) the antenna's total efficiency, e_{tot} , using (4.36) and (4.35), and (iv) the reflection coefficient at the antenna's active port, Γ_{in} , using (4.33). A number of full-wave simulations were carried out to examine the effects of various key physical parameters of the radiator, and finally to arrive at a design fulfilling the requirements mentioned before.

The optimized three-port radiator shown in Fig. 4.5, with an S-matrix of

$$\mathbf{S} = \begin{bmatrix} -0.23 - j0.32 & 0.26 + j0.43 & 0.26 + j0.43 \\ 0.26 + j0.43 & 0.16 + j0.49 & -0.19 - j0.11 \\ 0.26 + j0.43 & -0.19 - j0.11 & 0.16 + j0.49 \end{bmatrix}$$

at the design frequency, requires an arbitrary set of four reactance values from the curves given in Fig. 4.6 to form a QPSK beam-space MIMO antenna with a basis power imbalance ratio of 0.8 dB and a return loss of 19.6 dB. As shown in Fig. 4.6, there exists a range of the solutions where all four reactance values lie within the specified tuning range of the varactor diodes. From this range, we arbitrarily selected the set associated with $X_I = -200 \Omega$. Table 4.3 gives the selected set of reactance values and their corresponding bias voltages obtained according to Fig. 4.3a.

To sum up, Fig. 4.7 depicts a flowchart in which the beam-space MIMO antenna design procedure is illustrated step by step.

4.3.2 Results and Discussion

The optimized three-port radiator was fabricated, and each of the two varactor diodes under test was soldered at the place of corresponding passive port as depicted in Fig. 4.8. The reflection coefficient of the antenna was measured for all four operational states, and compared to the results obtained from the simulations. As shown in Fig. 4.9, excellent agreement between

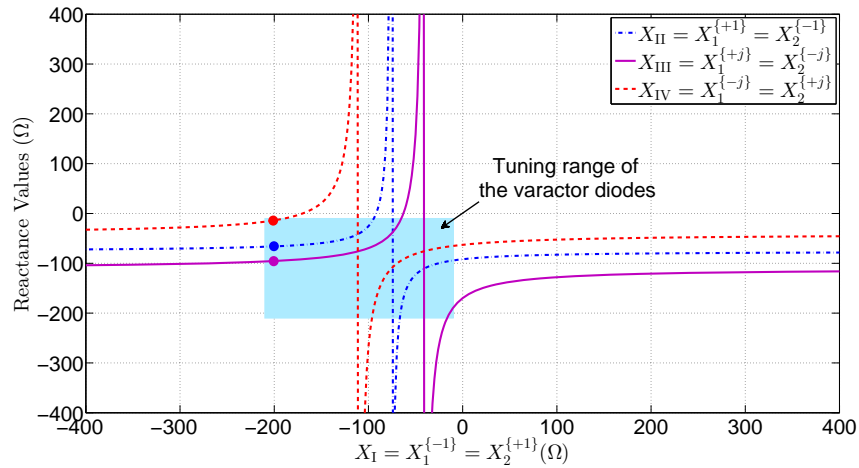


Figure 4.6: Required reactance values at the passive ports of the optimized three-port radiator as a function of the free parameter X_I . The possible tuning range of the varactor diodes has been specified by a solid rectangle.

Table 4.3: Selected reactance set and corresponding bias voltages of the varactor diodes.

Antenna State	x_r	$X_1^{x_r}$ (Ω)	$X_2^{x_r}$ (Ω)	$V_{\text{bias},1}$ (V)	$V_{\text{bias},2}$ (V)
1	-1	-200.0	-66.0	-17.83	-5.11
2	+1	-66.0	-200.0	-5.15	-17.78
3	+j	-95.4	-13.8	-7.92	-0.94
4	-j	-13.8	-95.4	-0.75	-7.40

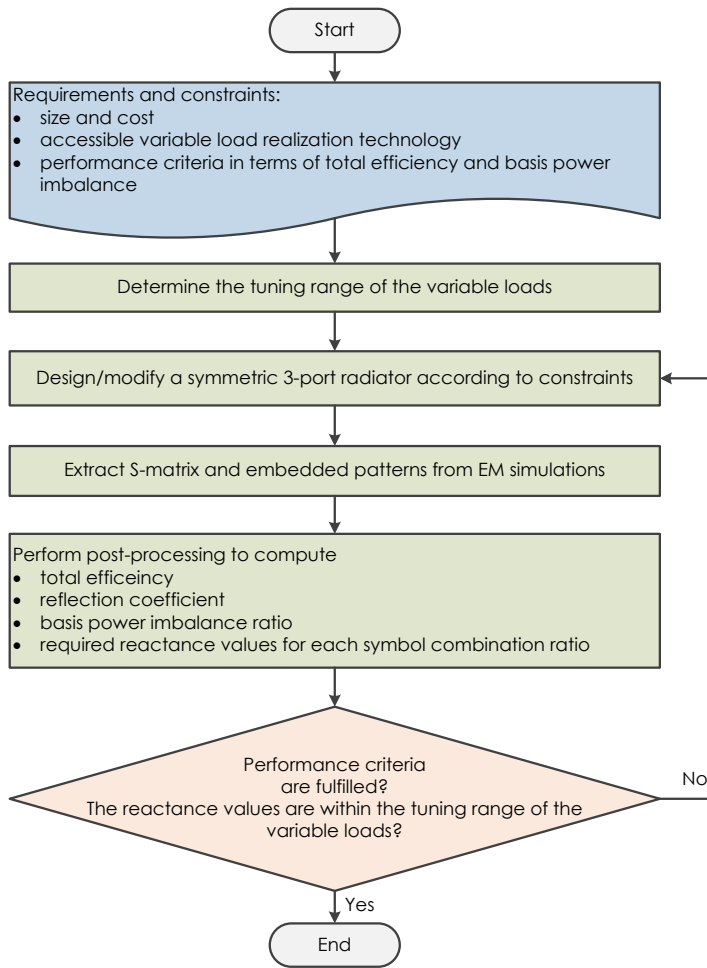


Figure 4.7: Flowchart of the beam-space MIMO antenna design.

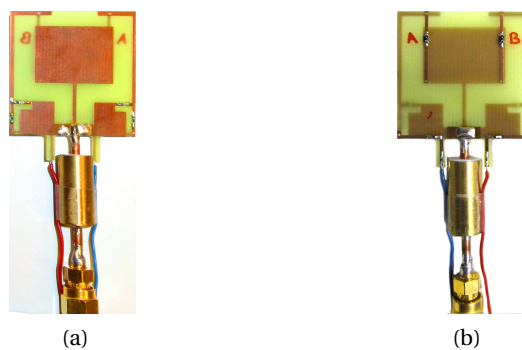


Figure 4.8: Fabricated QPSK beam-space MIMO antenna. (a) Top view. (b) Bottom view.

the measured and simulated data validates the accuracy of the modeling technique. Note that the operation bandwidth of the balun choke is narrow, and thus the simulation results may be inaccurate as the frequency deviates from the design frequency. The antenna yields a

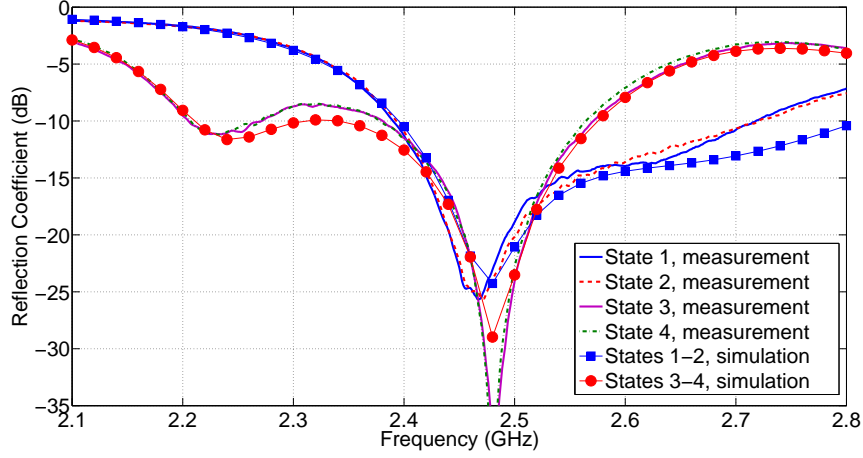


Figure 4.9: Reflection coefficient of the QPSK beam-space MIMO antenna.

measured bandwidth of 7.0% relative to the design frequency for a reference of -10 dB over all the states, while variations of the input impedance around the design frequency are negligible.

Fig. 4.10 shows the radiation patterns of the antenna obtained from the full-wave simulations. As expected from the radiator's symmetry and the permutation of the reactance values at the passive ports, the radiation patterns in State 1 and State 2, i.e., $\mathcal{E}_u^{\{jX_{I1}, jX_{II}\}}(\Omega)$ and $\mathcal{E}_u^{\{jX_{II}, jX_{I1}\}}(\Omega)$, and the radiation patterns in State 3 and State 4, i.e., $\mathcal{E}_u^{\{jX_{III}, jX_{IV}\}}(\Omega)$ and $\mathcal{E}_u^{\{jX_{IV}, jX_{III}\}}(\Omega)$, form mirror image pattern pairs with regard to the plane of symmetry at $\varphi = 90^\circ - 270^\circ$ (i.e., yz -plane).

Accordingly, the basis patterns were computed by using (4.6). The corresponding angular basis patterns of the antenna prototype are shown in Fig. 4.11. The virtual antenna associated with the first basis $\mathcal{B}_1(\Omega)$ has a bowl-like radiation pattern, while the second basis pattern $\mathcal{B}_2(\Omega)$ is bi-directional and broadside. Considering the thermal loss in the dielectric substrate, metallic parts, and resistance of the lumped components, the antenna yields a radiation efficiency of 75% over all the states.

Since beam-space MIMO transmission is inherently conditional on proper and precise pattern reconfiguration, any imperfection in the antenna implementation (such as biasing imprecision, near-field coupling, and fabrication tolerances) may affect the modulation quality of the transmitted signals by distorting the location of the constellation points. This distortion can be represented by the error vector magnitude (EVM) [92], which is reformulated for the fabricated QPSK beam-space MIMO as

$$\text{EVM}_{\text{rms}}(\Omega) = \left[\frac{\frac{1}{4} \sum_{s=1}^4 \left\| \mathcal{B}_1(\Omega) + x_{r,s} \mathcal{B}_2(\Omega) - \mathcal{E}_u^{\{jX_1^{[x_{r,s}]}, jX_2^{[x_{r,s}]}\}}(\Omega) \right\|^2}{\frac{1}{4} \sum_{s=1}^4 \left\| \mathcal{B}_1(\Omega) + x_{r,s} \mathcal{B}_2(\Omega) \right\|^2} \right]^{1/2}, \quad (4.40)$$

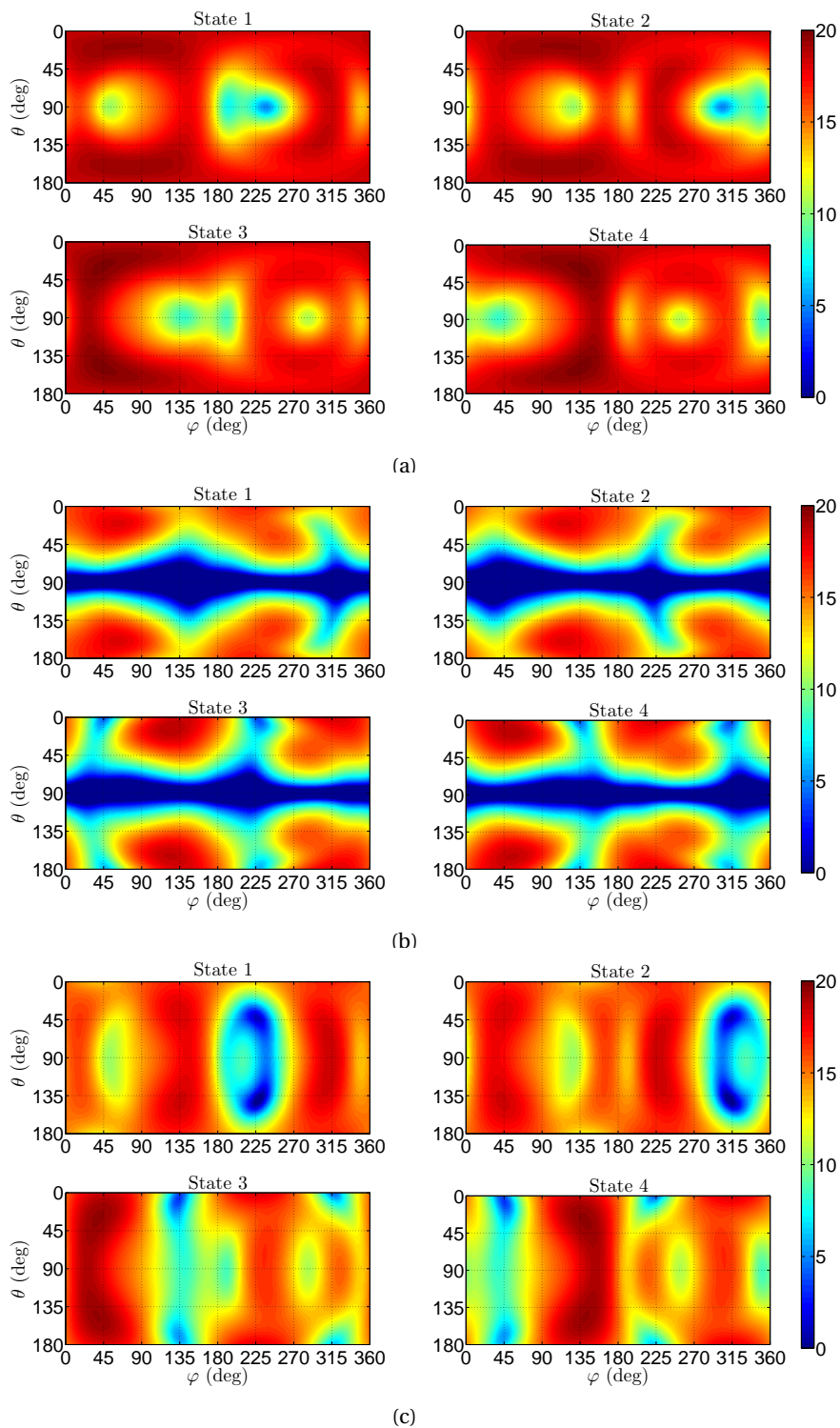


Figure 4.10: 3D view of the antenna's radiation patterns in dB at 2.45 GHz; (a) the total magnitude, (b) the magnitude of the θ -component, and (c) the magnitude of the φ -component.

4.3. Design Procedure and Antenna Prototype

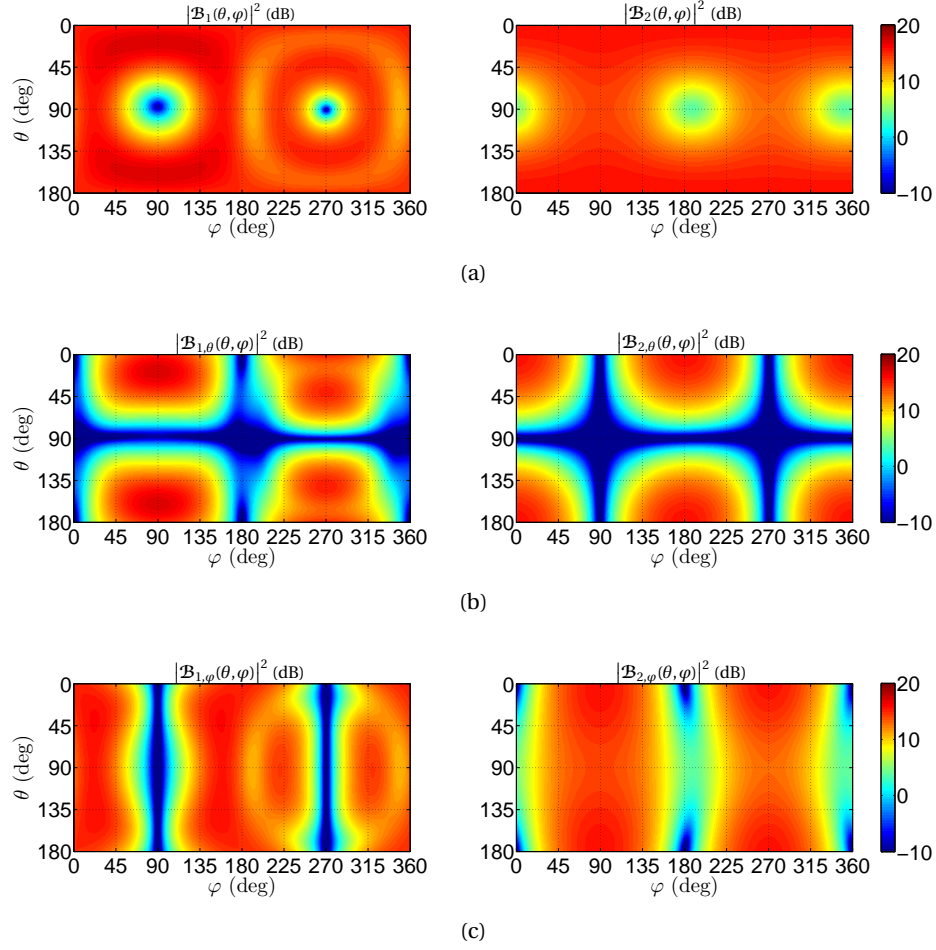


Figure 4.11: 3D view of the antenna's basis patterns in dB at 2.45 GHz; (a) the total magnitude, (b) the magnitude of the θ -component, and (c) the magnitude of the φ -component.

where $\{x_{r,s}\}_{s=1}^4$ denotes the four possible symbol combination ratios. To evaluate the EVM of the fabricated beam-space MIMO antenna, the complex radiation pattern was measured in an anechoic chamber while exciting the antenna with a reference power (see Fig. 4.12). The measurements were carried out for the four antenna states and in the two different planes, $\varphi = 0^\circ - 180^\circ$ (xz -plane) and $\varphi = 90^\circ - 270^\circ$ (yz -plane), at 2.45 GHz. The results are shown in Fig. 4.13. The EVM of the fabricated antenna is less than -20 dB in both planes, with an average of -27.2 dB and -23.9 dB in the planes of $\varphi = 0^\circ - 180^\circ$ and $\varphi = 90^\circ - 270^\circ$, respectively. This reveals good modulation quality despite omnipresent residual imperfections in the antenna implementation and measurement procedures.

To get some insight into the multiplexing performance of the designed antenna under QPSK signaling, we carried out similar capacity analyses as in Section 3.8.2 based on the obtained full-wave simulation results at the design frequency. As shown in Fig. 4.14, in high-SNR region the channel capacity of a beam-space MIMO system utilizing the designed antenna converges

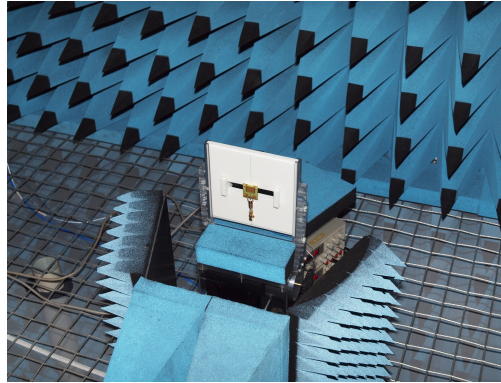


Figure 4.12: Setup for far-field measurements of the fully-operational QPSK beam-space MIMO antenna in an anechoic chamber.

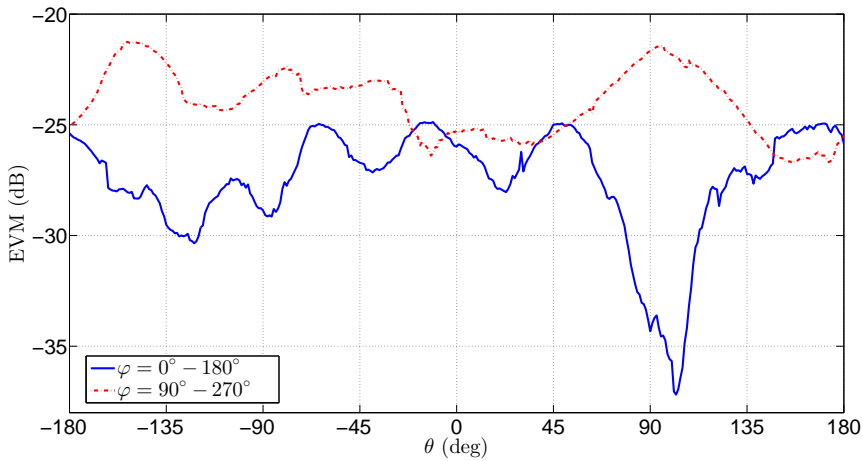


Figure 4.13: Measured EVM of the QPSK beam-space MIMO antenna.

to that of an ideal 2×2 conventional MIMO system having an identity transmit correlation matrix. The discrepancy between the curves in the low-SNR region is due to the designed antenna's losses. For the sake of comparison, Fig. 4.14 also shows the capacity curve of a SISO system having the same transmit total efficiency. We can thus conclude that the proposed multiplexing approach performs as expected.

4.4 Conclusion

In this chapter, we described an efficient beam-space MIMO approach for multiplexing two PSK data streams of any modulation order via a single RF chain and a single load-modulated antenna. The proposed approach not only provides a constant impedance response over all the operational states, but also uses purely reactive loads at the passive ports. Moreover, it replaces the multiplexing of basis patterns with the multiplexing of basis vectors, and

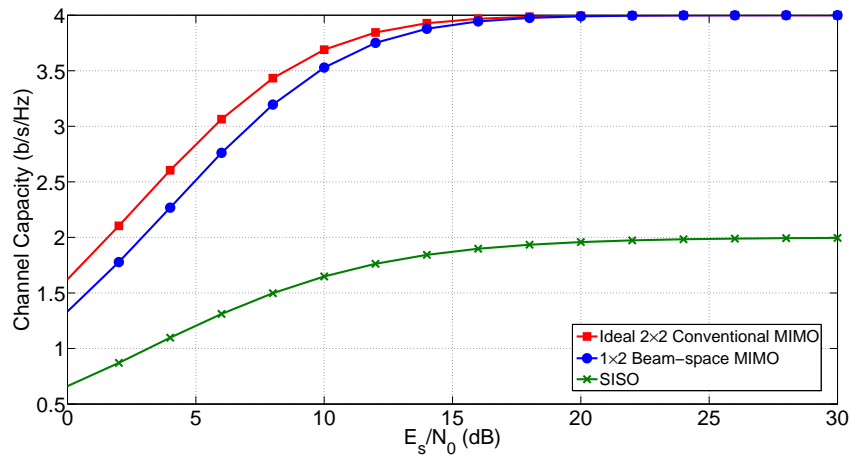


Figure 4.14: Channel capacity under QPSK signaling as a function of E_s/N_0 . The capacity was calculated based on the Monte-Carlo averaging on $1e+6$ random channel and noise realizations while assuming a Kronecker flat-fading channel modeling. Pulse shaping is not included.

provides closed-form formulas to compute the required reactance values of the variable loads and the performance parameters such as the basis power imbalance ratio and the total efficiency. The theory and design method were successfully illustrated by the first example of a realistic compact single-radio antenna capable of transmitting two QPSK data streams with passive loads and constant input impedance. Excellent agreement between the simulation and measurement results was obtained using an accurate design technique. These results constitute a crucial step towards MIMO with simpler and cheaper RF hardware for real-life wireless terminals.

5 Beam-Space MIMO: Over-the-Air Experiments

[...] *One being asked what a learned man without practice resembled, replied:
‘A bee without honey.’*

— Saadi, Gulistan, Principles of Social Conduct, Maxim 74

5.1 Overview

In Chapter 2, it was shown that beam-space MIMO replaces multiple ‘RF chain-antenna connections’ with a more economical single-radio pattern-reconfigurable antenna at the transmitter while keeping conventional MIMO architecture at the receiver. This particularly-designed transmit antenna exactly emulates the conventional MIMO transmission by mapping multiple symbols onto an orthogonal set of virtual basis patterns. Afterwards, we designed and fabricated two fully-operational beam-space MIMO antenna prototypes for BPSK and QPSK signaling in Chapters 3 and 4, respectively, and verified their capability to create the required radiation patterns through far-field simulations and measurements. In the first part of this chapter, we aim at experimentally validating the concept of beam-space multiplexing utilizing the fabricated antenna prototypes. To this purpose, we perform over-the-air experiments using a testbed constructed from off-the-shelf hardware and software components.

As discussed in Section 2.2.2, the orthogonality of the radiation patterns in conventional MIMO or equivalently the orthogonality of the basis patterns in beam-space MIMO leads to achieving uncorrelated channels provided that there is an infinite number of randomly and uniformly located ideal scatterers to form a uniform scattering medium in the entire space. In this situation, the symbol streams transmitted by a beam-space MIMO antenna experience multipath fading in a manner similar to conventional MIMO transmission. Therefore, in rich-scattering environments beam-space MIMO can match the performance of conventional MIMO with a corresponding constellation alphabet. However, in real propagation environments the angular spread of the multipath components is not wide enough, and thus orthogonal radiation (or basis) patterns do not guarantee the decorrelation of the MIMO

Parts of this chapter have been published earlier in [23, 24].

channels. In the case of conventional MIMO, numerous studies have been conducted to investigate the system performance in real channels (see, for instance, [93–95]), showing that inadequate scattering leading to channel decorrelation impairment has a significant impact on the performance limits of MIMO systems. However, little is known about the performance of beam-space MIMO in real propagation environments. Unlike in conventional MIMO where generally transmit antennas, separated by a certain minimum distance, have omni-directional similarly-polarized radiation patterns, basis patterns in beam-space MIMO have different polarization characteristics and propagate from a single radiating structure towards different directions in space. This may make the performance of beam-space MIMO more affected by the channel geometry. To further investigate this issue, in this chapter we conduct a measurement campaign to compare the performance of beam-space MIMO with conventional MIMO under realistic propagation conditions. To this purpose, experimental measurements of the channel matrix, \mathbf{H} , are taken in line-of-sight (LOS) and NLOS multipath environments for both systems utilizing the testbeds developed earlier. The MIMO capacity and the bit error rate (BER) are then estimated by running Monte-Carlo simulations over the measured channel matrices for different SNR values, where the i.i.d. Gaussian noise is generated in the numerical simulations.

The rest of this chapter is organized as follows. In Section 5.2, we first show that a conventional linear MIMO receiver is able to decode the data streams transmitted from a beam-space MIMO transmitter. Section 5.3 describes the beam-space MIMO testbed, and presents the validation results. In Section 5.4, we first discuss the experiment procedure for the performance analysis, and then present and analyze the obtained results from over-the-air measurements. For the sake of brevity, only the testbed and experiments associated with QPSK signaling are included.

5.2 Receiver Architecture for Beam-Space MIMO

Let us start with conventional MIMO systems, where the signal received at each receive antenna is a linear combination of the symbols transmitted from the transmit antennas and the noise according to the input-output relation given by (2.1). In other words, data streams launched from different transmit antennas interfere with each other at the receive antennas as they occupy the same resources in time and frequency. Therefore, an appropriate signal processing technique must then be exploited at the receiver to separate the various streams from one another. The maximum likelihood (ML) receiver performs vector decoding and achieves optimal error performance, but involving prohibitive computational complexity. Computationally efficient alternatives are linear receivers like zero-forcing (ZF) and minimum mean square error (MMSE) which first separate the transmitted data streams, and then independently decode each of the streams. In this thesis, we focus on the ZF receiver as a practical sub-optimal solution offering significant computational complexity reduction with tolerable performance degradation [96]. If perfect channel state information is known at the

receiver, the ZF receiver estimates the transmit symbol vector, \mathbf{x} , as

$$\hat{\mathbf{x}} = \mathbf{H}^\dagger \mathbf{y} = \mathbf{H}^\dagger (\mathbf{H}\mathbf{x} + \mathbf{n}) = \mathbf{x} + \mathbf{H}^\dagger \mathbf{n}, \quad (5.1)$$

where $\mathbf{H}^\dagger = (\mathbf{H}^H \mathbf{H})^{-1} \mathbf{H}^H$ denotes the Moore-Penrose inverse of the channel matrix [95]. Obviously, in the case the number of receive antennas is equal to the number of transmit antennas, namely $P = Q$, $\mathbf{H}^\dagger = \mathbf{H}^{-1}$.

In beam-space MIMO, the radiation pattern of the transmit antenna is reconfigured at each symbol period such that the symbols to be multiplexed are mapped onto the virtual basis patterns in the far-field (recall from Section 2.3 that in conventional MIMO these symbols are mapped onto the embedded radiation patterns of the transmit antennas). The signal transmitted by the beam-space MIMO antenna is then received using a multi-element antenna array at the receiving end. For the sake of clarity, let us restrict our attention to the case where two PSK data streams are transmitted in the far-field from the PSK beam-space MIMO antenna proposed in Chapter 4, and received using a classical two-element array. According to the channel modeling approach formulated in (2.2), the response of the m th receive antenna when illuminated by the beam-space MIMO antenna's radiation pattern $\mathcal{E}_u^{\{x_r\}}(\Omega)$ can be expressed as

$$\begin{aligned} h_m^{\{x_r\}} &= \iint_{\Omega_{\text{Rx}}, \Omega_{\text{Tx}}} \mathcal{F}_{\text{Rx}, m}^T(\Omega_{\text{Rx}}) \mathcal{O}(\Omega_{\text{Rx}}, \Omega_{\text{Tx}}) \mathcal{E}_u^{\{x_r\}}(\Omega_{\text{Tx}}) d\Omega_{\text{Tx}} d\Omega_{\text{Rx}} \\ &= \iint_{\Omega_{\text{Rx}}, \Omega_{\text{Tx}}} \mathcal{F}_{\text{Rx}, m}^T(\Omega_{\text{Rx}}) \mathcal{O}(\Omega_{\text{Rx}}, \Omega_{\text{Tx}}) [\mathcal{B}_1(\Omega_{\text{Tx}}) + x_r \mathcal{B}_2(\Omega_{\text{Tx}})] d\Omega_{\text{Tx}} d\Omega_{\text{Rx}} \\ &= \tilde{h}_{m1} + x_r \tilde{h}_{m2}, \end{aligned} \quad (5.2)$$

where \tilde{h}_{m1} and \tilde{h}_{m2} are the responses of the m th receive antenna to the virtual basis patterns $\mathcal{B}_1(\Omega)$ and $\mathcal{B}_2(\Omega)$, respectively. Note that in this chapter we replaced the superscript notation $\{jX_1^{\{x_r\}}, jX_2^{\{x_r\}}\}$ introduced in Chapter 4 with $\{x_r\}$ for the sake of compactness. Recalling that the first stream, x_1 , is up-converted and fed into the beam-space MIMO antenna, the received signal vector at the two receive antennas becomes

$$\mathbf{y}^{\{x_r\}} = x_1 \begin{bmatrix} h_1^{\{x_r\}} \\ h_2^{\{x_r\}} \end{bmatrix} + \mathbf{n} = x_1 \begin{bmatrix} \tilde{h}_{11} + x_r \tilde{h}_{12} \\ \tilde{h}_{21} + x_r \tilde{h}_{22} \end{bmatrix} + \mathbf{n} = \begin{bmatrix} \tilde{h}_{11} & \tilde{h}_{12} \\ \tilde{h}_{21} & \tilde{h}_{22} \end{bmatrix} \begin{bmatrix} x_1 \\ x_2 \end{bmatrix} + \mathbf{n}, \quad (5.3)$$

where \mathbf{n} represents the receive noise vector, and $\{x_1, x_2\}$ are the assumed transmitted symbols. Under ideal conditions, where the modulation on the orthogonal basis patterns is perfect, (5.3) is valid for all the possible values of x_r . Therefore, the beam-space MIMO system model follows the conventional MIMO system model, i.e.,

$$\mathbf{y} = \mathbf{H}\mathbf{x} + \mathbf{n}, \quad (5.4)$$

where

$$\mathbf{H} = \begin{bmatrix} \bar{h}_{11} & \bar{h}_{12} \\ \bar{h}_{21} & \bar{h}_{22} \end{bmatrix} \quad (5.5)$$

is the channel matrix. Accordingly, a linear ZF receiver followed by component-wise quantization to the nearest constellation point can recover the two transmitted streams.

5.3 Proof-of-Concept Experiments

In this section, the general features of our over-the-air testbed are presented, followed by a description of the main design decisions concerning the transmitter and receiver subsystems. Finally, the results obtained in the testbed are presented.

5.3.1 Testbed Setup

To build a real-time testbed, we combined the NI software defined radio platforms [97] and the LabVIEW communications system design software [98], providing a unified hardware and software design flow. Fig. 5.1 shows a schematic of the testbed setup, where the transmit and receive modules were connected to the host computer via a network switch.

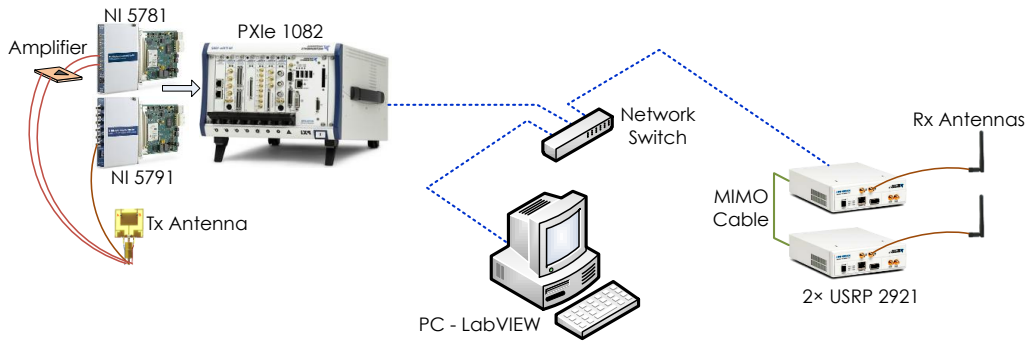


Figure 5.1: The hardware connectivity in the beam-space MIMO testbed.

At the transmitting end, we used the NI FlexRIO product family [99], which includes reconfigurable field-programmable gate arrays (FPGAs) for real-time processing and deterministic control. Particularly, one RF transceiver adapter module (NI 5791) and one baseband transceiver adapter module (NI 5781) were used to produce the required single RF signal (fed into the antenna's active port) and the control signals (for controlling the variable loads' states), respectively. Both modules were connected to a NI PXIe-1082 real-time host machine, and controlled by NI FlexRIO FPGA modules. The voltage dynamic range at the outputs of the baseband NI 5781 module is limited to 1 V peak-to-peak (i.e., between ± 0.5 V), while, as shown in Table 4.3, a bias voltage range from -18 V to 0 V is required for the varactor diodes

embedded in the beam-space MIMO antenna. Therefore, an amplifier circuit was used to increase the voltage range of the load-control signals. Fig. 5.2 shows the amplifier design, implemented using two LM6171 high-speed, low-power, low-distortion feedback amplifiers from Texas Instruments. To achieve an asymmetric tuning range (namely, from -20 V to 0 V rather than from -10 V to $+10\text{ V}$), a constant voltage offset of $+10\text{ V}$ was applied through the inner conductor of the coaxial cable using a bias tee to the common side of the varactor diodes. Table 5.1 gives the required voltage values at the amplifier outputs for different antenna states.

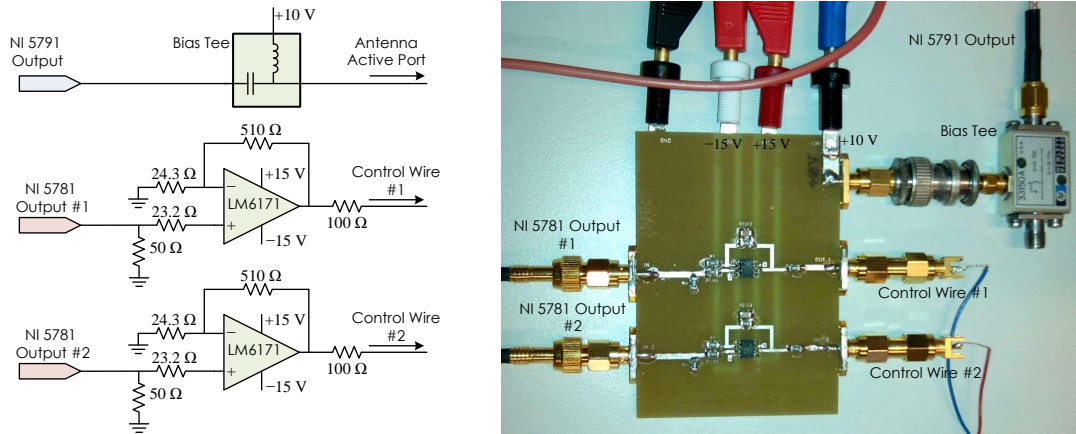


Figure 5.2: Amplifier circuit used for amplifying the baseband control signals.

Table 5.1: Actual biasing voltages versus voltages at the amplifier outputs.

Antenna State	x_r	$V_{\text{bias},1}$ (V)	$V_{\text{bias},2}$ (V)	$V_{\text{amp},1}$ (V)	$V_{\text{amp},2}$ (V)
1	-1	-17.83	-5.11	-7.83	4.89
2	$+1$	-5.15	-17.78	4.85	-7.78
3	$+j$	-7.92	-0.94	2.08	9.06
4	$-j$	-0.75	-7.40	9.25	2.60

At the receiving end, we employed two standard 2.4 GHz ‘rubber duck’ antennas, each connected to a NI Universal Software Radio Peripheral (USR2921) device [100]. A MIMO cable was used to synchronize the USRP pair in time and frequency. Unlike the transmitter, the receiver did not run on a real-time host. Instead, as shown in Fig. 5.1, the USRP devices were connected to the host computer where the processing operation was performed.

5.3.2 System Design and Functionality

To perform an over-the-air experiment, the main software calls the transmission and reception programs. The transmission program, which is compiled and deployed on the host machine,

supports a frame-based transmission. The procedure starts by generating two frames of symbols for single-radio MIMO transmission. Fig. 5.3 illustrates the structure of the frames. The first part of each frame includes N_s repetitions of a pseudo-random synchronization sequence, which is used at the receiver for the timing acquisition and the estimation of the frequency offset between the transmitter and the receiver [101]. The synchronization sequence of the second frame is selected according to that of the first frame in such a way that the symbol combination ratio in this part becomes constantly equal to -1 , forcing the antenna to radiate in its first state ($\mathcal{S} = 1$). The next part of each frame contains two training sequences, which will be used at the receiver to estimate the channel matrix. The first sequences of the two frames are identical to guarantee a symbol combination ratio of $+1$ in the first phase of the training, while the second training sequences are selected such that the symbol combination ratio becomes equal to -1 . The remainder of the frames is dedicated to the data segments.

In the next step, the symbols of the first frame are oversampled, and pulse-shaped with a root raised cosine filter before passing them to the RF channel. Simultaneously, in the baseband path the control signals are generated according to the ratio of the symbols in the two frames and based on Table 5.1. Since the variable loads of the antenna need to be modulated at the symbol rate of the RF channel, the control signals are also oversampled with the same factor as the RF signal. The RF and baseband samples are then uploaded to their corresponding FPGAs. A network communication link is established between the transmitter and the receiver to send the system parameters, the synchronization and training sequences, and the matched filter coefficients. After triggering the two transceiver adapter modules at the same time, the RF and baseband control samples are supplied to the NI 5791 and NI 5781 modules, respectively. A handshaking protocol between the transmitter and the receiver is used to ensure that the frame transmission occurs within the observation window of the receiver.

The reception program, which is run on the host computer, collects the network stream from the transmitter and the received data samples through the USRP devices, and then performs conventional signal processing operations, such as frequency offset estimation and correction, timing synchronization, channel estimation, and zero-forcing equalization, in

	Synchronization Part (N_s Repetitions)				Training Part (2 Phases)		Data Part
Frame #1	Sync. Seq. #1	Sync. Seq. #1	...	Sync. Seq. #1	Training Sequence #1	Training Sequence #1	Data Sequence #1
Frame #2	Sync. Seq. #2	Sync. Seq. #2	...	Sync. Seq. #2	Training Sequence #1	Training Sequence #2	Data Sequence #2

(a)

	Synchronization Part (N_s Repetitions)				Training Part (2 Phases)		Data Part
\mathcal{S}	1	1	...	1	2	1	{1, 2, 3, 4}
x_r	-1	-1	...	-1	+1	-1	{-1, +1, +j, -j}

(b)

Figure 5.3: (a) Frame structure used for beam-space MIMO experiments. (b) Corresponding antenna state, \mathcal{S} , and the symbol combination ratio, x_r , during the frame transmission.

order to decouple the two QPSK symbol streams. Fig. 5.4 shows the block diagram of the receiver.

According to (5.4) and (5.5), under ideal conditions the first and second training phases stimulate

$$\mathbf{y}_{t,1} = \begin{bmatrix} \hat{h}_{11} + \hat{h}_{12} \\ \hat{h}_{21} + \hat{h}_{22} \end{bmatrix} \mathbf{t}_1 + \mathbf{n}_1 = \begin{bmatrix} \hat{h}_{11} & \hat{h}_{12} \\ \hat{h}_{21} & \hat{h}_{22} \end{bmatrix} \begin{bmatrix} \mathbf{t}_1 \\ \mathbf{t}_1 \end{bmatrix} + \mathbf{n}_1$$

and

$$\mathbf{y}_{t,2} = \begin{bmatrix} \hat{h}_{11} - \hat{h}_{12} \\ \hat{h}_{21} - \hat{h}_{22} \end{bmatrix} \mathbf{t}_1 + \mathbf{n}_2 = \begin{bmatrix} \hat{h}_{11} & \hat{h}_{12} \\ \hat{h}_{21} & \hat{h}_{22} \end{bmatrix} \begin{bmatrix} \mathbf{t}_1 \\ -\mathbf{t}_1 \end{bmatrix} + \mathbf{n}_2$$

at the two receive antennas, respectively, where \mathbf{t}_1 denotes the training sequence. Therefore, the realization of the channel matrix can be estimated using the least square approach as

$$\hat{\mathbf{H}} = \begin{bmatrix} \hat{h}_{11} & \hat{h}_{12} \\ \hat{h}_{21} & \hat{h}_{22} \end{bmatrix} = \begin{bmatrix} \mathbf{y}_{t,1} & \mathbf{y}_{t,2} \end{bmatrix} \mathbf{T}^H (\mathbf{T} \mathbf{T}^H)^{-1}, \quad (5.6)$$

where

$$\mathbf{T} = \begin{bmatrix} \mathbf{t}_1 & \mathbf{t}_1 \\ \mathbf{t}_1 & -\mathbf{t}_1 \end{bmatrix}.$$

Once the channel matrix has been estimated, the ZF decoder simply multiplies the decimated received signal vector with the inverse of the channel matrix as discussed earlier in Section 5.2.

5.3.3 Results

The over-the-air experiment was carried out in an indoor NLOS laboratory environment at EPFL. The key specifications of the testbed are summarized in Table 5.2. Fig. 5.5 depicts the

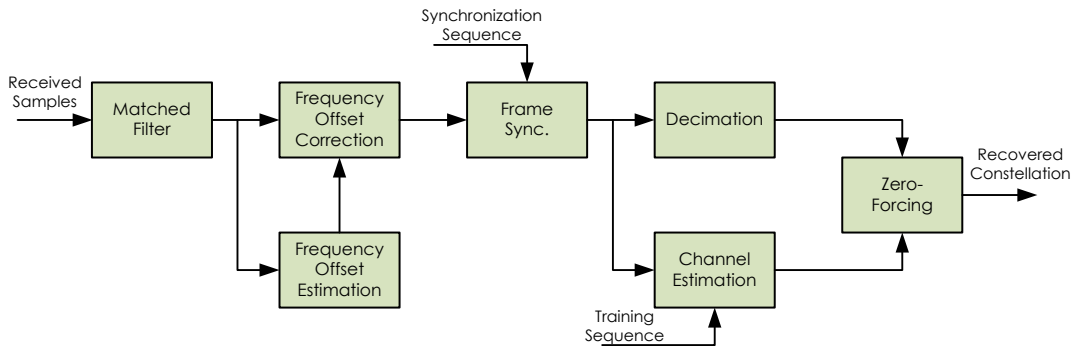


Figure 5.4: Receiver block diagram.

Chapter 5. Beam-Space MIMO: Over-the-Air Experiments

control waveforms at the outputs of the amplifiers, where the voltage levels are in good agreement with the desired values in Table 5.1. Fig. 5.6 shows the recovered symbol constellations after ZF equalization. It is clearly observed that the two QPSK streams were properly recovered. This experiment confirms the excellent behavior of the designed antenna, and constitutes the first successful single-radio MIMO transmission of QPSK signals.

Table 5.2: System parameters used in the validation experiment.

Frequency	\mathcal{N}_s	Sync. Seq. Symbols	Training Seq. Symbols	Data Seq. Symbols	Tx Sampling Rate	Symbol Rate	Rx Sampling Rate
2.45 GHz	4	32	64	256	100 MHz	390.625 kHz	1562.5 kHz

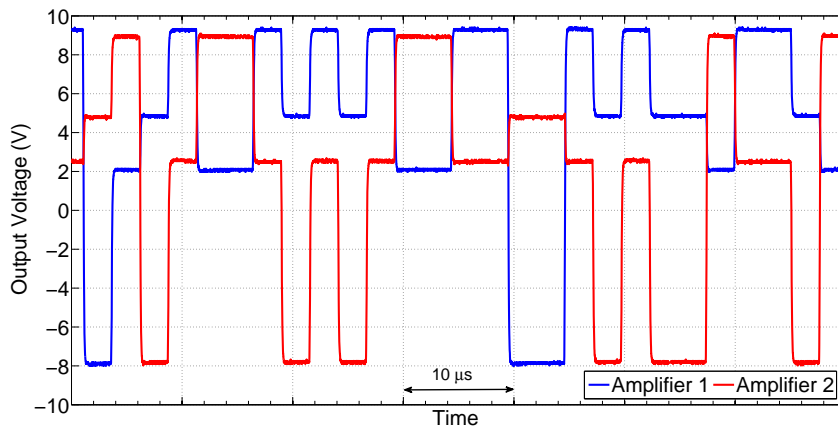


Figure 5.5: Baseband control signals (during the data segment) at the outputs of the amplifier.

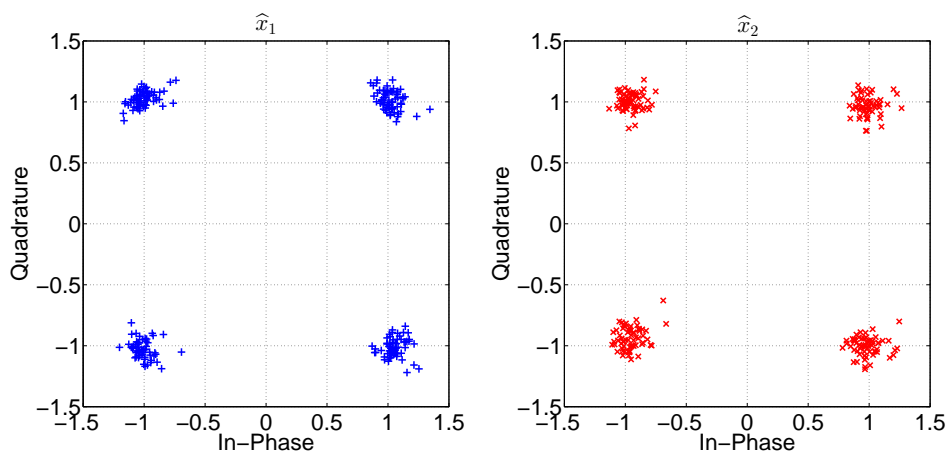


Figure 5.6: Scatter plot of received signal constellation after ZF equalization.

5.4 Performance Analysis

In this section, the performance of the beam-space MIMO is compared with that of conventional 2×2 MIMO under realistic propagation conditions. The section starts by outlining the experimental procedure and the performance criteria. Then, the measurement setup and scenarios are briefly described. Finally, the obtained results are presented and analyzed.

5.4.1 Experimental Methodology and Procedure

Wireless systems are subject to strong multipath fading as objects in the propagation environment tend to reflect, scatter, and diffract the propagating electromagnetic waves. Fading may lead to a 20-30 dB fluctuation in the received signal strength when moving the transmit and/or receive antenna(s) over very short distances typically on the order of the signal wavelength. Therefore, taking measurements of a wireless system only at one transmitter-receiver position pair in space is obviously insufficient for the performance analysis. To achieve more representative performance results, it is necessary to spatially average the performance by taking a high density of separate measurements for different spatial positions of the transmit or receive antenna(s) over an area of several wavelengths. Following the assumption of a stationary channel, results will be the same regardless of whether the transmit or receive antenna(s) are moved.

Following the above, Fig. 5.7 shows the experimental procedure adopted in this thesis for the performance analysis of beam-space MIMO (and conventional MIMO) in realistic environments. In the first phase, a frame-based measurement setup is employed to collect measurements of sufficient channel realizations across space. At each spatial point, the measurement is repeated several times to reduce the impact of temporal channel variations, for instance caused by possible movement of people in the environment. Multiple temporal measurements also allow removing any measurements corrupted by external interference in the same frequency band (for instance, 802.11 Wi-Fi transmissions). For each spatial-temporal channel realization, the channel matrix, denoted by $\hat{\mathbf{H}}[s, t]^1$, is simply estimated by transmitting and receiving known training sequences as discussed earlier in Section 5.3.2 and formulated in (5.6). In addition to the channel matrix, the error rate corresponding to the test data sequences embedded in the transmitted frames is estimated, which will be used only for measurement validation.

In the second phase, link performance parameters are extracted based on the taken channel measurements. First, the records with a measured error rate greater than a given threshold are removed from the data set. Afterwards, for each spatial realization the average channel matrix, $\hat{\mathbf{H}}_{\text{av}}[s]$, is computed over valid temporal snapshots. Average channel matrices are then normalized to force unit average power received at each antenna independent of the total power radiated from the transmitter. This normalization, when the input vector is defined

¹ $s \in \{1, 2, \dots, \mathcal{S}\}$ and $t \in \{1, 2, \dots, \mathcal{T}\}$ are the discrete spatial and temporal indices.

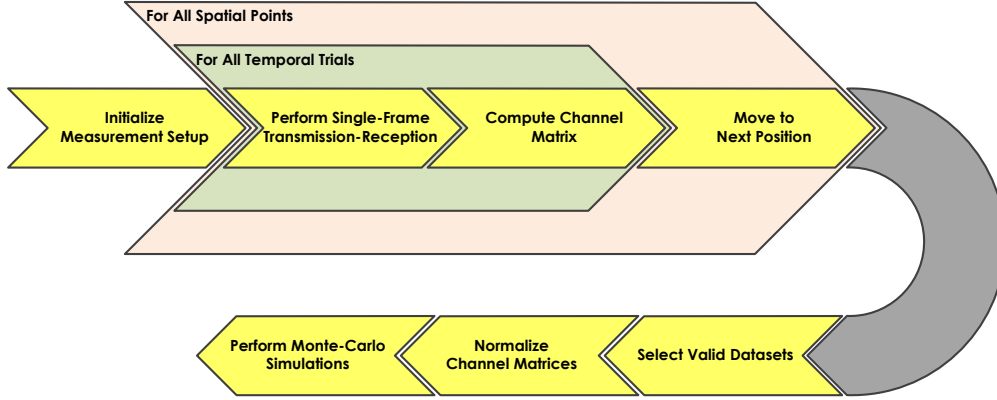


Figure 5.7: Diagram outlining the experimental procedure for the measurement of the channel matrices and the computation of mutual information and BER.

according to (A.1), is equivalent to

$$\left[\frac{1}{\mathcal{L}} \sum_{s=1}^{\mathcal{L}} \|\hat{\mathbf{H}}_{\text{av, norm}}[s]\|^2 \right]^{1/2} = 2, \quad (5.7)$$

where $\hat{\mathbf{H}}_{\text{av, norm}}[s]$ denotes the normalized channel matrices. Now, as discussed in Appendix A, the capacity can be estimated using the mutual information, which is computed by taking the expectation over the normalized channel matrices and noise using Monte-Carlo technique. Since the measured SNR from the experiments cannot be easily altered, a wide range of SNR values are considered by adding appropriately scaled i.i.d. Gaussian noise to the measurements. Similarly, the average BER is computed by running Monte-Carlo simulations over the same set of channel matrices for different SNR operating points and independent of other factors (such as transmit EVM and RF impairments).

5.4.2 Measurement Setup

Fig. 5.8a shows the experimental platform employed for performing our measurements of beam-space MIMO. The pieces of the equipment are very similar to the ones employed for constructing the testbed in Section 5.3.1, except that a XY positioner is added, allowing to change the position of the transmit antenna. Fig. 5.9a shows the used XY positioner, which provides a movement area of $310 \text{ mm} \times 390 \text{ mm}$ (equivalent to $2.5\lambda_0 \times 3.2\lambda_0$ at 2.45 GHz)² with a spatial accuracy of 0.1 mm . By programming its Arduino UNO microcontroller using the provided software, the positioner can be controlled using G-code commands through its USB port. As shown in Fig. 5.9b, a fixture made of ABS-M30, fabricated using 3D printing technology, is used to mount the antenna(s) on the moving terminal of the positioner.

To perform measurements of conventional MIMO, the platform shown in Fig. 5.8b is employed.

² λ_0 denotes the free-space wavelength.

The receiver side is the same as that of beam-space MIMO. However, at the transmitter side the NI 5781 module is replaced with another NI 5791 module to allow producing the second RF signal. Moreover, two standard 2.4 GHz antennas, identical to the ones at the receiving

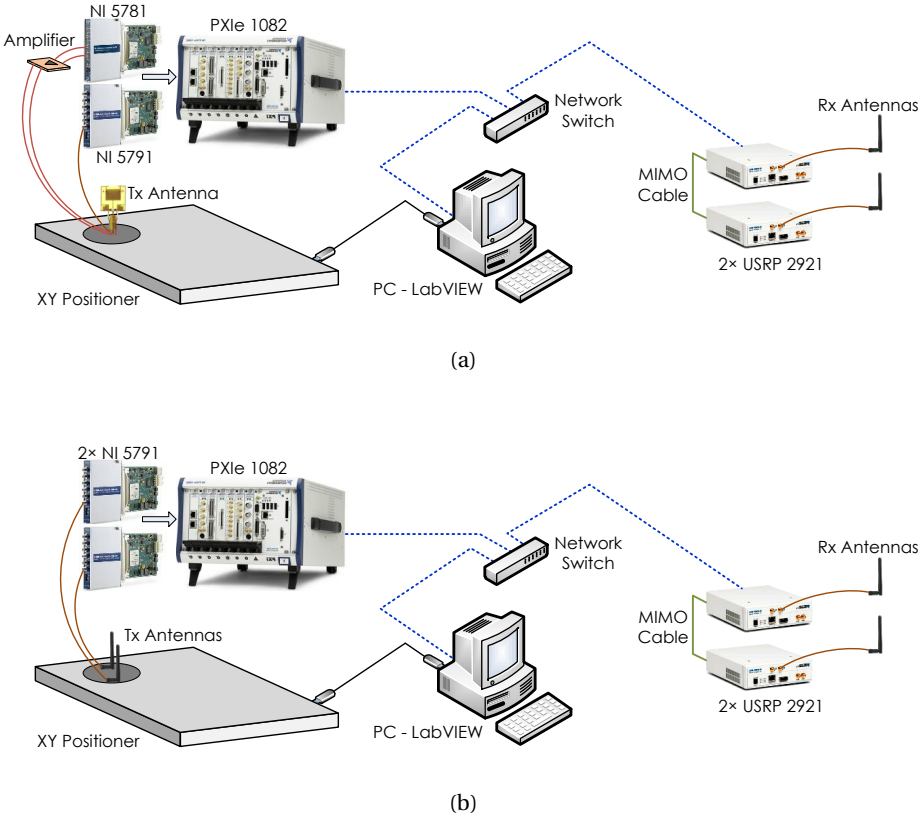


Figure 5.8: (a) Experimental Platform used for the performance analysis of beam-space MIMO. (b) Experimental Platform used for the performance analysis of conventional 2x2 MIMO.

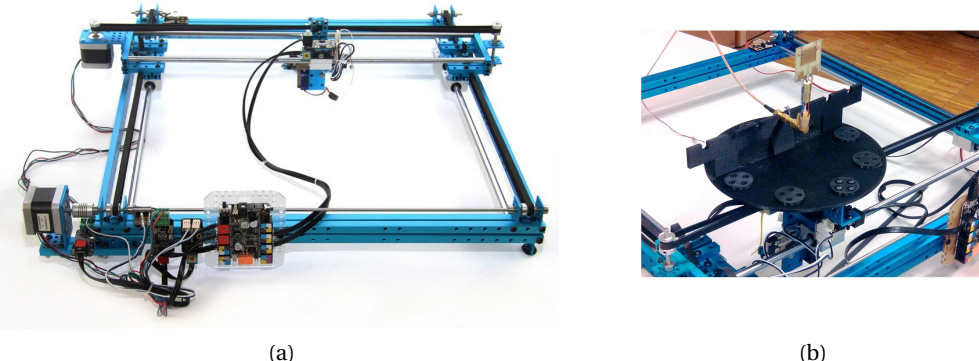


Figure 5.9: (a) XY positioner used in our measurement campaign [102]. (b) Antenna support fixture mounted on the positioner.

side, are utilized as transmit antennas.

To carry out a set of measurements using either the beam-space MIMO platform or the conventional MIMO platform, the main LabVIEW program first initiates the positioner by moving the antenna(s) to the initial location. The program then calls the transmission and reception programs. As expected, the transmission program for conventional MIMO measurements is different from the one discussed in Section 5.3.2 as the symbols of both frames are passed to their corresponding RF channels after oversampling and pulse-shaping. Fig. 5.10 illustrates the frame structure used for conventional MIMO measurements. It can be seen that when one of the two antennas transmits the synchronization or training sequence, the other antenna remains silent. The system parameters used in our measurement campaign are selected according to Table 5.2. We would like to stress that, although including the data segment in the frames is not essential in our experiments, we still dedicate half of the frame length to the data sequences. As stated in Section 5.4.1, the information obtained from decoding the data segment is used to eliminate the measurements corrupted due to an incorrect frequency offset estimation or external interference. According to the procedure outlined in Section 5.4.1, once the measurements are repeated 11 times ($\mathcal{T} = 11$) at a given spatial point, the main program commands the positioner to move to the next point. The same procedure is followed for the next transmit antenna locations. As depicted in Fig. 5.11, the measurements are taken over 400 points ($\mathcal{S} = 400$) in a rectangular 20×20 grid with an area of $310 \text{ mm} \times 370 \text{ mm}$, corresponding to $2.5\lambda_0 \times 3.0\lambda_0$ at 2.45 GHz. Spatial steps in the x and y directions of the positioner are 16.3 mm and 19.5 mm, respectively.

	Synchronization Part (N_s Repetitions)				Training Part (2 Phases)		Data Part
Frame #1	Sync. Seq.	Sync. Seq.	...	Sync. Seq.	Training Sequence #1	–	Data Sequence #1
Frame #2	–	–	...	–	–	Training Sequence #2	Data Sequence #2

Figure 5.10: Frame structure used for conventional MIMO experiments.

5.4.3 Measurement Results

The measurements were conducted in a typical laboratory environment at EPFL, shown in Fig. 5.12, with a considerable number of scattering objects, such as laboratory equipment, furniture, large metal storage cabinets, and other ‘clutter’. Fig. 5.13 depicts the floor plan of the laboratory. Two different measurement scenarios were considered. In the first scenario, hereafter denoted as scenario I, there was no LOS path between the transmitter and the receiver. The second scenario, hereafter denoted as scenario II, was designed such that the channel became largely LOS, however, NLOS components were also expected due to reflections from objects, walls, and ceiling. For each considered scenario, the measurements were carried out using both beam-space MIMO and conventional MIMO platforms. The experiments were conducted at night to reduce the effects of movement in the channel as well as the risk of unwanted external interference. Each set of 4400 experimental measurements

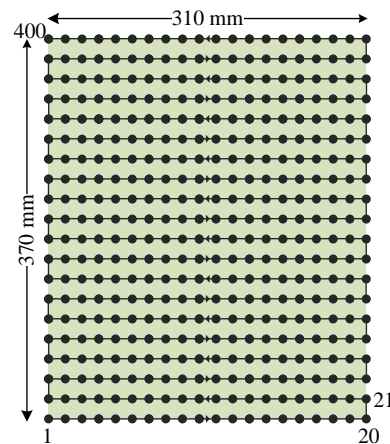


Figure 5.11: Measurement points for transmit antenna(s).



Figure 5.12: Laboratory where the experiments were performed.

took approximately 7 hours to complete. To minimize nonlinearities associated with the varactor diodes used as the variable loads in the beam-space MIMO antenna, the RF voltage swing on the diodes was kept much lower compared to their bias voltage. Accordingly, the RF power input to the beam-space MIMO antenna was limited to 0 dBm. In conventional MIMO experiments, the RF power to each of the transmit antennas was 0 dBm. Note that the transmit power difference was later compensated for when normalizing the channel matrices.

Scenario I - NLOS

Three sets of experiments were conducted for this scenario:

- The conventional MIMO platform was employed, with all the transmit and receive antennas vertically polarized. The spacing between the transmit antennas was 120 mm (approximately λ_0 at 2.45 GHz), while the receive antennas were 240 mm apart.

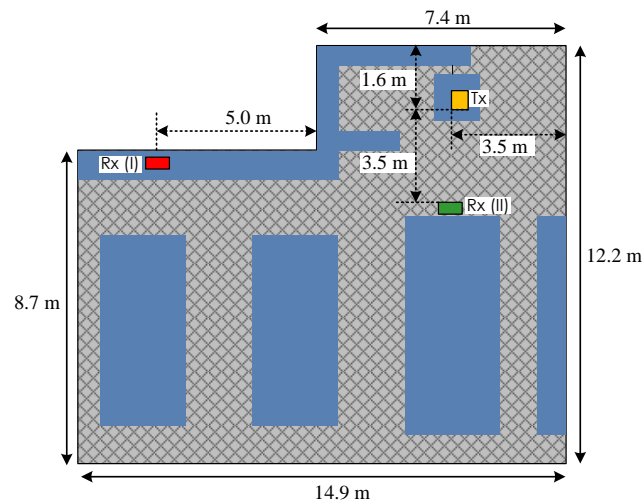


Figure 5.13: Floor plan of the measurement environment and the positions of the transmitter and the receiver. Blue areas represent the work desks and storage cabinets. The receiver location is marked by a red/green rectangle in the first/second scenario.

- The beam-space MIMO platform was used, with the receive antennas vertically polarized and 240 mm apart (see Fig. 5.14a).
- The beam-space MIMO platform was used, with the receive antennas angled at 45° and 240 mm apart (see Fig. 5.14b), to examine the impact of altering the relative polarization of the receive antennas.



Figure 5.14: Polarization of the receive antennas; (a) vertically polarized, (b) perpendicular angled at 45° .

Channel matrices for the measurements with a error rate greater than 10% in decoding the data sequences were excluded from the data set used in the analysis as these were often found to be corrupted by external interference or had failed to correctly synchronize or decode. Table 5.3 shows the number of valid measurements recorded for each experiment. For all three experiments, in more than 88% of the total 400 spatial points there were at least one valid temporal measurement. Moreover, the measured SNR from the experiments was typically at least 20 dB.

Table 5.3: Valid measurements.

Experiment	Total Valid Measurements	Valid Spatial Points
Conventional MIMO	3795 (86.3%)	360 (90.0%)
Beam-Space MIMO, Rx Antennas Vertically Polarized	3863 (87.8%)	371 (92.7%)
Beam-Space MIMO, Rx Antennas Angled at 45°	3593 (81.7%)	355 (88.7%)

Table 5.4 summarizes the average received power for the three experiments, where the 3 dB higher total input power in transmitting the data part in the conventional MIMO experiment is compensated for to ensure a fair comparison against the beam-space MIMO experiments. It is observed that nearly the same level of (spatially averaged) power was received for the conventional and beam-space MIMO experiments. In each experiment, the difference between the average power received at the two receive antennas during the transmission of the data segment is less than 0.6 dB.

Table 5.4: Global average of average received power.

Experiment	Average Power Received at Rx1 (dBm)			Average Power Received at Rx2 (dBm)		
	Data	1st Training	2nd Training	Data	1st Training	2nd Training
Conventional MIMO	-36.9	-36.3	-37.5	-36.4	-35.4	-37.7
Beam-Space MIMO, Rx Antennas Vertically Polarized	-36.0	-37.1	-35.1	-36.4	-38.1	-35.1
Beam-Space MIMO, Rx Antennas Angled at 45°	-37.4	-38.3	-36.5	-36.8	-36.5	-36.8

Table 5.5 gives the average received constellation error (RCE) of the data symbols received at both antennas. For each experiment, the average RCE was calculated first by averaging over all valid temporal snapshots and then by averaging over valid spatial points. It is observed that the average RCE of beam-space MIMO transmission is interestingly comparable with that of the conventional MIMO transmission even with non-idealities in the beam-space MIMO antenna.

Table 5.5: Average RCE of the received data.

Experiment	Average RCE (dB) at Rx1	Average RCE (dB) at Rx2
Conventional MIMO	-24.9	-24.8
Beam-Space MIMO, Rx Antennas Vertically Polarized	-24.6	-24.8
Beam-Space MIMO, Rx Antennas Angled at 45°	-24.6	-24.7

Fig. 5.15 shows the magnitude of the average channel matrices, $|\hat{\mathbf{H}}_{av}[s]|$, for the conventional MIMO experiment, when the transmit antennas were moved over the spatial grid. Fig. 5.16 and Fig. 5.17 show the same data for the two beam-space MIMO experiments, respectively.

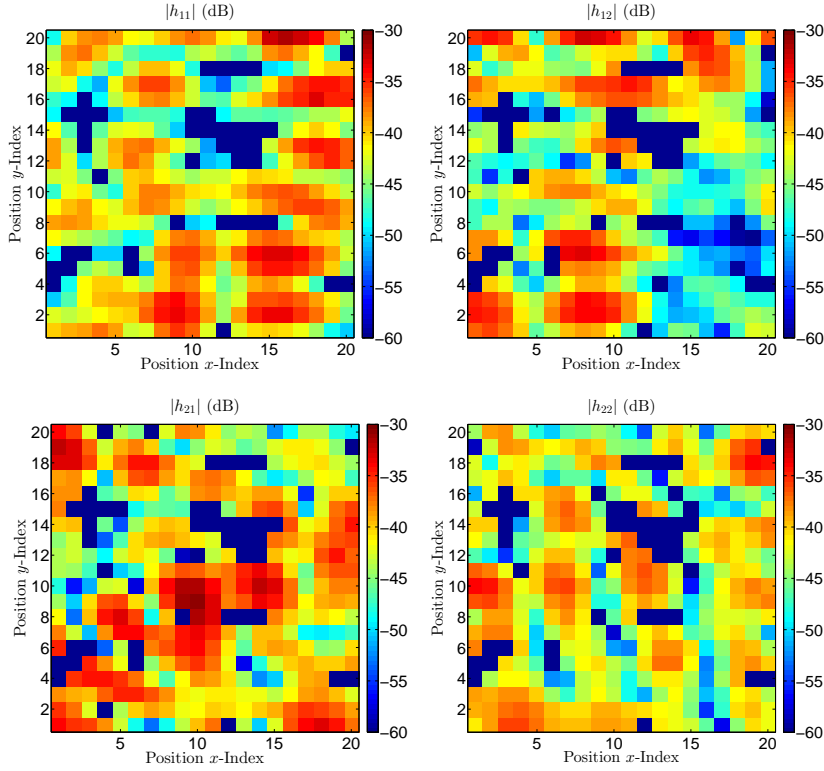


Figure 5.15: Magnitude of the channel coefficients in the conventional MIMO experiment regarding the position of the transmit antennas. Dark blue pixels show the locations with no valid measurement.

Having the normalized channel matrices $\hat{\mathbf{H}}_{av,norm}[s]$, the full spatial correlation matrix, \mathbf{R}_H , can be calculated using (2.8). Table 5.6 shows the magnitude of \mathbf{R}_H for the three experiments. From comparing the diagonal entries, we find that the power allocation in the beam-space MIMO channels is more uniform compared to the conventional MIMO channel. Moreover, the beam-space MIMO experiments yield slightly smaller correlation coefficients (off-diagonal entries of \mathbf{R}_H). Table 5.6 also gives the average of the channel ellipticity for each experiment. The channel ellipticity, $\gamma[s] \in [0, 1]$, is defined as the ratio of geometric and arithmetic means of the channel eigenvalues for each spatial realization, and used as a measure of multipath richness of a MIMO channel [103]. Fig. 5.18 compares the CDF of the channel ellipticity in the three experiments. It is clear that the eigenvalue spread of the beam-space MIMO channels is smaller.

Fig. 5.19 compares the mutual information curves as a function of the SNR per symbol. While in the lower and higher SNR regimes all three experiments yield nearly similar capacity

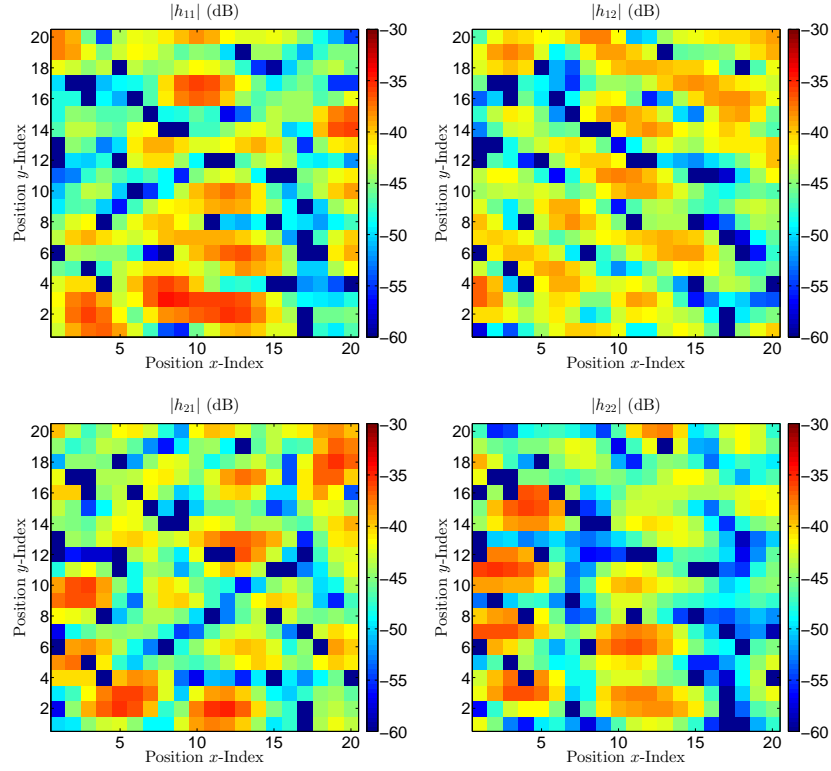


Figure 5.16: Magnitude of the channel coefficients in the beam-space MIMO experiment with the receive antennas vertically polarized regarding the position of the transmit antennas. Dark blue pixels show the locations with no valid measurement.

Table 5.6: Magnitude of the spatial correlation matrix and the channel ellipticity.

Experiment	$ \mathbf{R}_H $	Channel Ellipticity
Conventional MIMO	$\begin{bmatrix} 1.09 & 0.96 & 0.36 & 0.25 \\ 0.96 & 1.32 & 0.38 & 0.33 \\ 0.36 & 0.38 & 0.82 & 0.22 \\ 0.25 & 0.33 & 0.22 & 0.77 \end{bmatrix}$	0.53
Beam-Space MIMO, Rx Antennas Vertically Polarized	$\begin{bmatrix} 1.10 & 0.88 & 0.34 & 0.36 \\ 0.88 & 1.03 & 0.29 & 0.37 \\ 0.34 & 0.29 & 0.99 & 0.24 \\ 0.36 & 0.37 & 0.24 & 0.88 \end{bmatrix}$	0.61
Beam-Space MIMO, Rx Antennas Angled at 45°	$\begin{bmatrix} 0.97 & 0.84 & 0.21 & 0.25 \\ 0.84 & 1.09 & 0.18 & 0.33 \\ 0.21 & 0.18 & 0.88 & 0.13 \\ 0.25 & 0.33 & 0.13 & 1.06 \end{bmatrix}$	0.62

values, the beam-space MIMO systems slightly outperform in mid-range SNR values. In the conventional MIMO experiment, the power is equally distributed between the omnidirectional transmit antennas, which is not necessarily optimal for the considered NLOS scenario. Fig. 5.19 also includes the curves of the ergodic capacity as a validating tool for Monte-Carlo simulations.

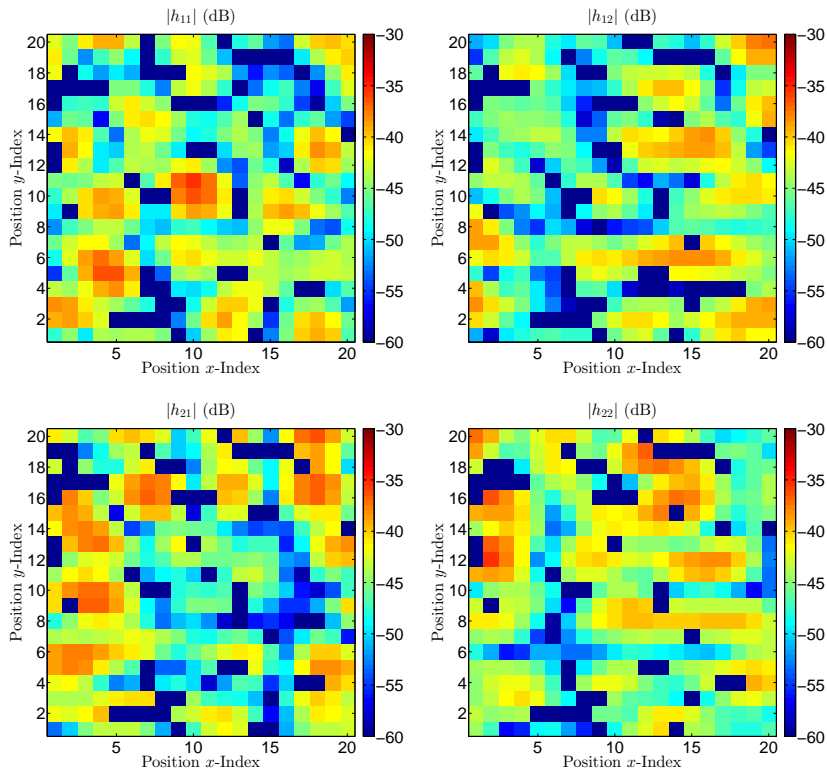


Figure 5.17: Magnitude of the channel coefficients in the beam-space MIMO experiment with the receive antennas angled at 45° regarding the position of the transmit antennas. Dark blue pixels show the locations with no valid measurement.

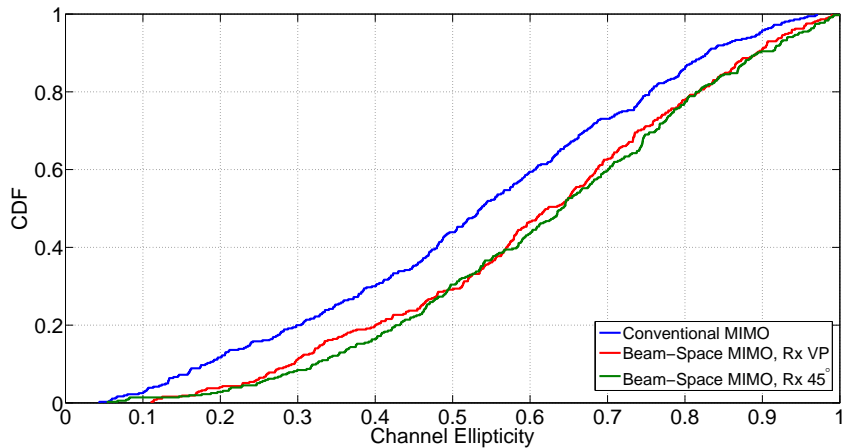


Figure 5.18: CDF of the channel ellipticity.

Clearly, in low-SNR regime (up to an SNR of 0 dB) the effect of signaling using the finite QPSK alphabet is negligible. Fig. 5.20 depicts the empirical CDF of the mutual information values for each experiment. While in low SNR values the conventional MIMO and beam-space MIMO

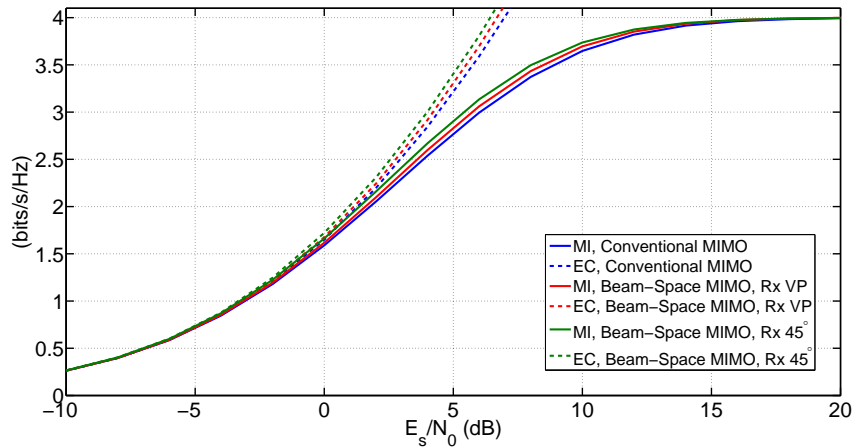


Figure 5.19: Mutual information (MI) and ergodic capacity (EC) curves obtained from Monte-Carlo simulations using the measured and normalized channel matrices.

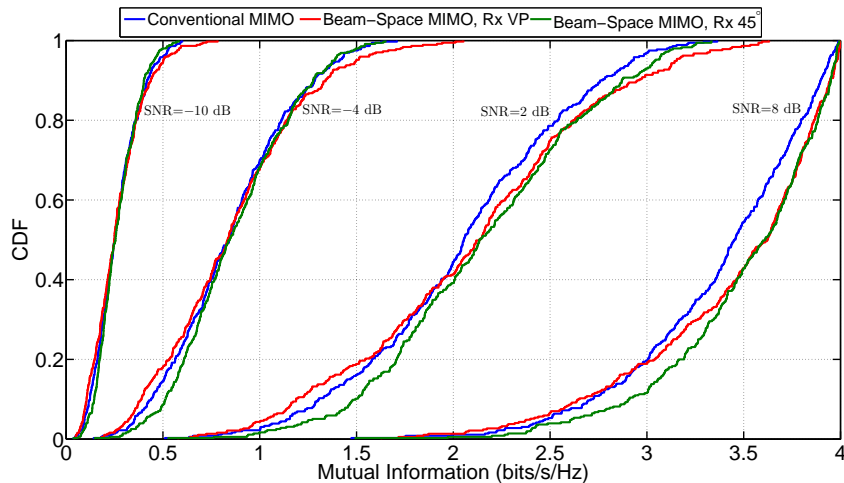


Figure 5.20: CDF of the mutual information for different SNR values.

experiments resulted in nearly identical distribution functions, in the mid-SNR region the beam-space MIMO systems clearly outperforms the conventional MIMO system.

The symbol error rate (SER) curves obtained from Monte-Carlo simulations are shown in Fig. 5.21. It is clear that the beam-space MIMO systems have better error performance compared to their conventional counterpart.

Scenario II - LOS

Four sets of experiments were conducted for this scenario:

- The conventional MIMO platform was employed, with all the transmit and receive

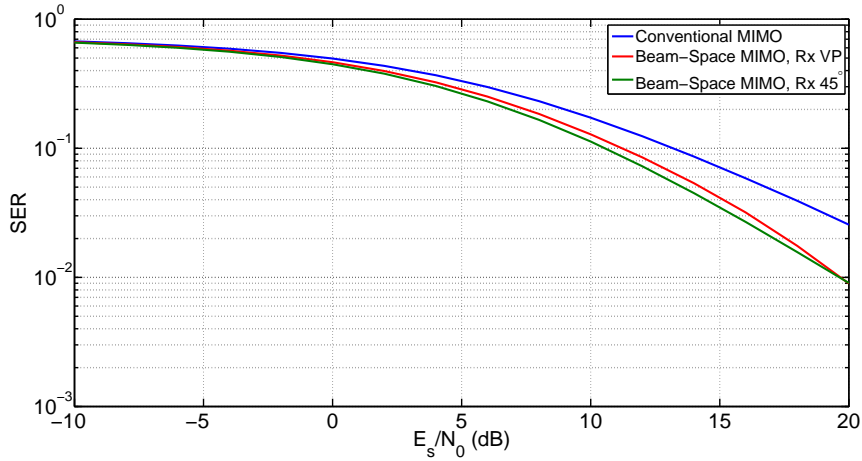


Figure 5.21: SER obtained from Monte-Carlo simulations using the measured and normalized channel matrices.

Table 5.7: Valid measurements.

Experiment	Total Valid Measurements	Valid Spatial Points
Conventional MIMO	4265 (96.9%)	396 (99.0%)
Beam-Space MIMO, Rx Antennas Vertically Polarized	4186 (95.1%)	391 (97.7%)
Beam-Space MIMO, Rx Antennas Vertically Polarized	4017 (91.3%)	379 (94.7%)
Beam-Space MIMO, Rx Antennas Angled at 45°, Tx Antenna Rotated	4128 (93.8%)	387 (96.7%)

antennas vertically polarized. The spacing between the transmit antennas was 120 mm (approximately λ_0 at 2.45 GHz), while the receive antennas were 240 mm apart.

- The beam-space MIMO platform was used, with the receive antennas vertically polarized and 240 mm apart.
- The beam-space MIMO platform was used, with the receive antennas angled at 45° and 240 mm apart.
- The beam-space MIMO platform was used, with the receive antennas angled at 45° and 240 mm apart, while rotating the beam-space MIMO transmit antenna by 180° about its vertical axis relative to the previous experiments.

Table 5.7 shows the number of valid measurements recorded for each experiment, using a 10% measured error rate threshold. For all four experiments, in more than 94% of the total 400 spatial points there were at least one valid temporal measurement. Moreover, the measured SNR from the experiments was typically at least 25 dB.

Table 5.8: Global average of average received power.

Experiment	Average Power Received at Rx1 (dB)			Average Power Received at Rx2 (dB)		
	Data	1st Training	2nd Training	Data	1st Training	2nd Training
Conventional MIMO	-23.6	-24.7	-22.8	-22.8	-23.5	-22.2
Beam-Space MIMO, Rx Antennas Vertically Polarized	-23.5	-23.7	-23.3	-24.3	-23.4	-25.5
Beam-Space MIMO, Rx Antennas Angled at 45°	-23.2	-22.6	-23.8	-23.6	-23.6	-23.5
Beam-Space MIMO, Rx Antennas Angled at 45°, Tx Antenna Rotated	-24.5	-26.5	-23.0	-23.6	-22.5	-25.0

Table 5.9: Magnitude of the spatial correlation matrix and the channel ellipticity.

Experiment	$ \mathbf{R}_H $	Channel Ellipticity
Conventional MIMO	$\begin{bmatrix} 0.70 & 0.71 & 0.57 & 0.25 \\ 0.71 & 0.94 & 0.60 & 0.72 \\ 0.57 & 0.60 & 1.10 & 0.66 \\ 0.61 & 0.72 & 0.66 & 1.26 \end{bmatrix}$	0.42
Beam-Space MIMO, Rx Antennas Vertically Polarized	$\begin{bmatrix} 1.78 & 1.41 & 0.18 & 0.21 \\ 1.41 & 1.54 & 0.15 & 0.20 \\ 0.18 & 0.15 & 0.42 & 0.02 \\ 0.21 & 0.20 & 0.02 & 0.26 \end{bmatrix}$	0.47
Beam-Space MIMO, Rx Antennas Angled at 45°	$\begin{bmatrix} 1.32 & 1.02 & 0.19 & 0.07 \\ 1.02 & 1.09 & 0.16 & 0.11 \\ 0.19 & 0.16 & 0.77 & 0.31 \\ 0.07 & 0.11 & 0.31 & 0.82 \end{bmatrix}$	0.63
Beam-Space MIMO, Rx Antennas Angled at 45°, Tx Antenna Rotated	$\begin{bmatrix} 1.12 & 0.99 & 0.35 & 0.31 \\ 0.99 & 1.24 & 0.33 & 0.35 \\ 0.35 & 0.33 & 0.68 & 0.37 \\ 0.31 & 0.35 & 0.37 & 0.95 \end{bmatrix}$	0.65

On the assumption that the total input power to the transmit antenna(s) was 0 dBm, Table 5.8 gives the global average of temporally-averaged received power for the four experiments. It is observed that the level of received power in the conventional MIMO experiment is, as expected, slightly higher than in the beam-space MIMO experiments.

The magnitude of the \mathbf{R}_H and the average of the channel ellipticity are given in Table 5.9. The most unbalanced power allocation occurred in the beam-space MIMO experiment with vertically polarized receive antennas, while all off-diagonal correlation coefficients were relatively high in the conventional MIMO experiment. As shown in Fig. 5.22, the beam-space MIMO experiments with angled receive antennas yielded in higher channel ellipticity, showing better performance in supporting parallel communication modes.

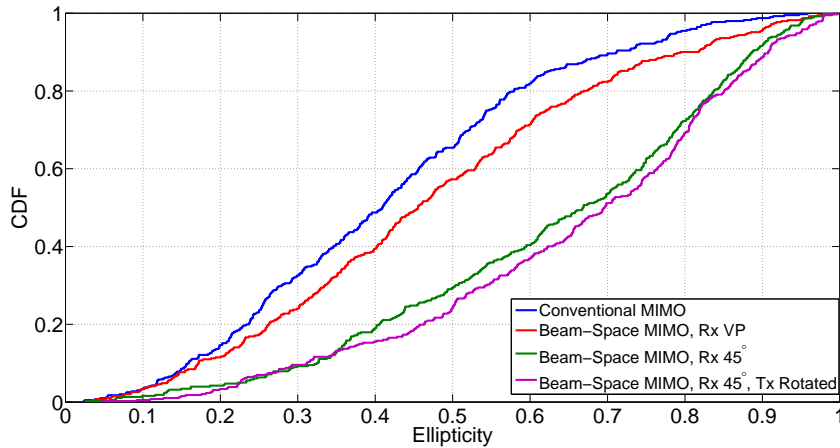


Figure 5.22: CDF of the channel ellipticity.

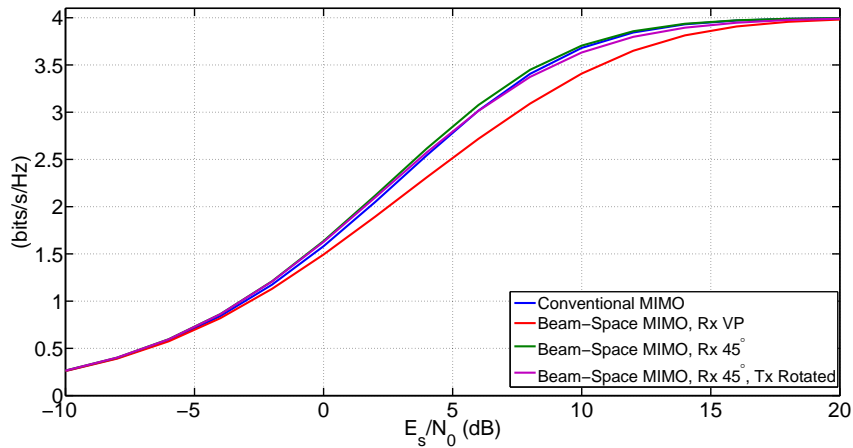


Figure 5.23: Mutual information curves obtained from Monte-Carlo simulations using the measured and normalized channel matrices.

The mutual information curves obtained from Monte-Carlo simulations are shown in Fig. 5.23. The conventional MIMO system and two beam-space MIMO systems with angled receive antennas yield very similar capacity performance. The beam-space MIMO system with vertical receive antennas underperforms the other three for mid-range SNR values, most likely due to its worse power allocation performance. Fig. 5.24 shows the empirical CDF of the mutual information values for each experiment. This shows that the performance of the beam-space MIMO system highly depends on the orientation of the transmit and receive antennas as the basis patterns of the beam-space MIMO antenna are not omni-directional and similarly-polarized.

Fig. 5.25 depicts the SER curves obtained from Monte-Carlo simulations. All three beam-space MIMO systems outperforms their conventional counterpart. However, the error performance

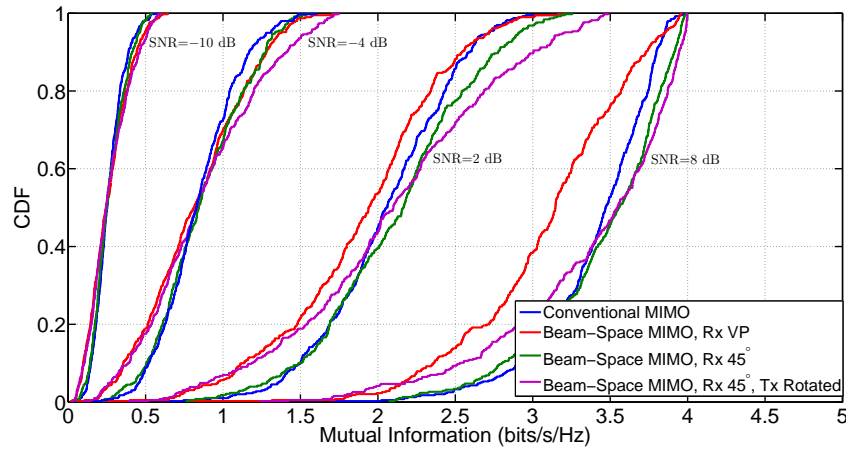


Figure 5.24: CDF of the mutual information for different SNR values.

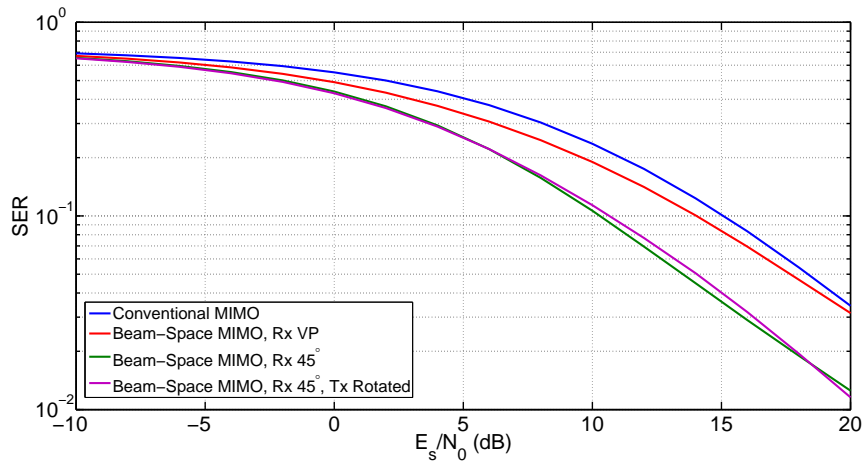


Figure 5.25: SER obtained from Monte-Carlo simulations using the measured and normalized channel matrices.

is strongly dependent on the polarization of the receive antennas.

5.5 Conclusion

In this chapter, we have described the construction of an open-loop real-time beam-space MIMO testbed consisting of transmit and receive subsystems. A software program generates the RF and baseband control waveforms with an appropriate frame format that allows reception, channel estimation and demodulation. Accordingly, the first successful MIMO transmission of QPSK signals with a single RF chain was empirically demonstrated while employing the beam-space MIMO fabricated in Chapter 4 as a transmit antenna and a conventional two-element array as receive antennas.

Afterwards, a measurement campaign was conducted to shed light on the performance of beam-space MIMO compared to that of conventional MIMO in real indoor channels. Experimental measurements of the channel matrix were carried out in LOS and NLOS scenarios for both MIMO systems. To correctly account for multipath fading, 400 measurements were taken over a 310 mm×370 mm area using an XY positioner. In addition, 11 temporal measurements were made at each of the 400 points to reduce the impact of movement in the channel and external interference. The mutual information and SER were computed by running Monte-Carlo simulations over the measured channel matrices and artificially generated i.i.d. Gaussian noise.

Results for the NLOS scenario showed that the mutual information performance of the beam-space and conventional MIMO systems were very similar, particularly at low- and high- SNR ranges. The beam-space MIMO system achieved up to 4.4% higher mutual information than the conventional MIMO system for an SNR of 6 dB. The SER performance comparison showed that the beam-space MIMO system outperformed its conventional counterpart, resulting in a gain of 3-3.5 dB for an SER level of 0.03. Both mutual information and SER in beam-space MIMO were slightly affected by the change in the polarization of the receive antennas.

On the other hand, analyses in the LOS scenario confirmed that directional exotically-polarized basis patterns of the beam-space MIMO antenna could cause the system performance to strongly depend on the orientation of receive and transmit antennas. While the mutual information of the beam-space MIMO system with vertically polarized receive antennas was approximately 10% lower (at a SNR of 6 dB) than the conventional MIMO system, the use of orthogonally-polarized receive antennas for beam-space MIMO regained the capacity performance losses. Nevertheless, beam-space MIMO exhibited better SER performance compared to conventional MIMO.

6 Beam-Space MIMO: Near-Field Perturbation Effects

*The sky enriches the earth with rain, and the earth gives it dust in return.
Every vessel exudes whatever it contains.*

— Saadi, Gulistan, Principles of Social Conduct, Maxim 95

6.1 Overview

It is well known that the near-field interaction with immediate operating environment affects the antenna characteristics such as input impedance and radiation properties. In the case of typical handheld terminals, comprehensive numerical and experimental studies have been conducted either to investigate the operator's hand and head effects on the operation of antennas, or to evaluate the dissipated power in the operator's body and corresponding specific absorption rate (SAR) [104–108]. As for any classical antenna, the near-field interaction causes usual effects on the characteristics of a beam-space MIMO antenna. However, since beam-space MIMO systems employ the antenna's radiation pattern as a knob to aurally encode information, they are expected to be inherently prone to multiplexing performance degradation in the presence of external perturbation. This makes the study of near-field interaction influence on beam-space MIMO distinct from those carried out for the case of conventional systems. This issue has been considered in this thesis for the first time.

The rest of this chapter is organized as follows. In Section 6.2, the effects of near-field perturbation on beam-space MIMO operation are discussed in theory. In Section 6.3, the user effects are evaluated in different operating scenarios for a BPSK beam-space MIMO antenna, and the role of different antenna parameters on channel capacity reduction is discussed. Moreover, the impact of tuning the reactance values of the antenna's variable loads to take into account the user interaction at the design level is examined. Section 6.4 extends the study to the case of higher order modulation schemes, where beam-space MIMO operation under QPSK signaling in the presence of the user body is analyzed.

Parts of this chapter have been published earlier in [25–27].

6.2 Near-Field Perturbation Effects in Beam-Space MIMO

This study is based on the beam-space MIMO antenna system introduced in Section 4.2.4 and schematically shown in Fig. 4.2. Let us assume that the beam-space MIMO antenna has been designed for operation in free space, and there is no mechanism for adapting the reactance values of the variable loads to the antenna's immediate environment. Recalling from Chapter 4, to multiplex each arbitrary symbol combination of $\{x_1, x_2\}$ from the considered signal constellation diagram, the variable loads are reconfigured such that the antenna's actual radiation pattern becomes

$$\begin{aligned}\mathcal{E}_o(\Omega) &= x_1 \mathcal{E}_u^{\{x_r\}}(\Omega) = x_1 [\mathcal{B}_1(\Omega) + x_r \mathcal{B}_2(\Omega)] \\ &= x_1 \mathcal{B}_1(\Omega) + x_2 \mathcal{B}_2(\Omega).\end{aligned}\quad (6.1)$$

where according to (4.6) and (4.26), the basis patterns, \mathcal{B}_1 and \mathcal{B}_2 , can be expressed as

$$\mathcal{B}_1(\Omega) = \frac{\mathcal{E}_u^{\{+1\}}(\Omega) + \mathcal{E}_u^{\{-1\}}(\Omega)}{2} \quad (6.2a)$$

$$\mathcal{B}_2(\Omega) = \frac{\mathcal{E}_u^{\{+1\}}(\Omega) - \mathcal{E}_u^{\{-1\}}(\Omega)}{2}. \quad (6.2b)$$

Note that for the sake of compactness in this chapter, we replaced the superscript notation $\{jX_1^{\{x_r\}}, jX_2^{\{x_r\}}\}$ introduced in Chapter 4 with $\{x_r\}$. The geometry of the antenna system ensures that $\mathcal{E}_u^{\{-1\}}(\Omega)$ and $\mathcal{E}_u^{\{+1\}}(\Omega)$ form a mirror image pattern pair, and therefore guarantees the orthogonality of the basis patterns. As discussed in Section 5.2, the signal transmitted by the beam-space MIMO antenna is received using a two-element array. It can be perfectly decoded by a conventional linear MIMO detector following the conventional MIMO system model, thanks to the ideal linear pattern decomposition given in (6.1).

The effects of near-field perturbation on beam-space MIMO operation can be classified into three main levels. In the first level, beam-space MIMO suffers from the *typical* effects encountered in any SISO or MIMO antenna system, namely, the variations of the impedance matching and the radiation properties. More precisely, the perturbed antenna's radiation pattern can be expressed as

$$\mathcal{E}_{u,\text{per}}^{\{x_r\}}(\Omega) = \Xi^{\{x_r\}}(\Omega) \mathcal{E}_u^{\{x_r\}}(\Omega), \quad (6.3)$$

where $\Xi^{\{x_r\}}(\Omega)$ represents the angular perturbation factor when multiplexing symbol pairs with a ratio of x_r .

The second level includes the effects on the characteristics of the basis patterns. According to the definition in (6.2), the updated basis becomes

$$\mathcal{B}_{1,\text{per}}(\Omega) = \frac{\mathcal{E}_{u,\text{per}}^{\{+1\}}(\Omega) + \mathcal{E}_{u,\text{per}}^{\{-1\}}(\Omega)}{2}$$

6.2. Near-Field Perturbation Effects in Beam-Space MIMO

$$= \frac{\Xi^{\{+1\}}(\Omega)\mathcal{E}_u^{\{+1\}}(\Omega) + \Xi^{\{-1\}}(\Omega)\mathcal{E}_u^{\{-1\}}(\Omega)}{2} \quad (6.4a)$$

$$\begin{aligned} \mathcal{B}_{2,\text{per}}(\Omega) &= \frac{\mathcal{E}_{u,\text{per}}^{\{+1\}}(\Omega) - \mathcal{E}_{u,\text{per}}^{\{-1\}}(\Omega)}{2} \\ &= \frac{\Xi^{\{+1\}}(\Omega)\mathcal{E}_u^{\{+1\}}(\Omega) - \Xi^{\{-1\}}(\Omega)\mathcal{E}_u^{\{-1\}}(\Omega)}{2} \end{aligned} \quad (6.4b)$$

Since the perturbation factors $\Xi^{\{+1\}}(\Omega)$ and $\Xi^{\{-1\}}(\Omega)$ are generally unequal, (i) the power radiated by each of two basis patterns is weighted by a different coefficient, and (ii) the perturbed antenna's radiation patterns $\mathcal{E}_{u,\text{per}}^{\{+1\}}(\Omega)$ and $\mathcal{E}_{u,\text{per}}^{\{-1\}}(\Omega)$ no longer form a mirror image pattern pair. Therefore, not only the basis power imbalance ratio, r , changes, but also the basis orthogonality is no longer guaranteed.

In the third level, near-field interaction of the beam-space MIMO antenna with its immediate environment affects the constellation points mapped over the basis patterns. According to (6.3) and (6.4), it can be shown that in general for $x_r \neq \pm 1$,

$$\Xi^{\{x_r\}}(\Omega)\mathcal{E}_u^{\{x_r\}}(\Omega) \neq \frac{1+x_r}{2}\Xi^{\{+1\}}(\Omega)\mathcal{E}_u^{\{+1\}}(\Omega) + \frac{1-x_r}{2}\Xi^{\{-1\}}(\Omega)\mathcal{E}_u^{\{-1\}}(\Omega). \quad (6.5)$$

Therefore, (6.1), and consequently the conventional MIMO system model in (5.4) no longer hold except for $x_r = \pm 1$, namely,

$$\mathcal{E}_{o,\text{per}}(\Omega) = x_1\mathcal{E}_{u,\text{per}}^{\{x_r\}}(\Omega) = x_1\mathcal{B}_{1,\text{per}}(\Omega) + x_2\mathcal{B}_{2,\text{per}}(\Omega) \quad \text{for } x_r = \pm 1, \quad (6.6a)$$

$$\mathcal{E}_{o,\text{per}}(\Omega) = x_1\mathcal{E}_{u,\text{per}}^{\{x_r\}}(\Omega) \neq x_1\mathcal{B}_{1,\text{per}}(\Omega) + x_2\mathcal{B}_{2,\text{per}}(\Omega) \quad \text{for } x_r \neq \pm 1. \quad (6.6b)$$

This means that even though the antenna is reconfigured at each symbol period according to x_r , the symbols with $x_r \neq \pm 1$ are not correctly mapped onto the basis patterns, and their corresponding constellation points are not in the ideal locations when the receiver assumes the conventional MIMO system model in (5.4). As discussed in Section 4.3.2, the modulation distortion can be quantified by the EVM. The analytic expression of the EVM given in (4.40) can be updated for a perturbed beam-space MIMO antenna as

$$\text{EVM}_{\text{rms}}(\Omega) = \left[\frac{\frac{1}{N} \sum_{s=1}^N \left\| \mathcal{B}_{1,\text{per}}(\Omega) + x_{r,s}\mathcal{B}_{2,\text{per}}(\Omega) - \mathcal{E}_{u,\text{per}}^{\{x_r,s\}}(\Omega) \right\|^2}{\frac{1}{N} \sum_{s=1}^N \left\| \mathcal{B}_{1,\text{per}}(\Omega) + x_{r,s}\mathcal{B}_{2,\text{per}}(\Omega) \right\|^2} \right]^{1/2}, \quad (6.7)$$

where $\{x_{r,s}\}_{s=1}^N$ denotes the N possible symbol combination ratios for the considered IQ constellation. Such phase shift and/or amplitude error in turn may result in incorrect interpretation of the signal at the ZF receiver as (5.1) is no longer correct.

Finally, it is worth noting that secondary user effects are not particular to beam-space MIMO.

Conventional MIMO also suffers from its own specific effects such as variations of the power balance and the isolation among multiple antennas in near-field interaction scenarios.

6.3 User Effects: a Case Study of BPSK Beam-Space MIMO Antenna

In this section, we analyze the performance of the BPSK beam-space MIMO antenna designed in Section 3.8 in the three human body interaction scenarios shown in Fig. 6.1. Full-sized homogeneous specific anthropomorphic mannequins (SAM) were used to model the user's hand and head, where the average dielectric properties of all corresponding tissues were selected according to the data reported in [109]. The full-wave electromagnetic simulations were performed using Ansys HFSS.

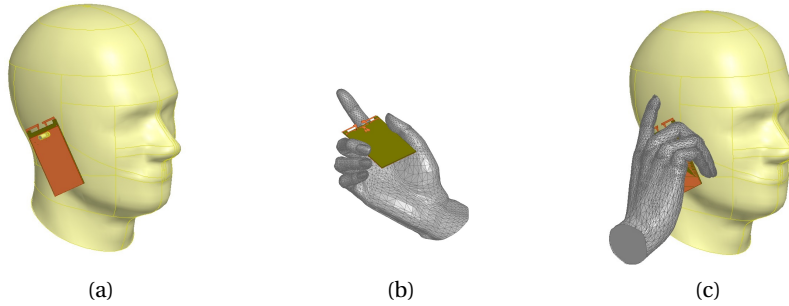


Figure 6.1: The placement of the beam-space MIMO antenna under study in different scenarios: (a) nearby SAM head phantom, (b) in SAM hand phantom, and (c) in SAM hand phantom nearby SAM head phantom. SAM phantoms are taken from CST MWS [110].

Fig. 6.2 shows the antenna's reflection coefficient for different user body interaction scenarios. As expected, the impedance matching of the antenna slightly changes when placed near the body. Moreover, the reflection coefficient is no longer constant over the antenna states due to the asymmetry of the operating environment. However, these variations are rather insignificant as the return loss remains better than 10 dB over the operation frequency range.

The variations of the radiation properties are summarized in Table 6.1. The total efficiency of the antenna is severely degraded when placed in close proximity to the user body, dropping down from 74% in free space to below 10% in the 'in hand-near head' scenario. Since according to Fig. 6.2 the mismatch loss is almost unchanged, the efficiency reduction can be attributed to the absorption in body tissues.

It is observed from Table 6.1 that the parameters specific to beam-space MIMO are also affected by the presence of the user. Power imbalance ratio between the basis patterns, r , varies between -3.0 dB to 6.1 dB for different cases studied. Moreover, the basis correlation is increased from 0 ($-\infty$ dB) in free space to -6.8 dB in the 'in hand' scenario, which is still acceptable for MIMO operation. Table 6.1 also shows the effect of the distance d between

6.3. User Effects: a Case Study of BPSK Beam-Space MIMO Antenna

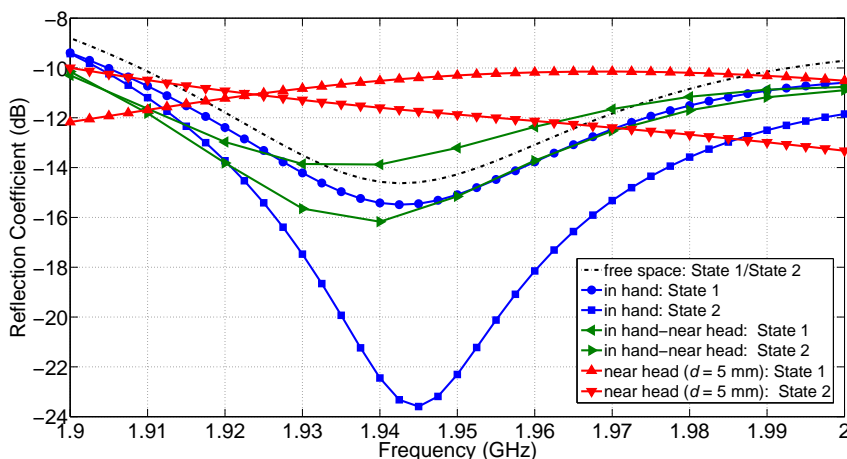


Figure 6.2: Reflection coefficient of the beam-space MIMO antenna under study. The parameter d determines the minimum spacing between the antenna and the head.

Table 6.1: User body effects on the performance of the beam-space MIMO antenna.

Scenario	Total Efficiency in $\mathcal{S} = 1$, $e_{\text{tot},1}$	Total Efficiency in $\mathcal{S} = 2$, $e_{\text{tot},2}$	Power Imbalance Ratio, r (dB)	Basis Correlation, $\frac{ \mathcal{R}_{\mathcal{B}_1\mathcal{B}_2} }{[\mathcal{P}_{\mathcal{B}_1}\mathcal{P}_{\mathcal{B}_2}]^{1/2}}$ (dB)
free space	73.9%	73.9%	-1.3	$-\infty$
in hand	37.7%	41.7%	2.1	-19.2
in hand-near head	7.6%	9.5%	-0.5	-10.5
near head ($d = 5$ mm)	11.2%	14.2%	6.1	-6.8
near head ($d = 7.5$ mm)	15.6%	20.4%	-3.0	-12.2
near head ($d = 10$ mm)	21.2%	26.6%	-0.9	-16.4

the antenna and the head, where as expected smaller distances result in higher degradations in the efficiency and the basis correlation. Please note that since the phase of the radiation patterns is very sensitive to external perturbation, the power imbalance ratio does not evolve monotonously with respect to d .

Furthermore, capacity analyses were carried out for the different scenarios. We assumed the transmission of two BPSK signals using the beam-space MIMO antenna over a Kronecker narrowband flat-fading channel and the reception using two uncorrelated antenna elements. Fig. 6.3 shows the channel capacity of the MIMO system with respect to E_s/N_0 . It is observed that the system throughput is severely degraded in the presence of the user particularly in the low-SNR regime. The channel capacity is decreased by 41% from 1.92 b/s/Hz in free space to 1.14 b/s/Hz in the ‘in hand-near head’ scenario for a SNR of 10 dB. Obviously, for high SNR values the effect of the impairments is less pronounced, thus the curves approach each other. It is also informative to evaluate the achievable capacity improvement in the different

operating scenarios by measuring the ratio between the channel capacity of the MIMO system and that of a SISO system with the same average total efficiency (i.e., $\frac{1}{2}[e_{\text{tot},1} + e_{\text{tot},2}]$). As shown in Fig. 6.4, the multiplexing capability of the MIMO system is not much affected by the user's presence in most cases. In the worst case (i.e., in the 'near head' scenario with $d = 5$ mm), where the specific parameters of beam-space MIMO are severely affected, reduction in the improvement with respect to the free-space case is less than 21%. However, in general the channel capacity is improved by at least 95% with beam-space multiplexing.

Finally, it is important to assess the contribution of each parameter impairment to the total performance degradation. To this aim, we selected the 'near head' scenario with $d = 5$ mm as

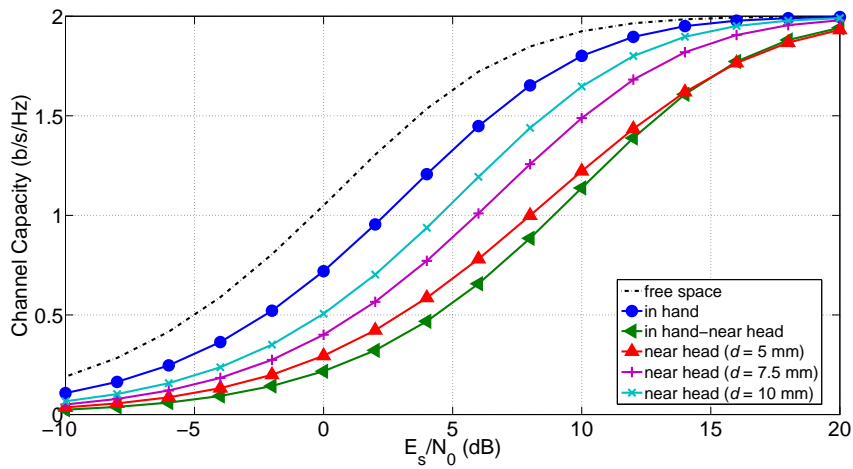


Figure 6.3: Channel capacity under BPSK signaling as a function of E_s/N_0 . The capacity was calculated based on the Monte-Carlo averaging on $1e+6$ random channel and noise realizations. Pulse shaping is not included.

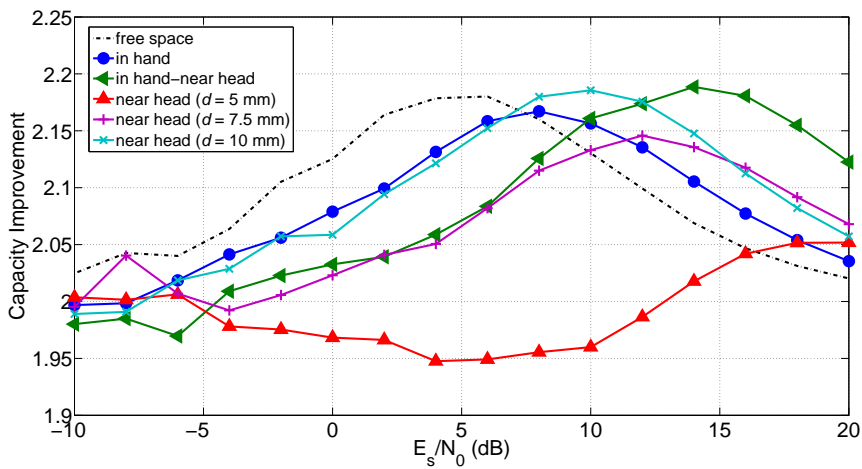


Figure 6.4: Achievable capacity improvement as a function of E_s/N_0 for different scenarios.

6.3. User Effects: a Case Study of BPSK Beam-Space MIMO Antenna

the reference, and compared the multiplexing efficiency¹ of the MIMO system in three new cases shown in Table 6.2. In each case, only one of the antenna parameters (i.e., the average total efficiency, the power imbalance ratio, and the basis correlation) was changed while the other two were left constant. The results are shown in Fig. 6.5, where it is immediately observed that the main contributor is the antenna efficiency. While the multiplexing efficiency is significantly affected by doubling the total efficiency, the contribution of halving the basis power imbalance ratio is less pronounced especially in lower SNR. The graph also shows that a negligible multiplexing efficiency enhancement is achieved when the correlation of non-ideal basis patterns is decreased by 3 dB.

These results demonstrate that throughput reduction is mainly caused by the absorption in user body tissues rather than by the impairment of the basis power imbalance ratio and the basis correlation. Therefore, we can conclude that under BPSK signaling beam-space MIMO is not more vulnerable to the user effects than conventional MIMO systems, and has the potential to perform very well in typical human body interaction scenarios.

Table 6.2: Case studies for assessing the contribution of each parameter impairment to beam-space MIMO performance degradation.

Scenario	Total Efficiency in $S = 1$, $e_{\text{tot},1}$	Total Efficiency in $S = 2$, $e_{\text{tot},2}$	Power Imbalance Ratio, r (dB)	Basis Correlation, $\frac{ \mathcal{R}_{B_1 B_2} }{[\mathcal{P}_{B_1} \mathcal{P}_{B_2}]^{1/2}}$ (dB)
Reference	11.2%	14.2%	6.1	-6.8
Case (i)	11.2%	14.2%	6.1	-9.8
Case (ii)	22.4%	28.4%	6.1	-6.8
Case (iii)	11.2%	14.2%	3.1	-6.8

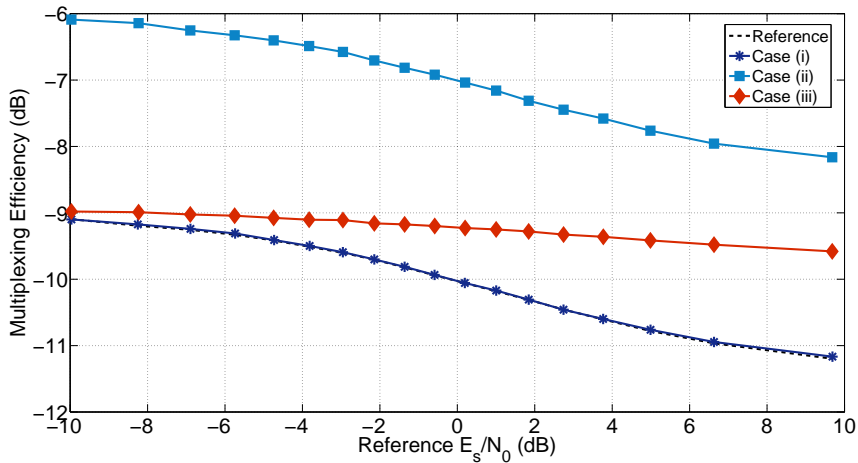


Figure 6.5: Multiplexing efficiency variations versus antenna performance parameters.

¹The multiplexing efficiency measures the loss of efficiency in SNR when using a real multiple-antenna prototype in an i.i.d. channel to achieve the same capacity as that of an ideal array in the same i.i.d. channel [111].

6.3.1 Adaptive Variable Loads

A possible way of decreasing the user effects is to adapt the antenna parameters in real time to the immediate environment, or in a lower complexity to take into account the user's presence in an average way a priori in the antenna design procedure. Since the beam-space MIMO antenna naturally embeds variable reactive loads, this can be realized by selecting the loads in such a way that maximum possible channel capacity in each operating scenario is achieved.

To this aim, we computed the channel capacity for a 2D range of reactive loads $\{Z_I, Z_{II}\} = \{jX_I, jX_{II}\}$ (with a resolution of 10Ω) at the passive ports of the designed three-port radiator under assumptions identical to those above. Fig. 6.6 shows a contour plot of the channel capacity for the 'in hand' scenario where the reactance values of the original and adaptive designs are indicated by '+' and 'x', respectively. Although the optimal reactance values are different from those of the p-i-n diodes, the improvement achieved is negligible. Table 6.3 summarizes changes of the channel capacity for each operating scenario. The use of adaptive reactive loads improves the channel capacity by only less than 4% while extra computational cost and hardware complexity is added to the beam-space MIMO system. This is fully in agreement with the results obtained earlier since adapting reactive loads mainly affects the basis power imbalance ratio and the basis correlation rather than the total efficiency.

6.4 User Effects: a Case Study of QPSK Beam-Space MIMO Antenna

The study carried out in the previous section confirms the suitability of using beam-space MIMO in near-field interaction scenarios under BPSK signaling. However, it cannot immediately be generalized to higher-order modulation schemes, where the external perturbation

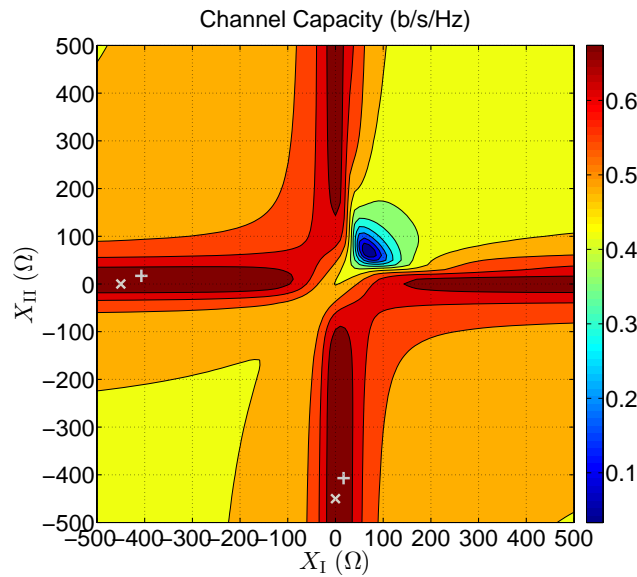


Figure 6.6: Contour map of the channel capacity with respect to X_I and X_{II} for a E_s/N_0 of 0 dB.

6.4. User Effects: a Case Study of QPSK Beam-Space MIMO Antenna

Table 6.3: Load optimization effect on the channel capacity for a E_s/N_0 of 0 dB. MI_0 and MI_{opt} are the channel capacity values when the antenna embeds the p-i-n diodes and the optimal loads, respectively.

Scenario	MI_0 (b/s/Hz)	MI_{opt} (b/s/Hz)	Relative Difference
in hand	0.72	0.74	2.5%
in hand-near head	0.22	0.23	3.8%
near head ($d = 5$ mm)	0.29	0.30	3.1%
near head ($d = 7.5$ mm)	0.40	0.41	2.5%
near head ($d = 10$ mm)	0.51	0.53	2.9%

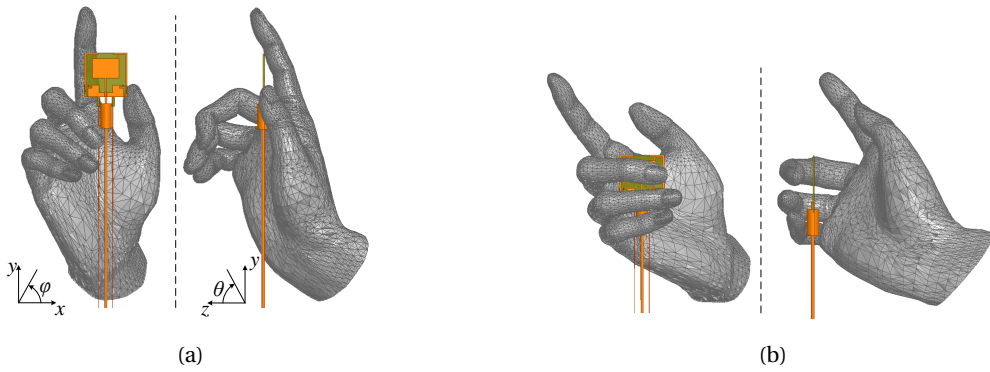


Figure 6.7: The placement of the QPSK beam-space MIMO antenna under study near the SAM hand ($\epsilon_r = 31.0$ and $\sigma = 1.64 \text{ S.m}^{-1}$). SAM phantom is taken from CST MWS [110].

could also cause the third level of effects, namely the deviation of the actual constellation points from their ideal locations when decoding on the assumption of a conventional MIMO system model. In this section, we analyze the performance of the QPSK beam-space MIMO antenna designed in Section 4.3 in the presence a full-sized homogeneous SAM hand phantom in two different scenarios (see Fig. 6.7). The average permittivity and conductivity of all hand tissues were selected according to the materials' properties given in [112].

Table 6.4 summarizes the variations of the antenna characteristics. Obviously, the input impedance and the radiation efficiency are no longer constant over the antenna states. The variations of the return loss are rather negligible as the antenna's active port is still well matched. By contrast, due to the absorption in hand tissues the radiation efficiency is degraded by a significant factor whose value depends on the antenna state.

Table 6.4 also shows that the power imbalance ratio and the correlation of the basis patterns are affected by the presence of the hand. The power imbalance ratio is degraded from 0.8 dB in free space to 2.1 dB and 5.2 dB in hand interaction cases. The basis correlation is also increased to -11.9 dB in the worst case, which is still sufficiently good for MIMO operation. As discussed in the previous section, the impairments of basis power imbalance ratio and basis

Table 6.4: User body effects on the characteristics of the beam-space MIMO antenna.

Scenario	x_r	Return Loss (dB)	Radiation Efficiency	Power Imbalance Ratio (dB)	Basis Correlation (dB)
free space	-1	19.6	75%	0.8	$-\infty$
	+1	19.6	75%		
	+j	19.6	75%		
	-j	19.6	75%		
in hand (Fig. 6.7a)	-1	22.5	42%	2.1	-11.9
	+1	15.7	28%		
	+j	13.8	42%		
	-j	24.2	27%		
in hand (Fig. 6.7b)	-1	12.9	26%	5.2	-19.1
	+1	26.4	22%		
	+j	20.1	24%		
	-j	13.3	20%		

decorrelation show a less pronounced degradation effect on the multiplexing performance of the beam-space MIMO antenna.

For a receiver that assumes the conventional MIMO input-output relation in (5.4), it is important to evaluate the modulation quality of the transmitted signals in the two near-field interaction scenarios. Fig. 6.8 shows the constellation diagram of the signals radiated by the perturbed beam-space MIMO antenna at a given solid angle and compares them with the corresponding points expected from (6.1). While the signal has eight of the actual constellation points precisely at the ideal locations, the other eight (corresponding to the symbols with a ratio of $x_r = \pm j$) are displaced. Fig. 6.9 shows the EVM as a function of the solid angle, calculated using (6.7). It is observed that the modulation quality is drastically degraded in the entire space. The degradation is highly dependent on the solid angle and the perturbation.

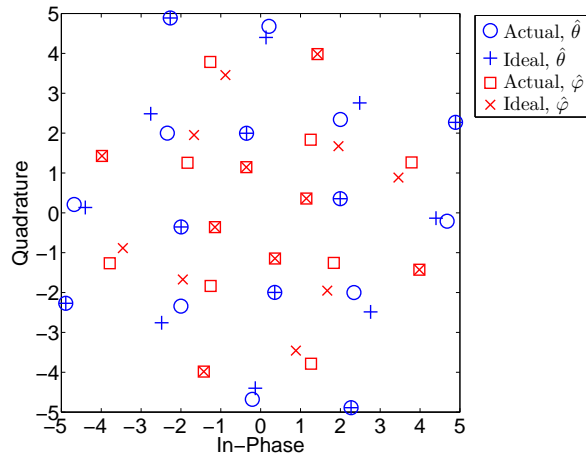


Figure 6.8: Constellation distortion of the transmitted signals at $\{\theta, \varphi\} = \{45^\circ, 294^\circ\}$ when placing the antenna near the hand (Fig. 6.7a).

6.4. User Effects: a Case Study of QPSK Beam-Space MIMO Antenna

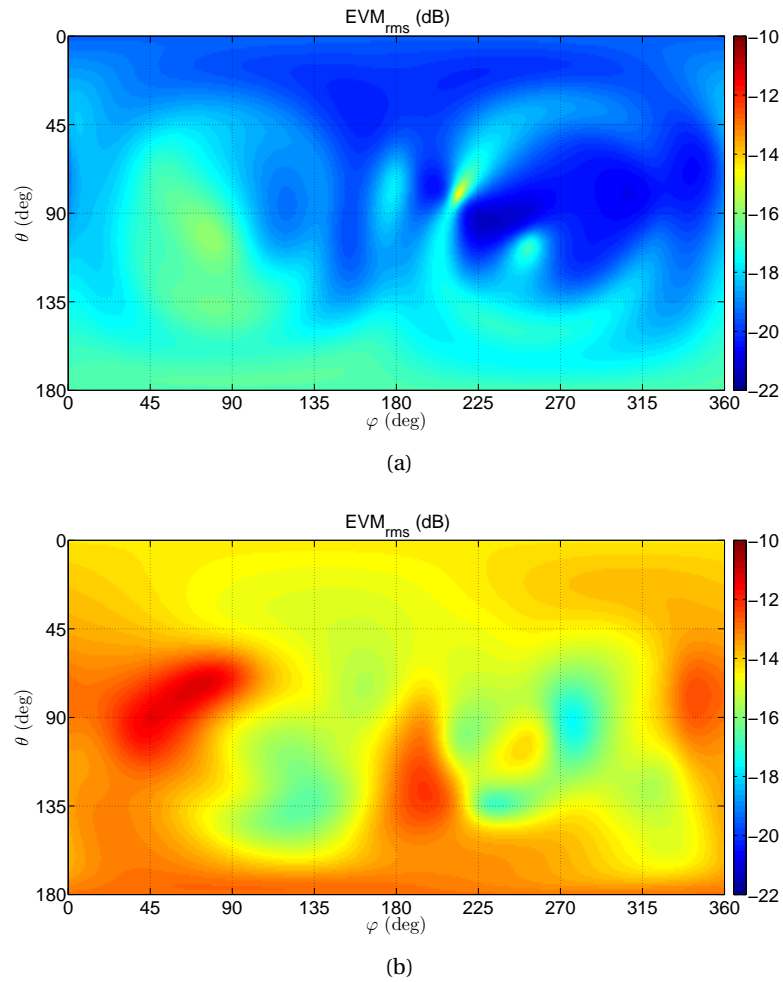


Figure 6.9: EVM of the transmitted signals when placing the antenna near the hand; (a) in the case of Fig. 6.7a, and (b) in the case of Fig. 6.7b.

Assuming a uniform field distribution (e.g., in a rich-scattering environment), the average EVM is -18.5 dB and -14.2 dB in the two scenarios, respectively.

Finally, to investigate the linear MIMO decoder performance under such EVM degradation, the RCE after zero-forcing equalization was calculated for 1.4 million random single-path LOS transmit-receive scenarios (while neglecting the noise component). As an example, Fig. 6.10 shows the perturbed constellation diagrams of the equalized symbols for a given transmit-receive scenario. In both diagrams, there are three possible locations for each symbol: the ideal location when the QPSK beam-space MIMO antenna radiates in State 1 and State 2, and the other two when the antenna functions in State 3 and State 4. The cumulative distribution functions of RCE values over different locations in space are depicted in Fig. 6.11. It can be seen that the error is more pronounced for the second decoded symbol while depending significantly on the geometry of near-field interaction. In noisy channels, such errors may result in increased BER of the beam-space MIMO system.

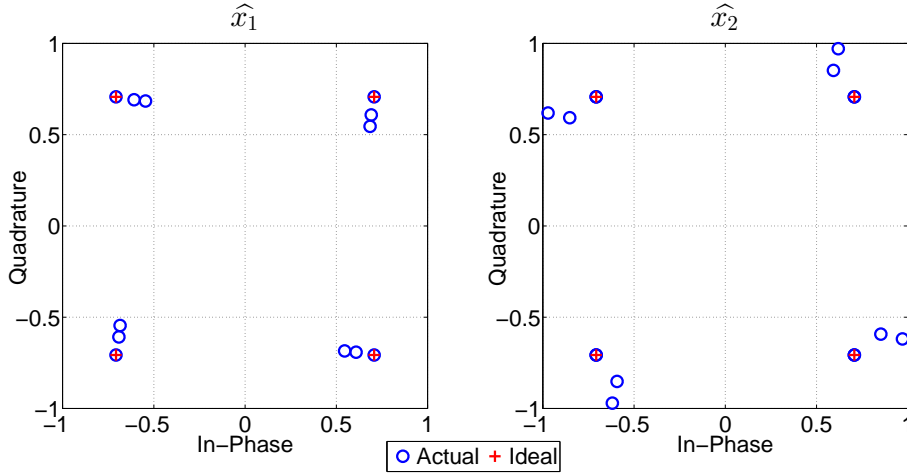


Figure 6.10: Constellation distortion of the received signals for the receiving antennas at $\{\theta_1, \varphi_1, \theta_2, \varphi_2\} = \{45^\circ, 294^\circ, 45^\circ, 298^\circ\}$ when placing the transmitting antenna near the hand (Fig. 6.7a).

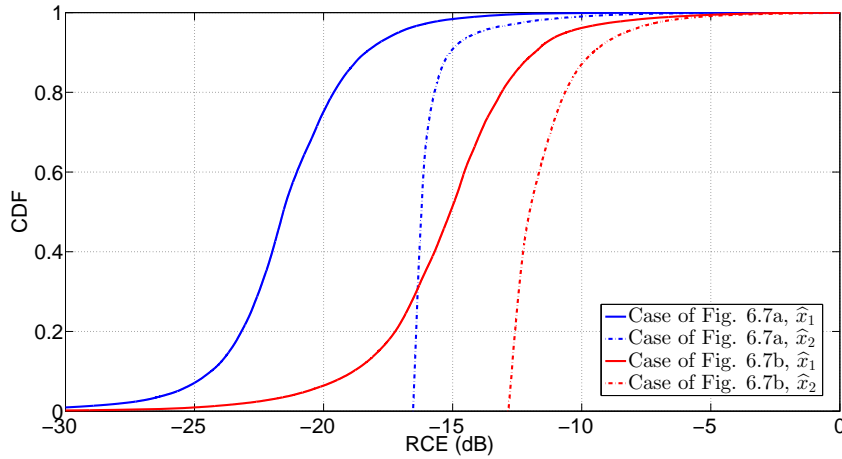


Figure 6.11: CDF plot of the RCE of the received signal for 1.4×10^6 random single-path LOS transmit-receive scenarios while considering two receive antennas with an angular distance of 3° - 5° .

6.5 Conclusion

In this chapter, we presented a first study of beam-space MIMO operation in the presence of external perturbation. In addition to usual effects such as total efficiency reduction, the near-field interaction with a beam-space MIMO antenna deteriorates the orthonormality of the basis patterns and the modulation quality of the transmitted signal. We showed that under BPSK signaling throughput reduction is mainly caused by power dissipation in surrounding objects rather than by variations of the power imbalance ratio and the correlation between the basis patterns. Accordingly, adapting reactive loads of the beam-space MIMO antenna

does not necessarily result in significant performance improvement. Therefore, similar to the case of conventional MIMO antennas, optimizing the geometry of beam-space MIMO antennas could be a possible solution to overcome the low radiation efficiency issue and thereby minimize the effects of the immediate operating environment. For higher-order modulation schemes, it was shown that near-field interaction with the beam-space MIMO antenna causes the actual constellation points to deviate from their ideal locations, thereby increasing the EVM of the transmitted signal. Such degraded modulation quality can then result in incorrect interpretation of the signal at ZF receivers. This emphasizes the importance of reconsidering the decoding approach for beam-space MIMO systems in user interaction applications.

7 Beam-Space MIMO: Out-of-Band Radiation Suppression

*Whosoever formeth an intimacy with the enemies of his friends,
does so to injure the latter.*
— Saadi, Gulistan, Principles of Social Conduct, Admonition 14

7.1 Overview

For implementing the beam-space MIMO concept, it is indispensable to use load-modulated antennas with the capability of symbol-rate pattern reconfiguration. According to the beam-space MIMO objective, the symbol vector to be transmitted at each symbol interval determines the antenna's radiation pattern and consequently the states of the embedded variable loads. Like any other switching system, improper switching of the variable loads at symbol transitions can give rise to bandwidth expansion of the radiated signal in beam-space MIMO. Therefore, even with a pulse shaping filter included in the path of the data stream directly fed to the single RF chain, the beam-space MIMO system may fail to meet required spectral mask constraints.

To provide some insight about this out-of-band radiation phenomenon, spectrum measurements in real propagation conditions were carried out while the BPSK beam-space MIMO antenna developed in Section 3.8 was multiplexing two random BPSK data streams. As shown in Fig. 7.1, when the antenna works in a single state (i.e., the case where no p-i-n diode switching occurs), a clean spectral mask is achieved thanks to the pulse shaping filter employed on the RF path. However, when the states of the p-i-n diodes are changed using high slew rate rectangular pulses, the system suffers from high out-of-band radiation.

Though the out-of-band radiation in beam-space MIMO has barely been mentioned before, it is extremely important for practical applications. In this chapter, we investigate this issue for the first time, and propose a potential solution to reduce the effects of symbol-rate pattern reconfiguration on the bandwidth of transmitted signals. The rest of this chapter is organized as follows. Section 7.2 presents a first study on the operation of beam-space MIMO antennas in the time domain. In Section 7.3, an approach based on shaping the time-domain response

of the embedded variable loads is described. Then, the proposed approach is illustrated by numerical examples and early experimental results.

7.2 Time-Domain Study of Beam-Space MIMO Antennas

Let us recall the single-feed load-modulated antenna solution proposed in Section 4.2 for implementing the beam-space MIMO concept. As depicted in Fig. 7.2, the antenna can be viewed as a combination of two subsystems, namely the three-port radiator and the two variable loads. The radiator is a linear time-invariant (LTI) system. Therefore, as discussed in Section 3.3, it can be fully characterized in the frequency domain by the transfer functions, namely the scattering matrix $\mathcal{S}(f)$ and the embedded radiation patterns $\{\mathcal{F}_p(f, \Omega)\}_{p=0}^2$. According to (3.1), $\mathcal{S}(f)$ describes the relation between the incident power waves $\{a_p(f)\}_{p=0}^2$ and the reflected power waves $\{b_p(f)\}_{p=0}^2$. The embedded radiation patterns are also representations of the

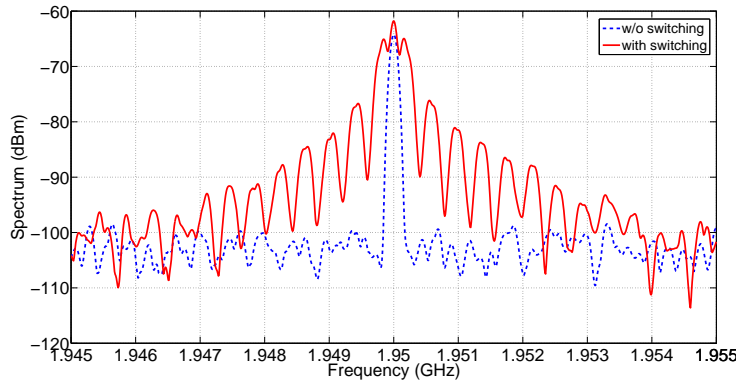


Figure 7.1: Bandwidth expansion caused by abrupt switching of the variable loads (the p-i-n diodes) for the BPSK beam-space MIMO antenna fabricated in Chapter 3. The symbol rate of transmission was 390625 symbols/s. A root-raised cosine pulse shaping filter with a roll-off factor of 0.5 was used on the RF path.

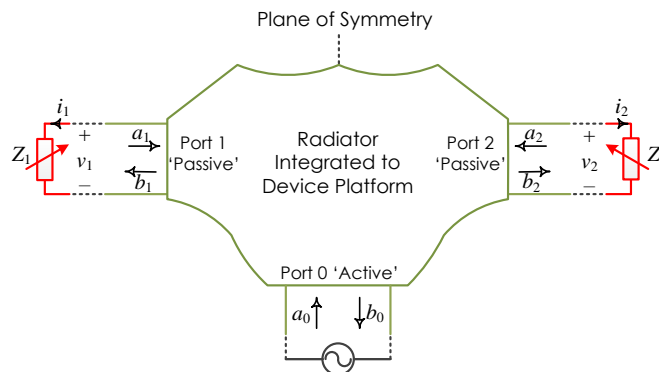


Figure 7.2: Beam-space MIMO antenna presented in Chapter 4 as a combination of time-variant and time-invariant subsystems.

relation between $\{a_p(f)\}_{p=0}^2$ and the total radiated field $\mathcal{E}_\circ(f, \Omega)$ as given in (3.4). According to Fig. 7.2, the power waves at the radiator's passive ports are related to the ordinary voltages $\{v_p(f)\}_{p=1}^2$ and currents $\{i_p(f)\}_{p=1}^2$ as

$$a_p(f) = \frac{v_p(f) - Z_0 i_p(f)}{2|\Re\{Z_0\}|^{1/2}} \quad (7.1a)$$

$$b_p(f) = \frac{v_p(f) + Z_0^* i_p(f)}{2|\Re\{Z_0\}|^{1/2}}, \quad (7.1b)$$

where Z_0 denotes the reference impedance.

In the time domain, the input-output relationship of the radiator is given by

$$\tilde{b}_p(t) = \sum_{q=0}^2 \tilde{S}_{pq}(t) * \tilde{a}_q(t) \quad (7.2)$$

and

$$\tilde{\mathcal{E}}_\circ(t, \Omega) = \sum_{q=0}^2 \tilde{\mathcal{F}}_q(t, \Omega) * \tilde{a}_q(t), \quad (7.3)$$

where $*$ denotes time-domain convolution, and $\tilde{S}_{pq}(t)$ and $\tilde{\mathcal{F}}_q(t, \Omega)$ can be found by the inverse Fourier transform or through rational polynomial fitting from the frequency-domain parameters. If Z_0 is taken as purely real (which is typically the case in practical systems), (7.1) is also valid in the time domain, i.e.,

$$\tilde{a}_p(t) = \frac{\tilde{v}_p(t) - Z_0 \tilde{i}_p(t)}{2Z_0^{1/2}} \quad (7.4a)$$

$$\tilde{b}_p(t) = \frac{\tilde{v}_p(t) + Z_0 \tilde{i}_p(t)}{2Z_0^{1/2}}, \quad (7.4b)$$

or equivalently,

$$\tilde{v}_p(t) = Z_0^{1/2} [\tilde{b}_p(t) + \tilde{a}_p(t)] \quad (7.5a)$$

$$\tilde{i}_p(t) = Z_0^{-1/2} [\tilde{b}_p(t) - \tilde{a}_p(t)]. \quad (7.5b)$$

According to (7.2) and (7.5), at each passive port k there are three equations and four unknowns $\{\tilde{a}_p(t), \tilde{b}_p(t), \tilde{v}_p(t), \tilde{i}_p(t)\}$. The fourth equation is obtained from Kirchhoff's circuit laws for determining the relationship between the voltage and the current for each terminating variable load.

The second subsystem, composed of the variable loads at the passive ports of the radiator, exhibits time-varying voltage-current ratios, and cannot be described by impedance or ad-

mittance in the frequency domain. From the definition of the impulse response of linear time-variant (LTV) systems, the input-output relationship of the variable load at port k can be expressed by the convolution integral

$$\begin{aligned}\tilde{v}_p(t) &= \int \tilde{z}_p(\tau, t) \tilde{i}_p(t - \tau) d\tau \\ &= \int \tilde{z}_p(t - \tau, t) \tilde{i}_p(\tau) d\tau,\end{aligned}\quad (7.6)$$

where $\tilde{z}_p(\tau, t)$ is, here, referred to as the time-domain impedance response. The variable τ denotes the elapsed time, whereas the variable t is the observation time and describes the time-varying nature of the load. Accordingly, a rapidly time-varying load is indicated by fast changes associated with t [113]. Substituting the inverse Fourier transform of $\tilde{i}_p(\tau)$ in (7.6), we obtain

$$\begin{aligned}\tilde{v}_p(t) &= \int \tilde{z}_p(t - \tau, t) \tilde{i}_p(\tau) d\tau \\ &= \int \tilde{z}_p(t - \tau, t) \left(\int i_p(f_1) e^{j2\pi f_1 \tau} df_1 \right) d\tau \\ &= \int \left(\int \tilde{z}_p(t - \tau, t) e^{j2\pi f_1 \tau} d\tau \right) i_p(f_1) df_1 \\ &= \int \left(\int \tilde{z}_p(\tau, t) e^{-j2\pi f_1 \tau} d\tau \right) i_p(f_1) e^{j2\pi f_1 t} df_1 \\ &= \int z_p(f_1, t) i_p(f_1) e^{j2\pi f_1 t} df_1,\end{aligned}\quad (7.7)$$

where

$$z_p(f_1, t) = \int \tilde{z}_p(\tau, t) e^{-j2\pi f_1 \tau} d\tau \quad (7.8)$$

is the Fourier transform of $\tilde{z}_p(\tau, t)$ with respect to τ , and according to (7.7) can be roughly described as the notion of a time-varying impedance function. In other words, the variable load is characterized by a family of impedance functions, with one function for each value of t . Accordingly, the voltage of the variable load in the frequency domain can be obtained as

$$\begin{aligned}v_p(f) &= \int \tilde{v}_p(t) e^{-j2\pi f t} dt \\ &= \int \left(\int z_p(f_1, t) i_p(f_1) e^{j2\pi f_1 t} df_1 \right) e^{-j2\pi f t} dt \\ &= \int \left(\int z_p(f_1, t) e^{-j2\pi(f-f_1)t} dt \right) i_p(f_1) df_1 \\ &= \int z_p(f_1, f - f_1) i_p(f_1) df_1,\end{aligned}\quad (7.9)$$

where

$$z_p(f_1, f_2) = \int z_p(f_1, t) e^{-j2\pi f_2 t} dt = \iint \tilde{z}_p(\tau, t) e^{-j2\pi f_1 \tau} e^{-j2\pi f_2 t} d\tau dt \quad (7.10)$$

is the two-dimensional Fourier transform of $\tilde{Z}_p(\tau, t)$. It is observed from (7.9) that the input-output relationship of the variable load in the frequency domain involves a convolution in the second variable of $Z_p(f_1, f_2)$, showing the effect of the time-varying nature of the variable load in the frequency domain. Therefore, although the variable loads can be regarded as linear subsystems, they can produce out-of-input-band frequencies in their outputs, thereby behaving more like non-linear systems. In other words, the wave reflected from the variable loads at the passive ports possesses a wider frequency spectrum than the incident wave, consequently resulting in out-of-band radiation from the radiator.

7.3 Time-Domain Response Shaping of Variable Loads

One potential solution for reducing the out-of-band radiation of a beam-space MIMO antenna is to control the transient behavior of the pattern reconfiguration process. This can be accomplished by shaping the time-domain response of the embedded variable loads in such a way that the unwanted bandwidth expansion of the waves reflected from the loads is decreased to a level which is sufficiently low not to produce unacceptable out-of-band radiation according to the spectral mask requirement of the considered application.

7.3.1 Theoretical Analysis

Since the carrier frequency f_c of the RF signal is much higher than the symbol rate f_s (i.e., $f_c \gg f_s$), the antenna shows an approximately frequency-flat response within the transmission band. Therefore, the beam-space MIMO objective in the time domain can be given by

$$\tilde{\mathcal{E}}_o(t, \Omega) = \tilde{a}_0(t) [\mathcal{B}_1(f_c, \Omega) + \tilde{x}_r(t)\mathcal{B}_2(f_c, \Omega)], \quad (7.11)$$

where $\tilde{a}_0(t) = \tilde{s}_1(t)$ is the up-converted version of the first data stream $x_1[n]$, and $\tilde{x}_r(t_n) = x_r[n] = x_2[n]/x_1[n]$ for all $t_n = t_0 + n/f_s$ denoting the center of the symbol time slots. For the sake of simplicity, and without loss of generality, let us assume that the excitation to the radiator's active port is a single-frequency complex-valued signal¹, i.e., $\tilde{a}_0(t) = e^{j2\pi f_c t}$. Therefore, (7.11) is updated as

$$\tilde{\mathcal{E}}_o(t, \Omega) = e^{j2\pi f_c t} [\mathcal{B}_1(f_c, \Omega) + \tilde{x}_r(t)\mathcal{B}_2(f_c, \Omega)], \quad (7.12)$$

or equivalently in the frequency domain as

$$\begin{aligned} \mathcal{E}_o(f, \Omega) &= \delta(f - f_c) * [\mathcal{B}_1(f_c, \Omega)\delta(f) + \mathcal{B}_2(f_c, \Omega)x_r(f)] \\ &= \mathcal{B}_1(f_c, \Omega)\delta(f - f_c) + \mathcal{B}_2(f_c, \Omega)x_r(f - f_c), \end{aligned} \quad (7.13)$$

where $x_r(f)$ is the Fourier transform of the combination ratio signal $\tilde{x}_r(t)$. This shows how the transient behavior of the reconfigurable antenna affects the spectrum of the radiated signal.

¹This is equivalent to having a constant $x_1[n]$ for all n .

In particular, out-of-band radiation is directly controlled by the bandwidth of the combination ratio signal $\tilde{x}_r(t)$. The next step is to find the relationship between $\tilde{x}_r(t)$ and the time-domain responses of the variable loads.

Substituting (4.10) into (7.12), the time-domain radiation pattern can be written in terms of the embedded radiation patterns, i.e.,

$$\begin{aligned} \tilde{\mathcal{E}}_\circ(t, \Omega) = & e^{j2\pi f_c t} \mathcal{F}_0(f_c, \Omega) + e^{j2\pi f_c t} \left(a_{\mathcal{B}_1}^{\{Z_1, Z_{II}\}} + a_{\mathcal{B}_2}^{\{Z_1, Z_{II}\}} \tilde{x}_r(t) \right) \mathcal{F}_1(f_c, \Omega) \\ & + e^{j2\pi f_c t} \left(a_{\mathcal{B}_1}^{\{Z_1, Z_{II}\}} - a_{\mathcal{B}_2}^{\{Z_1, Z_{II}\}} \tilde{x}_r(t) \right) \mathcal{F}_2(f_c, \Omega), \end{aligned} \quad (7.14)$$

while according to (7.3) the unknowns $\tilde{a}_1(t)$ and $\tilde{a}_2(t)$ must satisfy

$$\tilde{\mathcal{E}}_\circ(t, \Omega) = e^{j2\pi f_c t} * \tilde{\mathcal{F}}_0(t, \Omega) + \tilde{a}_1(t) * \tilde{\mathcal{F}}_1(t, \Omega) + \tilde{a}_2(t) * \tilde{\mathcal{F}}_2(t, \Omega). \quad (7.15)$$

Taking the Fourier transforms of (7.14) and (7.15) gives

$$\begin{aligned} \mathcal{E}_\circ(f, \Omega) = & \mathcal{F}_0(f_c, \Omega) \delta(f - f_c) + \mathcal{F}_1(f_c, \Omega) \left(a_{\mathcal{B}_1}^{\{Z_1, Z_{II}\}} \delta(f - f_c) + a_{\mathcal{B}_2}^{\{Z_1, Z_{II}\}} x_r(f - f_c) \right) \\ & + \mathcal{F}_2(f_c, \Omega) \left(a_{\mathcal{B}_1}^{\{Z_1, Z_{II}\}} \delta(f - f_c) - a_{\mathcal{B}_2}^{\{Z_1, Z_{II}\}} x_r(f - f_c) \right), \end{aligned} \quad (7.16)$$

and

$$\mathcal{E}_\circ(f, \Omega) = \mathcal{F}_0(f_c, \Omega) \delta(f - f_c) + a_1(f) \mathcal{F}_1(f, \Omega) + a_2(f) \mathcal{F}_2(f, \Omega), \quad (7.17)$$

respectively. Comparing (7.16) and (7.17), we then have

$$a_1(f) \mathcal{F}_1(f, \Omega) = \mathcal{F}_1(f_c, \Omega) \left[a_{\mathcal{B}_1}^{\{Z_1, Z_{II}\}} \delta(f - f_c) + a_{\mathcal{B}_2}^{\{Z_1, Z_{II}\}} x_r(f - f_c) \right] \quad (7.18a)$$

$$a_2(f) \mathcal{F}_2(f, \Omega) = \mathcal{F}_2(f_c, \Omega) \left[a_{\mathcal{B}_1}^{\{Z_1, Z_{II}\}} \delta(f - f_c) - a_{\mathcal{B}_2}^{\{Z_1, Z_{II}\}} x_r(f - f_c) \right]. \quad (7.18b)$$

Let us recall that the symbol rate is much lower than the carrier frequency and the embedded radiation patterns are typically slowly frequency-varying, i.e.,

$$\mathcal{F}_p(f, \Omega) \simeq \mathcal{F}_p(f_c, \Omega) \quad \left| 1 - \frac{f}{f_c} \right| \leq \epsilon. \quad (7.19)$$

Therefore, (7.18) can be simplified as

$$a_1(f) \simeq a_{\mathcal{B}_1}^{\{Z_1, Z_{II}\}} \delta(f - f_c) + a_{\mathcal{B}_2}^{\{Z_1, Z_{II}\}} x_r(f - f_c) \quad (7.20a)$$

$$a_2(f) \simeq a_{\mathcal{B}_1}^{\{Z_1, Z_{II}\}} \delta(f - f_c) - a_{\mathcal{B}_2}^{\{Z_1, Z_{II}\}} x_r(f - f_c), \quad (7.20b)$$

or equivalently in the time domain,

$$\tilde{a}_1(t) \simeq e^{j2\pi f_c t} \left[a_{\mathcal{B}_1}^{\{Z_1, Z_{II}\}} + a_{\mathcal{B}_2}^{\{Z_1, Z_{II}\}} \tilde{x}_r(t) \right] \quad (7.21a)$$

7.3. Time-Domain Response Shaping of Variable Loads

$$\tilde{a}_2(t) \simeq e^{j2\pi f_c t} \left[a_{B_1}^{\{Z_I, Z_{II}\}} - a_{B_2}^{\{Z_I, Z_{II}\}} \tilde{x}_r(t) \right]. \quad (7.21b)$$

Drawing attention to the fact that the S-parameters are slowly varying in the frequency domain within the bandwidth of the incident power waves,

$$\mathbf{S}(f) \simeq \mathbf{S}(f_c) \quad \left| 1 - \frac{f}{f_c} \right| \leq \epsilon, \quad (7.22)$$

the reflected power waves can be calculated using (7.2) as

$$\begin{aligned} \tilde{b}_0(t) \simeq e^{j2\pi f_c t} & \left[S_{00}(f_c) + S_{01}(f_c) \left(a_{B_1}^{\{Z_I, Z_{II}\}} + a_{B_2}^{\{Z_I, Z_{II}\}} \tilde{x}_r(t) \right) \right. \\ & \left. + S_{02}(f_c) \left(a_{B_1}^{\{Z_I, Z_{II}\}} - a_{B_2}^{\{Z_I, Z_{II}\}} \tilde{x}_r(t) \right) \right] \end{aligned} \quad (7.23a)$$

$$\begin{aligned} \tilde{b}_1(t) \simeq e^{j2\pi f_c t} & \left[S_{10}(f_c) + S_{11}(f_c) \left(a_{B_1}^{\{Z_I, Z_{II}\}} + a_{B_2}^{\{Z_I, Z_{II}\}} \tilde{x}_r(t) \right) \right. \\ & \left. + S_{12}(f_c) \left(a_{B_1}^{\{Z_I, Z_{II}\}} - a_{B_2}^{\{Z_I, Z_{II}\}} \tilde{x}_r(t) \right) \right] \end{aligned} \quad (7.23b)$$

$$\begin{aligned} \tilde{b}_2(t) \simeq e^{j2\pi f_c t} & \left[S_{20}(f_c) + S_{21}(f_c) \left(a_{B_1}^{\{Z_I, Z_{II}\}} + a_{B_2}^{\{Z_I, Z_{II}\}} \tilde{x}_r(t) \right) \right. \\ & \left. + S_{22}(f_c) \left(a_{B_1}^{\{Z_I, Z_{II}\}} - a_{B_2}^{\{Z_I, Z_{II}\}} \tilde{x}_r(t) \right) \right]. \end{aligned} \quad (7.23c)$$

Substituting (7.21) and (7.23) in (7.5), the expressions for the voltage and current at the passive ports are obtained as multiplication of slowly time-varying and rapidly time-varying factors, i.e.,

$$\tilde{v}_p(t) = \tilde{v}_{p,\text{stv}}(t) e^{j2\pi f_c t} \quad (7.24a)$$

$$\tilde{i}_p(t) = \tilde{i}_{p,\text{stv}}(t) e^{j2\pi f_c t}, \quad (7.24b)$$

where

$$\begin{aligned} \tilde{v}_{1,\text{stv}}(t) \simeq Z_0^{1/2} & \left[S_{10}(f_c) + (S_{11}(f_c) + 1) \left(a_{B_1}^{\{Z_I, Z_{II}\}} + a_{B_2}^{\{Z_I, Z_{II}\}} \tilde{x}_r(t) \right) \right. \\ & \left. + S_{12}(f_c) \left(a_{B_1}^{\{Z_I, Z_{II}\}} - a_{B_2}^{\{Z_I, Z_{II}\}} \tilde{x}_r(t) \right) \right] \end{aligned} \quad (7.25a)$$

$$\begin{aligned} \tilde{i}_{1,\text{stv}}(t) \simeq Z_0^{-1/2} & \left[S_{10}(f_c) + (S_{11}(f_c) - 1) \left(a_{B_1}^{\{Z_I, Z_{II}\}} + a_{B_2}^{\{Z_I, Z_{II}\}} \tilde{x}_r(t) \right) \right. \\ & \left. + S_{12}(f_c) \left(a_{B_1}^{\{Z_I, Z_{II}\}} - a_{B_2}^{\{Z_I, Z_{II}\}} \tilde{x}_r(t) \right) \right] \end{aligned} \quad (7.25b)$$

$$\begin{aligned} \tilde{v}_{2,\text{stv}}(t) \simeq Z_0^{1/2} & \left[S_{20}(f_c) + S_{21}(f_c) \left(a_{B_1}^{\{Z_I, Z_{II}\}} + a_{B_2}^{\{Z_I, Z_{II}\}} \tilde{x}_r(t) \right) \right. \\ & \left. + (S_{22}(f_c) + 1) \left(a_{B_1}^{\{Z_I, Z_{II}\}} - a_{B_2}^{\{Z_I, Z_{II}\}} \tilde{x}_r(t) \right) \right] \end{aligned} \quad (7.25c)$$

$$\tilde{i}_{2,\text{stv}}(t) \simeq Z_0^{-1/2} \left[S_{20}(f_c) + S_{21}(f_c) \left(a_{B_1}^{\{Z_I, Z_{II}\}} + a_{B_2}^{\{Z_I, Z_{II}\}} \tilde{x}_r(t) \right) \right]$$

$$+ (S_{22}(f_c) - 1) \left(a_{\mathcal{B}_1}^{\{Z_1, Z_{11}\}} - a_{\mathcal{B}_2}^{\{Z_1, Z_{11}\}} \tilde{x}_r(t) \right) \Big] . \quad (7.25d)$$

Obviously, the embedded variable loads must follow the obtained voltage-current relationships. This can be reached by properly adjusting the time-domain responses of the time-varying control components inside the variable loads' circuits. Let us assume that series time-variant RC circuits are used as the variable loads,

$$\frac{d}{dt} [C_p(t) \tilde{v}_p(t) - R_p(t) C_p(t) \tilde{i}_p(t)] = \tilde{i}_p(t), \quad (7.26)$$

where $R_p(t)$ and $C_p(t)$ are the corresponding time-varying resistance and capacitance at the passive port p , respectively. Substituting (7.24) in (7.26), we obtain

$$\begin{aligned} j2\pi f_c [C_p(t) \tilde{v}_{p,\text{stv}}(t) - R_p(t) C_p(t) \tilde{i}_{p,\text{stv}}(t)] \\ + \frac{d}{dt} [C_p(t) \tilde{v}_{p,\text{stv}}(t) - R_p(t) C_p(t) \tilde{i}_{p,\text{stv}}(t)] = \tilde{i}_{p,\text{stv}}(t), \end{aligned} \quad (7.27)$$

or equivalently in the frequency domain,

$$j2\pi f_c \left(1 + \frac{f}{f_c} \right) \mathcal{F} \{ C_p(t) \tilde{v}_{p,\text{stv}}(t) - R_p(t) C_p(t) \tilde{i}_{p,\text{stv}}(t) \} = \mathcal{F} \{ \tilde{i}_{p,\text{stv}}(t) \}, \quad (7.28)$$

where \mathcal{F} denotes the Fourier transform operator. Since all the time-domain functions in (7.28) are slowly varying, the expression can be approximated as

$$j2\pi f_c \mathcal{F} \{ C_p(t) \tilde{v}_{p,\text{stv}}(t) - R_p(t) C_p(t) \tilde{i}_{p,\text{stv}}(t) \} \simeq \mathcal{F} \{ \tilde{i}_{p,\text{stv}}(t) \}. \quad (7.29)$$

Taking the inverse Fourier transform gives

$$j2\pi f_c [C_p(t) \tilde{v}_{p,\text{stv}}(t) - R_p(t) C_p(t) \tilde{i}_{p,\text{stv}}(t)] \simeq \tilde{i}_{p,\text{stv}}(t). \quad (7.30)$$

After some mathematical manipulation, we obtain

$$\tilde{v}_{p,\text{stv}}(t) \simeq \tilde{i}_{p,\text{stv}}(t) \left[R_p(t) + \frac{1}{j2\pi f_c C_p(t)} \right] = \tilde{i}_{p,\text{stv}}(t) [R_p(t) + jX_p(t)]. \quad (7.31)$$

Using (7.31) and (7.25), one can thus calculate the time-varying RC elements required for a desired time-domain response of the radiated field. A similar approach can be followed for other circuit configurations.

7.3.2 Numerical Results

In this section, we illustrate the proposed approach by applying it to the three-port radiator designed in Section 4.3 for QPSK signaling. As given in Table 4.1, there are four distinct values of the symbol combination ratio, i.e., $x_r[n] = \{-1, +1, +j, -j\}$. Let us consider the following three pulse shaping schemes.

7.3. Time-Domain Response Shaping of Variable Loads

- *Rectangular pulse shaping*: The time-domain symbol combination ratio signal is given by

$$\tilde{x}_r(t) = \sum_n x_r[n] \text{rect}\left(\frac{t - nT_s}{T_s}\right), \quad (7.32)$$

where $T_s = 1/f_s$ denotes the symbol period. As shown in Fig. 7.3, this pulse shaping scheme causes abrupt change of the antenna state at symbol transitions. Fig. 7.4 shows that $\tilde{x}_r(t)$, as expected, occupies a large bandwidth due to its sinc-shaped spectrum. Fig. 7.5 depicts the corresponding time-domain response of the reactive part for each variable load, obtained using (7.31). It is observed that the reactance values remain constant during the symbol period before abruptly changing at symbol transitions.

- *Raised-cosine pulse shaping*: The time-domain symbol combination ratio signal becomes

$$\tilde{x}_r(t) = \sum_n x_r[n] \text{sinc}\left(\frac{t - nT_s}{T_s}\right) \frac{\cos\left(\pi\beta \frac{t - nT_s}{T_s}\right)}{1 - 4\beta^2 \frac{(t - nT_s)^2}{T_s^2}}, \quad (7.33)$$

where β is the roll-off factor. Fig. 7.3 shows that the in-phase and quadrature components of $\tilde{x}_r(t)$ are smoothly varying over time. Therefore, a clean spectrum is obtained as depicted in Fig. 7.4. However, as the raised-cosine pulse shaping does not keep the magnitude of $\tilde{x}_r(t)$ constant, the condition of purely reactive loads (i.e., $|\tilde{x}_r(t)| = 1$, see Section 4.2.5 for further information) cannot be met and the resistive part of the variable loads becomes non-negligible and time-varying (see Fig. 7.6).

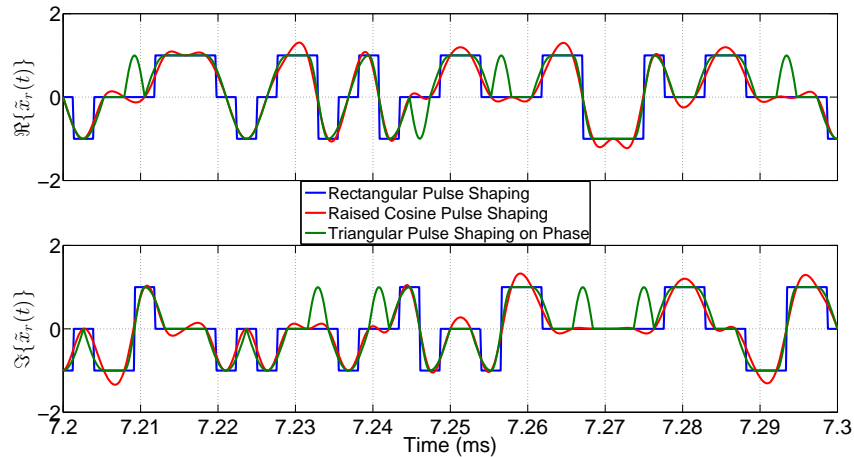


Figure 7.3: In-phase (top) and quadrature (bottom) components of the symbol combination ratio signal for different pulse shaping schemes. The symbol rate, f_s , is 380 ksymbols/s. For the raised-cosine scheme, $\beta = 0.5$.

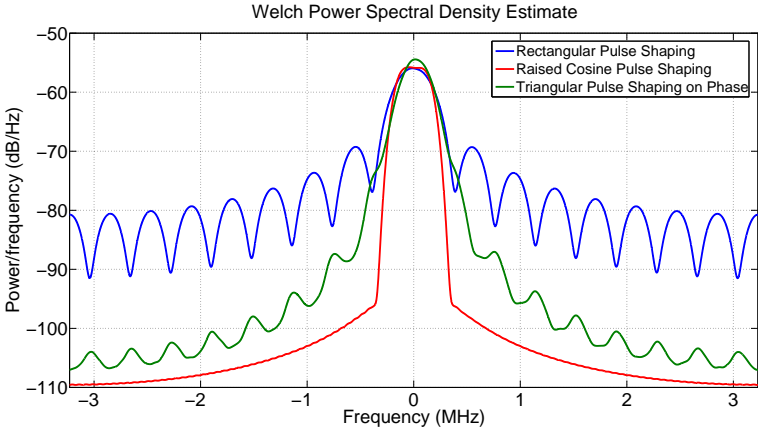


Figure 7.4: Power spectral density of the symbol combination ratio signal using Welch method for different pulse shaping schemes.

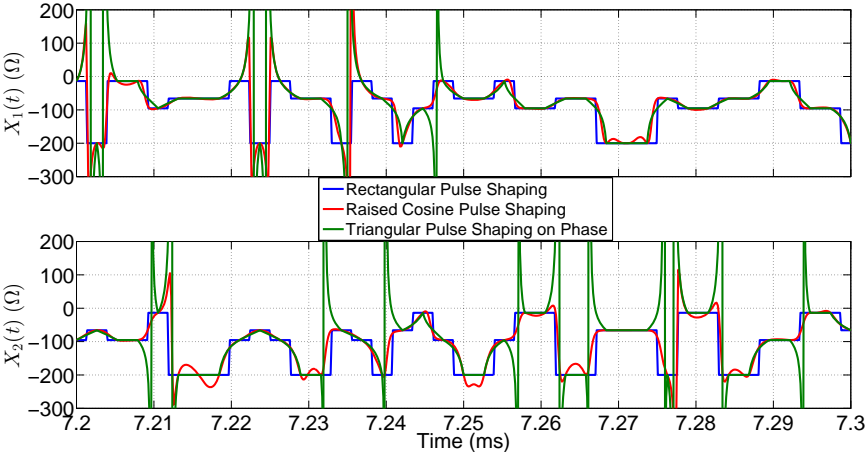


Figure 7.5: Time-domain response of the loads' reactive parts for different pulse shaping schemes.

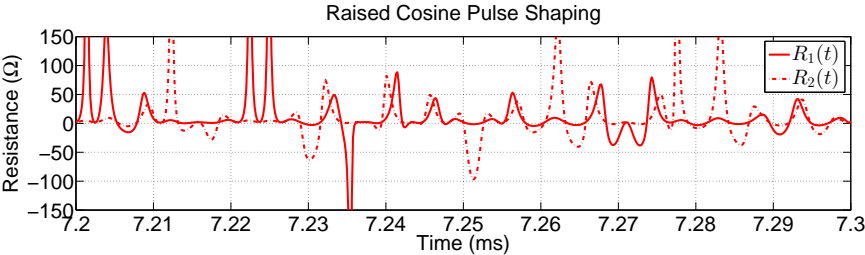


Figure 7.6: Time-domain response of the loads' resistive parts for the raised-cosine pulse shaping scheme.

7.3. Time-Domain Response Shaping of Variable Loads

- *Triangular pulse shaping on phase:* To hold the condition of purely reactive loads, the pulse shaping can be applied on the phase of $\tilde{x}_r(t)$. For instance, by linearly changing the phase over time, we obtain

$$\tilde{x}_r(t) = \exp\left(j \sum_n \angle x_r[n] \Lambda\left(\frac{t - nT_s}{T_s}\right)\right), \quad (7.34)$$

where $\Lambda(\cdot)$ denotes the triangular function. The in-phase and quadrature components of $\tilde{x}_r(t)$ are shown in Fig. 7.3. Transitions between the antenna states are often smooth and similar to those from the raised-cosine pulse shaping scheme. This can be also demonstrated by the power spectral density of $\tilde{x}_r(t)$ shown in Fig. 7.4, where the bandwidth expansion is significantly decreased compared to the rectangular pulse shaping scheme. The required time-domain response of the reactive part for each variable load is shown in Fig. 7.5.

We used the obtained time-domain responses of the variable loads, and calculated the power spectral density of the radiated signal using the mathematical derivations in Section 7.3.1. As shown in Fig. 7.7, a satisfactory reduction of out-of-band radiation is achievable by employing the proposed pulse shaping on phase. We also found out that the effect of clipping the reactance values at $\pm 500 \Omega$ on the bandwidth expansion of the radiated signal is negligible. As shown in Fig. 7.8a, the level of out-of-band radiation is not satisfactory when using only the reactive part solutions of the raised-cosine pulse shaping scheme and ignoring its time-varying resistance values.

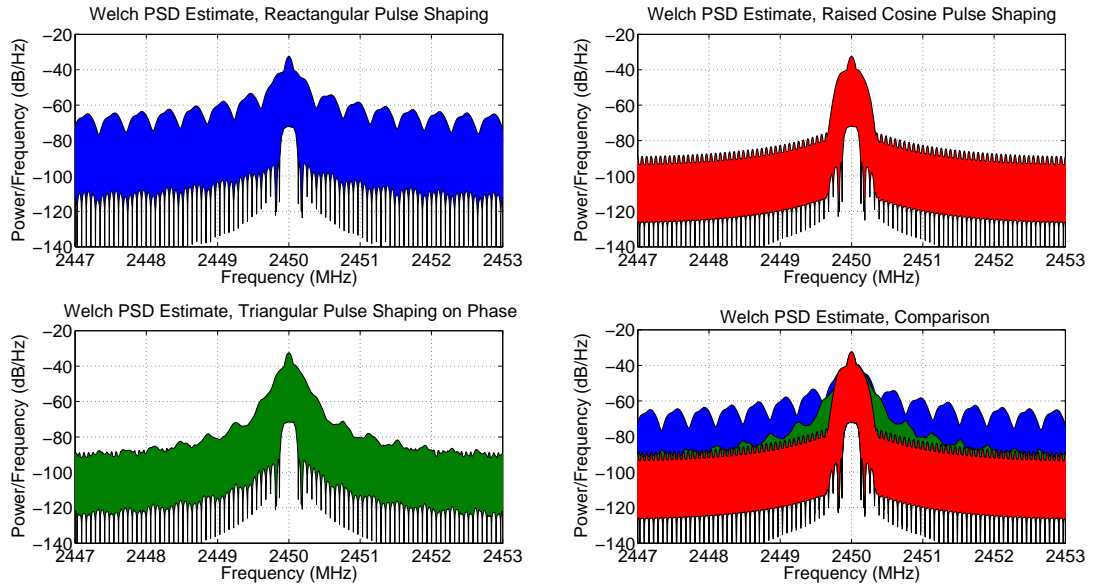


Figure 7.7: Power spectral density of the radiated signal for different pulse shaping schemes, calculated at 1000 random solid angles for both polarizations.

The pulse shaping can be also directly applied to the reactance values of the variable loads. Fig. 7.8b shows that the bandwidth expansion is decreased simply by linearly changing the reactance values over time. However, as the reactance values no longer satisfy (4.25), the reflected wave from the active port, $\tilde{b}_0(t)$, changes over time as shown in Fig. 7.9.

7.3.3 Practical Implementation and Preliminary Experiments

In the previous section, we showed that the out-of-band radiation in beam-space MIMO can be suppressed to an acceptable level by shaping the time-domain responses of the embedded variable loads. In practice, this can be achieved by carefully controlling the activation (control) waveforms of the variable loads, for instance by means of introducing a pre-distortion filter in the load control unit. However, such a task might be faced with a number of challenges. To properly shape the time-domain response of a variable load, knowing the dynamic relationship between the load's impedance value and its actuation waveform is required. Obviously, in scenarios where the symbol duration time is much longer than the load's switching transient times, it is not unreasonable to assume that the impedance is instantaneously determined by the actuation waveform, and thus to use the static impedance values obtained

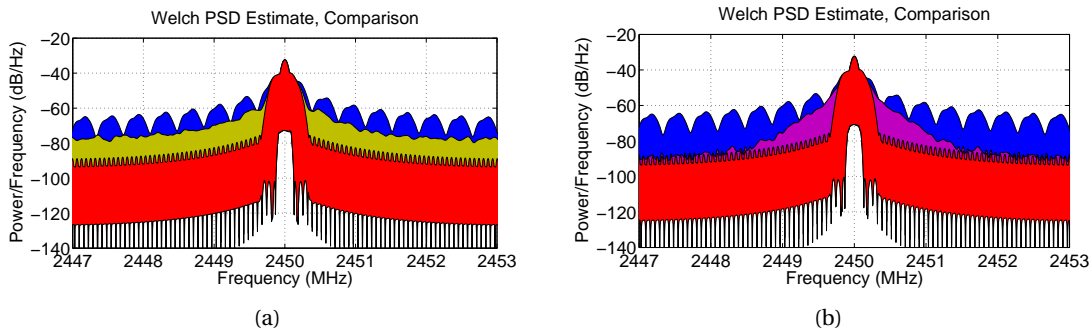


Figure 7.8: (a) Power spectral density of the radiated signal when using only the reactive part solutions of the raised-cosine pulse shaping scheme. (b) Power spectral density of the radiated signal when changing the reactances linearly over time. The blue and red densities are taken from Fig. 7.7 for comparison.

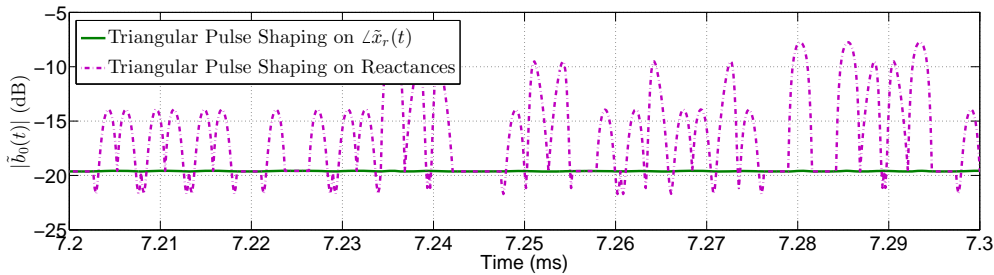


Figure 7.9: Time-varying $\tilde{b}_0(t)$ when directly shaping the reactance values over time.

from measurements in steady state circumstances.

The pre-distortion filter can be realized at least in two different ways. In a first approach, mathematical operations for shaping the activation waveform are carried out on the sampled control signals in the baseband load control unit. Another approach consists in using a simple analogue circuit (for example, a low-pass filter) in the path of the control waveform. Since the QPSK beam-space MIMO antenna embeds varactor diodes with smooth voltage-reactance behavior, a simple low-pass RC filter is sufficient to reduce the bandwidth expansion of the transmitted signals to an acceptable level. Fig. 7.10 shows the effect of the activation waveform shaping using a RC analogue filter. It is worth emphasizing that the bandwidth expansion effects can be further reduced by the use of proper digital pre-distortion filters as discussed in Section 7.3.2. On the other hand, for the BPSK beam-space MIMO antenna developed in Section 3.8, a well-controlled activation waveform is required due to employing p-i-n diodes with non-linear reactance-voltage relationships as the variable loads. Therefore, the use of a digital pre-distortion filter is more practical. As shown in Fig. 7.11, an initial design of the pre-distortion filter dramatically decreases the out-of-band radiation during the antenna operation. Fig. 7.12 depicts how the transient behavior of the actuation current and voltage waveforms are altered by introducing the pre-distortion filter.

7.4 Conclusion

In this chapter, we focused on the issue of the out-of-band radiation associated with transient behavior of the variable loads embedded in beam-space MIMO antennas. We first presented the analytical expressions of a beam-space MIMO antenna in the time domain by viewing it as a combination of time-invariant and time-variant subsystems. An effective approach for reducing the bandwidth expansion effect below a target level was proposed. The key idea of the proposed approach lies in employing more advanced control circuitry for shaping

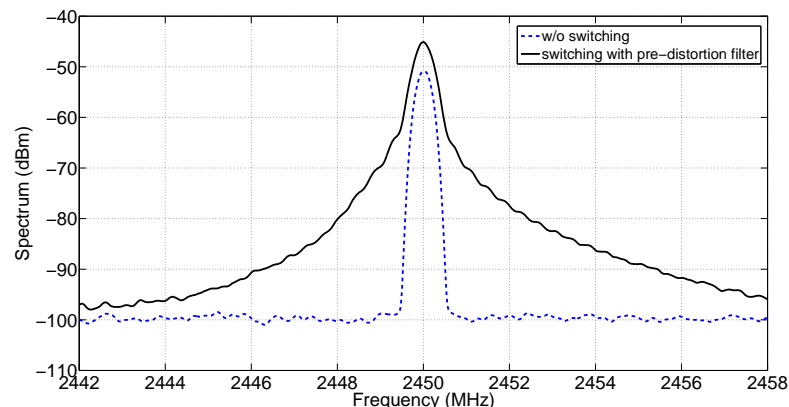


Figure 7.10: Effect of analogue pre-distortion filter on the out-of-band radiation from the QPSK beam-space MIMO antenna. The symbol rate of transmission was 390625 symbols/s.

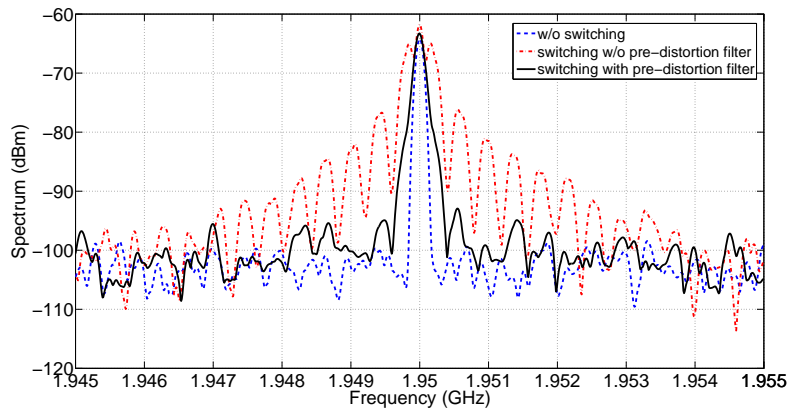


Figure 7.11: Effect of pre-distortion filter on out-of-band radiation from the BPSK beam-space MIMO antenna. The symbol rate of transmission was 390625 symbols/s.

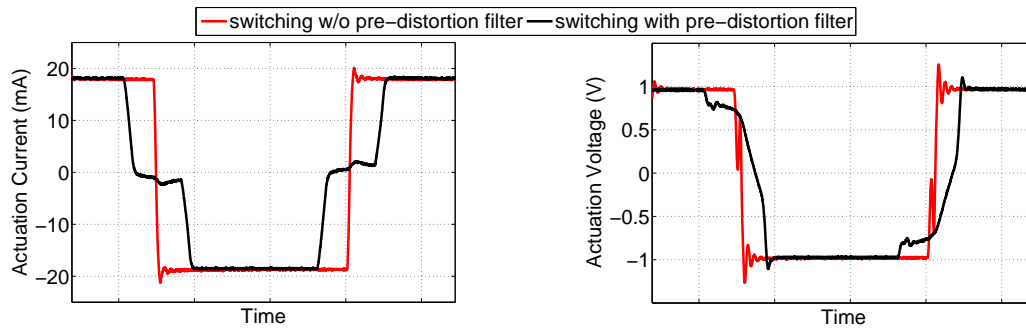


Figure 7.12: Shaping the actuation waveform using a digital pre-distortion filter for the BPSK beam-space MIMO antenna.

the time-domain response of the variable loads. Our numerical and experimental results confirmed the effectiveness and validity of the proposed approach.

8 Conclusions and Perspectives

Every one thinks his own intellect perfect, and his own child handsome.
— Saadi, Gulistan, Principles of Social Conduct, Maxim 31

The beam-space MIMO concept has emerged as a promising alternative to conventional MIMO, but with much simpler and more compact hardware. Its great advantage is that true MIMO transmission can be emulated by using a single RF chain and a reconfigurable antenna structure. This paves the way to exploit the MIMO benefits such as spectral efficiency enhancement in low-end user terminals and sensor nodes with strict complexity and size constraints.

Towards actual design and implementation of operating antennas for beam-space MIMO, there exist a variety of practical issues that have been overlooked in early theoretical and conceptual developments. This concerns different aspects such as the possibility of making built-in antenna designs which are compatible with small platforms, the difficulty in emulating high-order constellations for high spectral efficiency, the influence of near-field perturbation on the system performance, and the bandwidth expansion associated with transient behavior of the embedded controllable elements. In this context, this thesis lies at the crossroad of pure antenna/RF engineering concepts and radio coding techniques, with the aim to close some gaps between antenna engineering and communication theory for beam-space MIMO by exploring and addressing several key practical issues. In the following, the presented research work and the main contributions of the thesis are summarized, and conclusions along with an outlook on future work are provided.

Chapter 3: In this chapter, various modeling and design issues for implementing realistic beam-space MIMO antennas were discussed. Targeting integration in small portable platforms, single-radiator load-modulated antennas were proposed as alternatives to traditional switched parasitic arrays composed of physically-separate radiators. Moreover, it was proposed to employ the controllable elements such as varactor diodes directly as the variable loads in the design of load-modulated antennas. This minimizes effects of the circuit parasitics and avoids

the cumbersome design of complex reconfigurable load structures. It was shown how the pattern decomposition algorithm strongly affects the design procedure and functionality of beam-space MIMO antennas. The mirror image pattern pair approach for the basis definition was selected as it allows to fulfill the condition of purely reactive loads. In this context, a future research line would be to increase the dimensionality of the beam-space domain, for instance by employing radiators with two perpendicular mirror planes. Particular emphasis was also put on considerations related to the modeling of the variable loads. A practical approach for modeling reconfigurable lumped components in commercial full-wave solvers was presented, which ensures excellent agreement between simulation and measurement results. For clarity, all above-mentioned aspects were illustrated by a concrete example, namely, the first compact beam-space MIMO antenna for single-radio multiplexing of BPSK signals. Finally, a preliminary study on the possibility of including frequency reconfiguration in the beam-space MIMO antenna design was presented. The study promotes the convergence of MIMO and dynamic spectrum allocation via reduced-complexity hardware. A future work could address the actual implementation and testing of a frequency-flexible beam-space MIMO antenna system.

Chapter 4: A general framework for expressing the spatial multiplexing relation of the transmitted signals in beam-space MIMO only from the radiator's S-parameters and the impedance values of the modulating loads was introduced. This provides an effective strategy for spatially multiplexing PSK signals of any modulation order. The proposed approach employs only reactive reconfigurable loads, and ensures a constant impedance matching for all symbol combinations, thus overcoming stringent limitations of previous single-feed MIMO techniques in terms of complexity, efficiency and power consumption. The presented approach was illustrated by the design and measurements of a realistic compact antenna system optimized for multiplexing QPSK signals. Important directions for further research is to provide the necessary flexibility for supporting higher-order QAM signaling (e.g., 16-QAM or 64-QAM) and a larger number of multiplexed streams. Accordingly, the use of novel loading architectures such as digitally tunable capacitors or high-speed RF MEMS capacitance banks could be investigated to extend the capability of load-modulated antennas. The design and implementation of antennas for closed-loop channel-aware beam-space MIMO systems represents another interesting, yet challenging task for future work.

Chapter 5: An open-loop real-time beam-space MIMO testbed was constructed, and the first successful demonstration of single-radio single-antenna MIMO transmission under QPSK signaling was carried out. Afterwards, a measurement campaign was conducted to compare the performance of beam-space MIMO systems with their conventional counterparts in real LOS and NLOS indoor environments. Based on the results obtained from the considered scenarios, beam-space MIMO is not more vulnerable to the channel effects than conventional MIMO, and performs very well particularly in NLOS propagation environments. However, as expected from the fact that the basis patterns in beam-space MIMO are not omni-directional and similarly-polarized, it was shown that the beam-space MIMO system performance in the LOS scenario depends on the orientation of transmit and receive antennas. The constructed

real-time beam-space MIMO testbed can be utilized for a broad range of future research possibilities. The current measurement campaign can be extended by considering different indoor and outdoor environments. Another future work might concern the performance analysis of different receiver algorithms for beam-space MIMO. It will be also very informative to compare the performance of beam-space MIMO with other single-radio MIMO techniques such as spatial modulation [16].

Chapter 6: Beam-space MIMO operation in the presence of near-field perturbation was studied for the first time. It was shown that the near-field interaction with antennas degrades the orthonormality of the basis patterns in beam-space MIMO. However, the contribution of the orthonormality impairment to the total performance degradation is not as significant as the effect of power dissipation in lossy surrounding objects. Furthermore, the influence of near-field perturbation on the modulation quality of transmitted signals was studied. It was shown that in the case of higher order modulation formats the assumption of the conventional MIMO input-output relation and the use of ZF receiver may lead to BER performance degradation. In this context, future research should be directed to develop efficient algorithms to mitigate the impact of modulation impairments at a maximum-likelihood receiver.

Chapter 7: The out-of-band radiation phenomenon related to transient behavior of the embedded variable loads in beam-space MIMO antennas was discussed. To overcome this issue, a solution based on time-domain response shaping of the variable loads was proposed, and was partially demonstrated in early experiments. Future work should focus on the design and realization of pre-distortion filters that precisely provide activation waveforms that minimize out-of-band radiation.

The beam-space multiplexing approach with purely reactive loading proposed in this thesis, is confined to the modulation formats whose chosen constellation points are positioned on the unit circle, such as PSK and minimum-shift keying (MSK). Modern modulation schemes such as orthogonal frequency-division multiplexing (OFDM) convert simple constant envelope modulations into highly complex analogue modulation waveforms, which are extremely difficult to emulate with realistic beam-space MIMO hardware. Hence, the beam-space MIMO approach is more likely to find its way to several RF transceiver architectures like the ones used in wireless sensor nodes as well as wireless modems supporting constant envelope signal formats. PSK is widely utilized in existing applications and standards due to its constant amplitude of the modulated carrier signal. Particularly, the standards IEEE 802.15.1 (Blue tooth), IEEE 802.15.4 (ZigBee), IEEE 802.15.6 and ISO/IEC 1443 (identification cards) uses a variety of PSK schemes depending on the application requirements such as noise/interference resistance, spectral efficiency, hardware complexity, and power consumption. The IEEE 802.15.6 standard, targeting the wireless body area network (WBAN) medical and non-medical applications, also uses digital phase modulations such as Gaussian minimum-shift keying (GMSK) and differential phase shift keying (DPSK). Medical applications of WBAN appear in the health-care area, such as collection and transmission of vital information of patients to a remote monitoring station. On the other hand, gaming and social networking applications of WBAN

Chapter 8. Conclusions and Perspectives

are increasingly considered. The ability to transmit high data-rate bursts as enabled by the beam-space MIMO technique might help further reducing duty cycle in some very low power applications such as WBAN, hence leading to extra power saving.

Another possible future area in which the beam-space technique can be used, is impulse radio communications in unlicensed bandwidth around 60 GHz. The simple use of the proposed technique in multiplexing two PSK signals can yield higher data rates than that of current ultra-wideband impulse radio configurations. Moreover, it can be shown that a beam-space MIMO antenna, in its current forms, can support multiplexed transmission of a PSK signal simultaneous with any other modulated signal (e.g., a 256-QAM datastream). This feature might find applications in secure communications.

Finally, it is very important to note that the hardware used for the beam-space MIMO technique can readily be used to achieve gains other than straightforward spatial multiplexing. Indeed, the developed antenna hardware can be used to operate in the following modes.

- On the transmitting side for spatial multiplexing. This is the baseline functionality described in this thesis.
- On the transmitting side for space-time coding diversity.
- On the transmitting side for beam-forming in highly dynamic wireless environments by dynamically selecting the best available pattern.
- On the receiving side for receive pattern diversity, namely, slow pattern reconfiguration to dynamically compensate for channel variation, or rapid pattern switching for over-sampling in the receive mode. This can also be useful for analogue diversity at the user terminal in multi-user MIMO.

A PSK Constrained MIMO Capacity

By definition, the capacity determines a fundamental limit on the transmission rates of the MIMO channel with an unrestricted input. However, the discrete capacity, i.e., the mutual information between the inputs from a finite alphabet and continuous outputs, apparently makes more practical sense for actual MIMO systems, which employ finite modulation techniques such as PSK and QAM. The evaluation of the discrete capacity has been the subject of numerous studies over the last years (for instance, see [114–119]). In the following, we briefly discuss the PSK input-constrained MIMO capacity, from the mathematical formulation directly based on the definition to its calculation approach.

Let us recall the $P \times Q$ MIMO channel described in Section 2.2 by $\mathbf{y} = \mathbf{H}\mathbf{x} + \mathbf{n}$. The M -ary PSK input constraint can be enforced by defining the input vector as

$$\mathbf{x} \in \mathbf{X} \triangleq \left\{ [x_1, x_2, \dots, x_P]^T \mid x_p = \frac{1}{\sqrt{P}} \exp\left(\frac{j2\pi m}{M}\right), 1 \leq p \leq P, 0 \leq m \leq M-1 \right\}. \quad (\text{A.1})$$

The definition of \mathbf{X} also ensures uniform power allocation at the baseband of the transmitter. Therefore, the average energy applied to each transmit radiation pattern is $1/P$. We assume that elements of \mathbf{H} are complex random variables, each with variance of 1 and mean of 0, whereas elements of \mathbf{n} are i.i.d. complex Gaussian random variables $\sim \mathcal{N}_c(0, \sigma^2)$, where $\sigma^2 = 1/\gamma_s$, and γ_s denotes the symbol SNR or the energy-per-symbol to noise-power-spectral-density ratio (E_s/N_0) [116].

Under the assumption that the input vector, \mathbf{x} , and the channel matrix, \mathbf{H} , are independent, the average mutual information between \mathbf{x} and \mathbf{y} , with the channel realization \mathbf{H} known at the receiver, is given by

$$I(\mathbf{x}; \mathbf{y}) = \mathbb{E}_{\mathbf{H}} \{ I(\mathbf{x}; \mathbf{y} | \mathbf{H}) \}, \quad (\text{A.2})$$

where $I(\mathbf{x}; \mathbf{y} | \mathbf{H})$ denotes the instantaneous mutual information between \mathbf{x} and \mathbf{y} [118], and is

Appendix A. PSK Constrained MIMO Capacity

defined as

$$\begin{aligned}
 I(\mathbf{x}; \mathbf{y} | \mathbf{H}) &= H(\mathbf{x} | \mathbf{H}) - H(\mathbf{x} | \mathbf{y}, \mathbf{H}) \\
 &= P \log_2 M - \frac{1}{M^P} \sum_{m=1}^{M^P} \mathbb{E}_{\mathbf{n}} \left\{ \log_2 \sum_{q=1}^{M^P} \exp \left(-\frac{\|\mathbf{H}\mathbf{x}_m + \mathbf{n} - \mathbf{H}\mathbf{x}_q\|^2 - \|\mathbf{n}\|^2}{\sigma^2} \right) \right\}, \quad (\text{A.3})
 \end{aligned}$$

where $H(\cdot)$ is the entropy function. Hence, it follows from (A.2) and (A.3) that

$$I(\mathbf{x}; \mathbf{y}) = P \log_2 M - \frac{1}{M^P} \mathbb{E}_{\mathbf{H}} \left\{ \sum_{m=1}^{M^P} \mathbb{E}_{\mathbf{n}} \left\{ \log_2 \sum_{q=1}^{M^P} \exp \left(-\frac{\|\mathbf{H}\mathbf{x}_m + \mathbf{n} - \mathbf{H}\mathbf{x}_q\|^2 - \|\mathbf{n}\|^2}{\sigma^2} \right) \right\} \right\}. \quad (\text{A.4})$$

Numerical evaluation of (A.4), however, is computationally complex using conventional methods since it contains multi-variate numerical integrals and summations. The problem can be overcome by using Monte Carlo integration to evaluate the expectations. Monte-Carlo integration is performed by evaluating the function of interest at a number of random points, following a certain sampling distribution, and averaging the function values over these points [120–122].

Bibliography

- [1] G. J. Foschini and M. J. Gans, "On limits of wireless communications in a fading environment when using multiple antennas," *Wireless Personal Communications*, vol. 6, pp. 311–335, 1998.
- [2] E. Telatar, "Capacity of multi-antenna gaussian channels," *European Transactions on Telecommunications*, vol. 10, pp. 585–595, 1999.
- [3] C. Oestges and B. Clerckx, *MIMO Wireless Communications: From Real-World Propagation to Space-Time Code Design*. Orlando, FL, USA: Academic Press, Inc., 2007.
- [4] A. Tulino, A. Lozano, and S. Verdu, "Impact of antenna correlation on the capacity of multi-antenna channels," *IEEE Transactions on Information Theory*, vol. 51, no. 7, pp. 2491–2509, July 2005.
- [5] F. De Flaviis, L. Jofre, M. . C. Publishers, and R. Jordi, *Multiantenna Systems for MIMO Communications*, ser. Synthesis Lectures on Antennas and Propagation Series. Morgan & Claypool Publishers, 2008. [Online]. Available: <http://books.google.ch/books?id=Gz-2adSCk0gC>
- [6] S. Dossche, S. Blanch, and J. Romeu, "Optimum antenna matching to minimise signal correlation on a two-port antenna diversity system," *Electronics Lett.*, vol. 40, no. 19, pp. 1164–1165, 2004.
- [7] J. Wallace and M. Jensen, "Termination-dependent diversity performance of coupled antennas: network theory analysis," *IEEE Trans. Antennas Propag.*, vol. 52, no. 1, pp. 98–105, 2004.
- [8] S. Sanayei and A. Nosratinia, "Antenna selection in MIMO systems," *IEEE Commun. Mag.*, vol. 42, no. 10, pp. 68–73, 2004.
- [9] I. Bahceci, T. Duman, and Y. Altunbasak, "Antenna selection for multiple-antenna transmission systems: performance analysis and code construction," *IEEE Transactions on Information Theory*, vol. 49, no. 10, pp. 2669–2681, Oct 2003.
- [10] I. t. Santamaria, "Optimal MIMO transmission schemes with adaptive antenna combining in the RF path," in *Eur. Signal Process. Conf. (EUSIPCO 2008)*, 2008.

Bibliography

- [11] F. Gholam, J. Via, and I. Sanatamaria, "Beamforming design for simplified analog antenna combining architectures," *IEEE Transactions on Vehicular Technology*, vol. 60, no. 5, pp. 2373–2378, Jun 2011.
- [12] M. Lari, S. Bassam, A. Mohammadi, and F. Ghannouchi, "Time-multiplexed single front-end multiple-input multiple-output receivers with preserved diversity gain," *IET Commun.*, vol. 5, no. 6, pp. 789–796, 2011.
- [13] F. Tzeng, A. Jahanian, D. Pi, and P. Heydari, "A CMOS code-modulated path-sharing multi-antenna receiver front-end," *IEEE J. Solid-State Circuits*, vol. 44, no. 5, pp. 1321–1335, 2009.
- [14] R. Mesleh, H. Haas, S. Sinanovic, C. W. Ahn, and S. Yun, "Spatial modulation," *Vehicular Technology, IEEE Transactions on*, vol. 57, no. 4, pp. 2228–2241, July 2008.
- [15] Y. Chau and S.-H. Yu, "Space modulation on wireless fading channels," in *54th IEEE Vehicular Technology Conference*, vol. 3, 2001, pp. 1668–1671.
- [16] M. Di Renzo, H. Haas, and P. M. Grant, "Spatial modulation for multiple-antenna wireless systems: a survey," *IEEE Commun. Mag.*, vol. 49, no. 12, pp. 182–191, 2011.
- [17] A. Kalis, A. Kanatas, and C. Papadias, "A novel approach to MIMO transmission using a single RF front end," *IEEE J. Sel. Areas Commun.*, vol. 26, no. 6, pp. 972–980, 2008.
- [18] *Parasitic antenna arrays for wireless MIMO systems*. Springer, 2014, ch. Design and implementation of parasitic antenna arrays for BeamSpace-MIMO.
- [19] M. Yousefbeiki and J. Perruisseau-Carrier, "Towards compact and frequency-tunable antenna solutions for MIMO transmission with a single RF chain," *IEEE Transactions on Antennas and Propagation*, vol. 62, no. 3, pp. 1065–1073, March 2014.
- [20] —, "Pattern-reconfigurable built-in antenna for data multiplexing with a single radio," in *7th European Conference on Antennas and Propagation (EuCAP)*, April 2013, pp. 515–518.
- [21] —, "A practical technique for accurately modeling reconfigurable lumped components in commercial full-wave solvers [europaap corner]," *IEEE Antennas and Propagation Magazine*, vol. 54, no. 5, pp. 298–303, Oct 2012.
- [22] M. Yousefbeiki, O. Alrabadi, and J. Perruisseau-Carrier, "Efficient MIMO transmission of PSK signals with a single-radio reconfigurable antenna," *IEEE Transactions on Communications*, vol. 62, no. 2, pp. 567–577, February 2014.
- [23] M. Yousefbeiki, A. P. Burg, and J. Perruisseau-Carrier, "Spatial multiplexing of QPSK signals with a single radio: antenna design and over-the-air experiments," submitted to *IEEE Transactions on Antennas and Propagation*.

-
- [24] M. Yousefbeiki, A. Austin, J. R. Mosig, and A. P. Burg, "Performance analysis of beam-space MIMO in real channels," submitted to *IEEE Transactions on Antennas and Propagation*.
- [25] M. Yousefbeiki, H. Najibi, and J. Perruisseau-Carrier, "User effects in beam-space MIMO," *IEEE Antennas and Wireless Propagation Letters*, vol. 12, pp. 1716–1719, 2013.
- [26] M. Yousefbeiki, J. R. Mosig, and A. P. Burg, "Effect of external perturbation on constellation points in beam-space MIMO," submitted to *IEEE Antennas and Wireless Propagation Letters*.
- [27] —, "Effect of external perturbation on constellation points in beam-space MIMO," in *9th European Conference on Antennas and Propagation (EuCAP)*, April 2015.
- [28] M. Yousefbeiki, P. Belanovic, A. P. Burg, and J. Perruisseau-Carrier, "True MIMO transmission using a single RF-chain and antenna: recent developments," in *8th European Conference on Antennas and Propagation (EuCAP)*, April 2014.
- [29] C. nee Chuah, J. M. Kahn, and D. Tse, "Capacity of multi-antenna array systems in indoor wireless environment," in *IEEE Globecom*, 1998, pp. 1894–1899.
- [30] D. shan Shiu, G. Foschini, M. Gans, and J. Kahn, "Fading correlation and its effect on the capacity of multielement antenna systems," *IEEE Transactions on Communications*, vol. 48, no. 3, pp. 502–513, Mar 2000.
- [31] A. Sayeed, "Deconstructing multiantenna fading channels," *IEEE Transactions on Signal Processing*, vol. 50, no. 10, pp. 2563–2579, Oct 2002.
- [32] V. Veeravalli, Y. Liang, and A. Sayeed, "Correlated MIMO wireless channels: capacity, optimal signaling, and asymptotics," *IEEE Transactions on Information Theory*, vol. 51, no. 6, pp. 2058–2072, June 2005.
- [33] W. Weichselberger, M. Herdin, H. Ozelik, and E. Bonek, "A stochastic MIMO channel model with joint correlation of both link ends," *IEEE Transactions on Wireless Communications*, vol. 5, no. 1, pp. 90–100, Jan 2006.
- [34] C. Waldschmidt, S. Schulteis, and W. Wiesbeck, "Complete rf system model for analysis of compact MIMO arrays," *IEEE Transactions on Vehicular Technology*, vol. 53, no. 3, pp. 579–586, May 2004.
- [35] M. Shafi, M. Zhang, A. Moustakas, P. Smith, A. Molisch, F. Tufvesson, and S. Simon, "Polarized MIMO channels in 3-D: models, measurements and mutual information," *IEEE Journal on Selected Areas in Communications*, vol. 24, no. 3, pp. 514–527, March 2006.
- [36] F. Sharifabad, M. Jensen, and Z. Yun, "Closed-form evaluation of the MIMO channel spatial covariance," *IEEE Transactions on Antennas and Propagation*, vol. 61, no. 2, pp. 901–909, Feb 2013.

Bibliography

- [37] D. Pozar, "The active element pattern," *IEEE Transactions on Antennas and Propagation*, vol. 42, no. 8, pp. 1176–1178, 1994.
- [38] A. Tulino, A. Lozano, and S. Verdu, "Impact of antenna correlation on the capacity of multiantenna channels," *IEEE Transactions on Information Theory*, vol. 51, no. 7, pp. 2491–2509, July 2005.
- [39] E. Jorswieck and H. Boche, "Optimal transmission strategies and impact of correlation in multiantenna systems with different types of channel state information," *IEEE Transactions on Signal Processing*, vol. 52, no. 12, pp. 3440–3453, Dec 2004.
- [40] D. Chizhik, G. Foschini, M. Gans, and R. Valenzuela, "Keyholes, correlations, and capacities of multielement transmit and receive antennas," *IEEE Transactions on Wireless Communications*, vol. 1, no. 2, pp. 361–368, Apr 2002.
- [41] R. Nabar, H. Bolcskei, V. Erceg, D. Gesbert, and A. Paulraj, "Performance of multiantenna signaling techniques in the presence of polarization diversity," *IEEE Transactions on Signal Processing*, vol. 50, no. 10, pp. 2553–2562, Oct 2002.
- [42] C. Waldschmidt and W. Wiesbeck, "Compact wide-band multimode antennas for MIMO and diversity," *IEEE Transactions on Antennas and Propagation*, vol. 52, no. 8, pp. 1963–1969, Aug 2004.
- [43] A. Grau, J. Romeu, S. Blanch, L. Jofre, and F. De Flaviis, "Optimization of linear multielement antennas for selection combining by means of a butler matrix in different MIMO environments," *IEEE Transactions on Antennas and Propagation*, vol. 54, no. 11, pp. 3251–3264, Nov 2006.
- [44] R. Ramirez-Gutierrez, L. Zhang, J. Elmirghani, and A. Almutairi, "Antenna beam pattern modulation for MIMO channels," in *8th International Wireless Communications and Mobile Computing Conference (IWCMC)*, Aug 2012, pp. 591–595.
- [45] R. Ramirez-Gutierrez, L. Zhang, and J. Elmirghani, "Antenna pattern shift keying modulation for MIMO channels," in *Proceedings of the 19th European Wireless Conference (EW)*, April 2013, pp. 1–5.
- [46] A. Kalis, C. Papadias, and A. Kanatas, "An ESPAR antenna for beamspace-MIMO systems using PSK modulation schemes," in *IEEE International Conference on Communications*, June 2007, pp. 5348–5353.
- [47] V. Barousis, A. Kanatas, A. Kalis, and C. Papadias, "A stochastic beamforming algorithm for ESPAR antennas," *IEEE Antennas and Wireless Propagation Letters*, vol. 7, pp. 745–748, 2008.
- [48] E. Thomatos, P. Vasileiou, and A. Kanatas, "Genetic algorithm applied to beamspace-multiple-input and multiple-output single-radio frequency front-end reconfigurable transceivers," *IET Microwaves, Antennas Propagation*, vol. 8, no. 9, pp. 679–687, June 2014.

- [49] O. Alrabadi, C. Papadias, A. Kalis, N. Marchetti, and R. Prasad, "MIMO transmission and reception techniques using three-element ESPAR antennas," *IEEE Communications Letters*, vol. 13, no. 4, pp. 236–238, April 2009.
- [50] O. Alrabadi, A. Kalis, C. Papadias, and A. Kanatas, "Spatial multiplexing by decomposing the far-field of a compact ESPAR antenna," in *IEEE 19th International Symposium on Personal, Indoor and Mobile Radio Communications*, Sept 2008, pp. 1–5.
- [51] O. Alrabadi, C. Papadias, A. Kalis, and R. Prasad, "A universal encoding scheme for MIMO transmission using a single active element for PSK modulation schemes," *IEEE Transactions on Wireless Communications*, vol. 8, no. 10, pp. 5133–5142, 2009.
- [52] V. Barousis, A. Kanatas, and A. Kalis, "Beamspace-domain analysis of single-RF front-end MIMO systems," *IEEE Transactions on Vehicular Technology*, vol. 60, no. 3, pp. 1195–1199, 2011.
- [53] V. Barousis and A. G. Kanatas, "Aerial degrees of freedom of parasitic arrays for single RF front-end MIMO transceivers," *Progress In Electromagnetics Research B*, 2011.
- [54] O. Alrabadi, J. Perruisseau-Carrier, and A. Kalis, "MIMO transmission using a single RF source: Theory and antenna design," *IEEE Transactions on Antennas and Propagation*, vol. 60, no. 2, pp. 654–664, 2012.
- [55] J. Perruisseau-Carrier, O. Alrabadi, and A. Kalis, "Implementation of a reconfigurable parasitic antenna for beam-space BPSK transmissions," in *2010 European Microwave Conference (EuMC)*, 2010, pp. 644–647.
- [56] O. Alrabadi, C. Divarathne, P. Tragas, A. Kalis, N. Marchetti, C. Papadias, and R. Prasad, "Spatial multiplexing with a single radio: Proof-of-concept experiments in an indoor environment with a 2.6-GHz prototype," *IEEE Communications Letters*, vol. 15, no. 2, pp. 178–180, February 2011.
- [57] P. Vasileiou, K. Maliatsos, E. Thomatos, and A. Kanatas, "Reconfigurable orthonormal basis patterns using ESPAR antennas," *IEEE Antennas and Wireless Propagation Letters*, vol. 12, pp. 448–451, 2013.
- [58] K. Maliatsos, P. N. Vasileiou, and A. G. Kanatas, "V-BLAST reception for beamspace MIMO systems with limited feedback," in *IEEE 24th International Symposium on Personal Indoor and Mobile Radio Communications (PIMRC)*, Sept 2013, pp. 1034–1039.
- [59] K. Maliatsos, P. Vasileiou, and A. Kanatas, "Channel estimation and link level evaluation of adaptive beamspace MIMO systems," in *3rd International Conference on Wireless Communications, Vehicular Technology, Information Theory and Aerospace Electronic Systems (VITAE)*, June 2013, pp. 1–5.
- [60] B. Han, V. Barousis, C. Papadias, A. Kalis, and R. Prasad, "MIMO over ESPAR with 16-QAM modulation," *IEEE Wireless Communications Letters*, vol. 2, no. 6, pp. 687–690, December 2013.

Bibliography

- [61] V. Barousis and C. Papadias, "Arbitrary precoding with single-fed parasitic arrays: Closed-form expressions and design guidelines," *IEEE Wireless Communications Letters*, vol. 3, no. 2, pp. 229–232, April 2014.
- [62] B. Schaer, K. Rambabu, J. Bornemann, and R. Vahldieck, "Design of reactive parasitic elements in electronic beam steering arrays," *Antennas and Propagation, IEEE Transactions on*, vol. 53, no. 6, pp. 1998–2003, June 2005.
- [63] Y. Nakane, T. Noguchi, and Y. Kuwahara, "Trial model of adaptive antenna equipped with switched loads on parasitic elements," *IEEE Transactions on Antennas and Propagation*, vol. 53, no. 10, pp. 3398–3402, 2005.
- [64] R. Vaughan, "Switched parasitic elements for antenna diversity," *IEEE Transactions on Antennas and Propagation*, vol. 47, no. 2, pp. 399–405, Feb 1999.
- [65] D. Wilcox, E. Tsakalaki, A. Kortun, T. Ratnarajah, C. Papadias, and M. Sellathurai, "On spatial domain cognitive radio using single-radio parasitic antenna arrays," *IEEE Journal on Selected Areas in Communications*, vol. 31, no. 3, pp. 571–580, March 2013.
- [66] R. Harrington, "Reactively controlled directive arrays," *IEEE Transactions on Antennas and Propagation*, vol. 26, no. 3, pp. 390–395, 1978.
- [67] R. Schlub and D. V. Thiel, "Switched parasitic antenna on a finite ground plane with conductive sleeve," *IEEE Transactions on Antennas and Propagation*, vol. 52, no. 5, pp. 1343–1347, May 2004.
- [68] H. Kawakami and T. Ohira, "Electrically steerable passive array radiator (ESPAR) antennas," *IEEE Antennas and Propagation Magazine*, vol. 47, no. 2, pp. 43–50, April 2005.
- [69] M. Wennstrom and T. Svantesson, "An antenna solution for MIMO channels: the switched parasitic antenna," in *12th IEEE International Symposium on Personal, Indoor and Mobile Radio Communications*, vol. 1, Sep 2001, pp. 159–163.
- [70] T. Taga and K. Tsunekawa, "Performance analysis of a built-in planar inverted F antenna for 800 MHz band portable radio units," *IEEE Journal on Selected Areas in Communications*, vol. 5, no. 5, pp. 921–929, Jun 1987.
- [71] Z. Du, K. Gong, J. Fu, B. Gao, and Z. Feng, "A compact planar inverted-F antenna with a PBG-type ground plane for mobile communications," *IEEE Transactions on Vehicular Technology*, vol. 52, no. 3, pp. 483–489, May 2003.
- [72] K. Fujimoto, *Mobile Antenna Systems Handbook*, ser. Artech House antennas and propagation library. Artech House, 2008. [Online]. Available: <http://books.google.ch/books?id=VbCCJhjO4OcC>
- [73] C. Rowell and R. Murch, "A capacitively loaded PIFA for compact mobile telephone handsets," *IEEE Transactions on Antennas and Propagation*, vol. 45, no. 5, pp. 837–842, May 1997.

- [74] M. Islam and M. Ali, "Elevation plane beam scanning of a novel parasitic array radiator antenna for 1900 MHz mobile handheld terminals," *IEEE Transactions on Antennas and Propagation*, vol. 58, no. 10, pp. 3344–3352, Oct 2010.
- [75] L. Petit, L. Dussopt, and J.-M. Laheurte, "MEMS-switched parasitic-antenna array for radiation pattern diversity," *IEEE Transactions on Antennas and Propagation*, vol. 54, no. 9, pp. 2624–2631, 2006.
- [76] S. Stein, "On cross coupling in multiple-beam antennas," *IRE Transactions on Antennas and Propagation*, vol. 10, no. 5, pp. 548–557, 1962.
- [77] A. Grau, J. Romeu, M.-J. Lee, S. Blanch, L. Jofre, and F. De Flaviis, "A dual-linearly-polarized MEMS-reconfigurable antenna for narrowband MIMO communication systems," *IEEE Transactions on Antennas and Propagation*, vol. 58, no. 1, pp. 4–17, Jan 2010.
- [78] O. Bayraktar, O. Civi, and T. Akin, "Beam switching reflectarray monolithically integrated with RF MEMS switches," *IEEE Transactions on Antennas and Propagation*, vol. 60, no. 2, pp. 854–862, Feb 2012.
- [79] J. Perruisseau-Carrier, P. Pardo-Carrera, and P. Miskovsky, "Modeling, design and characterization of a very wideband slot antenna with reconfigurable band rejection," *IEEE Transactions on Antennas and Propagation*, vol. 58, no. 7, pp. 2218–2226, July 2010.
- [80] J. Perruisseau-Carrier, K. Topalli, and T. Akin, "Low-loss Ku-band artificial transmission line with MEMS tuning capability," *IEEE Microwave and Wireless Components Letters*, vol. 19, no. 6, pp. 377–379, June 2009.
- [81] M. Hamid, P. Gardner, P. Hall, and F. Ghanem, "Switched-band Vivaldi antenna," *IEEE Transactions on Antennas and Propagation*, vol. 59, no. 5, pp. 1472–1480, May 2011.
- [82] A. Clemente, L. Dussopt, R. Sauleau, P. Potier, and P. Pouliguen, "1-bit reconfigurable unit cell based on PIN diodes for transmit-array applications in X-band," *IEEE Transactions on Antennas and Propagation*, vol. 60, no. 5, pp. 2260–2269, May 2012.
- [83] J. Lau and S. Hum, "Analysis and characterization of a multipole reconfigurable transmitarray element," *IEEE Transactions on Antennas and Propagation*, vol. 59, no. 1, pp. 70–79, Jan 2011.
- [84] W. Cheney and D. Kincaid, *Linear Algebra: Theory and Applications*, ser. Jones & Bartlett Learning International Series in Mathematic. Jones & Bartlett Learning, 2010. [Online]. Available: <http://books.google.ch/books?id=S0imN2t11qwC>
- [85] G. F. Engen and C. A. Hoer, "Thru-Reflect-Line: An improved technique for calibrating the dual six-port automatic network analyzer," *IEEE Transactions on Microwave Theory and Techniques*, vol. 27, no. 12, pp. 987–993, Dec 1979.

Bibliography

- [86] J. Perruisseau-Carrier, F. Bongard, R. Golubovic-Niciforovic, R. Torres-Sanchez, and J. Mosig, "Contributions to the modeling and design of reconfigurable reflecting cells embedding discrete control elements," *IEEE Transactions on Microwave Theory and Techniques*, vol. 58, no. 6, pp. 1621–1628, June 2010.
- [87] J. Kermaol, L. Schumacher, K. Pedersen, P. Mogensen, and F. Frederiksen, "A stochastic MIMO radio channel model with experimental validation," *IEEE Journal on Selected Areas in Communications*, vol. 20, no. 6, pp. 1211–1226, 2002.
- [88] J. Mitola and J. Maguire, G.Q., "Cognitive radio: making software radios more personal," *IEEE Personal Communications*, vol. 6, no. 4, pp. 13–18, Aug 1999.
- [89] S. Haykin, "Cognitive radio: brain-empowered wireless communications," *IEEE Journal on Selected Areas in Communications*, vol. 23, no. 2, pp. 201–220, Feb 2005.
- [90] R. Bains and R. Muller, "Using parasitic elements for implementing the rotating antenna for MIMO receivers," *IEEE Transactions on Wireless Communications*, vol. 7, no. 11, pp. 4522–4533, November 2008.
- [91] S. Mason and H. Zimmermann, *Electronic circuits, signals, and systems*. Wiley, 1965.
- [92] R. Hassun, M. Flaherty, R. Matrecci, and M. Taylor, "Effective evaluation of link quality using error vector magnitude techniques," in *Wireless Communications Conference*, Aug 1997, pp. 89–94.
- [93] O. Souihli and T. Ohtsuki, "Benefits of rich scattering in MIMO channels: A graph-theoretical perspective," *IEEE Communications Letters*, vol. 17, no. 1, pp. 23–26, January 2013.
- [94] J. Wallace and M. Jensen, "Modeling the indoor MIMO wireless channel," *IEEE Transactions on Antennas and Propagation*, vol. 50, no. 5, pp. 591–599, May 2002.
- [95] A. Paulraj, D. GORE, R. Nabar, and H. Bolcskei, "An overview of MIMO communications - a key to gigabit wireless," *Proceedings of the IEEE*, vol. 92, no. 2, pp. 198–218, Feb 2004.
- [96] C. Wang, E. Au, R. Murch, W. H. Mow, R. Cheng, and V. Lau, "On the performance of the MIMO zero-forcing receiver in the presence of channel estimation error," *IEEE Transactions on Wireless Communications*, vol. 6, no. 3, pp. 805–810, March 2007.
- [97] National Instruments, "Software Defined Radio," Available: <http://www.ni.com/sdr/>.
- [98] —, "LabVIEW System Design Software," Available: <http://www.ni.com/labview/>.
- [99] —, "NI FlexRIO," Available: <http://www.ni.com/flexrio/>.
- [100] —, "USRP," Available: <http://www.ni.com/sdr/usrp/>.
- [101] T. Schmidl and D. Cox, "Robust frequency and timing synchronization for OFDM," *IEEE Transactions on Communications*, vol. 45, no. 12, pp. 1613–1621, Dec 1997.

- [102] Makeblock, "XY-Plotter Robot Kit," Available: <http://www.makeblock.cc/xy-plotter-robot-kit-v2-0-with-electronic/>.
- [103] J. Salo, P. Suvikunnas, H. El-Sallabi, and P. Vainikainen, "Ellipticity statistic as measure of MIMO multipath richness," *Electronics Letters*, vol. 42, no. 3, pp. 160–162, Feb 2006.
- [104] J. Toftgard, S. Hornsleth, and J. Andersen, "Effects on portable antennas of the presence of a person," *IEEE Transactions on Antennas and Propagation*, vol. 41, no. 6, pp. 739–746, Jun 1993.
- [105] J. Krogerus, J. Toivanen, C. Icheln, and P. Vainikainen, "Effect of the human body on total radiated power and the 3-D radiation pattern of mobile handsets," *IEEE Transactions on Instrumentation and Measurement*, vol. 56, no. 6, pp. 2375–2385, Dec 2007.
- [106] N. Chavannes, R. Tay, N. Nikoloski, and N. Kuster, "Suitability of FDTD-based TCAD tools RF design of mobile phones," *IEEE Antennas and Propagation Magazine*, vol. 45, no. 6, pp. 52–66, Dec 2003.
- [107] W. Yu, S. Yang, C.-L. Tang, and D. Tu, "Accurate simulation of the radiation performance of a mobile slide phone in a hand-head position," *IEEE Antennas and Propagation Magazine*, vol. 52, no. 2, pp. 168–177, April 2010.
- [108] J. Holopainen, O. Kivekas, J. Ilvonen, R. Valkonen, C. Icheln, and P. Vainikainen, "Effect of the user's hands on the operation of lower UHF-band mobile terminal antennas: Focus on digital television receiver," *IEEE Transactions on Electromagnetic Compatibility*, vol. 53, no. 3, pp. 831–841, Aug 2011.
- [109] K. Fujimoto and J. James, *Mobile Antenna Systems Handbook*, ser. Antennas and Propagation Library. Artech House, 2001. [Online]. Available: <https://books.google.ch/books?id=TWlwRSYIpKAC>
- [110] CST, "CST MICROWAVE STUDIO," Available: <https://www.cst.com/Products/CSTMWS>.
- [111] R. Tian, B. K. Lau, and Z. Ying, "Multiplexing efficiency of MIMO antennas," *IEEE Antennas and Wireless Propagation Letters*, vol. 10, pp. 183–186, 2011.
- [112] C. Gabriel, "Tissue equivalent material for hand phantoms," *Physics in Medicine and Biology*, vol. 52, no. 14, p. 4205, 2007. [Online]. Available: <http://stacks.iop.org/0031-9155/52/i=14/a=012>
- [113] W. Tranter, K. Shanmugan, T. Rappaport, and K. Kosbar, *Principles of Communication Systems Simulation with Wireless Applications*, 1st ed. Upper Saddle River, NJ, USA: Prentice Hall Press, 2003.
- [114] B. Hochwald and S. ten Brink, "Achieving near-capacity on a multiple-antenna channel," *IEEE Transactions on Communications*, vol. 51, no. 3, pp. 389–399, March 2003.

Bibliography

- [115] J. Baltersee, G. Fock, and H. Meyr, "Achievable rate of MIMO channels with data-aided channel estimation and perfect interleaving," *IEEE Journal on Selected Areas in Communications*, vol. 19, no. 12, pp. 2358–2368, Dec 2001.
- [116] W. He and C. Georghiades, "Computing the capacity of a MIMO fading channel under PSK signaling," *IEEE Transactions on Information Theory*, vol. 51, no. 5, pp. 1794–1803, May 2005.
- [117] K. Kato, M. Osaki, M. Sasaki, and O. Hirota, "Quantum detection and mutual information for QAM and PSK signals," *IEEE Transactions on Communications*, vol. 47, no. 2, pp. 248–254, Feb 1999.
- [118] C. Xiao and Y. Zheng, "On the mutual information and power allocation for vector Gaussian channels with finite discrete inputs," in *IEEE Global Telecommunications Conference*, Nov 2008, pp. 1–5.
- [119] C. Xiao, Y. Zheng, and Z. Ding, "Globally optimal linear precoders for finite alphabet signals over complex vector Gaussian channels," *IEEE Transactions on Signal Processing*, vol. 59, no. 7, pp. 3301–3314, July 2011.
- [120] G. Ungerboeck, "Channel coding with multilevel/phase signals," *IEEE Transactions on Information Theory*, vol. 28, no. 1, pp. 55–67, Jan 1982.
- [121] K. Shanmugam and P. Balaban, "A modified Monte-Carlo simulation technique for the evaluation of error rate in digital communication systems," *IEEE Transactions on Communications*, vol. 28, no. 11, pp. 1916–1924, Nov 1980.
- [122] G. Kramer, I. Marić, and R. D. Yates, "Cooperative communications," *Foundations and Trends® in Networking*, vol. 1, no. 3-4, pp. 271–425, 2007.

MOHSEN YOUSEFBEIKI

Rue de la Blancherie 29
1022 Chavannes-près-Renens, Switzerland
Tel: +41 78 824 4975
E-mail: yousefbei@gmail.com

30.07.1983
Swiss B permit
Married



EXECUTIVE SUMMARY

- » PhD Degree from Ecole Polytechnique Fédérale de Lausanne (EPFL)
- » Antenna Design Specialist with experience on RF/Microwave Circuit and System Design
- » Experienced at working at the crossroad of pure EM concepts and Radio Coding techniques
- » Interested in interdisciplinary and frontier topics in Electrical Engineering

RESEARCH INTERESTS

- » Antenna Theory and Design
- » Wireless Communications
- » RF and Microwave Circuit and System Design
- » Numerical Methods in EM and Optics
- » Signal Processing and Optimization

EDUCATION

10.2010-07.2015 PhD in Electrical Engineering at EPFL, Switzerland

- » Doctoral assistant at the Laboratory of Electromagnetics and Acoustics (LEMA)
- » Thesis: Reconfigurable Antennas for Beam-Space MIMO Transmission with a Single Radio
- » Advisors: late Prof. J. Perruisseau-Carrier, Prof. J. R. Mosig, Prof. A. P. Burg

09.2005-03.2008 Master in Electrical Engineering at University of Tehran, Iran

- » Major in Telecommunications, Fields and Waves
- » Thesis: Analysis and Design of Feed Networks of Planar Antenna Arrays Implemented using SIW Technology
- » Advisors: Prof. M. Shahabadi, Prof. J. Rashed-Mohassel

09.2001-09.2005 Bachelor in Electrical Engineering at University of Tehran, Iran

- » Major in Telecommunications, Fields and Waves
- » Thesis: Gain Enhancement of Patch Antennas using Ground Plane Shaping

HONORS AND AWARDS

- » **2013**, Finalist of the ESoA-EuCAP young scientist award.
- » **2008**, Ranked 1st among M.Sc. graduates at College of Engineering.
- » **2005**, Among "Reserved Exceptional Students" to enter the Master program at University of Tehran without entrance exam.
- » **1996**, Ranked 1st in the nationwide scientific competitions among grade 7 (junior high school) students.

RESEARCH PROJECTS

PhD Thesis

Summary: Development of a novel and disruptive concept, called beam-space MIMO, for transmitting multiple data streams using a single RF chain and a compact reconfigurable antenna structure. The first ever integrated beam-space MIMO antennas for transmission of BPSK and QPSK data streams were designed and fabricated, and successfully employed for multiplexing data streams over the air. This work laid the foundation for highly efficient, small and low-cost MIMO terminal designs for various applications like wireless sensor nodes and wireless modems.

Keywords: Beam-space MIMO, reconfigurable antenna, reduced-complexity MIMO, single-radio MIMO, spatial multiplexing.

Achievements: one international patent, one book chapter, six journal papers, four conference papers.

Master Thesis

Summary: Analysis and design of feed networks of planar antenna arrays implemented using substrate integrated waveguide (SIW) technology. First, a 16×8 microstrip antenna array using a parallel-series feed with reduced conductor traces was designed and fabricated. The feed network connects antenna elements with about 50% reduction in conductor traces compared to the conventional arrays with equal number of radiating elements. Second, feed networks of microstrip antenna arrays using SIW technology in one-layer or two-layer configurations were realized, aiming at reducing unwanted feed radiation along with typical advantages of planar structures.

Keywords: feed network, microstrip antennas, planar antenna arrays, substrate integrated waveguide.

Achievements: two journal papers, two conference papers.

PROFESSIONAL EXPERIENCE

- 10.2014-01.2015 ETRI (Electronics and Telecommunications Research Institute, Korea) - EPFL**
- » Design/Measurement Engineer
 - » Performance analysis of beam-space MIMO systems in real indoor environments.
- 10.2013-03.2014 ETRI (Electronics and Telecommunications Research Institute, Korea) - EPFL**
- » Antenna System Design Engineer
 - » The first ever fully-functional QPSK multiple-input-multiple-output (MIMO) antenna system using a single RF chain and a compact antenna was designed and fabricated in less than 4 months.
 - » The antenna system was successfully employed for multiplexing two QPSK data streams over the air, enabling spectral efficiency enhancement at a reduced RF complexity and cost.
- 04.2009-07.2010 Shahid Rezaei Research Center, Sharif University of Technology, Iran**
- » Antenna/Propagation Engineer, Manager of Antennas and Propagation Group
 - » Design and development of HF systems for very long-range communications through ionosphere
- 06.2006-03.2007 ITRC (Iran Telecommunication Research Center) – University of Tehran**
- » Design Engineer
 - » Design and fabrication of different microwave modules of a RF front-end on substrate integrated waveguide (SIW) for a digital microwave link at 18 GHz. The use of SIW technology in order to reduce radiation loss while aiming for low-profile and low-cost implementation.
- 06.2004-09.2004 Electronics Research and Production Co. (TAKTA), Iran**
- » Summer Intern
 - » Study and design of filters for high-power UHF transmitters.

PUBLICATIONS

Book Chapter:

- » Julien Perruisseau-Carrier and Mohsen Yousefbeiki, "Design and implementation of parasitic antenna arrays for beam-space-MIMO," Chapter in "Parasitic antenna arrays for wireless MIMO systems", Springer, 2014, pp. 149-170.

Patent:

- » Julien Perruisseau-Carrier and Mohsen Yousefbeiki, "MIMO antenna," International Patent, PCT/EP2013/070613.

Journals:

- » M. Yousefbeiki, A. Austin, J. R. Mosig and A. P. Burg, "Performance Analysis of beam-space MIMO in real indoor channels," submitted to *IEEE Transactions on Antennas and Propagation*.
- » M. Yousefbeiki, J. R. Mosig and A. P. Burg, "Effect of external perturbation on constellation points in beam-space MIMO," submitted to *IEEE Antennas and Wireless Propagation Letters*.
- » M. Yousefbeiki, A. P. Burg and J. Perruisseau-Carrier, "Spatial multiplexing of QPSK signals with a single radio: antenna design and over-the-air experiments," submitted to *IEEE Transactions on Antennas and Propagation*.
- » M. Yousefbeiki and J. Perruisseau-Carrier, "Efficient MIMO transmission of PSK signals with a single-radio reconfigurable antenna," *IEEE Transactions on Communications*, vol. 62, no. 2, pp. 567-577, 2014.

- » M. Yousefbei and J. Perruisseau-Carrier, "Towards compact and frequency-tunable antenna solutions for single-RF-chain MIMO," *IEEE Transactions on Antennas and Propagation*, vol. 62, no. 3, pp. 1065-1073, 2014.
- » M. Yousefbei, H. Najibi, and J. Perruisseau-Carrier, "User effects in beam-space MIMO," *IEEE Antennas and Wireless Propagation Letters*, vol. 12, pp. 1716-1719, 2013.
- » M. Yousefbei and J. Perruisseau-Carrier, "A practical technique to accurately model reconfigurable lumped components in commercial full-wave solvers," *IEEE Antennas and Propagation Magazine*, vol. 54, no. 5, pp. 298-303, Oct. 2012.
- » M. Yousefbei and M. Shahabadi, "Substrate-Integrated-Waveguide Feed Network for Microstrip Antenna Arrays," *Microwave and Optical Technology Letters*, vol. 51, no. 7, pp. 1619-1621, Jul. 2009.
- » M. Yousefbei, A. Enayati, M. Shahabadi, and D. Busuioc, "Parallel-series feed network with improved G/T performance for high-gain microstrip antenna arrays," *Electronics Letters*, vol. 44, no. 3, pp. 180-182, Jan. 2008.

Conferences:

- » M. Yousefbei, P. Belanovic, A. Burg, and J. Perruisseau-Carrier, "True MIMO transmission using a single RF-chain and antenna: Recent developments," in *8th European Conference on Antennas and Propagation (EUCAP'2014)*, The Hague, Netherlands, Apr. 2014, pp. 3438-3441.
- » M. Yousefbei and J. Perruisseau-Carrier, "Pattern-reconfigurable built-in antenna for data multiplexing with a single radio," in *7th European Conference on Antennas and Propagation (EUCAP'2013)*, Gothenburg, Sweden, Apr. 2013, pp. 515-518.
- » J. Perruisseau-Carrier, M. Yousefbei, O. N. Alrabadi, and A. Kalis, "Data multiplexing with a single antenna structure and front-end: antenna-coding techniques and design examples (invited)," in *IEEE International Symposium on Antennas and Propagation and USNC/URSI National Radio Science Meeting*, Chicago, IL, USA, Jul. 2012.
- » M. Yousefbei, A. A. Domenech, J. R. Mosig, and C. A. Fernandes, "Ku-Band dielectric-loaded SIW horn for vertically-polarized multi-sector antennas," in *6th European Conference on Antennas and Propagation (EUCAP'2012)*, Prague, Czech Republic, Mar. 2012, pp. 2367-2371.
- » M. Yousefbei, M. Abdolhamidi, A. Enayati, and M. Shahabadi, "A wideband slot-coupled substrate integrated waveguide (SIW)-to-microstrip power divider for microstrip array feed network," in *Applied Electromagnetics Conference*, Kolkata, India, Dec. 2007.
- » H. Aliakbarian, A. Enayati, M. Yousefbei, and M. Shahabadi, "Low-radiation-loss waveguide-to-microstrip transition using a double slit configuration for microstrip array feeding," in *Asia-Pacific Microwave Conference (APMC'07)*, Bangkok, Thailand, Dec. 2007, pp. 639-642.

COMPUTER SKILLS

Software Packages: MATLAB, Ansys HFSS, CST Microwave Studio, Agilent ADS, Ansoft Designer, FEKO, NI LabVIEW, Solidworks

Programming Skills: MATLAB, C++, R

LANGUAGES

Persian: Mother Tongue

English: Fluent

French: Beginner (A2-B1)

German: Beginner (A1)

REFERENCES

- » **Prof. Juan R. Mosig**, Professor of Electrical Engineering at EPFL, Lausanne, Switzerland
Email: juan.mosig@epfl.ch
- » **Prof. Andreas P. Burg**, Professor of Electrical Engineering at EPFL, Lausanne, Switzerland
Email: andreas.burg@epfl.ch
- » **Prof. Mahmoud Shahabadi**, Professor of Electrical Engineering at University of Tehran, Tehran, Iran
Email: shahabad@ut.ac.ir
- » **Prof. Reza Faraji-Dana**, Professor of Electrical Engineering at the University of Tehran, Tehran, Iran
Email: reza@ut.ac.ir